Atmospheric Emissions from the UK Oil and Gas Industry

Shona E. Wilde

Ph.D.

University of York

Chemistry

March 2021

Abstract

Since 2014, oil and gas (O&G) production in the UK has experienced a resurgence, increasing by 20%. However, increased development has sparked environmental concerns surrounding the industry. At all stages of the O&G life-cycle harmful air pollutants are released, negatively impacting air quality and climate at the local, regional and global scale. However, the full range of emissions remains relatively unknown due to the vast number of potential sources and lack of observational data. The current inventories are generally limited by self-reporting and inaccurate emission factors, which subsequently hinders the assessment of human health and climate risks. This thesis addresses these issues by providing valuable measurement data relating to both onshore and offshore O&G production in the UK. First, an extensive analysis of airborne trace gas measurements over four regions of the North Sea, where few observations currently exist, is presented. Volatile organic compound (VOC) enhancement ratios were utilised to indicate the prevalence of O&G production as the key source of VOCs in these regions and to investigate the VOC composition related to the type of fossil-fuel product. Second, a mass balance analysis was applied to airborne measurements of plumes downwind of O&G platforms to quantify emissions from single facilities. A general underestimation in relation to the reported emissions of both methane (CH_4) and total VOCs was found. Distinct enhancements of VOCs, not reflected in the bottom-up reporting were concurrent with oil loading operations, identifying a key area for review in the current methodology. Finally, ground-based monitoring at a UK shale gas site, combined with a machine learning technique, revealed well-pad preparation as a significant, understudied source of nitrogen oxides (NO_x). This demonstrated a need to consider all stages in the well life-cycle in order to gain a true understanding of the impacts from an air quality perspective.

Contents

List of Tables

List of Figures

Acknowledgements

I first thank my supervisors, Ruth Purvis, Jim Hopkins and Ally Lewis for their continued support and advice throughout all aspects of this PhD. I feel lucky to have had such a fantastic team of supervisors behind me. Huge thanks also go to all my friends and colleagues in the Wolfson Atmospheric Chemistry Laboratories (WACL), who were always there to provide help, motivation or maybe just some laughs! Thanks for making WACL such a lovely place to work.

During my PhD I had the opportunity to be part of some amazing fieldwork campaigns, from Kirby Misperton to Uganda! I thank everyone involved, particularly Ruth, James, Marv, Stuart, Grace & Ioana for making the experiences so enjoyable. I learnt a lot and made some incredible memories. Thanks also go to Pamela for help with the aircraft VOC data and to Ralph for guidance regarding the mass flux calculations.

Special thanks to Freya for being a continual source of inspiration and motivation, as well as for always cheering me up when I needed it. You are the best friend anyone could wish for!

To Stu, thank you for the constant love and encouragement during the last few years. Thank you for always being there for me, despite living miles apart.

Finally, I thank Mum, Dad, Katie and Tom for their never-ending support and reassurance. Thank you for keeping me going and always having confidence in me throughout my studies. I could not have done it without you!

Declaration

I declare that this thesis is a presentation of original work and I am the sole author. This work has not previously been presented for an award at this, or any other, University. All sources are acknowledged as References. Chapter 3 is based on a peer reviewed publication with myself as the lead author. The details of the article are:

> **Wilde, S. E.**, Dominutti, P. A., Allen, G., Andrews, S. J., Bateson, P., Bauguitte, S. J.-B., Burton, R. R., Colfescu, I., France, J., Hopkins, J. R., Huang, L., Jones, A. E., Lachlan-Cope, T., Lee, J. D., Lewis, A. C., Mobbs, S. D., Weiss, A., Young, S., and Purvis, R. M. Speciation of VOC emissions related to offshore North Sea oil and gas production. *Atmospheric Chemistry and Physics* 21.5 (2021), pp.3741–3762.
> URL:https://acp.copernicus.org/articles/21/3741/2021/

1

Introduction

1.1 Global air quality

The air we breathe is an essential element on which life on Earth depends. Acute and long-term exposure to poor ambient air quality has exclusively negative effects on both the environment and human health. In recent years, air pollution has risen to the top of environmental concerns worldwide, such that 3.4 million premature deaths were attributed to outdoor air pollution in 2017.[1] This figure continues to grow and so, as of 2019, air pollution became the 4th leading risk factor for premature death globally, behind only dietary risks, tobacco and high blood pressure.[2] However, the impacts of poor air quality are not felt equally across the globe. Developing and low-income countries such as India, typically face the highest burden, resulting in the largest number of deaths attributable to air pollution (Figure 1.1).

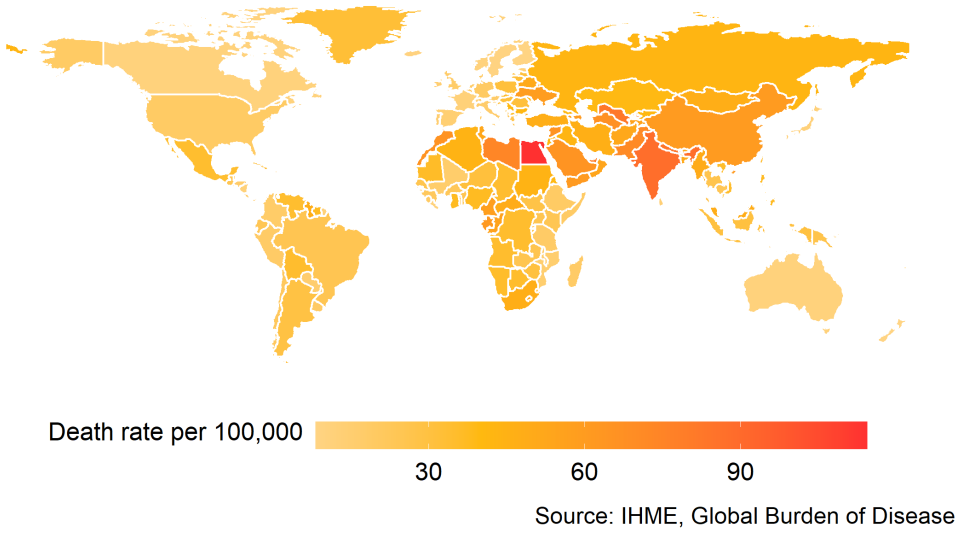

Figure 1.1: *The number of deaths attributed to outdoor ozone and particulate matter pollution per 100,000 in 2017.*[1]

Over the past several decades, air quality has improved in many high-income countries due to investment in alternative, cleaner fuels and the implementation of strict air quality intervention policies.[3] Figure 1.2 shows the number of deaths attributable to air pollution in 1990 compared to 2017 in each country. The data is plotted as a ratio of deaths in 1990 to deaths in 2017, against deaths in 2017. The majority of European countries sit above the 1:1 line, showing a decline in air pollution-related deaths. However, developing countries, along with many Asian and African countries show the opposite trend and typically suffer the worst air quality. Population explosions coupled with rapid urbanisation has led to the growth of dense urban centres, where the population is exposed to high concentrations of air pollutants.[4] Moreover, such countries lack the capital for advanced air pollution control and clean energy production.[5] Solid fuels such as coal and wood are often used as an energy resource, leading to dangerous levels of indoor air pollution in housing that is generally poorly ventilated. The disparity between socio-economic development and air pollution exposure also extends to the developed world, where a recent UK study concluded *"in respect of traffic emissions the*

poor pollute the least and are polluted the most".[6] This issue was recently exposed in the UK due to the death of Ella Adoo-Kissi-Debrah, a 9 year old girl from south-east London, who became the first person in the UK to have air pollution listed as a cause of death.[7] Despite extensive scientific research into the causes and complex interactions between air pollutants, the environment and human health, the quality of the air we breathe still remains an issue at the forefront of global health.

Figure 1.2: *Ratio of deaths attributed to outdoor air pollution in 1990 and 2017 against attributable deaths in 2017. The dashed line represents parity, where the number of deaths were equal in 1990 and 2017. Note the log scale on the x-axis.*

1.2 Air pollutants

Air pollution is defined as an *"atmospheric condition in which substances are present at concentrations higher than their normal ambient levels to produce measurable adverse effects on humans, animals, vegetation, or materials"*.[8] This definition acknowledges the fact that air pollutants have both natural and anthropogenic sources. For example, methane (CH_4) is introduced to the atmosphere by natural processes such as the breakdown of organic material and the decay of plant matter in wetlands, but is also emitted from human sources such as oil and gas (O&G) extraction and landfills. Therefore, the atmospheric abundance of a species is influenced by the accumulation of both natural and man-made emissions. Despite this, the primary issues due to air pollution are typically associated with anthropogenic emissions from traffic, industrial and domestic sources.

Within primary and secondary pollutants, there are thousands of unique compounds, which exist in both the gas and particle phases. However, there are certain "criteria" pollutants which are regularly monitored and for which legislation regarding the quantity of emissions exists. These are the species with the strongest evidence of health effects and are therefore targetted in mitigation policies. These species include: particulate matter (PM), of various size fractions, the most common of which are $PM_{2.5}$ and PM_{10} (PM with a diameter of less than 2.5 and 10 microns respectively), ozone (O_3), nitrogen dioxide (NO_2), sulphur dioxide (SO_2) and carbon monoxide (CO). All the aforementioned species are primary pollutants with the exception of O_3, which is a secondary pollutant formed photochemically from the emissions of nitrogen oxides (NO_x) and volatile organic compounds (VOCs) (Section 1.5.1). Additional, less widely monitored species also include benzene, 1,3-butadiene, polycyclic aromatic hydrocarbons (PAHs) and heavy metals such as lead and arsenic. Exposure to these species has been widely linked to increases in mortality and hospital admissions due to respiratory and cardiovascular disease.[9] Whilst those effects usually emerge from prolonged exposure to significantly enhanced levels of air pollutants, milder effects, such as headaches, shortness of breath and eye irritation have also been noted at very low levels of exposure.[10] Furthermore, air pollution is thought to threaten brain health, with long term exposure linked to dementia[11] and more nuanced symptoms such as behaviour change and lack of concen-

tration associated with lower levels of exposure.[12]

Elevated levels of air pollutants have also been found to impact ecosystems. Specifically, tropospheric O_3 damages plants, causing reduced survival and hence has been linked to reduced crop yields around the world.[13] One study estimated that O_3 may reduce yields by up to 227 million tonnes a year.[14] Similarly, emissions of nitrogen-containing species (ammonia (NH_3) and NO_x) and SO_2 are deposited in water, soil and on vegetation as "acid rain", which can affect the soil acidity. Acidification effects a plants ability to grow and can therefore lead to changes in species composition and reduce biodiversity.[15]

Consequently, the World Health organisation (WHO) recommends concentrations of these pollutants must be maintained under thresholds to reduce harm to both human and environmental health. The guideline values are displayed in Table 1.1. Since both long and short-term exposure to air contaminants can have negative impacts, multiple guideline values over different aggregation periods exist for some pollutants. However, it is unclear whether true threshold concentrations below which there are no effects on health exist.

Table 1.1: *World Health Organisation (WHO) guideline values for air quality.*[16]

Pollutant	**Limit value**	**Limit type**
$PM_{2.5}$	10 μg m^{-3}	Annual mean
	25 μg m^{-3}	24-hour mean
PM_{10}	20 μg m^{-3}	Annual mean
	50 μg m^{-3}	24 hour mean
O_3	100 μg m^{-3}	8-hour mean
NO_2	40 μg m^{-3}	Annual mean
	200 μg m^{-3}	1-hour mean
SO_2	20 μg m^{-3}	24-hour mean
	500 μg m^{-3}	10-minute mean

1.2.1 Volatile organic compounds

Air pollutants of interest are not limited to those in Table 1.1. The term VOC refers to the myriad of carbon-containing compounds present in mixing ratios at the parts per

trillion (ppt)–parts per billion (ppb) level.[17] By definition, this excludes the three most abundant, but generally less reactive, carbon-containing compounds: carbon dioxide (CO_2), CH_4 and carbon monoxide (CO), which are present in much larger mixing ratios and behave differently in the atmosphere. Whilst there is no definitive list of every VOC, they are typically compounds with less than 15 carbon-atoms, which have a high vapour pressure and low boiling point. Examples of VOCs include ethane, propane, benzene, and isoprene.

VOCs have a huge number of sources, which are both biogenic and anthropogenic in origin.[18] By mass, the majority of global VOC emissions are emitted naturally from vegetation. The global annual flux of biogenic VOC is estimated at approximately 1000 Tg, with isoprene accounting for half of this emission.[19] However, in urban environments anthropogenic sources of VOCs are the most prevalent, emitting approximately 142 Tg of carbon per year in the form of VOCs.[20] The anthropogenic contribution to VOC emissions is dominated by combustion processes (vehicle exhausts and biomass burning) and the extraction of fossil fuels (oil, gas, coal).[21] Other sources include organic solvents and landfills.[22] VOC emissions from vehicles are primarily composed of species containing multiple bonds (double or triple) such as ethene, acetylene, butene and toluene.[23,24] Emissions from O&G extraction are compositionally different to those from combustion. O&G production platforms are strong point sources of both CH_4 and VOCs, where trace-gas emissions are typically dominated by alkanes (ethane, propane, butanes, pentanes, hexanes), along with some aromatic species such as benzene and toluene.[25]

Interest in VOC emissions is primarily due to their role as precursors to tropospheric O_3[26] and SOA formation (Section 1.5). However, some species, such as 1,3-butadiene are directly hazardous to human and plant health.[27] Similarly, benzene is a recognised human carcinogenic compound,[28] predominantly emitted from industrial and domestic combustion processes in addition to evaporative emissions from road transport.[29] Therefore, the European Commission sets standards for these two species. It is written that benzene should not exceed an annual mean of 5 μg m^{-3} and the maximum annual running mean of 1,3-butadiene should not exceed 2.25 μg m^{-3}.[30]

1.3 Air pollution and climate

Atmospheric emissions also play a key role in global climate change. Since the pre-industrial period (between 1850–1900), the Earth's temperature has been rising at an unprecedented rate. The year 2019 was declared the second warmest year in the 140-year record and nine of the warmest ten years have occurred since 2005.[31] The increases in global temperature are strongly linked to the accumulation of greenhouse gases (GHG) such as carbon dioxide (CO_2) and CH_4 in the atmosphere. Anthropogenic emissions of greenhouse gases have also increased since the pre-industrial era, driven mainly by the combustion of fossil fuels resulting from economic and population growth. This has led to strong enhancements of the atmospheric concentrations of these pollutants. Figure 1.3 shows global CO_2 emissions superimposed onto global "climate stripes". Climate stripes are a visual representation of long-term temperature trends. Each "stripe" represents a year, coloured by the global temperature anomaly for each year, compared to the average throughout a 30-year reference period (1971–2000).[32] The average temperature in the reference period is set as the boundary between blue (cooler) and red (warmer) colours. Figure 1.3 exposes the correlation between rising global temperatures and emissions of CO_2, particularly in the past two decades. Furthermore, global atmospheric CO_2 reached a record high of 409.8$\pm$0.1 ppm in 2019.[33] This figure continued to rise in 2020, totalling 412.5 ppm, despite the economic slowdown caused by the coronavirus pandemic.

Greenhouse gases work to warm the planet by absorbing and radiating heat from the Earth's land and ocean surfaces. Whilst this effect is necessary to prevent the planets average temperature dropping below zero, high concentrations of greenhouse gases have tipped the Earth's energy budget out of balance by trapping additional heat and thus raising the average temperature. Perturbations in the Earth's radiative energy budget are described by the term *"radiative forcing"* (RF). RF is defined as the change in net irradiance (W m^{-2}) at the tropopause imposed by external factors, where positive forcing results in warming and negative forcing leads to cooling.[34] CO_2 and CH_4 are the most radiatively important gases with an RF of +1.83 W m^{-2} and +0.61 W m^{-2}, respectively.[35]

The effect of CO_2 is particularly potent due to its high atmospheric concentrations

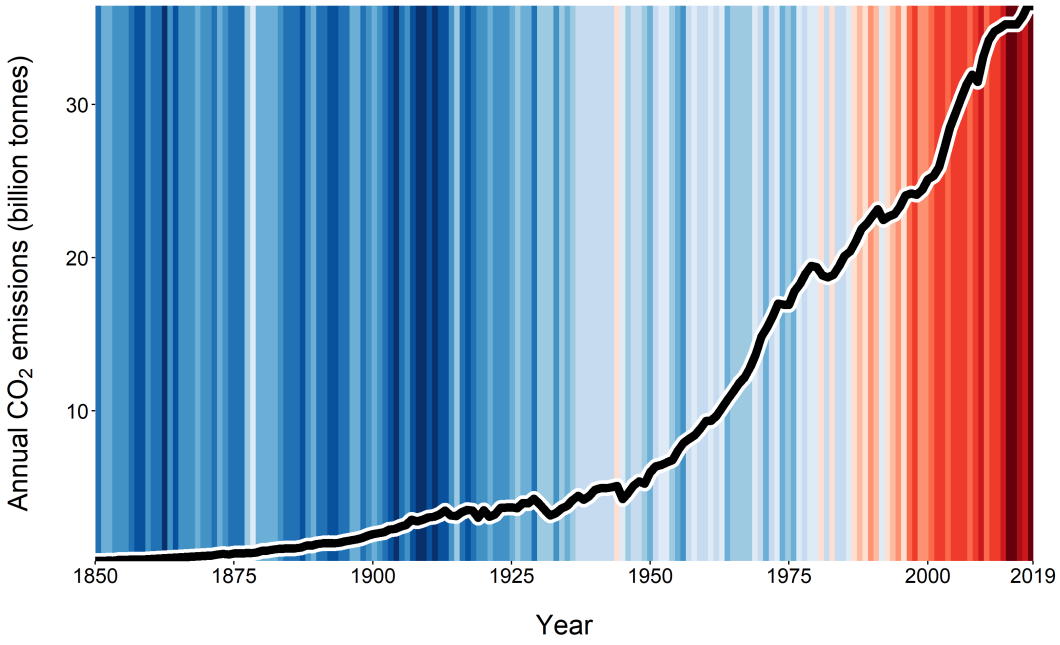

Figure 1.3: *"Climate stripes" showing the global average temperature compared to a 1971-2000 reference period.[32] Superimposed is the annual global CO_2 emissions (black line).[33]*

(408 ppm compared to 1850 ppb of CH_4 in 2017)[36] and long lifetime within the atmosphere (100s of years), meaning it's warming effect acts over large temporal scales. However, rising CO_2 is tempered by oceanic uptake, which accounts for a third of anthropogenic carbon emitted into the atmosphere.[37] It is estimated that between 1750–2011, the cumulative anthropogenic CO_2 emissions were 2040±310 Gt. Of these emissions, around 40% have remained in the atmosphere with the remainder removed from the atmosphere by vegetation and the ocean.[38] Without this sink, global CO_2 would be now approximately 450 ppm and therefore the current rate of climate change would be exacerbated.[37] However, oceanic CO_2 uptake can also have detrimental effects on the environment. It causes reductions in pH and alters the fundamental balance of oceanic chemicals, leading to ocean acidification.[39]

In terms of RF, CH_4 is not as powerful as CO_2, primarily due to it's much shorter atmospheric lifetime, which is approximately 12–15 years.[40] However, a tonne of CH_4 is

more much efficient at absorbing heat compared to the equivalent weight of CO_2. Therefore over shorter time-scales, CH_4 is a much more effective greenhouse gas. The global warming potential (GWP) was developed to facilitate the comparison of different trace gases with respect to their influence on the climate system. It is defined as *"the heat absorbed by any greenhouse gas in the atmosphere, as a multiple of the heat that would be absorbed by the same mass of CO_2"*.[41] GWP is often assessed over short time scales of either 20, 50 or 100 years. In terms of CH_4, $GWP_{[100]}$ = 28, meaning it is 28 times more potent than the equivalent mass of CO_2 over a 100-year period.[41]

There are also indirect effects of atmospheric CH_4, such as the fact that CH_4 is a precursor to O_3, which is itself a GHG with an RF of +0.35 W m^{-2}.[41] Chemical oxidation of CH_4 via reaction with the hydroxyl radical (OH) is the major removal pathway for CH_4 and leads to the production of other climate active gases (CO_2 and O_3). Tropospheric concentrations of OH are governed by the CH_4 abundance such that, the net effect is that emissions of CH_4 suppress the concentrations of OH. This reduces the primary CH_4 sink and prolongs the CH_4 lifetime, which amplifies the response of CH_4 concentrations to changes in emissions. This is known as the CH_4 feedback.[42] This feedback increases the RF, GWP, and environmental impact of CH_4 emissions. Therefore, it is recognised that reducing CH_4 emissions is crucial to slow the rate of warming.

The oxidizing capacity of the troposphere and hence the atmospheric lifetime of CH_4 is also controlled by emissions of NO_x, CO and VOCs. These species indirectly act as GHGs through their influence on atmospheric chemistry. Warming effects are predominantly induced by changes in the burden of tropospheric O_3. This burden has increased, particularly in the Northern Hemisphere, since 1850 due to the growth in emissions of NO_x.[43] Moreover, VOCs react with OH in the presence of NO_x and sunlight to produce O_3 and are therefore indirectly associated with positive RF and hence warming. On the other hand, NO_x can also lead to negative RF and have cooling impacts. Excess burdens of OH can build up in regions with high NO_x emissions, which therefore increases the strength of the sink for CH_4 removal with OH and decreases the CH_4 burden.[44]

Overall, reducing CH_4 is an attractive option for jointly addressing both climate and air quality goals. Concentrations of CH_4 have been rising steadily again since 2007 following a reasonably steady period throughout the 1990s and early 2000's.[45] Evidence shows

that this growth has accelerated in the last 4 years, for which the causes are not yet fully understood.[46] In 2019, atmospheric CH_4 concentrations reached a record high, peaking at 1877 ppb, which was 260% of pre-industrial levels.[47] This could have disastrous implications for the climate goals agreed under the Paris Agreement, which aims to limit global warming to *"well below 2 °C"*, preferably 1.5 °C, compared to pre-industrial levels.[48] According to the Emissions Gap Report 2019 by the UN Environment Programme, countries must increase their mitigation commitments in 2020 by a factor of three to achieve the well below 2 °C goal, and by more than a factor of five to achieve the 1.5 °C goal.[49]

CH_4 has six major sources; natural wetlands, paddy rice fields, livestock, biomass burning, aerobic decomposition of organic waste and the exploitation and transport of fossil fuels.[50] Of these sources, anthropogenic emissions are estimated to contribute at least 60% to total CH_4 emissions.[51] Furthermore, the global fossil fuel industry (production and usage of natural gas, oil and coal) is thought to contribute 15–22% of global CH_4 emissions.[52,53] Since natural sources are typically much harder to control and anthropogenic emissions are relatively large by comparison, reducing CH_4 emissions from the fossil fuel industry is an appealing option if the Paris Agreement aims are to be attained.[46] Furthermore, modelling studies show that neither the climate or air quality benefits of CH_4 mitigation depend strongly upon the location of the CH_4 emission reductions. This implies that the lowest cost emission controls can be targeted, which means targetting CH_4 as a mitigation strategy for global warming is also accessible to the developing world.[54]

1.4 The influence of meteorology

The fate of atmospheric pollutants is not only influenced by emissions, but also by chemical transformation, transport and deposition. Different meteorological conditions can significantly reduce or aggravate pollutant concentrations, which can directly influence human exposure. Figure 1.4 shows an example of a variable importance plot, which is commonly used to identify which variables are most influential when predicting pollutant concentrations.[55] Clearly, meteorological variables such as wind speed, air temperature and air mass origin (back trajectory cluster) are crucial for explaining air quality

observations. Often it is difficult to establish whether a decrease in pollutant concentrations is due to a reduction in emissions or changes in the weather conditions. In some cases, the horizontal and vertical transport of pollutants can have a greater effect on air quality than a change in emission source strength.[56] A selection of the variables in Figure 1.4 are discussed in more detail in the following paragraphs.

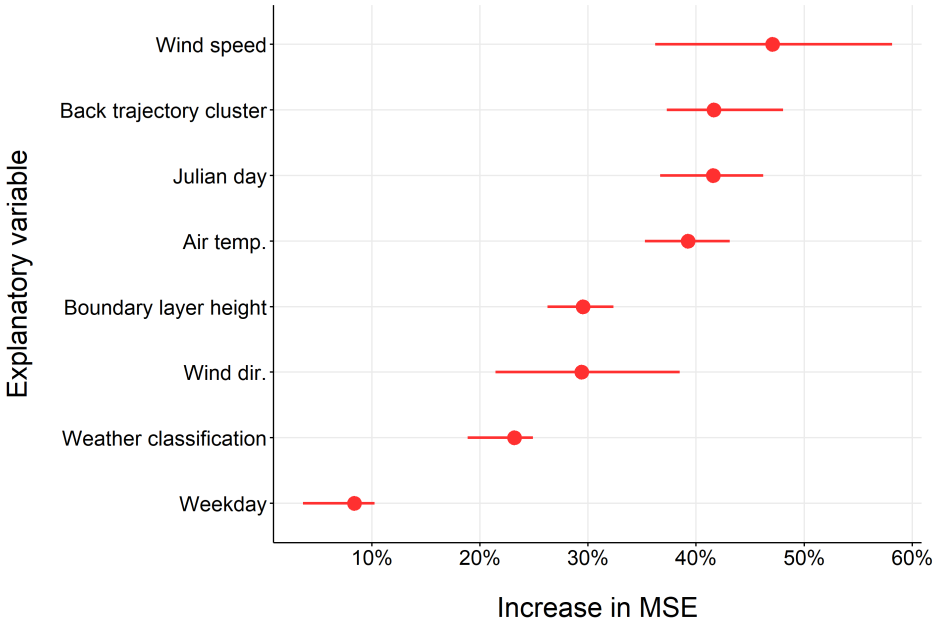

Figure 1.4: *Variable importance for predicting PM_{10} concentrations in Switzerland. Dots represent the mean increase in mean square error (MSE) and the lines represent the interquartile range for each variable. Adapted from Grange et al. [55].*

Pollutants emitted from sources at the surface accumulate in troposphere. This is the lowest layer of the atmosphere and typically extends up to an average altitude of 12 km. Approximately 75–80% of the mass in the atmosphere exists within the troposphere and almost all weather patterns occur within this layer.[57] The troposphere is bounded from the stratosphere (10–50 km) above by the tropopause, which is marked by a temperature inversion. This minimises mixing between the layers, which means most surface emissions are trapped in the troposphere. The troposphere is characterized by rapid vertical transport and mixing caused by surface heating. Therefore, the lowest part of the troposphere is the warmest and temperature typically declines with increasing altitude.[58]

The lowest layer of the troposphere is termed the planetary boundary layer (PBL). It is the region of the troposphere that is directly influenced by processes at the surface, such as pollutant emissions and heat transfer.[59] Surface heating drives the evolution of the PBL. The non-uniform nature of energy transfer between the surface and atmosphere means the PBL structure is highly variable on both temporal and spatial scales. The boundary layer height (BLH) varies from 100–3000 m and is typically much shallower and less variable over the ocean, since water can absorb large amounts of heat with relatively little temperature change.[59] On land, the lower heat capacity results in a greater diurnal variation and deeper mixing layers. The BLH governs the extent to which atmospheric emissions can disperse and mix in the vertical and is usually marked with a temperature inversion, which separates the PBL from the free troposphere. Pollutant concentrations are often influenced by the structure and diurnal variability of the boundary layer. As the PBL grows throughout the day, pollutants are diluted as they mix with cleaner air from the free troposphere. Similarly, as the PBL shrinks at nighttime in the absence of surface heating, emissions become more concentrated as they are confined to a smaller volume of the atmosphere.

Whilst the BLH dictates how pollutants can disperse in the vertical, wind speed and direction play an important role in the horizontal transport of emissions from the source. High wind speeds result in the rapid dispersion of pollutants, leading to lower concentrations in the vicinity of the source. However, this can lead to enhanced levels of pollution in areas downwind. Low wind speeds have the opposite effect, particularly in cold temperatures when the BLH is low, which results in the build-up of pollutants close to the source of emission. Similarly, the wind direction has a strong influence on pollutant concentrations since it directs the travel of emissions from their source. Concentrations are likely to be enhanced if the wind comes from a direction where industrial emissions are present in comparison to a direction which is lacking in point sources. A nice illustration of this is presented in Grange and Carslaw [56], where the Dover Landon Cliff monitoring site exclusively experienced high SO_2 concentrations under southerly winds, which favoured the transport of emissions from the Port of Dover to the monitoring site.

An additional factor to consider is the topography, which can prevent pollutants from being dispersed away from their source. The Uinta Basin of Utah functions as a topolog-

ical barrier, where the Wasatch Mountains to the west and the Uinta Mountains to the north provide a huge bowl, which can contain a stagnating air mass. Pollution episodes occur during a meteorological phenomenon known as *"cold-air pools"*, where surface cooling leads to stable vertical stratification of the PBL, trapping air laterally within the basin topography.[60] Furthermore, there are approximately 9,000 active O&G wells alongside extensive production and transport infrastructure in the Uinta Basin, which give rise to high levels of atmospheric pollution.[61] Emissions of O_3 precursors (NO_x and VOCs) from O&G production combined with cold air pools and enhanced photolysis, owing to the higher albedo of snow, drive wintertime pollution episodes in the basin and have resulted in numerous documented exceedances of the National Ambient Air Quality Standard (NAAQS) for O_3.[62,63]

Although most emissions of ambient air pollution originate from local or regional sources, larger scale meteorological process can also drive air quality. Pollutants which have significant atmospheric lifetimes and hence survive in the atmosphere for more than a few hours, can travel long distances away from their source. For example, in the UK, air pollution episodes of elevated surface PM concentrations can occur as a result of intercontinental transport. During Spring 2014, significantly enhanced PM_{10} concentrations were observed across the majority of monitoring sites in the UK, attributed to the transport of a Saharan dust plume. In addition, further study into the composition of the particles, found that the elevated PM was mainly composed of ammonium nitrate, driven by agricultural ammonia emissions in continental Europe. An area of high pressure located over Europe in combination with relatively low surface temperatures (8–14 °C) limited the evaporation of ammonium nitrate, enhancing the particle lifetime and the potential influence of its long-range transport.[64] It follows that reducing emissions in Europe would have similar benefits in reducing episodic PM concentrations in the UK. Therefore, in addition to local and regional efforts to mitigate air pollution, international cooperation is needed to address the impact of long-range, trans-boundary emissions.

1.5 Tropospheric chemistry of key pollutants

The quantity of a certain pollutant in the atmosphere at any one time depends on the balance that exists between its chemical sources and sinks. Species are continuously created and destroyed due to the complex web of chemical and physical processes that occur within the atmosphere. Whilst 99% of the mass within the atmosphere is composed of N_2 and O_2, much of the chemistry is driven by trace gases present in much lower abundances. One of the most important species is the hydroxyl radical (OH). Often referred to as the "*atmosphere's detergent"*, OH governs a high proportion of oxidation reactions within the atmosphere, despite being present in low concentrations. The mean northern and southern hemispheric OH concentrations are 0.91×10^6 molecules cm^{-3} and 1.03×10^6 molecules cm^{-3}, respectively.[65] The reaction of trace gases with oxidants such as OH is typically the rate determining step in their removal from the atmosphere. The most important OH formation mechanism globally is via the photolysis of O_3 (R1.1). This produces excited O(^{1}D) atoms which either react with water vapour to form OH radicals (R1.2), or are quenched by air molecules (R1.3).

$$O_3 + h\nu \longrightarrow O(^1D) + O_2 \quad (\lambda < 310 \text{ nm}) \tag{R1.1}$$

$$O(^1D) + H_2O \longrightarrow 2OH \tag{R1.2}$$

$$O(^1D) + M \longrightarrow O(^3P) + M \quad \text{M = } N_2 \text{ or } O_2 \tag{R1.3}$$

Additionally, the photolysis of nitrous acid (HONO) has been well documented as an important source of OH in the polluted urban atmosphere.[66,67] Potential formation pathways of HONO include direct emissions (vehicles, soil and biomass burning), reaction of NO with OH, and NO_2 conversion on ground or aerosol surfaces.[68] Production of OH occurs through HONO decomposition in the presence of sunlight, shown in R1.4.

$$HONO + h\nu \longrightarrow OH + NO \quad (300 \text{ nm} < \lambda < 405 \text{ nm}) \tag{R1.4}$$

Since OH is predominantly formed photochemically, OH concentrations are highest during the day before approaching zero at night. Therefore, removal by OH oxidation is predominantly a day time process. Ozonolysis is also a significant source of OH and is discussed in Section 1.5.2. At night, other processes take over and the night-time oxidant, the nitrate radical (NO_3), becomes dominant. The nitrate radical is generated by reaction of NO_2 with O_3 as in R1.5. The NO_3 radical reacts with NO_2 to form an equilibrium with N_2O_5 (R1.6), which is an important night-time source of nitric acid.[69] Both reactions R1.5 and R1.6 occur throughout the day, however NO_3 is readily photolysed by sunlight and so is heavily suppressed during daytime hours (R1.7).

$$NO_2 + O_3 \longrightarrow NO_3 + O_2 \tag{R1.5}$$

$$NO_3 + NO_2 \rightleftharpoons N_2O_5 \tag{R1.6}$$

$$NO_3 + h\nu \longrightarrow NO_2 + O(^3P) \quad (\lambda < 590 \text{ nm}) \tag{R1.7}$$

1.5.1 Tropospheric O_3 formation

The OH radical is part of a chemically coupled system involving HO_2, NO_x (NO and NO_2) and O_3. Changes in tropospheric O_3 are of concern for a variety of reasons, such that in many environments around the world, air pollution is characterised by the formation of secondary oxidants such as O_3. Whilst, it is not emitted directly, O_3 formation occurs through a series of photochemical reactions between primary emissions of NO_x and VOCs. Fundamentally, the production of O_3 in the troposphere relies on the photolysis of NO_2, which is the only significant anthropogenic source of O_3.[70] The photo-dissociation of NO_2 in sunlight yields NO along with $O(^3P)$ (the ground electronic state oxygen atom), as in R1.8. The subsequent association of $O(^3P)$ with O_2 via a termolecular reaction with a co-reactant (M) yields O_3 (R1.9). O_3 is destroyed through rapid reaction with NO to form NO_2 (R1.10). In clean atmospheres with low VOC concentrations this creates a system of net zero O_3 formation, called the photostationary steady state (PSS).

$$NO_2 + h\nu \longrightarrow NO + O(^3P) \quad (\lambda < 410 \text{ nm}) \tag{R1.8}$$

$$O(^3P) + O_2 + M \longrightarrow O_3 + M \tag{R1.9}$$

$$O_3 + NO \longrightarrow NO_2 + O_2 \tag{R1.10}$$

Reactive species which catalyse the oxidation of NO to NO_2 perturb the PSS and can therefore facilitate net O_3 production. The presence of VOCs (including CO and CH_4) propagates the formation of O_3 through reaction with OH. This process is illustrated using a general formula (RH) to represent VOCs in the following reaction scheme. In the first step, OH reacts with RH in the presence of O_2 to form peroxy radicals (RO_2) through the abstraction of a single hydrogen atom (R1.11). The simplest peroxy radical (HO_2) is formed from the oxidation of CO to CO_2 by OH (R1.12).

$$RH + OH \xrightarrow{O_2} RO_2 + H_2O \tag{R1.11}$$

$$CO + OH \xrightarrow{O_2} HO_2 + CO_2 \tag{R1.12}$$

Peroxy radicals can then oxidise NO to NO_2, as in R1.13. In high VOC, low NO_x regimes cross reactions between peroxy radicals dominate over R1.13, leading to the chain termination of radical cycling (R1.14).[71] Alkyl nitrates are also formed in a minor branch of the reaction of NO with organic peroxy radicals (R1.15).[72] The yield of alkyl nitrates varies with the structure of the R substituent and becomes increasingly important as the alkane gets larger. For example the yield of small alkyl groups (R = CH_3) is typically less than 1% but yields of up to 20% have been observed for biogenic VOCs.[73]

$$RO_2 + NO \longrightarrow RO + NO_2 \tag{R1.13}$$

$$RO_2 + RO_2 \longrightarrow products \tag{R1.14}$$

$$RO_2 + NO + M \longrightarrow RONO_2 + M \quad \text{(R1.15)}$$

R1.13 creates NO_2 without the destruction of an O_3 molecule as in R1.10, which leads to net production of O_3 via R1.8 and R1.9. The resulting alkoxy radical (RO) from R1.13 reacts rapidly with O_2 to form a carbonyl (RCHO) and HO_2 (R1.16).

$$RO + O_2 \longrightarrow RCHO + HO_2 \quad \text{(R1.16)}$$

In polluted conditions where there is an abundance of NO_x, R1.16 generally leads to additional peroxy-radical catalysed oxidation of NO to NO_2 and the regeneration of OH (R1.17).

$$HO_2 + NO \longrightarrow OH + NO_2 \quad \text{(R1.17)}$$

However, in low NO_x conditions, HO_2 reacts with O_3 leading to the catalytic destruction of O_3 (R1.18).

$$HO_2 + O_3 \longrightarrow OH + 2O_2 \quad \text{(R1.18)}$$

The scheme above demonstrates how OH oxidation of VOCs in the presence of NO_x can lead to the net production of O_3. However, depending on the concentration of NO_x, OH may have a another fate, where it reacts with NO_2 to form nitric acid (R1.19).[74] This represents a sink for both OH and NO_x.

$$OH + NO_2 + M \longrightarrow HNO_3 + M \quad \text{(R1.19)}$$

Clearly, there is a balance between net photochemical O_3 production and net photochemical O_3 destruction, which is highly dependent on the abundance of NO_x and VOCs. This dependence is best demonstrated using *"O_3 isopleth diagrams"*, as shown in Figure 1.5. Isopleth diagrams show the initial conditions which give rise to equivalent O_3 concentrations and these are connected by the relevant isopleth. Importantly, Figure 1.5 highlights the non-linearity of O_3 production with respect to NO_x and VOCs.

Figure 1.5 can be interpreted in term of two different chemical regimes, separated

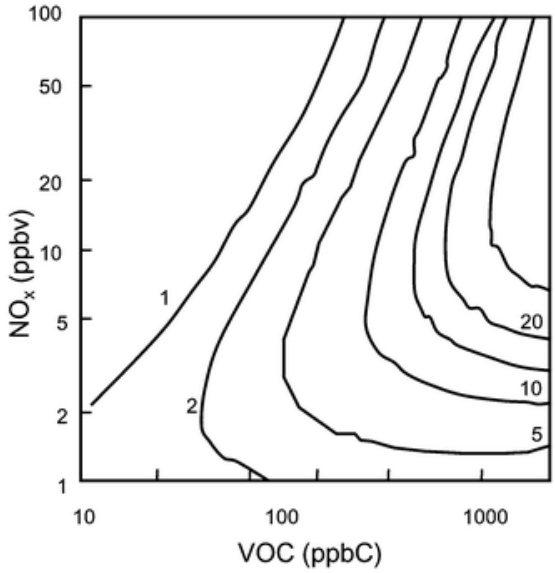

Figure 1.5: *Example O_3 isopleth diagram, showing the net rate of O_3 production in ppb as a function of VOC and NO_x mixing ratios. Figure taken from Monks [74].*

by the characteristic ridge line. To the left of the ridge line is the *VOC-limited* regime. Ratios of VOC/NO_x in this region are typical of highly polluted urban environments. Here, reducing the VOC concentrations at constant NO_x leads to lower peak O_3 concentrations. However, lowering NO_x concentrations at constant VOC would actually lead to higher peak O_3 until the ridge line is reached. In this relatively high-NO_x regime, NO_2 effectively competes with the VOCs for the OH radical (R1.19), slowing the production of peroxy radicals through VOC oxidation. As NO_x is decreased, more OH is available to react with VOCs (R1.1), leading to a greater production of O_3.[75]

To the right of the ridge line is the *NO_x-limited* regime, where VOC/NO_x ratios are characteristic of those in rural and suburban areas downwind of cities. In this region of relatively high VOC concentrations, there is a high abundance of available peroxy radicals to convert NO to NO_2, therefore reducing VOCs at constant NO_x has no effect on peak O_3 concentrations. However, the photolysis of NO_2 is an important source of O_3, therefore reducing NO_x directly leads to a decrease in O_3.[75]

Isopleth diagrams are often used to develop air quality policy and mitigation strategies. Due to the dominance of vehicular emissions in urban areas, NO_x is often a target for control policies. However, isopleths show that NO_x reductions can have significantly

different impacts depending on the VOC/NO_x ratio and the reactive mix of VOCs. Similarly, reducing VOCs is only effective under VOC-sensitive regimes, where NO_x is high. When the system is NO_x-limited, O_3 concentrations are not sensitive to the concentration or composition of VOCs.

1.5.2 VOC chemistry

In the atmosphere, VOCs primarily react with oxidants such as OH radicals, NO_3 radicals and O_3. The chemical structure of different VOCs determines how readily oxidation reactions take place and hence can dictate which species are most influential in O_3 production. The longevity of VOCs within the atmosphere is dependant on their atmospheric lifetimes with respect to these oxidants. The lifetime (τ) of a chemical (X) depends inversely on the rate constant (k_X) and the ambient concentration of X $([X])$, given by R1.20.

$$\tau = \frac{1}{k_X[X]} \tag{R1.20}$$

Table 1.2 shows the approximate lifetimes of selected VOCs (including CH_4) due to the reaction with OH, NO_3 and O_3. It is clear that the lifetime of CH_4 is much greater than the other VOCs, which is due to the high C-H bond dissociation energy. Therefore, CH_4 is sufficiently long-lived to play a significant role in terms of the global troposphere, as well as on a local and regional scale. Ethane is the longest lived non-methane hydrocarbon (NMHC) and together with propane is often poorly reproduced in chemical models in comparison to measurements.[76] This is attributed to underestimations in anthropogenic fossil fuel emissions.[76]

1.5.2.1 Alkanes

Alkanes react with OH radicals, slowly with NO_3 radicals, but not at measurable rates with O_3. The dominant loss process is through reaction with OH by H-atom abstraction from C-H bonds to form peroxy radicals, as described previously. Generally, the lifetime decreases with increasing chain length due to the number of abstractable H-atoms. Similarly, the lifetime also decreases with increasing complexity of the alkane. The C-H bond strength is largest for primary alkanes and smallest for tertiary alkanes, due to the rela-

tive stability of the radical that is formed. Therefore, abstraction of a tertiary H-atom is more favourable than a primary H-atom.[77]

Table 1.2: *Tropospheric lifetime of selected VOCs with respect to reaction with OH and NO_3 radicals and O_3.*[78]

VOC	OH	NO_3	O_3
Methane	~12 years	$>$ 120 years	$>$ 4,500 years
Ethane	60 days	$>$ 12 years	$>$ 4,500 years
Propane	13 days	$>$ 2.5 years	$>$ 4,500 years
n-Butane	6.1 days	$>$ 2.5 years	$>$ 4,500 years
n-Octane	1.8 days	260 days	$>$ 4,500 years
Ethene	1.8 days	225 days	9.7 days
Propene	7.0 hours	4.9 days	1.5 days
Acetylene	19 days	$>$ 2.5 years	5.8 years
Ethanol	4.7 days	$>$ 51 days	-
Benzene	12.5 days	$>$ 6 years	$>$ 4.5 years
Toluene	2.6 days	1.9 years	$>$ 4.5 years

1.5.2.2 Alkenes

Alkenes are reactive towards all three of OH, NO_3 and O_3. The reactions mainly proceed via addition to the C=C double bond(s). The high electron density in the double bond means it is susceptible to attack and therefore the lifetime of an alkene is shorter than its equivalent alkane. The major reaction pathway of alkenes with the OH radical involves OH addition to form β-hydroxyalkyl radicals, as shown in R1.21 for but-1-ene. The minor reaction pathway involves H-atom abstraction from the C-H bonds of the alkyl substituents and accounts for $<$ 10% of the overall reaction for but-1-ene at room temperature,[79] but is not discussed here.

$$CH_3CH_2CH=CH_2 \;+\; OH \xrightarrow{M} CH_3CH_2CH(OH)CH_2 \qquad \text{(R1.21)}$$

The β-hydroxyalkyl radicals react solely and quickly with O_2 to form β-hydroxyalkyl peroxy radicals (R1.22).[80] Analogous to the reactions of alkyl peroxy radicals, the β-

hydroxyalkyl peroxy radicals react with NO to form a hydroxyalkoxy radical and NO_2 (R1.23).[80] Similarly, the reactions of the NO_3 radical with alkenes proceed via addition to form a β-nitrooxyalkyl radical (R1.24). Subsequent reactions of β-nitrooxyalkyl radicals are analogous to those for hydroxyalkyl radicals formed from the corresponding reactions with OH.[80]

$$CH_3CH_2CH(OH)CH_2 + O_2 \xrightarrow{M} CH_3CH_2CH(OH)CH_2OO \quad \text{(R1.22)}$$

$$CH_3CH_2CH(OH)CH_2OO + NO \xrightarrow{M} CH_3CH_2CH(OH)CH_2O + NO_2 \quad \text{(R1.23)}$$

$$CH_3CH_2CH=CH_2 + NO_3 \xrightarrow{M} CH_3CH_2CHCH_2ONO_2 \quad \text{(R1.24)}$$

Alkenes react with O_3 via two distinct steps, displayed by the scheme in Figure 1.6. The first is addition of O_3 across the double bond to form a primary ozonide, followed by decomposition to a carbonyl and a carbonyl oxide, known as a Criegee intermediate (CI).[81] CIs are of interest as their decomposition can lead to significant, non-photolytic production of OH, HO_2 and RO_2 radicals, which can have impacts on the oxidising capacity of the atmosphere.[82] Measurements from field campaigns have shown that up to 30% of total OH radical production can be attributed to alkene ozonolysis.[83] CIs can also be collisionally stabilised through interactions with other molecules to form a stabilised CI (SCI). SCIs can be sufficiently long-lived to undergo bimolecular reactions and can affect climate through the formation of inorganic and organic aerosol. They have also been identified as an important additional oxidant species[84] and can contribute significantly to the sulphuric acid budget.[85] At high VOC to NO_x ratios and low relative humidity, the oxidation of SO_2[86] by SCIs is important for the production of organic acids and sulfate (SO_4^{2-}). The impact of this mechanism was quantified through simulations by Sarwar et al. [87], who suggested a maximum enhancement of up to 4 μg m^3 in SO_4^{2-} over a 24-hour period due to SCI chemistry. Given that SO_4^{2-} is a key component of atmospheric aerosol, SCIs can therefore have a direct influence on the Earth's radiative

balance.

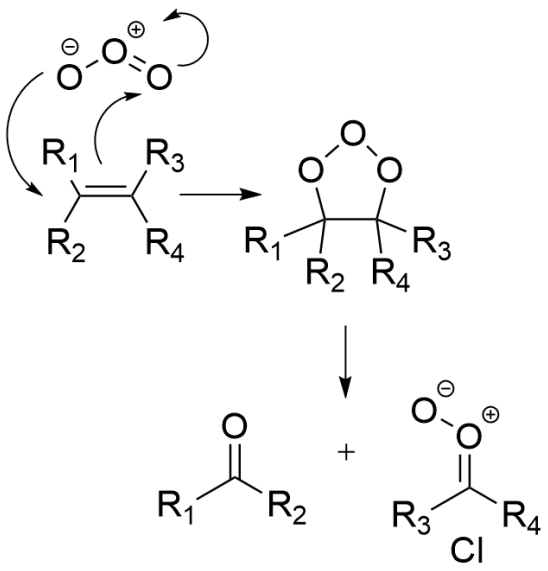

Figure 1.6: *Reaction scheme for O_3 addition to an alkene, forming a primary ozonide, followed by decomposition to a carbonyl and Criegee intermediate (CI). Adapted from Khan et al. [81]*

1.5.2.3 Aromatics

In terms of mono-aromatic compounds, benzene and alkyl-substituted benzenes such as toluene react with both OH and NO_3 radicals, where reaction with OH is the dominant removal process.[26] The OH reactions proceed in two ways, displayed by Figure 1.7. Firstly by H-atom abstraction, typically from the C-H bonds of alkyl substituent groups. The second pathway involves reversible OH addition to the aromatic ring to form an OH-aromatic adduct.[80] The H-atom abstraction is the minor pathway and accounts for $<$ 10% of the total reactions between OH and alkyl-substituted benzenes.[80] The alkyl-substituted benzyl radicals formed are analogous to the alkyl radicals discussed earlier and following the formation of a peroxy radical, react in the presence of NO to produce NO_2 and regenerate HO_x (R1.25–R1.27).

$$C_6H_5CH_2 + O_2 \xrightarrow{M} C_6H_5CH_2OO \qquad \text{(R1.25)}$$

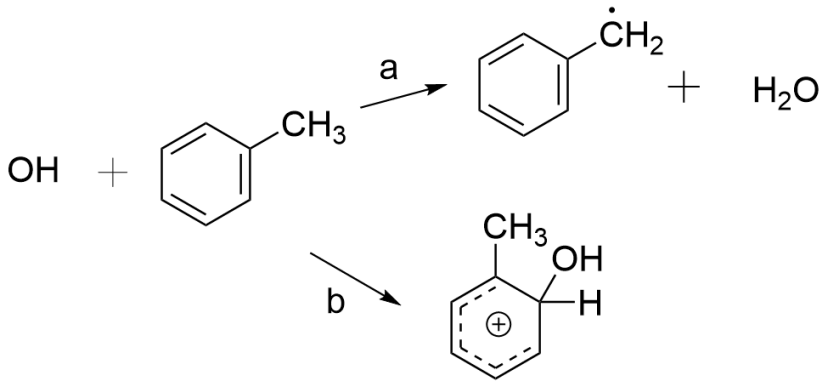

Figure 1.7: *Scheme showing reaction of OH with toluene by (a) H-abstraction from the alkyl substituent and (b) addition to form an OH-aromatic adduct. Adapted from Atkinson [80].*

$$C_6H_5CH_2OO + NO \xrightarrow{M} C_6H_5CH_2O + NO_2 \quad \text{(R1.26)}$$

$$C_6H_5CH_2O + O_2 \xrightarrow{M} C_6H_5CHO + HO_2 \quad \text{(R1.27)}$$

The major reaction pathway is the formation of OH-aromatic adducts (Figure 1.7, pathway b), which react rapidly with O_2 and NO_2. In polluted urban air masses, the dominant reaction of the OH adducts is with O_2 by either H-abstraction to give phenolic compounds or by addition to form peroxy radicals,[80] displayed in Figure 1.8. The phenolic route has been shown to be relatively minor and decreases for the more substituted aromatics.[88] For example, in the case of toluene this route accounts for only 16% of the total products.[89] In the peroxide-bicyclic pathway, the OH adduct reacts with O_2, losing aromaticity and forming a non-aromatic ring-retaining peroxy bicyclic peroxy radical (BPR). Under high-NO conditions, relevant to urban environments, BPRs also react with NO to form bicyclic oxy radicals, which decompose to ring-scission carbonyl products such as methyl-glyoxal and biacetyl.[90] This pathway is of importance since both ring-retaining and ring-scission compounds are expected to be low in volatility and contribute significantly to secondary organic aerosol (SOA) (Section 1.5.3).[91]

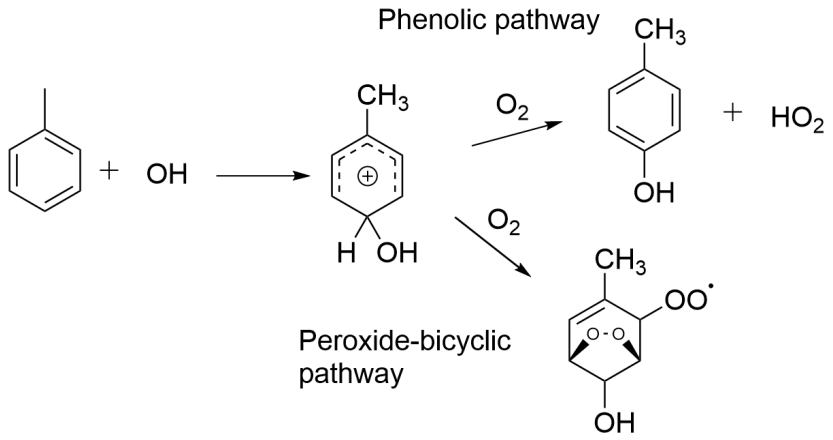

Figure 1.8: *Scheme showing two possible reaction pathways of the OH-aromatic adduct formed from the reaction of OH with toluene. Adapted from Atkinson [80].*

1.5.3 Secondary organic aerosol formation

Gas-phase reactions of VOCs are not only important for O_3 formation but also regarding that of SOA. SOA accounts for the major fraction of atmospheric aerosol and causes concern for a number of reasons. As a major contributor to fine particulate matter, SOAs have potentially negative respiratory health effects, particularly at the high concentrations found in urban environments. At the regional scale, SOAs can contribute to the formation of photochemical smog since they limit visibility by scattering and absorbing visible radiation.[92] At a global level, SOAs affect the Earth's radiative balance both directly and indirectly. The direct affect arises from the scattering of solar radiation, which results in the cooling of the Earth's surface.[93] Indirect effects occur through the change in cloud properties[94], where SOA act as nuclei for cloud formation by providing sites for surface and condensed-phase chemistry to take place in the atmosphere.

SOA is formed from the successive oxidation of VOCs, which occurs predominantly through reaction with OH, NO_3 or O_3 (Section 1.5.2). The oxidation process adds functional groups to the organic gas molecules, which lowers the vapour pressure, forming products of lower volatility that subsequently partition into the condensed phase.[95] The rate constants for oxidation reactions have been measured for a large number of VOCs, however those leading to significant SOA formation are typically the larger and more complex compounds, for which the rate constants are relatively unknown.

SOA formation can involve biogenic or anthropogenic VOCs. Specifically, chamber experiments indicate that biogenic VOCs such as monoterpenes have high aerosol formation yields.[96] Despite being among the most abundant biogenic VOCs, isoprene has generally been discarded as an important precursor of SOA due to the high volatility of it's known reaction products. However, there is an increasing volume of work showing that despite the low SOA yield, emissions are sufficiently large to make a significant contribution to particulate production.[97,98] The majority of anthropogenic SOA is produced from aromatic compounds from vehicle emissions.[99] In addition, the production of viscous crude oil and bitumen has also been noted as a potentially large source of SOA due to the evaporation of low-volatility organic vapours from mined material.[100] This could be particularly important in production and refining regions across the globe and should be considered when assessing the impacts of the O&G industry.[100]

1.6 Emissions from the oil and gas industry

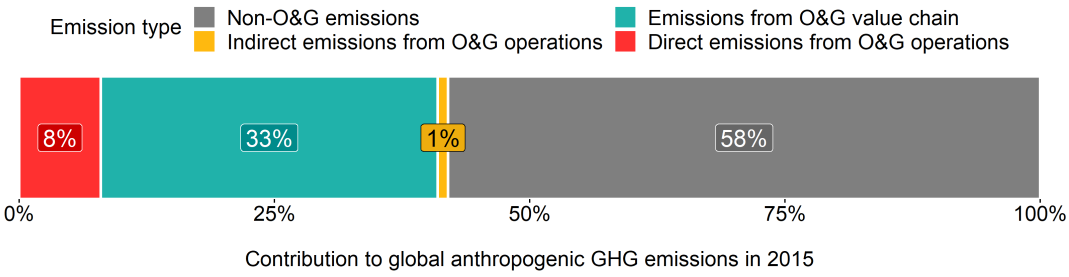

Figure 1.9: *Oil & gas share of global emissions in 2015.*[101]

Atmospheric emissions of GHGs from the O&G industry account for 42% of all global anthropogenic GHG emissions (Figure 1.9).[101] Included in this figure are direct and indirect emissions, in addition to those from the O&G value chain (product sale and use). Direct emissions are the most obvious to identify and are defined as those that result from the activity of interest. In the case of O&G extraction, this incorporates emissions from the well-head, but also vehicular emissions from company cars, vans or heavy goods vehicles (HGVs) used to transport equipment. Indirect emissions lie outside a company's

immediate control and are those resulting from the production of energy which is subsequently consumed by the company. Finally, there are emissions from the O&G value chain, sometimes described as *Scope 3* emissions. Scope 3 refers to emissions associated with the intended end-use of O&G products, namely the combustion of fossil fuels. O&G companies rarely acknowledge responsibility for these emissions, however downstream emissions from burning fossil fuels account for 60–90% of life-cycle emissions from O&G products.[102] Whilst this thesis focuses on the measurement of direct and in-direct emissions, it is worth noting that there are a myriad of downstream sources which contribute to the environmental impact of this industry.

1.6.1 Emission sources

The exploitation of fossil fuels takes place both on and offshore. Onshore emissions typically attract the most attention due to the potential impacts on air quality and human health in the immediate surroundings. As of 2019, the United States (US) was the biggest producer of natural gas in the world.[103] Production has grown at unprecedented rates in the US since 2010, stimulated by the emergence of new technologies such as hydraulic fracturing, which enabled the extraction of previously inaccessible shale deposits.[104] Concurrent with the increase in production has come an increase in associated emissions to the atmosphere.

There are numerous potential sources of air pollutants throughout all stages of the O&G extraction process, which vary in terms of both absolute amounts and composition.[105] Figure 1.10 shows a schematic of the potential species emitted at each stage of the extraction process. As the primary chemical constituent of natural gas (70–90%),[106] emissions of CH_4 occur during all stages as a result of intended or accidental releases. As a result, many studies focus on CH_4 and the associated climate impacts.[107,108] Quantifying CH_4 emissions is of particular interest since a key statistic put forward by Alvarez et al. [109] concluded that leakage of 3.2% or less would provide immediate net climate benefits for electricity production from natural gas compared to coal. However, in addition to CH_4, O&G activities are responsible for emissions of other compounds that can also perturb local and regional air quality. National emission inventories indicate that VOC and NO_x emissions from O&G supply chains in the US have significantly increased

over the past decade.[110] Elevated concentrations of VOCs and NO_x from O&G activities has been linked to both summer and winter photochemical O_3 formation,[62,111,112] the exposure to which is estimated to cause 1100–2700 premature deaths per year across the US by 2025.[113]

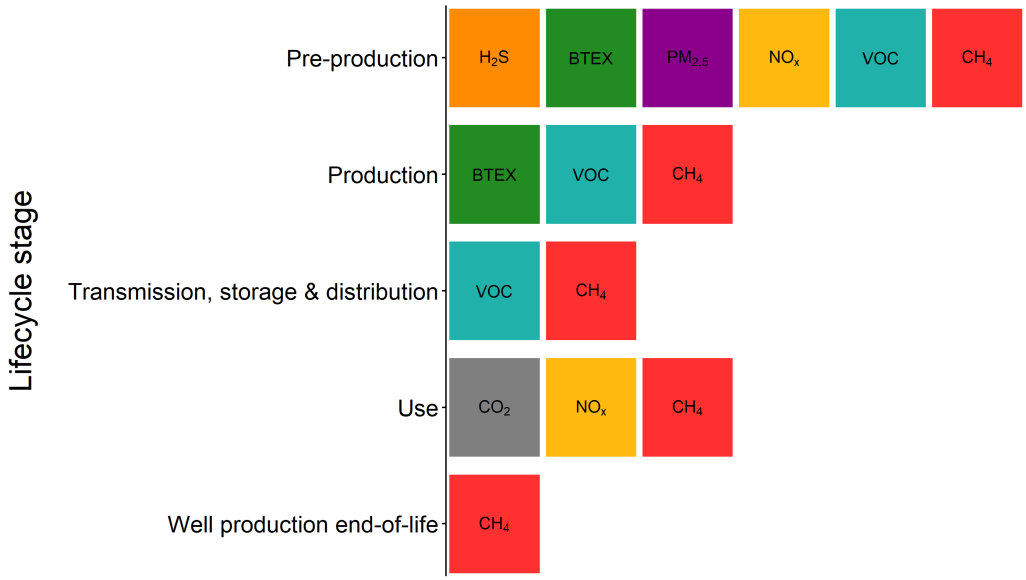

Figure 1.10: *Potential species emitted to the atmosphere during specific stages of the O&G life cycle (VOC = volatile organic compounds, BTEX = benzene, toluene, ethylbenzene and xylenes). Adapted from Moore et al. [114].*

Within Figure 1.10 there are five stages of the O&G life cycle all of which give rise to atmospheric emissions. The pre-production stage encompasses site exploration, road construction, rig assembly and drilling until the well is complete. In the case of a single well, pre-production may only take a few weeks, however these operations are often carried out for multiple wells on the same pad and therefore typically last months. Diesel-powered equipment, such as turbines and pumps are heavily used during site preparation. In addition, hydraulic fracturing requires large volumes of water, sand and chemicals to be continually transported to and from the well pads, leading to emissions from on and off-road diesel use.[115] Emissions from diesel combustion include fine particulate matter ($PM_{2.5}$) as well as NO_x and VOCs. Coarse particulate matter (PM_{10}) gen-

erated from tire wear, brake wear and resuspended road dust is also emitted but this is estimated to be a relatively small source compared to other O&G activities.[116] Stricter emissions standards for PM has led to the development of new control technologies such as diesel oxidation catalysts (DOCs) and catalysed diesel particulate filters (DPFs). The implementation of such devices has had positive impacts on diesel-related PM emissions. However, enhanced NO_2/NO_x ratios from catalyst-equipped diesel engines have been widely reported in both the US and Europe, which may have impacts on both ambient NO_2 concentrations and subsequent O_3 formation.[117]

During the pre-production phase, emissions continue throughout the drilling procedure. Along with CH_4, volumes of ethane (C_2H_6) and propane (C_3H_8) can be vented into the atmosphere as the drill exposes pockets of gas.[118] Meanwhile, exhaust emissions of PM and NO_x from diesel and natural gas powered engines for drilling rigs and pumps are also present. Upon completion of drilling, the well is then prepared to produce gas or oil. During well-completion, initial gas is flared and vented which produces emissions of CH_4, H_2S, VOCs, inclusive of BTEX (benzene, toluene, ethylbenzene and xylenes),[119] and formaldehyde if incomplete combustion of natural gas occurs.[111] Flowback operations used to clear the well and stimulate the flow of natural gas from the target shale also release emissions. Shaw et al. [120] estimated that 4 tonnes of CH_4 was emitted during a week long period at an exploratory shale gas site in Lancashire, UK during a nitrogen lift (a type of flowback operation). This equates to 143 tonnes CO_2 equivalents under the default 100-year time horizon, which is the approximate mass of CO_2 emitted from 142 London–New York flights.[120]

Similarly, the production phase generates emissions of atmospheric pollutants (Figure 1.10). Emission sources during this phase include well-head compressors and pumps, flare emissions, fugitive emissions from equipment, leaks during maintenance, and incomplete emissions capture.[114] These sources may be continuous or intermittent and predominantly result in the emissions of both CH_4 and VOCs. Flaring emissions are of particular concern since they essentially arise from the combustion of gas without utilisation of the energy that is released. For example, in the UK, the volume of flared and vented gas in offshore upstream O&G production was equivalent to 3% of the total natural gas produced in 2019.[121] The predominant reasons for flaring gas are either during

oil extraction, where it is produced as a by-product and cannot be processed or transported, or as a safety measure to relieve excess pressure.[122] Flare systems are installed on both onshore well-pads and offshore production platforms. Ideal conditions would result in more than 99% conversion of CH_4 to CO_2 and water vapour. However, real-world operating conditions are less efficient, which results in substantial emissions of CH_4, VOCs and NO_x, the composition of which is determined by the make-up of the input gas within the flare system.[122] Environmental and economical concerns have provoked the use of flare gas recovery systems (FGRS) in efforts to minimize the amount of gas being flared. Furthermore, the World Bank and the United Nations launched the *Zero Routine Flaring by 2030* initiative in 2015, which is now endorsed by over 30 governments and close to 40 oil companies around the world.[123]

Non-CH_4 emissions surrounding the remaining three phases in Figure 1.10 are less well documented than those from the pre-production and production phases. However, crude oil and liquid condensate storage tanks are estimated to be a significant source of VOCs. Onshore, once hydrocarbon liquids have been extracted from the well, they are stored in fixed-roof, atmospheric pressure tanks prior to pipeline or truck transportation. Offshore, the liquid is held in storage tanks on production platforms or floating production, storage and offloading (FPSO) vessels before transport. It is estimated that 66% of total non-CH_4 VOCs emitted by O&G operations in the Denver-Julesburg Basin in the north-east Colorado Front Range are attributable to storage tank emissions.[124] The most significant type of emissions from storage vessels are flash losses. They occur when pressurized hydrocarbon liquid containing dissolved gases is transferred to a fixed-roof tank at ambient pressure. This drop in pressure causes the light hydrocarbons dissolved in the crude oil or condensate to vaporize (flash) from the liquid stored in the tank and accumulate in the vapour space of the tank, where they are vented to the atmosphere.[125] Tank flashing occurs both on and offshore and the resulting emissions typically contain a heavier VOC mix compared to emissions from pneumatic drills and pumps, which are predominately raw natural gas (CH_4).[126]

In the offshore environment, crude oil is extracted and transferred ashore by either pipeline or shuttle tanker. The latter has potential to cause flashing emissions from multiple storage and loading procedures. Emissions of VOCs can occur first during loading

offshore when the tank is filled, and secondly when the oil is unloaded at an onshore terminal. Emissions during loading operations are non-uniform due to the stratification of vapour within the tank. Figure 1.11 shows an example of a typical saturation profile of vent gas throughout the loading operation. Typically, the gas vented from the tank once loading begins is relatively light in composition, whereas it becomes increasingly hydrocarbon-rich at the end when the heavier vapours residing lower down in the tank are expelled.[127] This makes the characterisation and mitigation of these emissions challenging. In the North Sea, approximately 30% of the UK's crude oil production and 70% of Norway's is loaded offshore.[127] In the case of Norway, it is estimated that more than 50% of its total VOC emissions occur during the storage and loading of crude oil.[128] Consequently, eco-friendly shuttle tankers, named "*E-Shuttle*", are being developed which implement VOC recovery technology to reduce emissions. The on-board VOC recovery plant uses compression and cooling phases to liquefy the hydrocarbons within the vapour to form liquid VOC (LVOC). The LVOC is stored on the vessel and subsequently re-used as fuel for the tanker, reducing both waste product and cutting VOC emissions by an estimated 42% on an annual basis.[128]

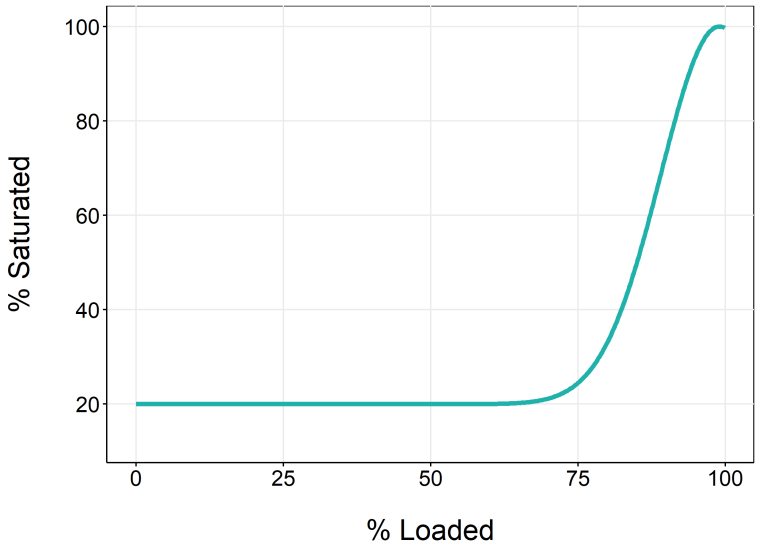

Figure 1.11: *Saturation profile of the vent gas as a function of the amount of liquid loaded into the tank. Adapted from Hill and Rudd [127].*

In summary, there are a vast array of emission sources from within the O&G sector, which extend throughout the entirety of the O&G life cycle. Natural gas is often seen as a cleaner alternative for electricity generation than burning coal, particularly with regard to climate impacts from GHG emissions. Shale gas life cycle emissions of GHGs are an estimated 33% lower than those for coal.[129] However, any potential benefits could be nuanced by emissions of NO_x and VOCs, important O_3 precursors, for which life cycle emissions are similar for natural gas and coal, but are generally less well studied.[130] A proactive approach in reducing emissions requires extensive monitoring before, during and after O&G development in order to determine the key emission sources for the myriad of air pollutants and the parameters that govern them. Furthermore, the classification of emissions during all stages of the life cycle is essential to understand all potential air quality and health impacts.

1.6.2 Oil and gas in the UK

Globally, the UK was the 19th biggest oil producer in 2020, producing 0.9 million barrels per day and accounting for 2.6% of global production (Figure 1.12).[131] As such, the O&G industry plays a central role in the UK economy. The UK is heavily reliant on the O&G industry for it's energy supply, such that O&G account for more than 75% of the UK's total primary energy needs.[132] Figure 1.13 shows the location of all known UK O&G fields. The UK's O&G sector is dominated by production from offshore reservoirs within the UK Continental Shelf (UKCS), which account for 98% of production.[133] Gas production predominately occurs in the southern North Sea off the coast of East Anglia, whereas oil is mainly extracted from platforms in the central North Sea, to the east of Aberdeen. Oil production also occurs much further north from fields located to the east and west of the Shetland Isles. On land, there are significant shale gas and oil reserves located in the Weald in south-east England, in addition to the Bowland Shale under Yorkshire and Lancashire. However, in November 2019 a moratorium was placed on hydraulic fracturing in England so little exploration has occurred to date. In terms of production, up until 2019, approximately 45 million barrels of oil equivalent (boe) had been recovered from the UKCS, with an estimated 10–20 billion boe still recoverable.[134] Since 2014, offshore production from the UKCS has increased by 20%, shown in Figure 1.14. This increase

was driven by major development projects in existing fields and production from upwards of 40 new fields.[134] Oil production from the UKCS is forecast to continue rising in the coming years. In particular, the West Shetland region has been the location of major investments to develop giant fields such as Clair Ridge. As such, oil fields in the West Shetland region are expected to account for 30% of UKCS output by 2025, compared to just 2% in 2014.[135]

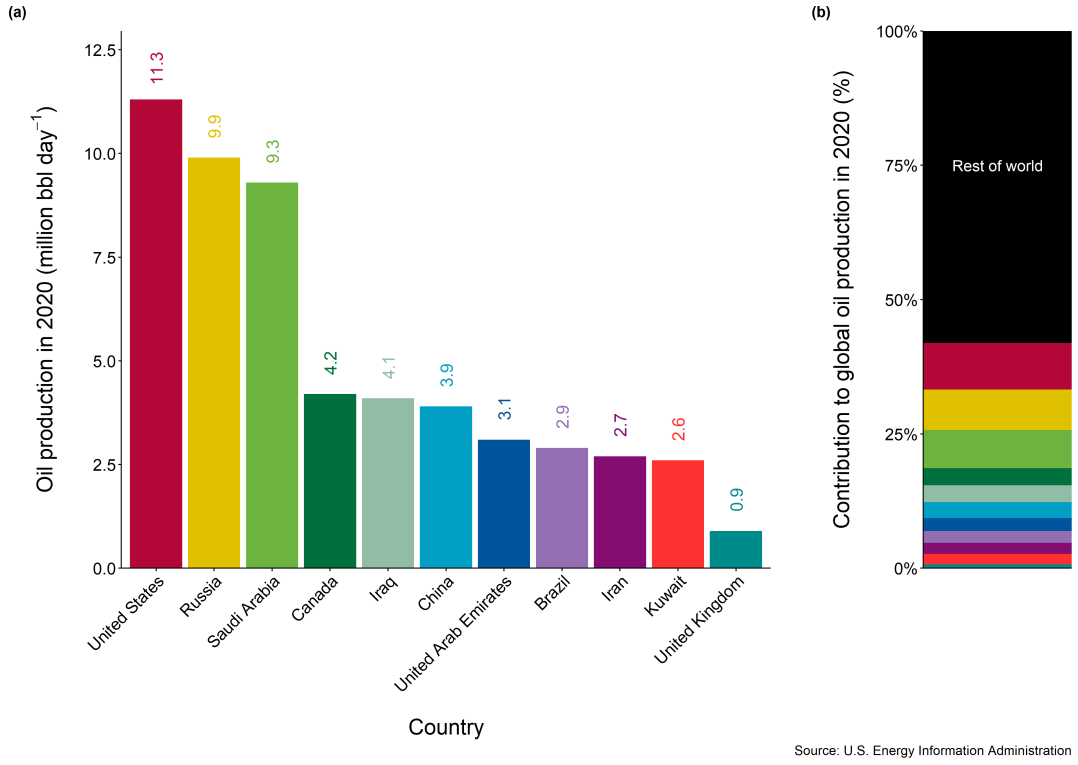

Figure 1.12: *(a) Oil production in 2020 from the ten biggest oil-producing countries and the UK (19th). (b) Contribution of each country in (a) to global oil production in 2020. Data was sourced from the U.S. Energy Information Administration.*[131]

Increased production is accompanied by increased concern about atmospheric emissions from the UK O&G industry. Since 1990, UK GHG emissions have followed a downward trend with a 43% reduction since 1990, as shown by Figure 1.15. The decline has been driven by changes in the methods of power generation. Specifically, the replacement of coal by gas, coupled with an increased renewable capacity. Despite the overall reduction in GHG emissions, in recent years GHG emissions from upstream O&G oper-

Figure 1.13: *Location of all UK O&G fields coloured by the corresponding field type. Cond = condensate, CBM = coal bed methane. Field shapefiles were obtained from the UK O&G Authority.*[136]

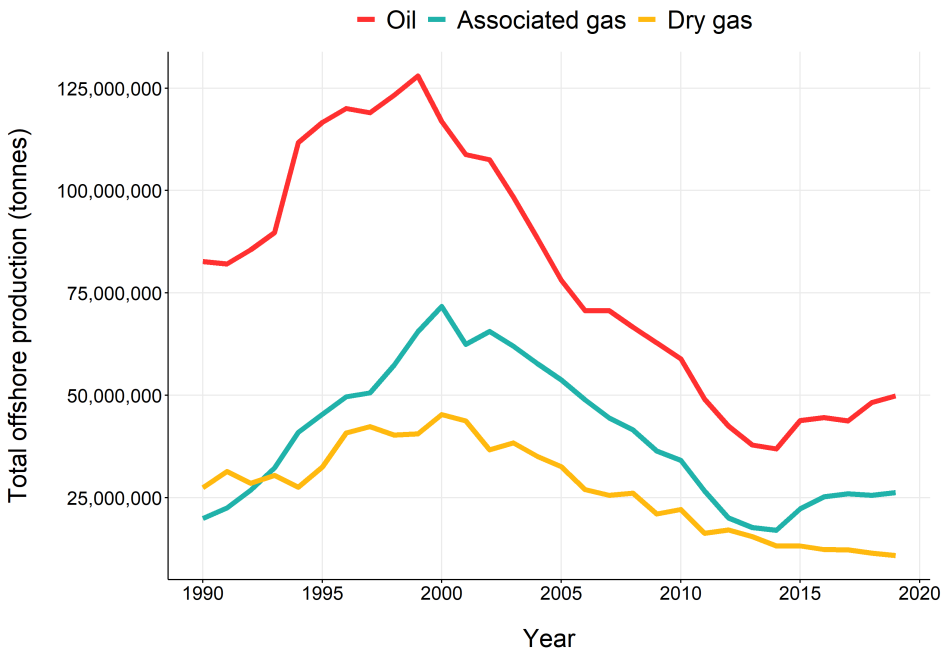

Figure 1.14: *Total UK offshore production of fossil fuels. Data was obtained from the UK Oil & Gas Authority.*[137]

ations have stabilised. Offshore O&G production contributed 3% of total UK GHG emissions in 2018 and the increase in production since 2014 coincided with a 5% increase in offshore CO_2 emissions throughout the same period. However, offshore CO_2 emissions decreased from 14.2 million tonnes in 2017, to 13.2 million tonnes in 2018 as a consequence of measures to reduce the quantity of gas flared, such as the World Bank's *Zero Routine Flaring* initiative, mentioned earlier.[137]

In contrast, there was a rise in offshore CH_4 emissions from 42,700 tonnes in 2017 to 43,500 tonnes in 2018.[137] Offshore CH_4 is predominantly emitted from a combination of vented sources and due to incomplete combustion of the flare, totalling 88% of offshore CH_4 emissions. A 53% increase in the mass of vented gas was observed in 2018 compared to 2017, rising to 95,100 tonnes. The composition of vented gas is approximately 51% CO_2, 25% VOCs and 24% CH_4. The increase in venting was dominated by abnormally high emissions from a single oil-producing installation with no infrastructure for exporting gas. Additionally, the gas from the reservoir had a CO_2 content sufficiently

high enough to prevent ignition of the flare, resulting in emissions of the un-burnt gas to the atmosphere.[137] This demonstrates how the occurrence of abnormal process conditions from a single installation can contribute a significant proportion of total offshore emissions. Consequently, venting has been identified as a key area for review where potential reductions in GHG emissions could be made.[137]

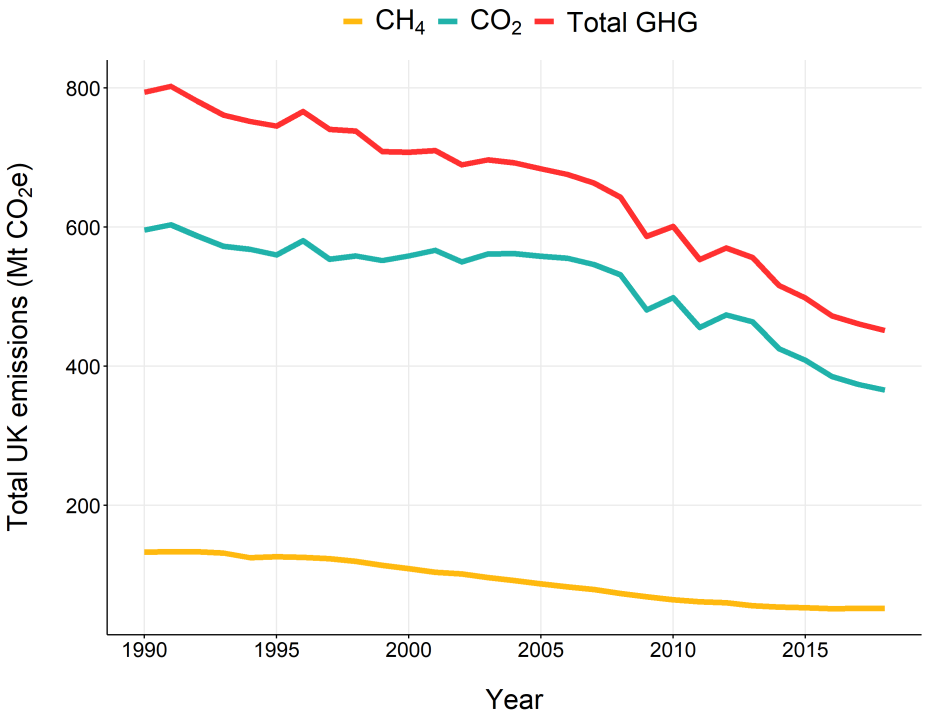

Figure 1.15: *Total UK greenhouse gas emissions. Data was obtained from the UK Oil & Gas Authority.*[137]

Offshore emissions of other air pollutants do not appear to follow the same falling trend as the GHGs. Figure 1.16 shows the CO_2 equivalent (CO_2e) emission intensity, essentially emission load per production unit, for total VOC, NO_x, SO_2, N_2O and CO. The emission intensity of NO_x and CO has been increasing since 2000, before peaking in 2015, where they been in decline up to 2018. These species are predominantly emitted from flaring and combustion processes and the trend is generally influenced by emissions reported from larger operators with greater production levels. These are typically oil platforms located in the Central North Sea and West Sheltand regions.[137] The emis-

sion intensity of total VOC also followed a positive trend since 2000, specifically from 2010 where a sharp increase was observed. Whist, there was a dip in 2016, emissions of offshore VOCs increased by 31% to 50,100 tonnes in 2018. Similarly, whilst total UK emissions of VOCs have been in decline since 1970, there was an increase of 1.6% between 2017–2018, attributed to a *"recent increase in operator-reported emissions related to venting and flaring at O&G installations"*.[138] Additionally, increased volumes of vented gas due to oil-loading operations has also contributed to the increase in VOC emissions offshore.[137]

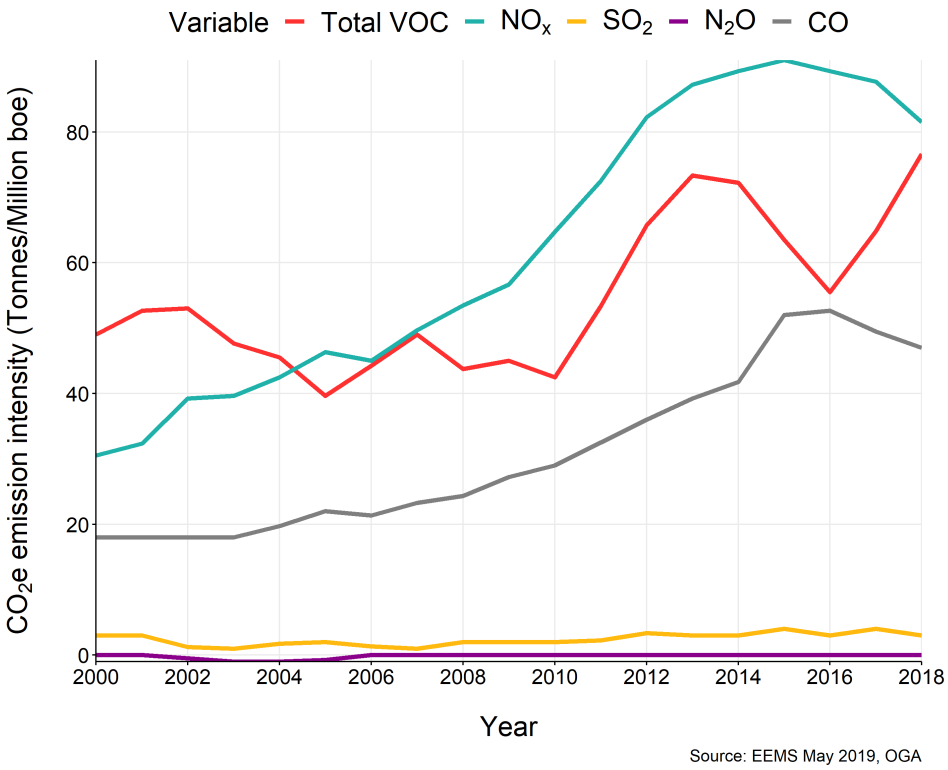

Figure 1.16: *Offshore CO_2e emission intensity for selected pollutants. Data was obtained from the UK Oil & Gas Authority.*[137]

Decreasing GHG emissions demonstrate a positive step towards cutting emissions from the offshore sector. However, it is vital that these reduction efforts are not compromised by increased emissions of other species. Therefore, studies surrounding the emissions of other air pollutants, particularly VOCs, will be valuable to understand the

current environmental impact of this industry and subsequently aid the focus of mitigation efforts. This is the main focus of this thesis, to assess VOC emissions from offshore O&G production in the North Sea to identify the key emission sources and evaluate how well these emissions are represented in the current reporting.

1.6.2.1 UK regulations

Emissions from the O&G industry are tightly controlled at the national, European and international level. Relevant legislation include the European Commission (EC) Directive on Integrated Pollution Prevention and Control (IPPC), which states that no offshore combustion installation can be operated except in accordance with a permit issued under the IPPC regulations. Similarly, venting and flaring are both subject to consent under the Petroleum Act 1998, the objective of which is to conserve gas since it is a finite energy resource. Therefore, operators require a *"Consent to Vent"*, which includes the venting of gases from crude oil storage tanks as well as gas released from FPSOs or shuttle tankers during oil loading operations. Additionally, emissions of NO_x, SO_2 and VOCs from ships are regulated by the International Maritime Organisation through the International Convention for the Prevention of Pollution from Ships (MAPRPOL). This legislation applies to the offshore sector as offshore installations and drilling rigs are defined as ships by MARPOL.

In the UK, offshore emissions are internally regulated by the Offshore Petroleum Regulator for Environment and Decommissioning (OPRED), part of the Department for Business, Energy and Industrial Strategy (BEIS). O&G operators must apply for a permit to emit species into the air or sea. Emissions are self-reported by the operator through the Environmental Emissions Monitoring System (EEMS), which is the primary data source used to represent the offshore sector in the National Atmospheric Emissions Inventory (NAEI). EEMS is regarded as the central element to confirm compliance with regulations surrounding atmospheric emissions from the UK O&G industry. It is also used as a tool to inform policy development and implementation in efforts to improve human and environmental health. Emissions of CO_2, CH_4, NO_x, N_2O, SO_2, CO and VOCs for each of three emission types (consumption, drilling & direct emission) are collated within EEMS. The resulting data is aggregated across all emission sources to calculate a total annual mass

emission per pollutant for each installation and terminal.[139]

The methodology within EEMS calculates emissions through the use of emission factors (EF) since direct monitoring is rarely available offshore. An EF is a representative value that relates the quantity of pollutant released with an associated activity.[140] An example EF describes the mass of NO_x emitted per gram of fuel consumed. R1.28 displays the equation for calculating the mass (M) of pollutant (g) emitted for a given source (s), where (A) is the activity factor for the source and (E) is the emission factor for the gas relative to the emission source.[139]

$$M_{gs} = E_{gs} \times A_s \tag{R1.28}$$

EF can either be calculated, or in the absence of suitable data, default values are substituted. Calculated EF are derived from local data, such as the composition of the flare and fuel gases, which is generally unique to the installation. Compositional analysis is typically conducted using Gas Chromatography (GC) and gives a breakdown of the gas in terms of component weight percentages (C_{wt}). The C_{wt} are then combined with known combustion factors to calculate the EF.[139] The alternative are default EF, which exist for every emission source and gas. They are taken from within the literature and are assumed to be suitably representative of their associated source.

EF are a key element within EEMS, which underpin the accuracy of the emissions reported from each installation and therefore the entirety of the offshore sector. To enable scientifically defensible policy development, it is critical that emissions are reported in a consistent and reliable manner. Out of date activity and emission factors can lead to the misrepresentation of emissions within inventories[141] and has the potential to misleadingly influence mitigation strategies. Similarly, this data is used as inputs to air quality models and could result in inaccurate forecasting. In this regard, very little work has been done to challenge the quality of the data inputted into EEMS. In the current methodology there is no independent way to confirm the reported emissions of atmospheric pollutants within EEMS are correct. An array of studies show there are often discrepancies between measured and reported emissions, commonly attributed to incorrect EF or the presence of *"super-emitters"* which are often unaccounted for.[141–144] To this end, verification of the EEMS database through comprehensive measurements

would be advantageous to determine if current techniques need to be reviewed or revised. This is, in part, addressed in Chapter 4.

1.7 Thesis outline

This thesis presents an evaluation of atmospheric emissions from both the onshore and offshore UK O&G industry. Extensive data sets were collected through ground-based and airborne measurements, which were combined with refined data processing and analysis techniques. This work concentrates on the magnitude and composition of emissions from the UK O&G sector, where there are currently very few observational constraints.

Chapter 2 presents an overview of the key instrumentation used in this work. The principles of operation are discussed along with calibration procedures and uncertainty calculations.

Chapter 3 presents a spatial analysis of airborne measurements of VOCs and other trace gases over four different regions of O&G production in the North Sea. VOC enhancement ratios are utilised to *(i)* differentiate O&G sources from urban fossil fuel sources and *(ii)* investigate the VOC composition as a function of the fossil fuel product produced (oil, gas, condensate). The important contributors to tropospheric O_3 are identified through calculation of the OH reactivity. The measurements are also compared to relevant VOC speciation profiles for offshore O&G production within the NAEI.

Chapter 4 presents airborne data collected downwind of North Sea O&G platforms. A mass balance approach is applied to quantify emissions of CH_4 and speciated VOCs from individual installations. The results are compared to those reported in EEMS to assess discrepancies or gaps in the current methodology for calculating offshore emissions. Specifically, the influence of oil loading operations onto shuttle tankers is investigated, potentially exposing a significantly underestimated source of VOCs.

Chapter 5 presents measurements made at a UK exploratory shale gas site in Kirby Misperton, North Yorkshire, at which permission for hydraulic fracturing was initially granted. A baseline characterisation of air quality is performed, allowing identification of the pre-existing emission sources and their influence on ambient concentrations. A

robust machine learning technique based on the random forest algorithm is applied to quantify the changes in atmospheric concentrations of NO_x and O_3 resulting from hydraulic fracturing operations, whilst accounting for changes in meteorology. Finally, the impact of the associated emissions is considered.

Chapter 6 gives a summary of the most important findings in this work and an overview of how the analyses could be extended in the future.

1.8 Degree of involvement

Chapter 3 and Chapter 4

Involved in all FAAM research flights from 2018 onwards. Participated in flight planning, experimental design and in-flight measurements of VOCs using the on-board WAS system. Processed all WAS data including the analysis of VOCs in the lab and work-up into mixing ratios. Also performed all data analysis.

Chapter 5

Involved in all aspects of ground-based data collection from October 2017 onwards. This included operating all instruments at the air quality monitoring site (O_3, NO_x, CH_4, CO_2, H_2S, SO_2, PM, WAS), performing calibrations and data processing. Also performed all data analysis.

2

Experimental

This chapter describes the key measurements which underpin the work in the rest of this thesis. Data was collected using both airborne and ground-based instrumentation. Table 2.1 summarises the instruments used, the species measured and on what platform. Further detail is described throughout this chapter including the measurement techniques and principles, calibration procedures and the calculation of uncertainties.

Table 2.1: *Air pollutant measurement summary.*

Instrument	**Species measured**	**Measurement platform**
Los Gatos Research Inc. Off-Axis Integrated Cavity Output Fast Greenhouse Gas Analyser (FGGA, model RMT-200)	CH_4, CO_2, H_2O	FAAM BAe-146
Los Gatos Research Ultraportable Greenhouse Gas Analyzer	CH_4, CO_2, H_2O	Ground-based monitoring site
Tunable Infrared Laser Direct Absorption Spectrometer (TILDAS, Aerodyne Research, Inc)	C_2H_6	FAAM BAe-146
Whole air sampling system (WAS)	Collection of discrete air samples	FAAM aircraft
Son of whole air sampling system (SWAS)	Collection of discrete air samples	BAS Twin Otter
SilcoCan 3L air sampling canister	Collection of discrete air samples	Ground-based monitoring site
Teledyne T200UP	NO, NO_2, NO_x	Ground-based monitoring site
ThermoFisher Model 49i Ozone Analyser	O_3	Ground-based monitoring site
Fidas 200	PM_{10}, PM_4, $PM_{2.5}$, PM_1, PM_{Total}	Ground-based monitoring site
ThermoFisher Model 250	H_2S, SO_2	Ground-based monitoring site
Gas chromatography with flame ionisation detection (GC-FID)	C_2–C_8 hydrocarbons	Laboratory

2.1 Airborne measurements

2.1.1 Atmospheric research aircraft

Chapter 3 and Chapter 4 are based on measurements made onboard the UK's atmospheric research aircraft. Operated by the Facility for Airborne Atmospheric Measurements (FAAM), the aircraft is a BAe-146-301, which has been in operation since 2003 (Figure 2.1). The aircraft can carry a payload of up to 4 tonnes of instrumentation, along with a maximum of 18 scientists and 3 crew members. Typical science sorties last 4–5 hours, flying at an altitude range of 15–10600 m, allowing measurements within both the boundary layer and the free troposphere. The FAAM aircraft is fitted with a wide range of scientific instrumentation. Fundamental meteorological variables such as wind speed, wind direction, air temperature, air pressure and humidity are measured on every flight. Similarly, a core set of atmospheric chemistry measurements are available on all flights for trace gas species such as nitrogen oxides (NO_x), ozone (O_3) and sulphur dioxide (SO_2), along with greenhouse gases (GHGs) such as carbon dioxide (CO_2) and methane (CH_4). Mission-specific instrumentation can also be added to the aircraft, increasing the range of species measured. Of relevance to this work was an instrument capable of measuring ethane (C_2H_6).

Figure 2.1: *The FAAM atmospheric research aircraft.*

Additional data for Chapter 3 was also collected on-board an instrumented DHC6 Twin Otter, operated by the British Antarctic Survey (Figure 2.2). Similar to the FAAM aircraft, the Twin Otter was equipped with instrumentation to measure atmospheric boundary layer parameters, including the boundary layer structure and stability, as well as a number of targeted chemical parameters. These included CH_4, CO_2, H_2O and C_2H_6 as well as whole-air sampling for subsequent analysis of a suite of VOCs. Further detail regarding the aircraft fit can be found in France et al. [145].

Figure 2.2: *The BAS Twin Otter.*

2.1.2 In-situ measurements

Airborne measurements of CH_4 and CO_2 at 1 Hz resolution were made using a modified Los Gatos Research Inc. Off-Axis Integrated Cavity Output Fast Greenhouse Gas Analyser (FGGA, model RMT-200), operated by FAAM. The instrument was calibrated in-flight against certified gas standards traceable to the World Meteorological Organisation (WMO) greenhouse gases scale. Calibration was performed using 3 gas standards; HIGH (CH_4∼2690 ppb, CO_2∼440 ppm), LOW (CH_4∼1690 ppb, CO_2∼370 ppm) and TARGET (CH_4∼1940 ppb, CO_2∼402 ppm). The slope and intercept values of the instrument were determined through a linear interpolation of sequential in-flight calibrations of the HIGH and LOW concentration standards. The precision of the CH_4 and CO_2 measurements was

determined from the regular in-flight TARGET calibrations and gave 1σ standard deviations of 1.77 ppb and 0.424 ppm, respectively. The total measurement uncertainty was calculated by combining the respective uncertainties for CH_4 and CO_2 associated with the target measurement (1.77 ppb and 0.424 ppm), the correction for the influence of water vapour based on quadratic fit coefficients from O'Shea et al. [146] (1.03 ppb and 0.150 ppm) and the uncertainty in the target gas concentration (2.00 ppb and 0.11 ppm). This gave overall uncertainties of 2.86 ppb for CH_4 and 0.463 ppm for CO_2 at 1 Hz. Further technical details of the instrument set-up and calibration procedures can be found elsewhere.[146–148]

Atmospheric C_2H_6 was monitored by a Tunable Infrared Laser Direct Absorption Spectrometer (TILDAS, Aerodyne Research, Inc).[149] This instrument applies a continuous wave laser operating in the mid-infrared region (at λ = 3.3 μm). Rapid tuning sweeps of the laser frequency result in the collection of thousands of spectra per second which are co-averaged. The resulting averaged spectrum is processed at a rate of 1 Hz using a non-linear least-squares fitting algorithm to determine mixing ratios. A path length of 76 m is achieved using a Herriott multipass cell in order to provide the sensitivity required for a trace gas measurement.

Calibration of the instrument was performed in-flight against two gas standards certified by the Swiss Federal Laboratories for Materials Science and Technology (EMPA); HIGH (C_2H_6 = 39.79 $\pm$ 0.14 ppb) and TARGET (C_2H_6 = 2.08 $\pm$ 0.02 ppb). Water vapour corrections were applied within the instrument software to account for changes in humidity during the flight as in Pitt et al. [150]. Uncertainties were calculated based on the standard deviation from the mean values during calibrations. The largest value was observed for the high standard, where 1σ = 0.086 ppb. The instrument has a quoted precision of 50 ppt for an averaging time of 10 s, therefore this is likely to be a conservative estimate of the uncertainty.

2.1.3 Whole air sampling

Discrete air sampling is available on the FAAM aircraft through use of the Whole Air Sample (WAS) system. Once collected, samples are later analysed by sensitive equipment not suited to in-flight operation. The WAS system consists of a set of 64 silica-passivated

stainless steel canisters of 3 L internal volume (Thames Restek) fitted in cases of 8, 9, and 15 canisters to the rear lower cargo hold of the aircraft (Figure 2.3).[147] Each case was connected to a stainless steel sample line (3/8 inch outside diameter), which was connected to an all stainless-steel assembly double-headed, three-phase, 400 Hz metal bellows pump (Senior Aerospace, USA). Air was drawn from the port-side main air sampling pipe into individual canisters, taking around 10 s to travel from the inlet at the front of the aircraft to the hold at the back.[147] Air was continuously flushed through the internal manifold of the cases prior to filling. Individual canisters were filled at user-specified times to a maximum pressure of 3.25 bar, giving an approximate sample volume of 9 L.

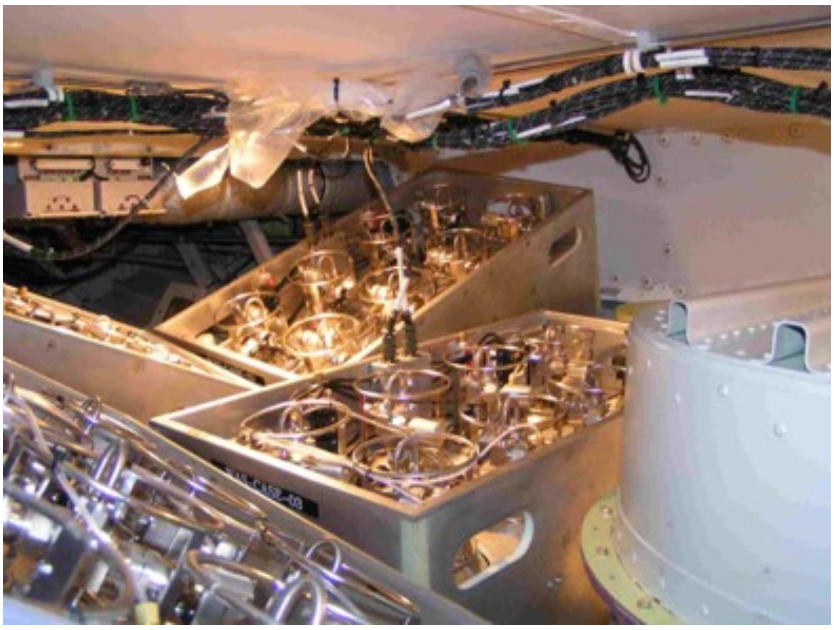

Figure 2.3: *Cases for the WAS system in the rear hold of the FAAM aircraft.*

A similar system, the Son of Whole Air Sampler (SWAS) was installed on the Twin Otter. This is an updated system housed in the aircraft cabin, rather than in the rear cargo hold to aid accessibility. Cases of Silonite coated (Entech) canisters are grouped together modularly within the aircraft rack. The SWAS has additional functionality, where cases comprise either 16 $\times$ 1.4 L canisters or 8 $\times$ 2 L canisters. The 1.4 L version has a single valve and was filled from vacuum to 3 atm gauge pressure. The 2 L version has valves at each end and could be filled either from vacuum or by flowing through at a variably set back-pressure before filling. The latter allowed greater control for the capture of

rapidly changing atmospheric events such as narrow pollutant plumes. Canisters from both systems took approximately 10–20 seconds to fill, corresponding to roughly 1–2 km of horizontal flight based on a typical aircraft speed of 100 m s^{-1}. Therefore, a single sample represents the average mixing ratio on a spatial scale of approximately 2 km.

2.2 Gas chromatography with flame ionisation detection

The whole air samples collected in-flight were analysed post-flight using gas chromatography with flame ionisation detection (GC-FID). Gas chromatography (GC) is a separation technique commonly used for the analysis of volatile organic compounds (VOCs) in the atmosphere.[151,152] Simply, an inert carrier gas (H_2 or He), known as the mobile phase, transports the sample through the GC system. The sample is injected into the GC inlet and onto an analytical column, the stationary phase, which is then heated. Heating causes compounds to elute at a time which is dependant on their interactions with the stationary phase and hence separation is achieved. Compounds are detected and quantified through the use of a flame ionization detector (FID). The FID combusts organic species to form ions, which create a current at the detectors electrode. The FID response is proportional to the amount of analyte present and dependant on the number of carbon atoms or molecular weight of the compound. GC coupled with FID is often used for long-term monitoring of VOCs, including the UK's Automatic Urban and Rural monitoring network (AURN), since it offers a high sensitivity to VOCs and a linear response over a wide range of concentrations.[153]

2.2.1 Instrumental set-up

Figure 2.4 shows the schematic of the lab-based GC system used in this work. Each case of whole air samples was connected to a single sampling port on a MARKES International CIA Advantage autosampler. Each canister in the case was sampled in turn using an automated trigger system developed at the University of York at a target flow rate of 50 mL min^{-1} for 10 minutes, giving a sample volume of 500 mL. Due to the low concentrations of VOCs in the air samples, pre-concentration was required before chromatographic analysis. To ensure the samples were dried before entering the pre-concentrator,

a water removal unit was added. This is an important step as water vapour can effect the efficiency of trapping in the pre-concentration stage and reduce the quality of the chromatography. Furthermore, water vapour can potentially cause damage to the columns in the GC oven. The water removal system consisted of an aluminium block cooled to -30 °C using a Stirling cooler. Inside the block was a glass condensation finger with two inlets on top to allow the flow of air in and out. Additionally, the top of the unit was heated to approximately 40 °C to prevent water condensing or freezing within the gas lines and blocking the flow of gas. Once dried, each gas or air sample was introduced directly into the pre-concentration unit, a MARKES International UNITY-2. Samples were injected onto a multi-bed sorbent-packed focusing trap (carbon based adsorbents with differing trapping efficiencies), which was electrically cooled to -20 °C. The trap was then heated rapidly from -20–300 °C in a stream of carrier gas to transfer the retained compounds into the GC. Between samples, the flow path was heated and lines purged to prevent carry-over from one sample to another. Separation of the compounds was achieved using an Agilent 7890B GC-FID system. An aluminium oxide (Al_2O_3, $NaSO_4$ deactivated) porous layer open tubular (PLOT) column (50 m length, 0.53 μm inside diameter, 10 μm film) was fitted inside the GC oven. The GC oven was heated from an initial temperature of 40 °C at a rate of 10 °C min^{-1} up to 110 °C, and then at a rate of 8 °C min^{-1} up to 200 °C, where the temperature was then held constant for 40 mins. This programme allowed for baseline-separation of the full range of VOCs of interest.

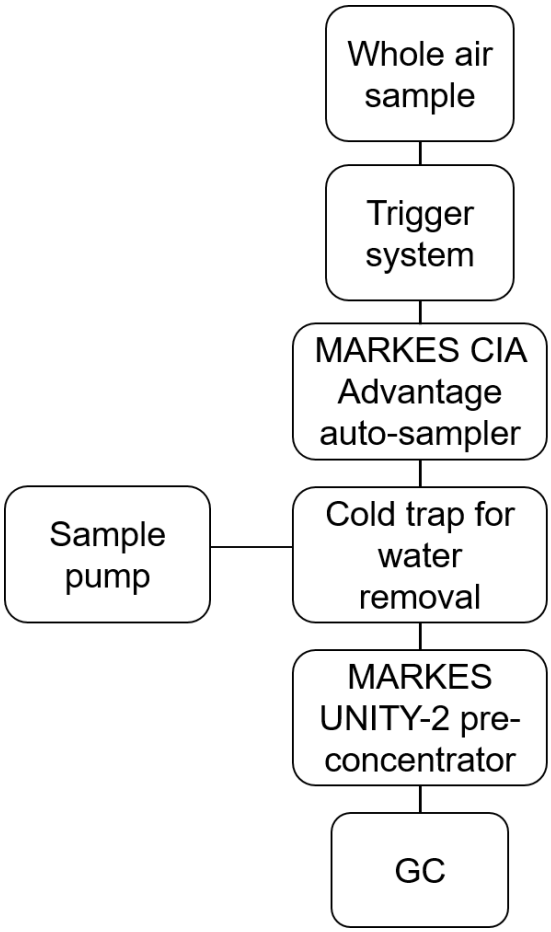

Figure 2.4: *Schematic of the lab-based GC system used for the analysis of whole air samples.*

2.2.2 Peak identification and calibration

Peak identification and calibration of the instrument was performed through reference to a National Physical Laboratory (NPL) certified 30-component, ppb-level, ozone precursor gas standard (NPL30, serial number: D386629). This calibration standard and method is within the World Meteorological Organisation Global Atmospheric Watch programme (WMO-GAW). A standard chromatogram for the NPL standard is shown in Figure 2.5. Heavier compounds such as the Trimethylbenzenes were also present in the standard, however the peaks were not well resolved and so were not quantified in this work. Peak integration was carried out using the GCWerks software, which performs automatic integration of peaks following identification based on the standard.

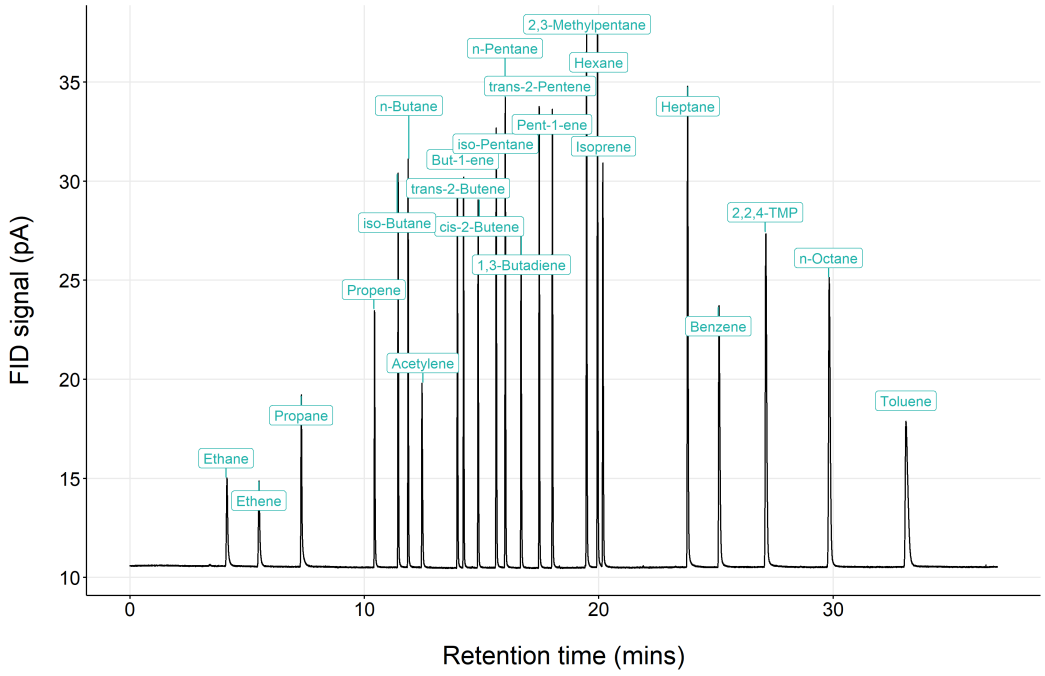

Figure 2.5: *Chromatogram for a typical NPL30 calibration.*

A typical sampling sequence for the analysis of whole air samples was comprised of five blank runs, followed by five calibrations, followed by the samples. Blanks of either purified compressed air or no-flow were performed to check for any possible contaminants within the GC system, which may affect the measured VOC mixing ratios. Figure 2.6a shows a typical series of five consecutive blank runs on the GC. For reference, the bottom panel (Figure 2.6b) shows the blank signals compared to an enhanced FID signal observed in ambient air. Blanks were generally clean, however in the case where peaks could be quantified, the mean peak area was subtracted from both the samples and calibrations to prevent overestimation of mixing ratios. Following blank correction, peak areas were converted to mixing ratios using an FID response factor $(\frac{peak\ area}{conc\ (ppb)})$ for each compound, where the peak area was the mean from each set of five calibrations. Additionally, a working standard composed of ambient air was run periodically on the lab GC system to check the instrument sensitivity over time. Drifts in sensitivity are not expected to influence the measurements here since calibrations were run prior to each set of samples and measurements were not performed over long periods of time. How-

ever, the precision of the working standard was used as an element in the uncertainty analysis (Section 2.2.3).

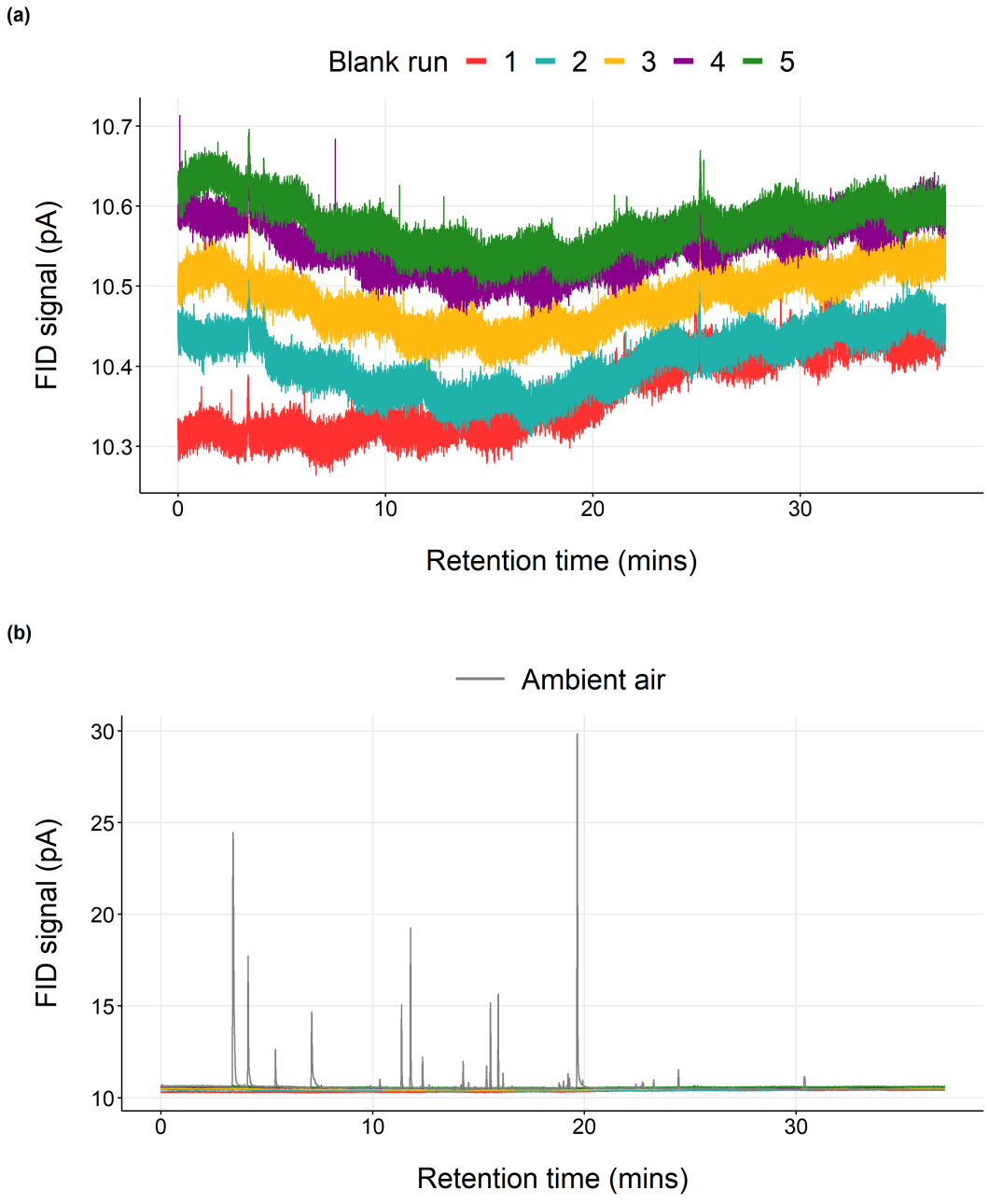

Figure 2.6: *(a) Chromatograms for a series of five consecutive blank runs. (b) Blanks overlayed onto a typical chromatogram for ambient air.*

The measured VOC mixing ratios in samples varied significantly. Figure 2.7 shows two

example chromatograms from whole air samples captured in regions of North Sea oil and gas (O&G) production. VOCs from O&G producing regions are typically dominated by light alkanes (C_2–C_5), as discussed in Chapter 3. However, the peak concentrations are highly spatially dependent on the location of plumes. Samples of high concentration were typically obtained within O&G plumes, whereas low concentration samples were captured outside plumes or in background air. In Figure 2.7, the largest peaks of ethane and propane corresponded to mixing ratios of 48 ppb and 98 ppb, respectively, compared to 2 ppb and 0.7 ppb in the out-of-plume sample.

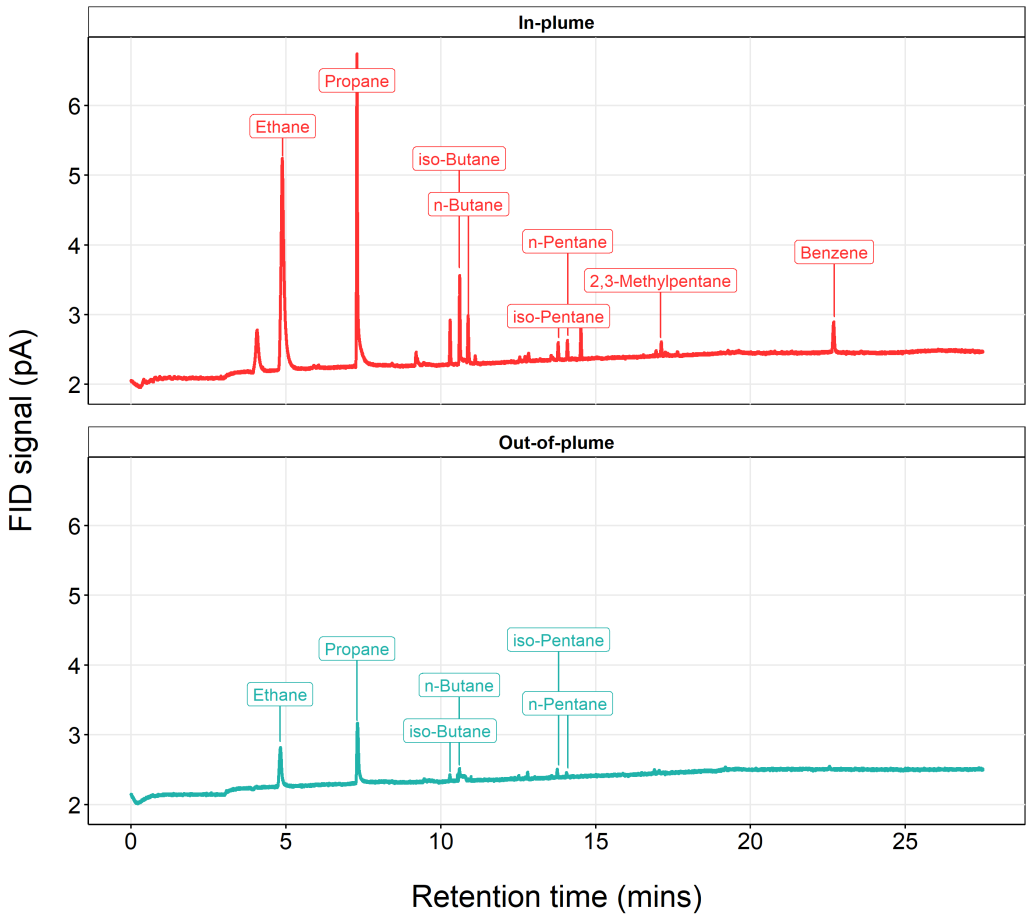

Figure 2.7: *Chromatograms showing high and low concentration samples obtained in regions of North Sea O&G production.*

2.2.3 Uncertainty analysis

The uncertainties for each VOC measurement were calculated following the Aerosol, Clouds and Trace Gases Research Infrastructure (ACTRIS) measurement guidelines.[154] The sources of uncertainty for the GC-FID were identified and combined in quadrature to yield an overall estimate of the uncertainty. The relative uncertainty in each concentration measurement ($\frac{\sigma(C)}{C}$) was calculated from the relative systematic uncertainties in the calibrations and blanks ($\frac{\sigma(C_{cal})}{C_{cal}}$, $\frac{\sigma(C_{blank})}{C_{blank}}$), combined with the instrument precision ($\frac{\sigma(C_{work\ std})}{C_{work\ std}} + \frac{1}{3}LOD$), as shown in R2.1.

$$\frac{\sigma(C)}{C} = \sqrt{\left(\frac{\sigma(C_{cal})}{C_{cal}}\right)^2 + \left(\frac{\sigma(C_{blank})}{C_{blank}}\right)^2 + \left(\frac{\sigma(C_{work\ std})}{C_{work\ std}} + \frac{1}{3}LOD\right)^2} \qquad \text{(R2.1)}$$

The relative calibration uncertainty ($\frac{\sigma(C_{cal})}{C_{cal}}$) was calculated from the quoted uncertainty for each compound within the NPL30 standard ($\sigma(C_{cal})$) and the quoted concentration of each compound in the cylinder (C_{cal}). The quoted uncertainties ranged from 0.05–0.08 ppb.

The relative blank uncertainty ($\frac{\sigma(C_{blank})}{C_{blank}}$) was calculated from the blank ratio, which was the ratio of the concentration in the sample to the mean concentration of each compound in the blanks. Each blank ratio corresponded to a relative error based on ACTRIS guidelines. For example, a blank ratio of 2 was assigned a relative error of 0.1.

The instrument precision was based on the stability of the working standard and the limit of detection (LOD) of the instrument. The working standard relative uncertainty for each compound ($\frac{\sigma(C_{work\ std})}{C_{work\ std}}$) was calculated from the standard deviation of the concentration in the working standard ($\sigma(C_{work\ std})$) and the mean concentration of each compound in the working standard ($C_{work\ std}$). Suitable standard runs during the periods before and after the analysis of the samples were manually selected for each sampling set. The LOD was calculated from the mean concentration and standard deviation of the blanks, before being multiplied by three, to give a 3σ value representing the 99.7% confidence interval. Therefore, when calculating the precision, the LOD was divided by three to obtain the standard deviation. Finally, the overall relative uncertainties were multiplied by a coverage factor ($k = 2$) to give an expanded uncertainty at the 95% confidence level. Concentration measurements below the LOD, were reported as half of the

LOD with a 100% uncertainty. VOC extended uncertainties during the analysis ranged from 0.72% to 8.37%, with the highest values typically obtained for *n*-octane, acetylene, and toluene. A full list of calculated uncertainties is given in Table 2.2.

Table 2.2: *Extended uncertainties for each quantified compound in the NPL30 calibration standard measured on the GC-FID system.*

Compound	**Uncertainty (%)**
Ethane	5.09
Ethene	2.99
Propane	2.87
Propene	1.97
iso-Butane	1.38
n-Butane	2.00
Acetylene	6.62
trans-2-Butene	1.13
But-1-ene	1.57
cis-2-Butene	0.83
iso-Pentane	1.85
n-Pentane	2.97
1,3-Butadiene	1.66
trans-2-Pentene	3.46
Pent-1-ene	0.99
2,3-Methylpentane	0.72
Hexane	1.08
Isoprene	5.28
Heptane	1.37
Benzene	1.59
2,2,4-TMP	1.84
n-Octane	5.80
Toluene	8.38

2.3 Ground-based measurements

2.3.1 NO_x measurements

Ground-based measurements of nitrogen oxides (NO_x = NO + NO_2), which underpin the analysis in Chapter 5, were made using a Teledyne T200UP Photolytic analyser. The analyser measures the amount of NO present in a gas by detecting the chemiluminescence which occurs when nitrogen oxide (NO) is exposed to ozone (O_3). The measurement of NO_x by chemiluminescence is widely employed, such that is the method of choice within the UK's AURN.[155] Chemiluminescence occurs in a two-step process, shown by R2.2 and R2.3. In the first step, NO reacts with excess O_3 to form an exited state NO_2 molecule (NO_2^*) and O_2. In the second step, the excited NO_2^* rapidly relaxes to the lowest stable energy state (ground state) and releases the excess energy in the form of a photon. The amount of light emitted exists in a linear relationship with the amount of NO present in the reaction cell. Therefore, by measuring the amount of light emitted, the quantity of NO in the sample can be determined. Light is measured using a photomultiplier tube (PMT), where the output voltage is proportional to the NO concentration.

$$NO + O_3 \longrightarrow NO_2{}^* + O_2 \tag{R2.2}$$

$$NO_2{}^* \longrightarrow NO_2 + h\upsilon \tag{R2.3}$$

2.3.1.1 NO_2 conversion

In order to quantify the amount of NO_2 by chemiluminescence, it must first be converted to NO. A common method of conversion is through a thermal conversion technique, involving the use of a heated molybdenum catalyst. This method offers a high conversion efficiency, however other atmospheric species such as nitric acid (HNO_3), HONO, peroxyacetyl nitrate (PAN) and alkyl nitrates (formation discussed in Section 1.5.1) can also be thermally broken down to NO, leading to the potential overestimation of NO_2 concentrations.[156] These interferences are typically more significant in remote and rural locations, where substantially aged masses are measured and NO_x makes a smaller con-

tribution to total odd nitrogen (NO_y).[157] Molybdenum converters are used in the UK's AURN and therefore the data may be subject to such overestimations. However, only PAN and HONO are believed to contribute significant interference at the ambient concentrations observed in the UK. It is estimated that PAN and HONO are likely to account for $\leq$ 2% and $\leq$ 5% of the NO_2 signal, respectively, under typical urban background conditions.[158] An alternative method, and the one used here, is to photochemically convert NO_2 to NO at a wavelength specific to NO_2 using a blue light converter (BLC), shown in R2.4. The sample gas is exposed to blue light from two high powered ultraviolet light-emitting diodes (LEDs) at narrow wavelengths, centred at 395 nm. This form of conversion is highly specific and minimises interference from other nitrogen compounds.[159]

$$NO_2 + h\nu \longrightarrow NO + O(^3P) \quad (\lambda < 410 \text{ nm}) \tag{R2.4}$$

2.3.1.2 Calibration

The calibration of the NO_x analyser was composed of three elements: a zero, an NO span and calculation of the NO_2 conversion efficiency (CE). The zero and span calibrations were conducted on a monthly basis at the field site. Figure 2.8 shows an example of the in-field calibration procedure. To obtain a zero measurement, a Sofnofil/charcoal trap was fitted to the inlet. The sample first passes through the Sofnofil beads, which oxidises the NO to NO_2 by using an oxidising agent of potassium permanganate. The NO_2 is then "scrubbed" by the activated charcoal. The trap was left in place until a stable zero reading could be obtained. The zero calibration was followed by a span calibration, which consisted of a known amount of NO being introduced to the analyser. NO standards were supplied by NPL and typically contained approximately 100 ppb of NO in N_2. As done for the zero, the span gas was flowed through the analyser until a stable reading was reached (Figure 2.8). Provided the calibrations were successful, both the zero and span calibrations were applied directly to the instrument.

The NO_2 to NO CE was calculated on an annual basis in the laboratory. Zero and span calibrations were performed prior to the CE calculation. A Gas Phase Titration (GPT) at both a high and a low NO_2 concentration was used to calculate the CE. The CE on the instrument was manually set to 100% prior to the calibration. First, a known amount

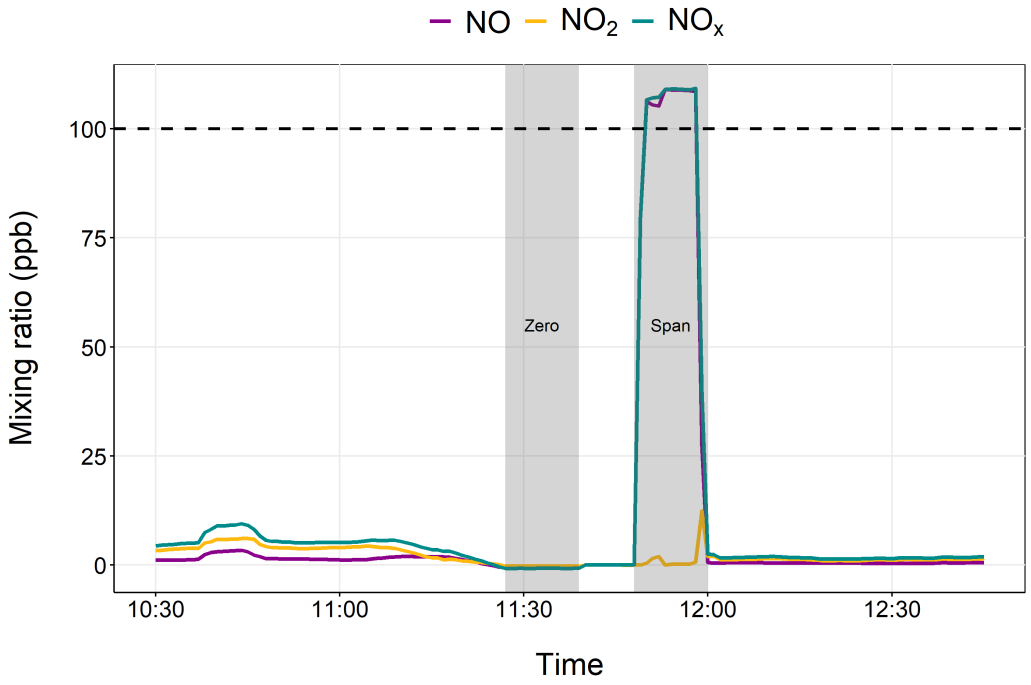

Figure 2.8: *Example in-field zero and span calibration of the NO_x analyser, shown by the grey shaded areas. The dashed line indicates the approximate NO concentration in the calibration cylinder.*

of NO_x ($[NO_x]_{ORIG}$) in form of NO was delivered to the analyser. This was titrated with O_3 at a concentration approximately 80–90% of the NO concentration to produce NO_2. The amount of NO_2 supplied ($[NO_2]_{SUPP}$) was calculated as the difference between the supplied NO and the NO remaining as part of the titration. Assuming a CE of 100%, the measured NO_x should remain constant during this process since all the NO_2 produced in the GPT should be converted back to NO. However, this is rarely the case and so a drop in total NO_x to a lower value ($[NO_x]_{REM}$) is observed. The CE was then calculated using R2.5.

$$CE\ (\%) = 1 - \frac{[NO_x]_{ORIG} - [NO_x]_{REM}}{[NO_2]_{SUPP}} \times 100 \tag{R2.5}$$

2.3.2 O_3 measurements

Ground-based O_3 measurements, also used in Chapter 5, were made using a Thermo Scientific Model 49i UV Photometric O_3 Analyser. The Model 49i operates on the principle that O_3 molecules absorb UV light at a wavelength of 254 nm. The degree to which the UV light is absorbed is directly related to the O_3 concentration as described by the Beer-Lambert Law (R2.6), where K is the molecular absorption coefficient (308 cm^{-1} at 0°C and 1 atm), L is the length of the cell (38 cm), C is the O_3 concentration in parts per million (ppm), I is the UV light intensity of the sample gas, and I_0 is the UV light intensity of the reference gas without O_3.

$$\frac{I}{I_0} = e^{-KLC} \tag{R2.6}$$

Within the analyser, the sample is split into two gas streams. One flows though an O_3 scrubber to become the reference gas (I_0), whilst the other is the sample gas (I). Both streams flow to a solenoid valve, which alternates the reference and sample gas streams between two separate cells every 10 s. Light at 254 nm is shone into each cell, where detectors measure the UV light intensities. The O_3 concentration of each cell is subsequently calculated according to R2.6. The final O_3 measurement is output as an average concentration across the two cells. This is regarded as a robust method of measuring O_3 since there are very few other atmospheric compounds which absorb at this wavelength, resulting in little interference and an accurate measurement.

2.3.2.1 Calibration

Zero calibrations of the O_3 analyser were carried out on a monthly basis in the field. A zero measurement was obtained by connecting an activated charcoal trap to the inlet of the instrument. O_3 is adsorbed onto the surface of the charcoal and thus scrubbed from the air. The trap was left in place until a stable reading was achieved. Figure 2.9 shows an example of a typical zero calibration, showing a consistent zero reading. The calibration was subsequently applied directly to the instrument. In addition, the instrument was calibrated annually against a Model 49i-PS Primary Standard over the calibration range 0–500 ppb at the University of York. The performance of the instrument was then vali-

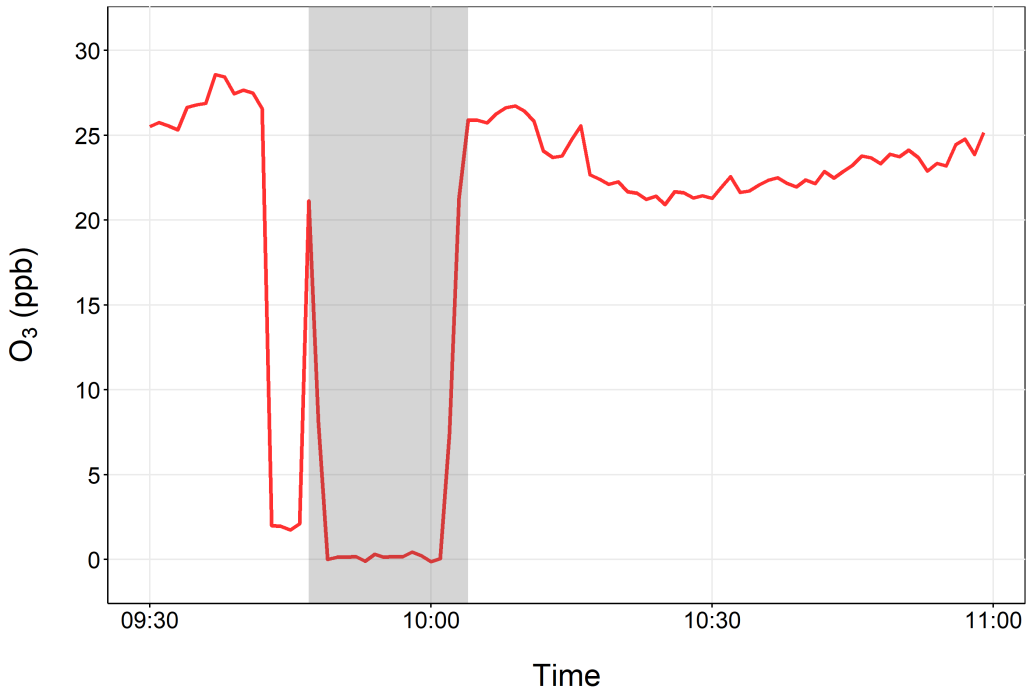

Figure 2.9: *Example in-field zero calibration of the O_3 analyser, highlighted by the grey shaded area.*

dated by comparison to well-calibrated O_3 instrumentation also housed at the University of York.

3

Speciation of VOC Emissions Related to North Sea Oil and Gas Production

This work was originally published in *Atmospheric Chemistry and Physics* on March 12, 2021.[†]

3.1 Introduction

Emissions from offshore oil and gas (O&G) production have been little studied in comparison to those from onshore production. Globally, offshore oil production accounted

[†]https://doi.org/10.5194/acp-21-3741-2021

for around 30% of the overall production in 2015.[160] The North Sea is home to the largest number of offshore rigs worldwide with 184 operational installations as of January 2018.[161] These are located across a number of different regions in the territorial waters of the United Kingdom (UK), Norway and the Netherlands. UK O&G production reached a seven year high in 2018 with an increase of more than 4% from 2017,[162] meaning production from the UK Continental Shelf (UKCS) met 59% of the O&G demand of the UK as of 2018.[137] The Norwegian sector is an evolving region of the North Sea with around 20 projects in various stages of development on the Norwegian Continental Shelf. Oil output is expected to grow by 43% from 2019 to 2024 as production from new fields begins and older facilities are upgraded.[163] The Netherlands was the second largest producer of natural gas in the EU in 2018.[164] The onshore Groningen field is by far the largest, however production is set to cease by 2022 due to induced seismicity above the field, meaning offshore, small field production may become increasingly important for the Dutch sector.

The release of air pollutants from O&G production has led to growing environmental and public scrutiny. Emissions of greenhouse gases such as methane (CH_4) are often the focus due to it's high global warming potential (Section 1.3).[165] Interest in emissions of volatile organic compounds (VOCs) from regions of O&G production arises because of their role as precursors to tropospheric ozone[62,112] and secondary organic aerosols (Sections 1.5.1 and 1.5.3). Both of these secondary pollutants have associated health and ecosystem effects.[119] Detailed measurements and quantification of VOCs and their subsequent reaction products is therefore needed in order to mitigate these air quality concerns.[166]

Emissions of VOCs can arise at all stages of the production process, such that crude oil processing was considered to be capable of emitting around 16% of the total global VOC emissions into the atmosphere in the late 20th century.[167] Sources include power generation sets, compressors, pumps, flaring off excess gas, cold venting during tank loading for transport on shuttle vessels and general fugitive emissions. Previous studies conducted in the United States have reported high VOC emissions for onshore wells and pads.[25,126,166,168–170] These studies have shown that comprehensive VOC characterization is crucial for source identification and to aid the estimation of effects of those emissions

on air quality in the surrounding regions.

The VOC composition of O&G emissions can be influenced by several variables, including the product being extracted (e.g. oil, gas or condensate), the geological composition of the reservoir, extraction techniques, age of the rig and infrastructure components. Offshore O&G emissions are naturally more difficult to measure due to lack of access to the installations and the large number of potential sources due to the complexity of offshore extraction. Offshore platforms are different to onshore well pads and their purpose and function are extremely varied, therefore it should not be assumed that studies quantifying onshore emissions will adequately represent emissions from the offshore sector. Few studies have examined VOC emissions from offshore facilities, whilst many of those that have follow "disaster" events, such as the Deepwater Horizon oil spill in the Gulf of Mexico in 2010[171,172] and the Elgin platform gas uncontrolled release in the North Sea in 2012.[147] Events such as these are uncommon and are therefore unlikely to be representative of VOC emissions from the offshore sector as a whole.

Offshore emissions are explicitly identified and reported in the UK National Atmospheric Emissions Inventory (NAEI). O&G operators are responsible for the self-reporting of these emissions for each offshore production platform. Whilst emissions of CH_4 are allocated to individual sources, only a total mass of VOC emission is reported for each point source platform, with no information relating to emissions of individual compounds. Some estimation of the relative speciation of VOCs is made in the inventory using historical speciation profiles, however these are generalised across source sectors and the overall uncertainties in these source profiles are not quantified. To date, VOCs in the North Sea have not been extensively studied. In this context, an improvement in the knowledge of VOC emissions from offshore O&G facilities is needed, in order to assess the potential impacts that these emissions can undergo in the atmosphere as well as improve the accuracy of emissions inventories.

3.1.1 Objectives

As key precursors to tropospheric O_3 formation, elevated levels of VOCs from regions of O&G production are known to negatively impact human and environmental health. However, few measurements exist regarding atmospheric emissions from North Sea

O&G facilities, even less so with respect to VOCs. The widespread O&G activity in the North Sea varies from gas-production in the south to predominantly oil-production in the north, with some gas-condensate production in-between. The chemical composition of each fossil-fuel product is unique to each basin but it is currently unclear whether this produces distinct emissions of VOCs or if such emissions remain uniform across the whole O&G sector. This work aims to *(i)* confirm O&G production as the key source of VOCs over the North Sea, *(ii)* quantify the source signatures of each primary extraction product though the use of emission ratios to expose spatial differences in emissions and *(iii)* compare the observed VOC speciation to source profiles within the UK emissions inventory to evaluate commonalities and discrepancies.

3.2 Methods

3.2.1 Measurement location and context

Measurements from a BAe-146 aircraft operated by the Facility for Airborne Atmospheric Measurements (FAAM) and a DHC6 Twin-Otter operated by the British Antarctic Survey (BAS) were made over a four-year period, beginning in 2015 and ending in summer 2019 (Section 2.1.1). The data used here were associated with a range of different projects: Baseline, Methane Observation and Yearly Assessment (MOYA), Climate and Clean Air Coalition (CCAC) and Assessing Atmospheric Emissions from the Oil and Gas Industry (AEOG). The flights surveyed a large number of O&G installations distributed across the whole of the North Sea. Data from a total of 28 flights (approximately 128 flying hours) across multiple airborne experiments were unified to generate a single data set for this analysis and are summarised in Table 3.1.

The spatial distribution of emissions attributed to O&G operations was evaluated by dividing the North Sea into four distinct regions, shown by the coloured boxes in Figure 3.1a. The regions were chosen for extended sampling because they contain high densities of offshore platforms and geologically distinct fossil-fuel producing reservoirs (Figure 3.1b), allowing for comparison of source signatures. The North UK region comprises oil, gas and condensate producing platforms serviced from Aberdeen and Hartlepool. The Britannia gas field, located 130 miles north east of Aberdeen is one of the

Table 3.1: *Summary of flight data used in this study. MOYA = Methane Observation and Yearly Assessment, CCAC = Climate and Clean Air Coalition, AEOG = Assessing Atmospheric Emissions from the Oil and Gas Industry. Baseline refers to a set of initial flights conducted in 2015 to serve as a comparison in future work. Regions are those defined in Figure 3.1a.*

Flight number	Date	Campaign	Region	Aircraft
B907	2015-05-13	Baseline	South UK	BAS Twin Otter
B908	2015-05-20	Baseline	South UK	BAS Twin Otter
B910	2015-05-26	Baseline	South UK	BAS Twin Otter
B912	2015-06-09	Baseline	South UK	BAS Twin Otter
B913	2015-06-23	Baseline	North UK	BAS Twin Otter
B918	2015-07-23	Baseline	North UK	BAS Twin Otter
C095	2018-04-19	CCAC	South UK	FAAM BAe-146
C096	2018-04-20	CCAC	South UK	FAAM BAe-146
C099	2018-04-25	AEOG	North UK	FAAM BAe-146
C100	2018-04-26	AEOG	West Shetland	FAAM BAe-146
C102	2018-04-27	AEOG	North UK	FAAM BAe-146
C112	2018-07-26	AEOG	North UK	FAAM BAe-146
C118	2018-09-11	AEOG	West Shetland	FAAM BAe-146
C119	2018-09-11	AEOG	North UK	FAAM BAe-146
C120	2018-09-12	AEOG	West Shetland	FAAM BAe-146
C121	2018-09-14	AEOG	North UK	FAAM BAe-146
C147	2019-03-04	AEOG	North UK	FAAM BAe-146
C148	2019-03-05	AEOG	West Shetland	FAAM BAe-146
C149	2019-03-06	AEOG	West Shetland	FAAM BAe-146
C150	2019-03-07	AEOG	West Shetland	FAAM BAe-146
B325	2019-04-30	CCAC	South UK	BAS Twin Otter
B327	2019-05-02	CCAC	South UK	BAS Twin Otter
B328	2019-05-03	CCAC	South UK	BAS Twin Otter
B329	2019-05-06	CCAC	South UK	BAS Twin Otter
C191	2019-07-29	MOYA	Norwegian Sector	FAAM BAe-146
C193	2019-07-30	MOYA	Norwegian Sector	FAAM BAe-146
C197	2019-08-02	MOYA	Norwegian Sector	FAAM BAe-146
C198	2019-08-02	MOYA	Norwegian Sector	FAAM BAe-146

largest fields in the North Sea.[173] The Norwegian Sector encompasses platforms in both the North and Norwegian Seas. Fields include Oseberg, and Asgard, which are Norway's seventh and eight biggest fields respectively. The South UK region includes a combination of fields located in the UK and Dutch sections of the North Sea. This region has the highest number of platforms. The largest field in this region is Leman, which has a current estimated production of 5.7 x 10^6 m^3 of gas per day.[174] Finally, the West Shetland region is a term that incorporates platforms located in the Schiehallion, Foinaven, Clair, Alligin, Lancaster and Solan oil fields. The surveyed area lies approximately 190 km west of the Shetland Isles. Recoverable reserves are estimated to be in the region of 250–600 million barrels of oil.[175]

Offshore field outlines and corresponding field types were obtained from the respective O&G authorities; The Oil and Gas Authority for UK fields,[136] the Norwegian Petroleum Directorate for Norwegian fields[176] and from the Geological Survey of The Netherlands for fields in the Dutch sector.[177] Each listed offshore field is assigned a field type of either oil, gas, condensate or a mixture. Often the dominant product of a field can change over time as reservoirs are depleted, therefore it is assumed that the field type listed is that of the most recent extraction product. Each region has distinct fossil-fuel producing reservoirs, shown in Figure 3.1c. West Shetland is entirely an oil producing region, whereas the South UK is dominated by gas production. The North UK is approximately a 50:50 mix of oil and condensate fields with a minor percentage of gas fields. The Norwegian sector contains an array of all offshore field types, which are assigned as mixed, where multiple products are extracted from the same well.

3.2.2 Instrumentation

Both aircraft were equipped with a suite of chemical and meteorological instrumentation. Basic atmospheric measurements including thermodynamic properties, wind and turbulence were included on both aircraft, from which information about the height, stability and structure of the atmosphere can be derived. 1 Hz measurements of carbon dioxide (CO_2), CH_4 and ethane (C_2H_6) were available on both aircraft and are described in Section 2.1.2. Additionally, whole air sample (WAS) systems were used for the collection of VOCs (Section 2.1.3). Further measurements of nitrogen oxides (NO_x), carbon

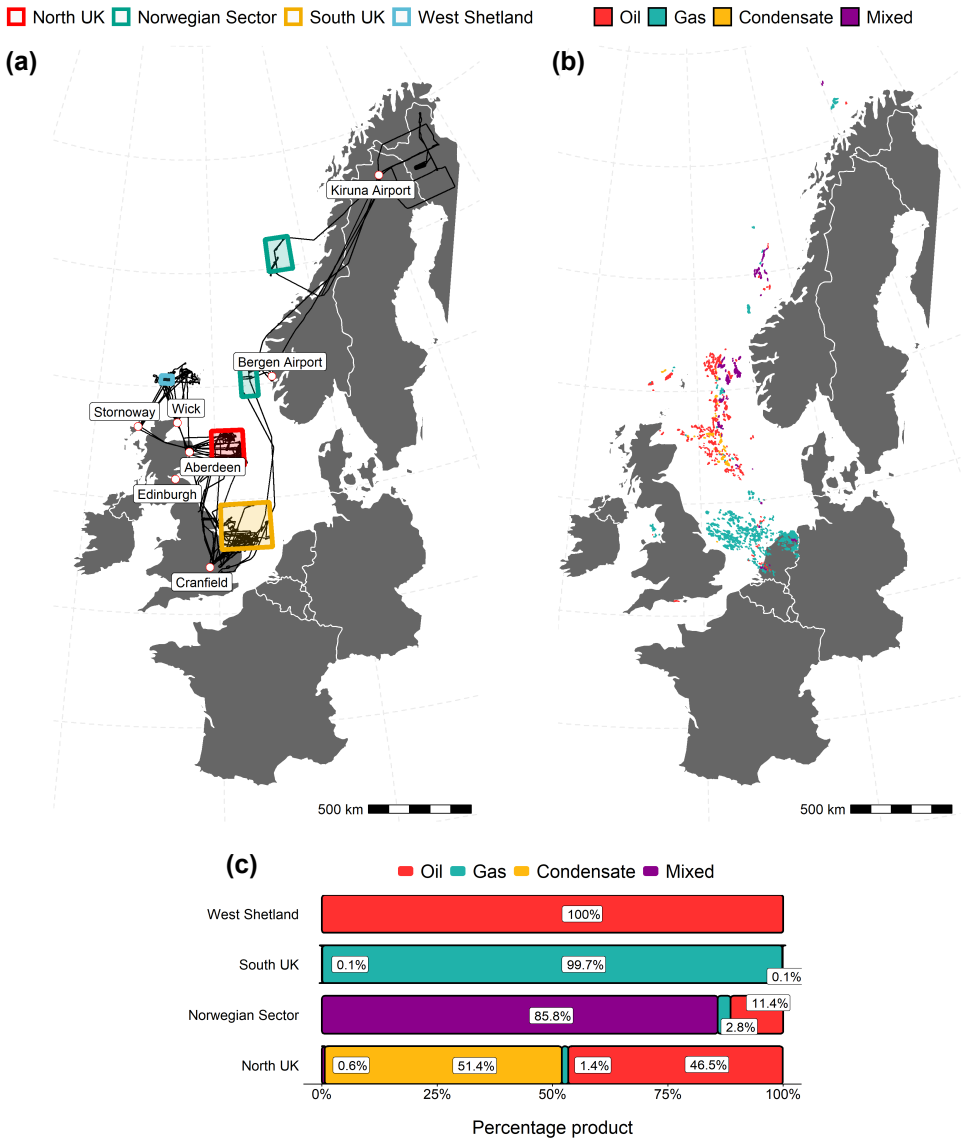

Figure 3.1: *(a) Regions of the North Sea defined for analysis. The black lines represent the flight tracks of the research aircraft. (b) Location of all offshore fields in the North Sea. Each polygon is coloured by the extraction product from each field. (c) Percentage contribution of each offshore field type to the total area of all fields in each region. Country polygons were obtained using the* ***rnaturalearth*** *R package.*[178]

monoxide (CO) and ozone (O_3) were available on some but not all of the flights and are not discussed here.

3.2.2.1 Aircraft whole air samples

Discrete ambient air samples were collected in evacuated canisters via an external inlet using unique sampling systems on board each aircraft. Both systems are based on the same principles and contain comparable components. In each system, evacuated stainless steel canisters, sealed with pneumatically actuated bellows valves (Swagelok, SS-BNVS4-C) were filled and pressurised in-flight by drawing air from the main sampling manifold. Air was continuously flushed through the internal manifold of the cases prior to filling. The WAS systems used on both the FAAM aircraft and Twin Otter are described in Section 2.1.3. The whole air samples were analysed post-flight using a dual-channel gas chromatograph with flame ionisation detection (GC-FID)[179], as detailed in Section 2.2.

3.2.3 Data selection

All flights took place in the daytime (08:00–17:00 local time). Flight data was filtered such that only observations contained within the boundaries of the defined regions (Figure 3.1a) and within the planetary boundary layer (PBL) were used in further analysis. Aircraft profiles at the beginning and end of each flight were used to determine the PBL depth. PBL profiles were generally conducted upwind of the area of interest and typically spanned an altitude range of 15–1500 m. Sharp decreases in the mole fractions of H_2O and CH_4 at a given altitude were used to indicate the PBL height, as a marker of transition to the free troposphere (typically < 500 m above sea level). Background mixing ratios of CH_4, CO_2 and C_2H_6 were determined using 1 Hz data during straight and level aircraft runs upwind of emission sources. Mixing ratios of pollutants were averaged over the whole run to give a value for each species per flight (Figure 3.2). Canister samples were captured solely within the PBL on each flight. A minimum of one sample was taken upwind of the area of the area of interest in order to assess background VOC mixing ratios. There were two types of flight modes implemented across this dataset; survey flights and plume-targeted flights. Since some data is likely to be biased high due to the oversam-

pling of plumes, a comparison of the absolute VOC mixing ratios is not performed here, instead the analysis is focused on hydrocarbon ratios since these should be unaffected by repeated sampling of high values. The number of samples obtained in each sampling region are shown in Table 3.2.

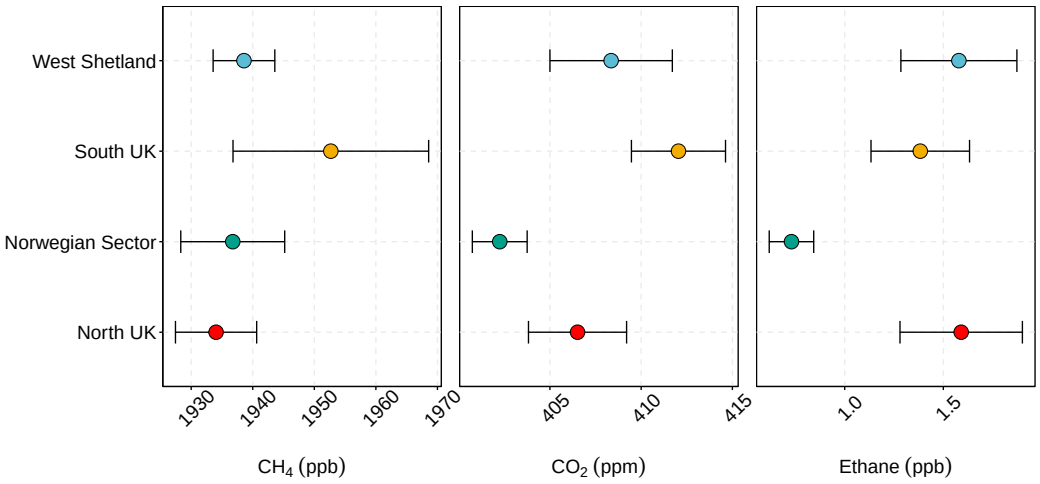

Figure 3.2: *Mean background mixing ratios of CH_4, CO_2 and ethane from all flights in each sampling region. Error bars represent one standard error.*

Table 3.2: *Number of whole air samples obtained in each defined region.*

Sampling region	Number of samples
Norwegian Sector	40
West Shetland	103
North UK	166
South UK	359

3.3 Results and discussion

3.3.1 VOC source attribution

3.3.1.1 Isomeric pentane ratio

Anthropogenic emission sources have distinctive VOC signatures and therefore their mixing ratios with respect to each other can be used for source identification and characterisation. Emissions from O&G operations can specifically be identified by examining the iso-pentane to n-pentane (iC_5/nC_5) enhancement ratio. This ratio is defined as the slope term obtained by the linear fit of their scatter plot.[25] These species are positional isomers meaning they have similar reactivity with respect to the hydroxyl radical (OH), which is the dominant sink of atmospheric alkanes[180] and consequently similar atmospheric lifetimes of around 65 hours at $[OH]_{avg} = 1.13 \times 10^6$ molecules cm^{-3} and T = 260 K.[181] Branched alkanes are also preferentially oxidised by nitrate radicals (NO_3), however the nitrate is readily photolysed by sunlight meaning concentrations are heavily suppressed during the day. Since all flights in this work took place in the daytime and transport times were of the order of a few hours, oxidation due to nitrate is assumed to have a negligible affect on the observed pentane ratios. As a result the ratio is largely independent of photochemical processing. Both species are also similarly affected by air mass mixing and dilution, therefore the ratio remains relatively unchanged during atmospheric transport and can be approximated to represent the ratio at the source of emission.[25]

The iC_5/nC_5 ratios for each region were calculated from the slope of a linear fit using reduced major axis regression.[182] This method is applied when the distinction between the dependent and independent variables is uncertain and deviations between fitted and observed data occur in both the x and y directions. Figure 3.3 shows the observed iC_5/nC_5 ratios for each sampling region in the North Sea. Results of the Pearson's correlation (r) indicated that there was a significant positive association for all regions (Norwegian sector: r(38) = 0.83, p <.001, West Shetland: r(91) = 1.00, p < .001, North UK: r(147) = 0.95, p < .001, South UK: r(338) = 0.98, p < .001). The numbers in parenthesis refer to the number of observations. The iC_5/nC_5 ratios observed were 1.12 for the Norwegian Sector, 1.08 for

West Shetland, 0.89 for the North UK and 1.24 for the South UK.

Numerous studies have been conducted characterising the iC_5/nC_5 emission ratio from both urban and O&G sources. A study by the United States Geological Survey (USGS) reported enhancement ratios for 14 different wells, finding that the isomers were present in approximately equal amounts with ratios ranging from 1–1.28.[183] Similarly Simpson et al. [169] observed a ratio of 1.10 in Alberta over oil sands mining operations. Gilman et al. [25] reported a ratio of 0.89 at the Boulder Atmospheric Observatory (BAO), concluding that measurements at BAO are strongly influenced by O&G emissions from the Denver-Julesburg Basin.[25] These studies show that the iC_5/nC_5 emission ratio is a robust indicator of O&G emissions for onshore environments. Of more relevance to this work are studies characterising emissions ratios from basins outside the US and in particular those offshore. Ryerson et al. [172] reported a ratio of 0.82 for the fluid released from the Deepwater Horizon explosion in the Gulf of Mexico. Few studies exist studying O&G emissions in the North Sea, however a study into the composition of natural gas condensate from a basin in the North Sea, reported an iC_5/nC_5 ratio of 0.84.[184]

The enhancement ratios calculated here are consistent with ratios reported in the literature for O&G emissions and significantly lower than those reported for urban and vehicular emissions.[185] Additional sources of emissions such as biomass burning are not expected to influence VOC mixing ratios in this region, therefore the iC_5/nC_5 ratio is a suitable tool for the differentiation of urban and O&G emissions. The iC_5/nC_5 ratio for urban and vehicular emissions is distinctly different to the ratio from O&G emissions. Amounts of branched alkanes, such as iso-pentane are increased during the refining process, therefore in processed products such as gasoline, iso-pentane is enhanced relative to n-pentane, resulting in a higher iC_5/nC_5 ratio.[186] The highest iC_5/nC_5 ratio was observed for the southern gas-producing region of the North Sea, suggesting a larger relative contribution of urban emissions to VOC mixing ratios. Anthropogenic emissions from the UK or continental Europe are likely to influence VOC mixing ratios here, resulting in a higher ratio. Literature values for urban centres in the UK have been reported as 2.97 by Schneidemesser et al. [187] at Marylebone Road, a roadside monitoring site located in the centre of London, UK. This agrees well with the vehicular emissions ratio of 2.95 reported in Dublin, Ireland.[188] The lowest ratio of 0.89, observed for the North

UK is in the lower range of ratios observed for O&G emissions but is similar to the value reported for North Sea condensate, consistent with the fact that more than 50% of reservoirs in this region produce condensate (Figure 3.1c). In summary, these results strongly indicate that the primary source of VOC emissions in the North Sea is from O&G operations.

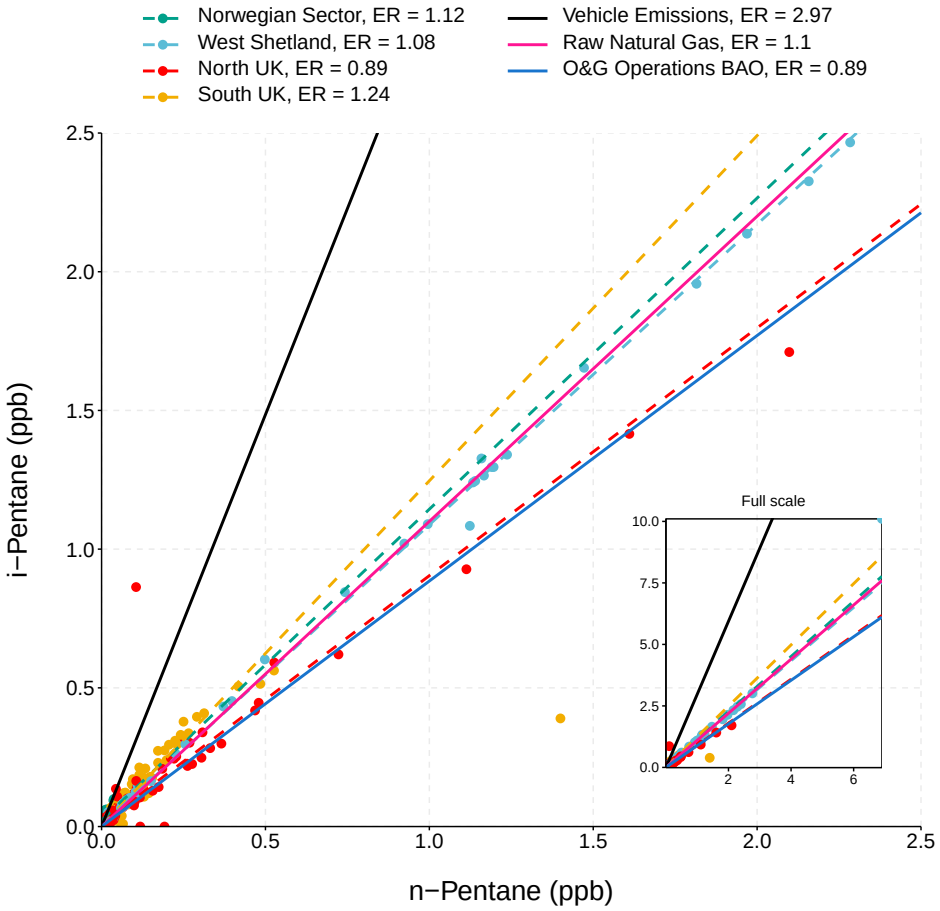

Figure 3.3: *Scatter plot of iso-pentane and n-pentane observations in each sampling region. Dashed lines indicate the linear fit for each region obtained by reduced major axis regression. The solid black line indicates the ratio from vehicular emissions[187], the solid pink line shows the ratio of raw natural gas in the North Sea obtained from the Department for Business, Energy and Industrial Strategy (BEIS) and the solid blue line indicates a typical ratio from O&G emission sources.[25] Inset shows the full range of observations.*

3.3.1.2 Correlations with tracer compounds

In order to identify the specific sources of VOCs in the each region of the North Sea, emission ratios of VOCs with tracer compounds of particular sources were examined. Mixing ratios of propane are often elevated in regions of O&G production. Light alkanes are often co-emitted in such regions and since propane is a well known tracer for O&G operations, a strong correlation with propane indicates a common source.[168] Acetylene is a common tracer for combustion emissions[189] and is therefore used in this work to identify emissions from anthropogenic urban activity. Emission ratios were calculated from the slope of a linear fit using reduced major axis regression for each region (Table 3.3). Species that were recorded below the limit of detection (LOD) of the GC-FID were classed as missing and hence those that were detected in less than half the samples from each region were excluded from the analysis. This only applied to samples obtained in the Norwegian sector, where in general mixing ratios of VOCs were significantly lower than other areas of the North Sea and thus similar to the LOD. Compounds affected from this sector included pent-1-ene, trans-2-pentene, 2,3-methylpentanes, isoprene, 2,2,4-trimethylpentane and n-octane.

Figure 3.4 shows the correlation of light alkanes with propane and acetylene and the emission ratios for other species are shown in Table 3.3. Pearson correlation coefficients (r) and corresponding p-values were also calculated for each compound. All C_2-C_5 alkanes (ethane, n-butane, iso-butane, n-pentane, iso-pentane) showed statistically significant correlations ($p<.001$) with propane across all regions of the North Sea. These species were tightly correlated with propane ($0.94 < r < 0.99$) in the North UK and West Shetland regions, suggesting they shared a common emission source. Furthermore, particularly weak correlations between C_2–C_5 alkanes and acetylene were observed in both the North UK and West Shetland ($r < 0.53$), supporting the conclusion that O&G activities were the dominant source of VOC emissions in these regions with little influence from other sources. Moderate correlations of light alkanes with propane ($0.67 < r < 0.93$) were observed in the Norwegian sector. However by comparison, poor relationships with acetylene were observed, suggesting vehicular emissions did not play a major role.

Ethane was the only compound emitted in greater quantities than propane and hence emission ratios >1 were observed. Emission ratios with propane ranged from 1.18 in

the North UK to 3.31 in the Norwegian sector. Previous work reported enhancement ratios of 1.09[25] and 1.00[190] at BAO downwind of onshore natural gas sources. Whilst a comparable ratio was observed in the North UK, all other regions were found to exhibit ratios 2–3 times higher. Derwent et al. [191] reported an ethane to propane ratio of 2.4 from natural gas leakage at Marylebone Road, London, suggesting that the high ratios observed in this work could be as a result of fugitive emissions of raw natural gas.

The weakest correlations between the light alkanes and propane were observed in the South UK ($0.53 < r < 0.87$). However, these species showed comparatively weaker correlations with acetylene ($0.10 < r < 0.52$), indicating O&G activities were also a key driver of VOC mixing ratios in this region. This was the only region which had strong propane correlations with combustion tracers such as alkenes (ethene and 1,3-butadiene), C_{6+} alkanes (hexane and heptane) and aromatic species (toluene) ($0.72 < r < 0.85$), suggesting a more complex mix of emission sources. These compounds were also well correlated with acetylene ($r > 0.78$), indicating an urban emission source. Marine traffic is also a likely source of some emissions in this region due to its proximity to the UK shipping lanes, in particular the Strait of Dover, one of the busiest shipping routes in the world.[192] A study of marine shipping emissions in China showed that alkanes and aromatics dominated the total identified VOCs from ship auxiliary engine exhausts, particularly alkanes with a carbon number greater than seven.[193] Therefore, the stronger correlations of hexane and heptane with propane in the South UK compared to other areas of the North Sea likely arise due to the influence of shipping on VOC measurements.

Despite evidence of additional emission sources in the South UK, the relative abundance of non-methane hydrocarbons (NMHCs) revealed source profiles characteristic of those expected from regions of O&G production (Figure 3.5). On a fractional basis, C_2–C_5 alkanes accounted for more than 83% of the total measured VOC concentration ($\mu g\ m^{-3}$) in all regions. This is comparable to measurements made in an onshore region of O&G production in North-eastern Colorado by Thompson et al. [194], where saturated alkanes contributed 90% at the gas field itself, 84% on the periphery of a drilling area and significantly less in an urban area of Denver (64%). Unsaturated and aromatic species typically account for a greater fraction of total VOC concentrations in urban areas. For example, Dominutti et al. [195] show that aromatic species contributed close to 50% of

the total concentration at an urban site in S$\widetilde{a}$o Paulo, which is also consistent with measurements made in Shanghai by Liu et al. [196]. In contrast, aromatic and unsaturated species accounted for less than 25% of the total measured VOC in all regions of the North Sea, providing further evidence that emissions were driven by O&G activities.

Table 3.3: *Emission ratios from the slope of the linear fit using reduced major axis regression, r^2 values and Pearson correlation coefficients (r) for tracer compounds with listed VOCs in each sampling region. Values are only shown for compounds which had correlations with tracer compounds with an $r^2 > 0.4$.*

	Acetylene (ppb ppb^{-1})			**Propane (ppb ppb^{-1})**		
Compound	**ER$_{C_2H_2}$**	**r^2**	**r**	**ER$_{C_3H_8}$**	**r^2**	**r**
North UK						
Ethane	—	—	—	1.181	0.943	0.971
iso-Butane	—	—	—	0.117	0.962	0.981
n-Butane	—	—	—	0.294	0.977	0.989
iso-Pentane	—	—	—	0.055	0.887	0.942
n-Pentane	—	—	—	0.061	0.976	0.988
trans-2-Pentene	0.008	0.653	0.808	0.000	0.484	0.696
Pent-1-ene	—	—	—	0.004	0.611	0.781
2,3-Methylpentanes	—	—	—	0.012	0.510	0.714
Hexane	—	—	—	0.013	0.749	0.866
Norwegian Sector						
Ethane	—	—	—	3.308	0.705	0.840
Propane	5.624	0.640	0.800	—	—	—
iso-Butane	1.788	0.581	0.763	0.318	0.856	0.925
n-Butane	—	—	—	0.421	0.717	0.847
Acetylene	—	—	—	0.178	0.640	0.800
But-1-ene	-0.071	0.662	-0.814	-0.013	0.462	-0.680
iso-Pentane	0.770	0.503	0.709	0.139	0.563	0.751
n-Pentane	—	—	—	0.243	0.452	0.672
Heptane	—	—	—	0.072	0.578	0.760

Benzene	—	—	—	0.098	0.411	0.641
West Shetland						
Ethane	—	—	—	2.481	0.990	0.995
iso-Butane	—	—	—	0.432	0.987	0.993
n-Butane	—	—	—	0.650	0.986	0.993
iso-Pentane	—	—	—	0.278	0.963	0.981
n-Pentane	—	—	—	0.258	0.957	0.978
trans-2-Pentene	—	—	—	0.006	0.497	0.705
2,3-Methylpentanes	—	—	—	0.099	0.843	0.918
Hexane	—	—	—	0.094	0.479	0.692
Isoprene	—	—	—	0.067	0.758	0.871
Benzene	—	—	—	0.031	0.425	0.652
Toluene	—	—	—	0.021	0.680	0.824
South UK						
Ethene	1.857	0.651	0.807	0.465	0.556	0.746
Propane	3.997	0.515	0.718	—	—	—
iso-Butane	1.585	0.455	0.674	0.397	0.632	0.795
n-Butane	—	—	—	0.584	0.758	0.870
Acetylene	—	—	—	0.250	0.515	0.718
iso-Pentane	1.112	0.433	0.658	0.279	0.654	0.808
1,3-Butadiene	0.167	0.823	0.907	0.037	0.519	0.721
2,3-Methylpentanes	0.235	0.651	0.807	0.059	0.524	0.724
Hexane	0.246	0.603	0.776	0.062	0.714	0.845
Heptane	0.209	0.603	0.776	0.052	0.529	0.727
2,2,4-trimethylpentane	0.148	0.493	0.702	—	—	—
Toluene	0.669	0.731	0.855	0.167	0.602	0.776

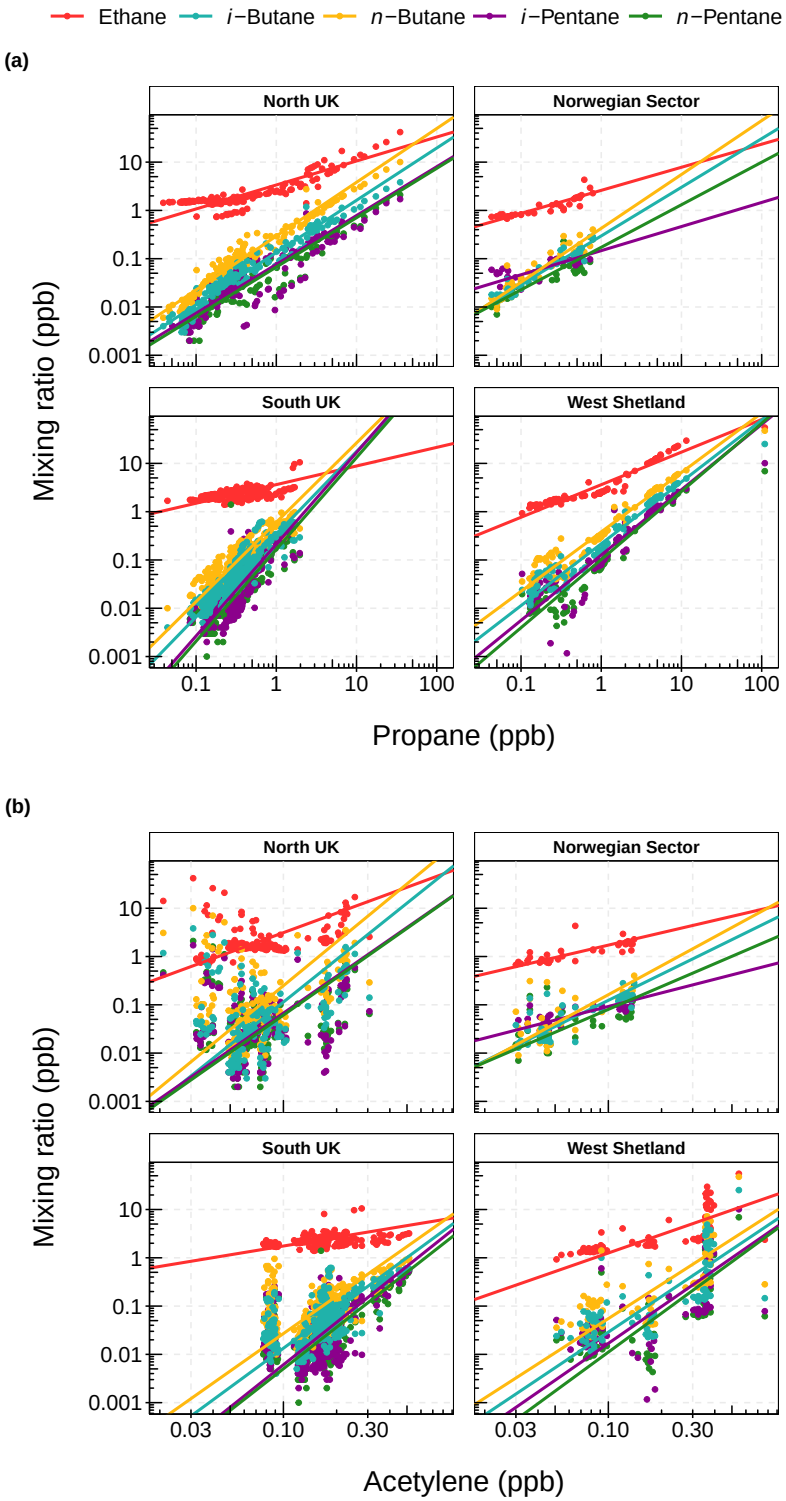

Figure 3.4: *Correlation of light alkanes with (a) propane and (b) acetylene in each sampling region. The solid lines represent the linear fit using reduced major axis regression. Note the log scale used on both axis.*

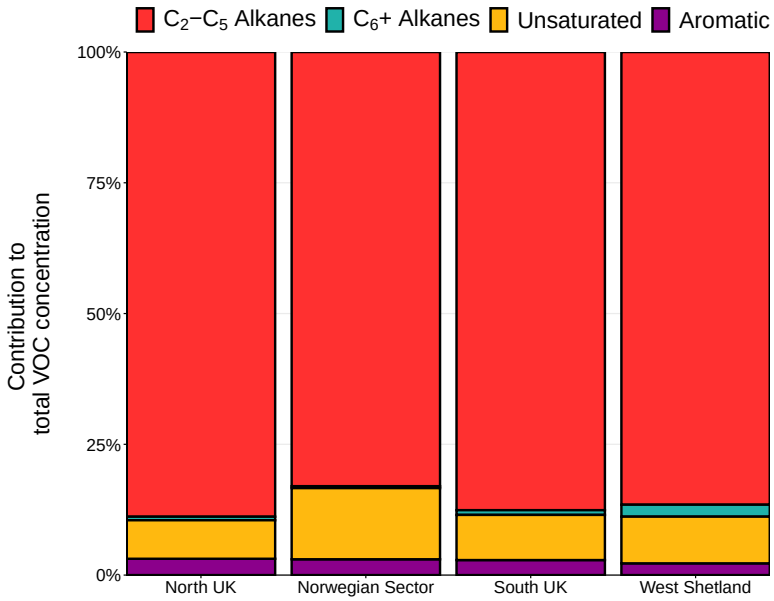

Figure 3.5: *Percentage contribution of each VOC group to total VOC concentrations in each region of the North Sea.*

3.3.1.3 Benzene-toluene ratio

The influence of urban emissions was further studied by utilising the benzene/toluene (B/T) emission ratio. Toluene is often co-emitted with benzene and the ratio of the two compounds is dependent on the source of emissions. Both are present in primary vehicle exhaust emissions[197] and from O&G sources as well as solvents, industry emissions and some natural emissions.[194,198] Toluene has a shorter atmospheric lifetime with respect to OH, therefore the B/T ratio can be used to estimate the photochemical age of an air mass.[199] The B/T ratio can also be used to evaluate the emission sources of measured VOCs. In particular, to distinguish traffic emissions from O&G emissions as in Halliday et al. [198], where ratios in the range of 0.41–0.83 indicate emissions originating from vehicles.[200]

Figure 3.6a shows the relationship between benzene and toluene for each region. As before, emission ratios were calculated using reduced major axis regression. Significant positive correlations ($p<.001$) were observed for all regions. Strong correlations

were observed in the North UK, Norwegian sector and West Shetland with Pearson correlation coefficients of r(163) = 0.95, r(37) = 0.94 and r(92) = 0.94 respectively, implying these compounds have a common source. The observed B/T emission ratio was 1.29 for the North UK, 1.24 for the Norwegian sector and 1.20 for West Shetland (Table 3.4), suggesting vehicle emissions were not the dominant source of these compounds since these values are higher than the typical observed range.[200] These values are consistent with findings from other O&G studies, which reported B/T ratios of around 1 from regions of O&G production.[190,201] A much weaker, albeit significant correlation between benzene and toluene was observed in the South UK (r(357) = 0.56, $p<.001$). It is evident from Figure 3.6a that there are two distinct segments of data with unique correlations between the two species; the first with considerably lower B/T ratios than observed in other regions of the North Sea, the second being characterised by enhancements in benzene mixing ratios and very small amounts of toluene.

Figure 3.6b shows the regression plot of benzene versus toluene for the South UK coloured by wind direction sector. Data with a B/T ratio between 0.41–0.83 (traffic emissions) is plotted with a diamond, accounting for 3.5% of the observations in the Southern region. A strong positive correlation was found to exist (r(14) = 0.92, $p<.001$) for the traffic source and the slope obtained from the linear fit was 0.60, in the centre of the range expected for vehicle emissions.[200] The traffic source was primarily observed when the wind direction was from the south or south-west, suggestive of air transported from the UK or from continental Europe polluted by urban vehicular emissions. A similar traffic source is also visible in the North UK data, similarly exclusively observed under southerly wind conditions. Air transported from the UK mainland or Europe is expected to reach the location of the aircraft flight tracks in less than a day. The estimated lifetimes for benzene and toluene are 2 weeks and 2 days respectively,[202] meaning emissions of benzene and toluene from urban areas are expected to remain well correlated on this relatively short spatial scale since they are also similarly affected by dilution and mixing.

There is a section of highly correlated data (r(214) = 0.81, $p<.001$) characterised by B/T ratios > 4 (squares, Figure 3.6b). High B/T ratios can be indicative of aged emissions due to the high proportion of benzene relative to toluene. However, given that the benzene mixing ratios observed were among the largest for all the regions studied, this is more

suggestive of an additional benzene source from the offshore platforms. Other compounds related to fossil fuel combustion and evaporation such as ethene and pent-1-ene were also enhanced in these samples, providing evidence of an additional combustion source enriched in benzene. There are a host of potential sources on drilling rigs including gas turbines, which are widely used for power generation, and compressors, both of which have previously been linked to elevated benzene mixing ratios.[203,204] The remaining fraction of data (33%) was attributed to O&G emissions and is plotted with a triangle in Figure 3.6b. This data was tightly correlated ($r(125) = 0.86$, $p<.001$) with an emission ratio of 1.12, in agreement with the range quoted by Swarthout et al. [190] from a wind direction dominated by natural gas emissions.

Table 3.4: *Benzene to toluene emission ratios (ER) for each sampling region along with corresponding r^2 values and Pearson correlation coefficients (r).*

	B/T (ppb ppb^{-1})		
Area	**ER**	**r^2**	**r**
North UK	1.29	0.91	0.95
Norwegian Sector	1.24	0.88	0.94
South UK	1.07	0.31	0.56
West Shetland	1.20	0.89	0.94

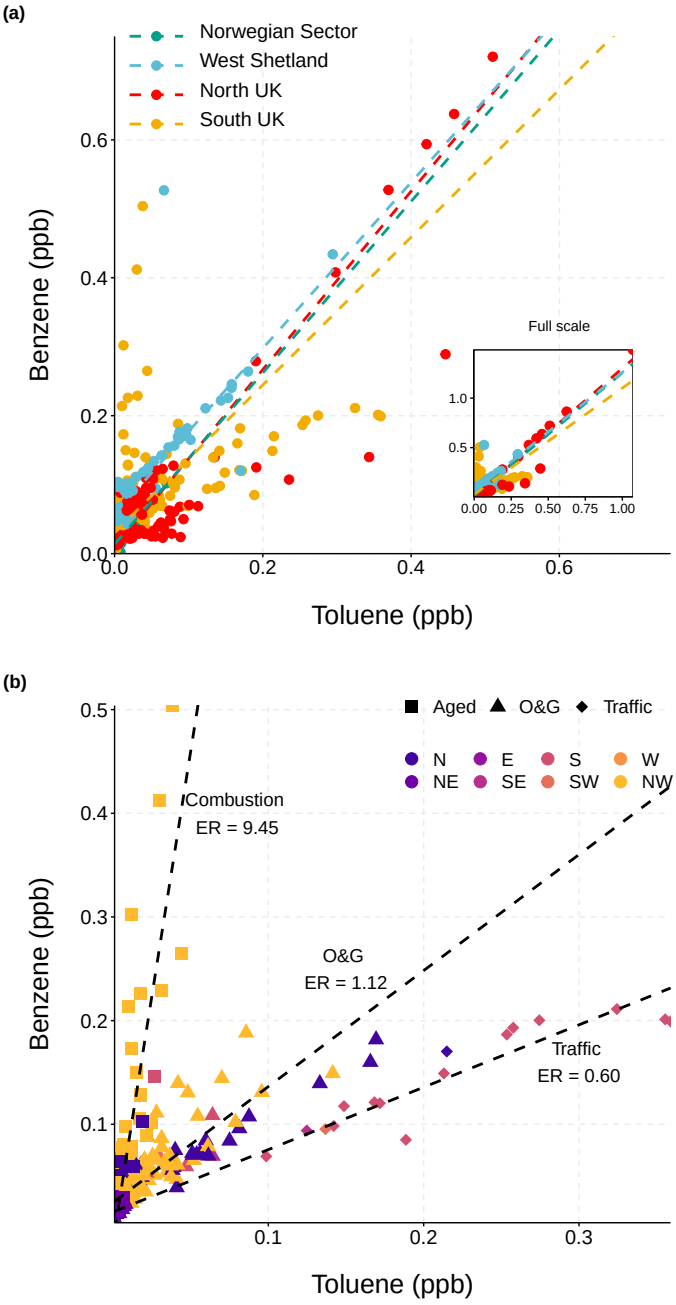

Figure 3.6: *(a) Scatter plot of benzene versus toluene for all sampling regions. Inset shows the full scale of observations. (b) The South UK only, where the colour represents the average wind sector during the time the sample was taken and the shape represents identified emission sources. In both figures the dashed lines indicate the linear fit obtained by reduced major axis regression.*

3.3.2 Emission profiles of VOCs from offshore fields

There are over 1000 individual offshore fields beneath the North Sea, each listed as a specific field type (Figure 3.1b). To further investigate the spatial differences in emissions and to derive the VOC emission profiles from each classification of offshore field, each 1 Hz observation and each VOC measurement was spatially joined to a specific offshore field and hence field type. For each flight, the regional background of CH_4, CO_2 and C_2H_6 was calculated as an average of mixing ratios on straight and level aircraft runs upwind of any emission sources. Additionally, background VOC mixing ratios were calculated as the average of the lowest 1st percentile of measurement data for each flight. Whole air samples identified as being dominated by traffic emissions using the B/T ratio ($0.41 < B/T < 0.83$) were removed prior to this analysis in order to more robustly compare the emissions from one field type to another.

3.3.2.1 CH_4 source identification

The molar enhancement ratio of C_2H_6 to CH_4 is commonly used for CH_4 source identification since C_2H_6 is emitted almost exclusively from fossil carbon sources, whereas CH_4 has a mix of sources. 1 Hz measurements of CH_4 and C_2H_6 were used to characterize the CH_4 sources in the North Sea. In this environment, a positive correlation implies that the CH_4 originates primarily from O&G sources, whereas a weak to no correlation suggests biogenic or industrial sources of CH_4.[168] These other sources include landfills, water treatment and cattle and are only associated with very low levels of C_2H_6, typically $<$ 0.2%.[149] CH_4 from O&G sources is often co-emitted with tracers such as C_2H_6, resulting in considerably higher ratios ranging from 0.01–0.30.[149]

The enhancement ratio (ΔC_2H_6 (ppb)/ΔCH_4 (ppb)) for each field type was obtained by first subtracting the average background estimates for each species during each flight from the observed enhancements over the North Sea. Any enhancement of CH_4 due to an anthropogenic combustion source was removed by utilising the $\Delta CH_4/\Delta CO_2$ ratio, which is the slope of the linear regression fit of enhanced mixing ratios of CH_4 and CO_2.[205] The predominant wind direction in the UK is from the south-west, meaning the measurements likely represent emissions from both offshore platforms and onshore coastal sources. Observations at remote offshore sites show that air masses dominated by an-

thropogenic combustion related emissions typically have $\Delta CH_4/\Delta CO_2$ ratios of less than 20 ppb ppm^{-1}.[206] Consequently this filter was applied to the data to remove the influence of anthropogenic emissions. Data with enhancement ratios above 20 ppb ppm^{-1} was assumed to be a mix of flaring and fugitive emissions and was therefore used in further analysis to compare the signatures of individual field types (Figure 3.7).

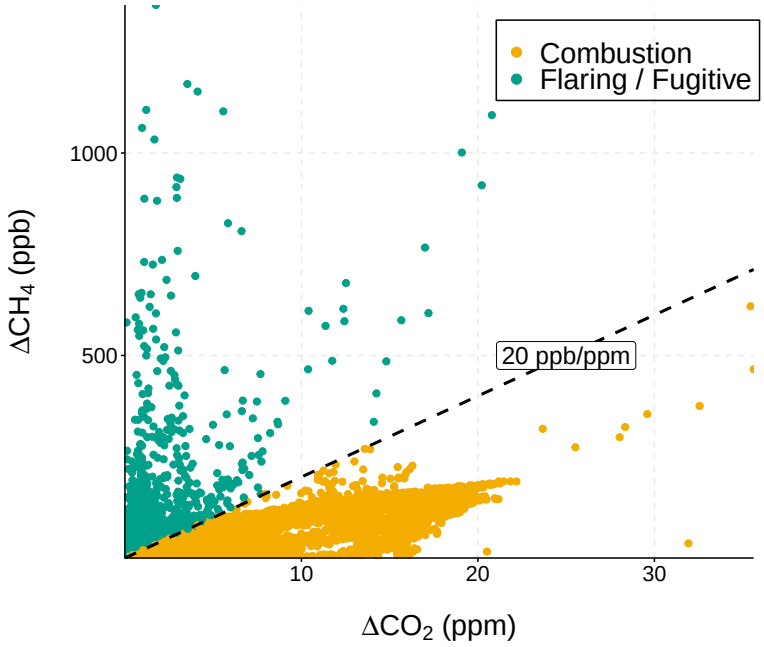

Figure 3.7: *Scatter plot of ΔCH_4 versus ΔCO_2. The dashed line shows an emission ratio of 20 ppb ppm^{-1} which was used for filtering data to remove the influence of anthropogenic emissions.*

The $\Delta C_2H_6/\Delta CH_4$ enhancement ratios were calculated using reduced major axis regression and the correlations were evaluated through the calculation of the Pearson's correlation coefficient. Figure 3.8 shows the scatter plot of C_2H_6 and CH_4 enhancements. Strong, positive correlations for field types of condensate, gas and oil were observed ($r(878) = 0.98$, $r(1433) = 0.93$ and $r(3385) = 0.81$) respectively with $p<.001$ in all cases), suggesting O&G emissions were the dominant source of CH_4. Mixed fields showed a weak but statistically significant correlation ($r(1256) = 0.28$, $p<.001$) along with notably smaller CH_4 enhancements compared to the other field types. CH_4 enhancements were observed

with a wide range of C_2H_6 enhancements, with ratios ranging from 0.03–0.18. Gas fields had the lowest enhancement ratio of 0.03, indicating dry-gas emissions dominated by CH_4.[149] The highest emission ratio of 0.18 was observed for oil fields. Emission ratios $>$ 0.06 have previously been observed from wet gas wells and are associated with gas containing a larger fraction of NMHCs.[149] Significant variability (smallest r) in the scatter of the data from oil fields was noted compared to other field types. Noticeably, oil fields in the West Shetland region had a higher C_2H_6 content (31%) than those in the North UK region (13%). This could be related to the difference in the transportation methods of the extracted oil in these two regions. In the North UK, pipelines are typically used to carry oil to shore, whereas West Shetland largely relies on shuttle tankers for oil export. VOC emissions associated with tanker loading can occur when oil is transferred from floating production storage and offloading (FPSO) vessels into shuttle tankers. During loading, light hydrocarbons dissolved in the crude oil vaporise from the liquid and accumulate in the vapour space of the tank. This increases the pressure inside the tank and therefore vapours are vented to the atmosphere.[125] Additionally, high enhancement ratios $>$ 0.85 have previously been attributed to condensate tank flash emissions,[207] therefore the increased enhancements of C_2H_6 observed here possibly arise due to venting of light hydrocarbons during loading. The range of emission ratios observed across the North Sea suggests that there is a significant spatial variability in the composition of natural gas and highlights the heterogeneity of emissions across the O&G sector.

3.3.2.2 VOC composition

The whole air samples obtained showed significant variations in VOC concentrations. Total hydrocarbon concentrations in a single sample ranged from 1.73 μg m^{-3} to 155 μg m^{-3}, reflecting the difference between a sample in clean background air, compared to a sample captured within a plume. To broadly compare the different offshore field types, VOCs were grouped into categories: light alkanes (C_2–C_5), heavy alkanes (C_6+), unsaturated and aromatic. Mixing ratios were first converted to concentrations (μg m^{-3}) in order to investigate which species contributed most to the total mass measured. Figure 3.9a shows the contribution of the VOC categories to total VOC concentrations for each field type. Among all the species quantified, C_2-C_5 alkanes (ethane, propane, n-butane, iso-butane,

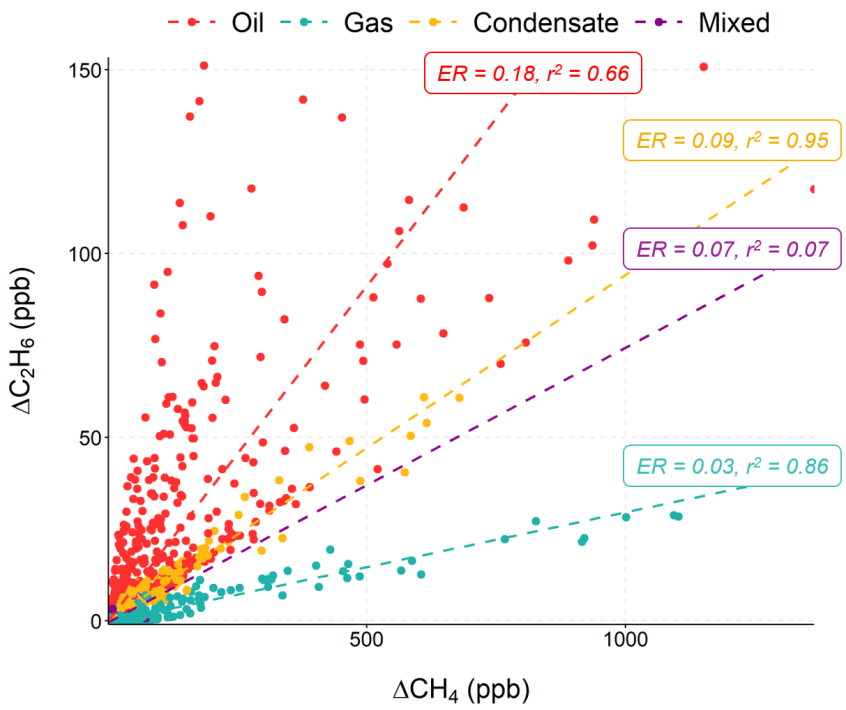

Figure 3.8: *Scatter plot of ΔC_2H_6 vs ΔCH_4 for each offshore field type. Observations were filtered to those with a $\Delta CH_4/\Delta CO_2$ ratio greater than 20 ppb ppm^{-1} as these were considered to be uninfluenced by anthropogenic urban emission sources. Dashed lines indicate the linear fit obtained from reduced major-axis regression.*

n-pentane and iso-pentane) were the most abundant group for all field types, accounting for, on average, 70.2% of the total measured mass. The largest contribution was for oil fields and the contributions of light alkanes in individual samples ranged from 14.0% to 98.4%, where ethane and propane were the dominant species. This is somewhat expected since elevated concentrations of short chained alkanes are characteristic of emissions from the O&G sector.[25] The contributions of heavy alkanes (hexane, heptane, octane, 2,3-methyl-pentanes, 2,2,4-trimethylpentane) was small for all field types ($<$ 8%), suggesting O&G production was not a key source of these compounds. Aromatic (benzene and toluene) and unsaturated (ethene, acetylene, propene, but-1-ene, trans-2-butene, cis-2-butene, 1,3-butadiene, trans-2-pentene, pent-1-ene and isoprene) species made similar average contributions to total VOC concentrations of 12.4% and 12.2% re-

spectively. The aromatic contribution for condensate fields was twice as high as any other field type (20.7%). Closer inspection revealed that this was driven by particularly high aromatic contributions observed from the Erskine field, located in the North UK region. The variation in individual samples from this field were small compared to the field-to-field variability, suggesting the difference in emissions is largely due to different practices and equipment on individual platforms, a point also raised by Warneke et al. [126] for onshore well pads. Contributions from unsaturated species ranged from 7.3% to 15.1%. Ethene and acetylene (ethyne) were the dominant species within this group, which is suggestive of more general industrial point sources, possibly combustion generators.[208]

3.3.2.3 OH reactivity

Oxidation of VOCs by the hydroxyl radical (OH) to form peroxy radicals is the rate determining step in the formation of tropospheric ozone. The potential of a VOC to form ozone depends on the concentration of the species, the reactivity towards OH and structure (number of C-C and C-H bonds). The OH reactivity can be used as a simple metric to identify the key species that most readily form peroxy radicals and subsequently produce ozone.[209] The OH reactivity (R_{OH-X}) for VOCs measured in the North Sea was calculated as the product of the rate constant for the reaction of VOC "X" with OH (k_{OH+X}) and the VOC mixing ratio (X, molecule cm^{-3}) using R3.1 and a method outlined in Abeleira et al. [210]. Rate constants at 298 K were obtained from Atkinson and Aschmann [211] and Atkinson and Arey [212].

$$R_{OH-X} = k_{OH+X}\,[X] \tag{R3.1}$$

Figure 3.9b shows the contribution of each VOC class, along with CH_4, to total OH reactivity for each offshore field type. Unsaturated compounds made the highest contribution to OH reactivity for all field types, contributing on average 55.5%, despite a low contribution of 12.2% to total VOC concentrations. Of all the compounds in this group, 1,3-butadiene made the largest contribution to OH reactivity since it is highly reactive towards OH, making it important for ozone production despite being present in low concentrations. Light alkanes were the second most important contributor to OH reactivity

for all field types. Despite being the most abundant group of compounds, contributions to OH reactivity were approximately half that of unsaturated species, with an average contribution of 31.8%. Contributions of light alkanes became increasingly important in the order: gas, oil, condensate. Previous studies conducted onshore have identified alkanes to be the largest contributors to OH reactivity in regions of O&G production, with alkenes and biogenics as minor contributors due to their relatively low abundance.[25] However, Figure 3.9b indicates that in the more remote offshore environment, where there are significantly less emission sources and VOC concentrations are generally lower, OH reactivity is dominated by fast reacting species with OH. These are likely emitted as a result of the more general combustion sources that exist on O&G platforms. By comparison, the contribution of CH_4 to total OH reactivity was minor for all field types, despite being the primary component of natural gas, exposing the importance of NMHCs in regard to O_3 formation. The greatest CH_4 contribution was observed for gas fields (2.87%), owing to the characteristics of dry-gas emissions, which are predominantly CH_4. Due to their slower reaction rates, alkanes such as ethane are likely to contribute to O_3 formation on larger spatial scales, rather than in the local environment. This is potentially more significant in regions of oil or condensate production where alkanes made a heavier contribution to total OH reactivity.

3.3.2.4 Excess mole fraction

In order to compare the emission profile of VOCs measured for each field type and to provide some general quantification of emissions, the relative abundance of VOCs to CH_4 was calculated. The "excess mole fraction" (EMF) is defined as the relative abundance of NMHCs to the sum of CH_4 and non-CH_4 mixing ratios.[213] The background NMHC mixing ratios ($NMHC_{BG}$) were defined as the lowest 1% of samples during each flight within each sampling region in the PBL and were subtracted from the total mixing ratios. Only compounds that were quantified on all flights were included in this analysis in order to keep the number of compounds making up the total NMHC mixing ratio consistent. This resulted in the exclusion of isoprene, pent-1-ene, trans-2-pentene and 2,2,4-trimethylpentane. The excess mole fraction was calculated for each field type using R3.2:

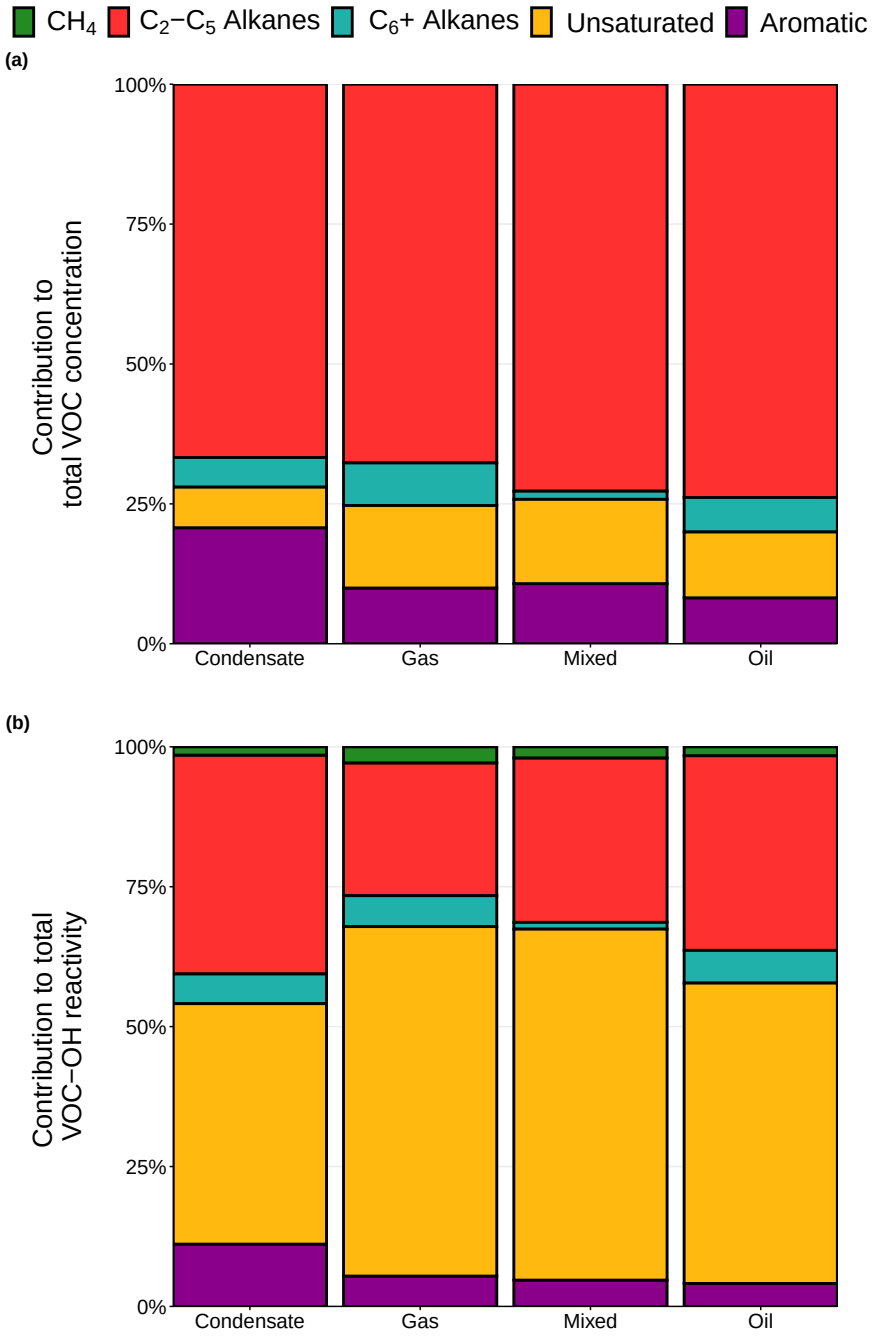

Figure 3.9: *Percentage contribution of different VOC categories to (a) total VOC concentrations by mass and (b) total VOC-OH reactivity measured for each field type. The contribution of CH_4 is shown only for OH reactivity to demonstrate the relative importance of the other VOCs in terms of O_3 formation.*

$$EMF = \frac{\sum([NMHC] - [NMHC]_{BG})}{([CH_4] - [CH_4]_{BG}) + \sum([NMHC] - [NMHC]_{BG})} \times 100 \qquad \text{(R3.2)}$$

Figure 3.10a shows the mean EMF calculated for each field type. Oil fields had the highest EMF of 28.3%. This indicates that the VOC mixture emitted by oil fields consists of heavier compounds compared to gas or condensate fields. Gas fields had the smallest amount of VOCs relative to CH_4, with an average EMF of 12.6%, representing the fact that natural gas is 70–90% CH_4. This is consistent with a study in the Uintah Basin by Warneke et al. [126] who found that oil wells had a higher VOC to CH_4 ratio to gas wells due to the heavier composition of hydrocarbons extracted by oil pads compared to gas. This is also consistent with Figure 3.9, where oil fields had the highest percentage contribution (82%) of C_2–C_5 alkanes to total VOC concentrations. Similarly Bourtsoukidis et al. [213] assigned high EMFs in the Arabian Peninsula to air originating from the oil fields and refineries of Iran and low EMFs to the gas fields of Turkmenistan. The EMF for condensate fields sits in the middle of those for O&G fields, with a mean value of 16.4%. This is somewhat expected since gas condensate is a mixture of low-boiling hydrocarbon liquids and is predominantly made up of pentane isomers with relatively small amounts of CH_4 or ethane.[214] Mixed fields had the lowest mean EMF of 12.3% but with the highest standard error of 2.55%. Fields listed as mixed are solely located in the Norwegian sector, where the term defines reservoirs where more than one fossil fuel product is extracted over the fields lifetime. The EMFs for individual fields in this region ranged from 2.5% to 33% (Figure 3.11) reflecting the individual characteristics of each reservoir and the differences in the types of production across this region.

The EMF can be related to water depth as displayed by Figure 3.10b, which shows the relative density distributions (smoothed histogram) of water depths for platforms in the North Sea. Generally the EMF increases with increasing water depth. Gas extraction principally occurs in water depths less than 100 m, which results in low EMFs and emissions dominated by CH_4. North Sea condensate is typically extracted in water depths between 50 m and 200 m, resulting in an increase in emissions of light alkanes relative to CH_4. Oil production is more greatly associated with deep water extraction. The greatest water depths were in the West Shetland region, with extraction taking place in water deeper than 400 m. Subsequently, when broken down by study region as well as field

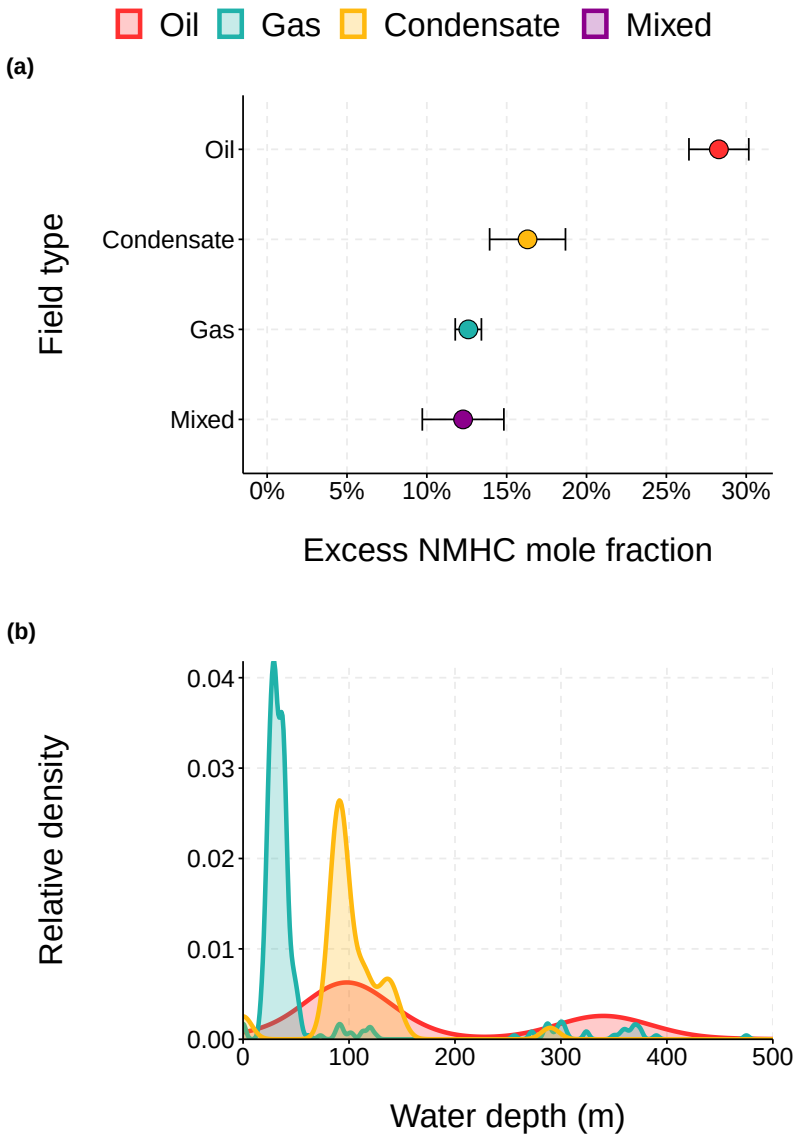

Figure 3.10: *(a) Mean excess mole fraction for each offshore field type. Error bars represent one standard error. (b) Smoothed density distribution of water depth obtained for each offshore field in the North Sea, coloured by field type. A depth of 305 m (1000 ft) defines deep water.*

type, the highest EMF of 38.1% was also observed for West Shetland, showing that deep water extraction results in emissions richer in higher molecular weight hydrocarbons relative to CH_4. Deep water extraction is increasing worldwide[215] and whilst one study found that deep water facilities had moderate emission rates compared to shallow water sites,[216] the difference in the composition of emissions could be significant in terms of O_3 production, since longer chained alkanes have shorter lifetimes with respect to OH and more C-C and C-H bonds than CH_4. This work shows that the EMF can be a useful tool in separating emissions from oil, gas or condensate exploitation and supports the conclusion that wet natural gas contains a more complex mix of NMHCs than dry natural gas.

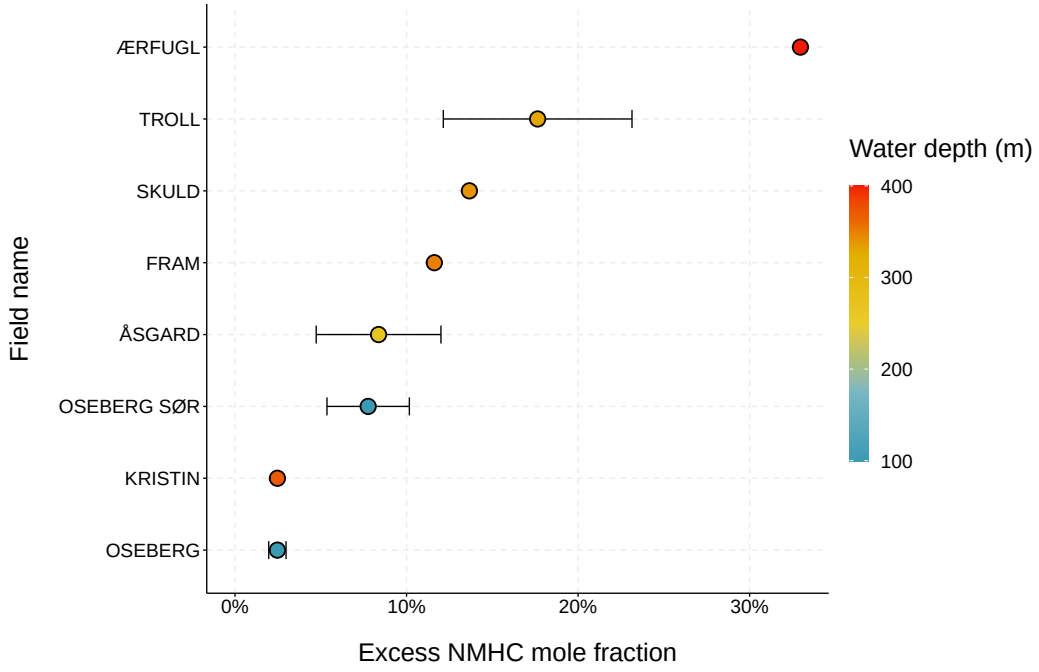

Figure 3.11: *Mean excess mole fraction for individual offshore fields in the Norwegian sector of the North Sea coloured by water depth. Error bars represent one standard error.*

3.3.3 Comparison of VOC speciation to emission inventories

The UK NAEI is the primary source of inventory information for the UK.[217] The inventory provides pollutant specific gridded emissions at a 1 km x 1 km resolution. Emis-

sions are split into source sectors such as road transport, waste, agriculture and offshore. Point source emissions are also included, such as individual offshore platforms or power plants. VOCs are generally represented in the form of total NMHC, with the exception of carcinogenic compounds benzene and 1,3-butadiene, which are quantified in the point source inventory. In order to extract specific VOC emissions estimates, the total NMHC estimate can be combined with source profiles from Passant [218]. This includes a series of NMHC species profiles which describe the VOC composition from each source, given as a percentage contribution to total NMHC emissions. The speciation profiles include over 600 different compounds from around 250 different sources. For each year in the NAEI the profiles are held constant and are applied to a new total VOC inventory. For well known sectors, constant profiles are assumed to be a reasonable approximation. However, for less well known sources, this could introduce uncertainty into emissions estimations, specifically in the context of modelling tropospheric ozone as the results are sensitive to the VOC speciation, which is used as model inputs. Incorrect speciation means it is difficult to accurately assess the impact of emissions.

In terms of offshore VOC speciation, four relevant profiles from Passant [218] were identified. These are listed as crude oil production, crude oil distribution, industrial combustion of gas and natural gas flares. Multiple sources are represented by a single profile meaning these profiles are used to represent the entire offshore sector, including emissions from flaring, venting, loading and storage. Figure 3.12 compares the emission ratios of VOCs to propane for these profiles to the North Sea measurements from this work. (Note the flaring profile was not included here due to the lack of common species between measurements and inventory.) All offshore field types show a consistent trend in Figure 3.12 with the VOC to propane ratio generally decreasing with increasing molecular weight, highlighting how O&G emissions are dominated by light alkanes. However the absolute values vary significantly, again exposing the non-uniform nature of emissions from the O&G sector.

The measurements closest resemble the oil production VOC profile from the NAEI, shown in Figure 3.12, particularly for emission ratios of some light alkanes (n-butane, n-pentane, iso-butane), which are both qualitatively and quantitatively consistent. Obvious differences are observed for species with a carbon number greater than 5. The ratio

for hexane is enhanced in the oil production profile compared to the observations, with the largest discrepancy seen for condensate fields. The opposite is true for the mono-aromatic species (benzene and toluene), where the enhancement ratio in the inventory profile is significantly lower than the measurement data for benzene and emissions of toluene are not included at all, suggesting the inventory may be lacking in some information. The gas combustion profile appears to capture similar trends to the measurements and also includes aromatic compounds benzene and toluene. However, this profile shows a higher contribution of VOCs relative to propane compared to observations for all species, potentially leading to the overestimation of some species should these profiles be used in the estimation of individual VOC emissions. The oil distribution profile is sparse in terms of the number of species reported, only including alkanes up to C_5 and no mono-aromatics. In addition, the quantitative values of emission ratios are dissimilar to the both the observations and the other inventory profiles, suggesting this profile does not well represent offshore O&G emissions.

This work shows that VOC emissions are unique to their source and therefore using a single profile to represent multiple emission sources will likely mean emissions are poorly described in the inventory. However, the measurements made here represent an accumulation of emissions from all potential sources located on offshore platforms, therefore it is unlikely that any one source-specific profile will agree entirely. Despite this, it is clear that the profiles are not inclusive of all species and that considerable variability exists in emissions from the O&G sector, which is not currently reflected in the inventory. In order to assess the accuracy of the NAEI source profiles, more detailed study into specific sources and activities is needed.

3.4 Conclusions

This study presents an overview of VOCs emitted from O&G operations in the North Sea, which is a rarely investigated but rapidly changing region. Data from 28 research flights were aggregated to provide a representative picture of the spatial distribution of VOCs across all regions of the North Sea. Enhancement ratios between pentane isomers identify O&G activities to be the dominant source. Characteristic enhancements of iso-pentane over n-pentane of 0.89, 1.08, and 1.12 in the North UK, West Shetland and

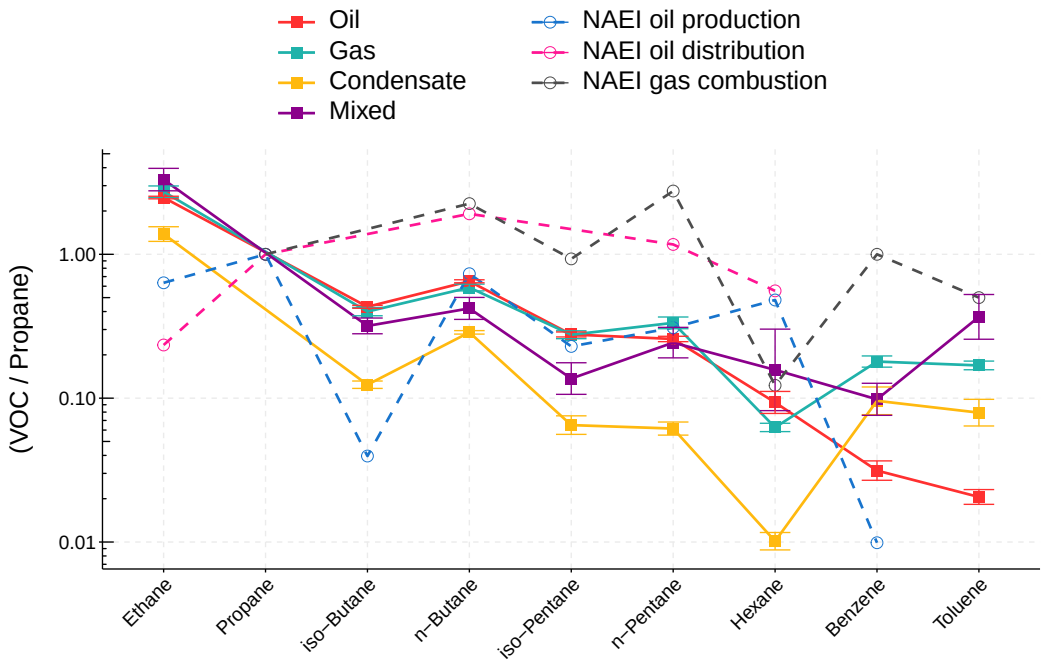

Figure 3.12: *Emission ratios of VOC with propane calculated by reduced major axis regression for each offshore field type (note the log scale). Error bars represent the 95% confidence intervals. The dashed lines show the ratio obtained from the NAEI speciation profiles in Passant [218] for oil production, oil distribution and gas combustion.*

Norwegian sector respectively, are consistent with literature values identifying emissions from O&G activities. A ratio of 1.24 ppb observed in the South UK provides evidence of an urban influence on emissions since branched isomers are more prevalent in refined products such as petrol. Enhancement ratios of individual VOCs with specific tracer compounds were utilised to determine the contribution from unique emission sources. Propane was used as an O&G tracer while acetylene was used to identify vehicular emissions. Strong correlations of light alkanes with propane and generally weak correlations with acetylene confirmed that hydrocarbon mixing ratios in the North Sea are primarily influenced by O&G production. Emissions originating from urban traffic sources were identified in the South UK through use of the benzene to toluene enhancement ratio, where approximately 4% of data from this region was characterised by a B/T ratio of 0.6, typical of traffic emissions.[200]

The source profiles of offshore field types were investigated in terms of the primary product; oil, gas, condensate or a mix of them. The C_2H_6 to CH_4 enhancement ratio highlighted the significant spatial variability in the composition of emissions from offshore O&G production. Ratios ranging from 0.03 to 0.18 indicated "wet" emission sources containing high ethane content as well as "dry" emissions primarily composed of CH_4. The distribution of individual VOCs was similar for all field types, with C_2–C_5 alkanes being the dominant species, however the relative contribution of VOCs to CH_4 was unique to each extraction product. The importance of studying VOCs in addition to CH_4 was exposed through calculations of VOC-OH reactivity, which showed unsaturated species, followed by light alkanes were the most important in terms of local O_3 formation. CH_4 contributed less than 3% despite its dominance in terms of emissions from this sector. Through calculation of the excess mole fraction, the diversity in emissions from O&G activities was emphasized. Deep water oil extraction resulted in emissions of hydrocarbon-rich, associated gas, whereas gas extraction in shallow waters yields emissions of CH_4-rich, non-associated gas. EMFs typically increased with water depth, suggesting that emissions of VOCs from O&G activities may become increasingly important relative to CH_4 in terms of their impact on air quality as current reservoirs are depleted and exploration shifts to more challenging, deeper waters.

A comparison of the measurement data to the source profiles found in the UK NAEI revealed several discrepancies in terms of relative speciation. The VOC to propane ratio for common species was compared to profiles relating to gas combustion, oil production and oil distribution. Whilst the profile for oil production agrees fairly well with measured molar ratios of light alkanes, deviations occurred for the higher carbon number hydrocarbons, particularly hexane, which was higher relative to propane in the inventory compared to measurements. Considerable differences were also seen for benzene and the absence of other aromatic species and alkenes in the inventory profiles suggest these sources are not completely characterised in the current inventory, although the overall mass of emissions may still be correct.

Overall, this work uses novel and unique data to provide a better understanding of a relatively understudied source of emissions from North Sea O&G production, which has the potential to impact local and regional air quality. The VOC speciation profiles estab-

lished here could be used to update the current inventory, providing a set of observational-based profiles specific to each fossil fuel product.

4

Emissions Estimates from North Sea Oil and Gas Facilities

4.1 Introduction

Accurate reporting of atmospheric emissions is at the core of assessing and mitigating environmental concerns resulting from industrial activities. Such reports are a crucial source of data which underpin the construction of emissions inventories. The inventories serve a wide range of purposes including facilitating the development of air quality relevant policies and mitigation efforts as well as to assess compliance against legally set thresholds.[142] Emission inventories for oil and gas (O&G) production are typically developed using "bottom-up" (BU) methods, which are based on component-level emissions. In these methods, emissions from individual components are measured and

subsequently scaled up by the total number of sources to produce an overall estimate for a facility. In the absence of such measurements, they are derived through a combination of source-specific emission factors and activity data prior to scaling.[143,219] Alternatively, "top-down" (TD) methods can be used, which typically involve measuring enhancements downwind of a point-source or region using aircraft, satellite or tower measurements to produce estimates which are representative of total atmospheric emissions.[124,141,205,216,220]

TD studies in regions of O&G production are commonly used to validate the BU estimates used in emission inventories. However, there are often discrepancies between results obtained with the two methods.[109] Possible uncertainties from TD methods arise due to the temporal variability in emissions. Intermittent sources such as flaring have the potential to be under- or over-estimated when emissions estimates are scaled up to daily or annual resolution. On the other hand, BU estimates are generally lower than those from TD studies.[221] However, BU methods potentially fail to include significant emission sources or severely underestimate those that are reported due to unsuitable emission factors or inaccurate activity data.[142] Moreover, component-level emission factors do not account for the effect of ageing equipment over time. New machinery is expected to perform efficiently, however over time degrades and becomes less efficient. This could potentially lead to inaccuracies in the BU estimates, which may be better captured by TD methods. Furthermore, there are additional uncertainties surrounding fugitive emissions, with a recent study in the North Sea exposing a potentially significant missing methane (CH_4) source within the inventory due to leakage from offshore platforms.[222] Therefore, a greater understanding of the inconsistencies between TD and BU methods is required to improve confidence in the overall emissions estimates from the O&G industry.

4.1.1 UK context

In the UK, emissions from upstream O&G sources are entirely operator-reported. Annual emissions estimates for atmospheric pollutants from all fixed and mobile installations are compiled within the Environmental Emissions Monitoring System (EEMS). The primary function of EEMS is to provide data regarding offshore O&G industry emissions,

which can be incorporated into the annual UK National Atmospheric Emissions Inventory (NAEI). Data relating to emissions of pollutants with environmental significance including CH_4, carbon monoxide (CO), nitrogen oxides (NO_x = NO + NO_2) and volatile organic compounds (VOCs) are uploaded to the database by the facility operators. Operators are required to report 100% of emissions from emitting installations and terminals from sources including flaring, venting, offshore tanker loading and emissions from exploration and development drilling rigs. Emissions relating to support vessels, tankers on-route, helicopters and seismic vessels are not included as these are reported elsewhere in the NAEI.[139]

4.1.2 Bottom-up calculations

Emissions of each pollutant from installations and terminals must be submitted to EEMS for each of three emission types and the associated sources within, displayed in Table 4.1. The direct monitoring of emissions is uncommon offshore since many operators do not have verified monitoring systems, largely due to the associated expense. Consequently, emissions for most sources are calculated from activity and emission factors (Section 1.6.2.1). Within EEMS, emission factors are split into two categories: calculated and default. Calculated emission factors are preferential since these are derived from local measurements made on a range of equipment and are therefore specific to the reporting installation. Alternatively, default emission factors exist for every source within EEMS. These are taken from references within the literature and are assumed to represent acceptable values for the associated emission source.[139] There are default emission factors for every plant component, which are different depending on the location (on- or off-shore) and the hydrocarbon type (gas, light crude oil or heavy crude oil.) Additionally, the default factors are adjusted based on the age of the installation or terminal. An *age adjustment factor* is applied, which relates to the commissioning date of the installation as in Table 4.2. Therefore, older platforms are expected to have higher emissions due to the degradation of equipment. However, these factors do not account for the reduced efficiency of equipment over time on platforms commissioned from 1988 onwards. Moreover, the use of default emission factors for multiple platforms assumes emissions are somewhat uniform between facilities, however the temporal and spatial

variability in emissions from the O&G industry is well documented.[126,223]

Table 4.1: *Emission types and sources within EEMS.*

Type	Source	Installations	Terminals
Consumption	Gas consumption – Plant operations	✔	✔
	Diesel consumption – Plant operations	✔	✔
	Fuel oil consumption – Plant operations	✔	✔
	Gas flaring	✔	✔
Direct emission	Gas venting	✔	✔
	Direct process emissions	✔	✔
	Oil loading	✔	✔
	Storage tanks	✖	✔
	Fugitive emissions	✔	✔
Drilling	Well testing	✔	✖
	Diesel consumption	✔	✖

Chapter 3 exposed the differences in emissions of VOCs related to unique offshore field types. The hydrocarbon composition of emissions was significantly different in regions of oil production compared to gas. However, the lack of compositional data and direct monitoring regarding VOCs means there are large uncertainties surrounding the quantity of emissions from O&G production. Given that VOCs are tightly coupled with both ozone (O_3) and secondary organic aerosol formation, as well as some direct human health impacts, inaccurate information regarding the breakdown by molecular composition hinders the complete assessment of environmental impacts from the O&G industry. As such, this work presents valuable aircraft-based measurement data from North Sea O&G facilities. This data is used to provide crucial quantitative emissions estimates of individual VOCs and subsequently evaluate the current BU methodology.

Table 4.2: *Installation age adjustment factors within EEMS.*

Commissioning date	Age adjustment factor
After 1998	1.0
1980–1988	1.3
Before 1980	1.5

4.1.3 Objectives

The reporting of offshore emissions in the UK is exclusively based on BU estimations provided by facility operators. The validation of such estimates is rarely attempted and the few studies that do are primarily concentrated around CH_4 with little focus on VOCs. This chapter details measurement data regarding emissions from O&G facilities in the North Sea, which may help to address some of the uncertainties surrounding offshore emissions. First, TD emission estimates of CH_4 and speciated VOCs are derived for four facilities. A mass balance approach was employed using in-situ, online CH_4 and ethane (C_2H_6) measurements coupled with the relative abundance of hydrocarbons in discrete air samples. Second, the aircraft-based estimates are used to assess the robustness of the current BU methodology by identifying the key areas and sources within the reporting which require further evaluation. Improved knowledge of these emissions will facilitate more accurate assessments of the impact of emissions from the offshore sector.

4.2 Methods

4.2.1 Instrumentation

Airborne measurements were conducted on-board the Facility for Airborne Atmospheric Measurements' (FAAM) BAe-146 research aircraft. In-situ measurements of CH_4 and C_2H_6 at a resolution of 1 Hz were made using a Los Gatos Research Fast Greenhouse Gas Analyser (FGGA, model RMT-200) and Tunable Infrared Laser Direct Absorption Spectrometer (TILDAS, Aerodyne Research, Inc), respectively. Discrete VOC measurements were made using the whole air sample (WAS) system on-board the aircraft, coupled with post-flight analysis by gas chromatography with flame ionization detection (GC-FID). Further technical details regarding the aircraft and instrumentation, including calibration procedures and uncertainty calculations are described in Chapter 2.

4.2.2 Campaign design

As part of *The Demonstration Of A Comprehensive Approach To Monitoring Emissions From Oil and Gas Installations* (AEOG) project, three five-day airborne campaigns took

place over the North Sea in April 2018, September 2018 and March 2019. Figure 4.1a shows the aircraft path during each flight used in this study. Airborne sampling was focused on two regions of the North Sea, displayed by the clusters of installations in Figure 4.1b. The first was the Central North Sea region located off the coast of Aberdeen. In particular, installations serving the Elgin-Franklin and Forties fields were targeted due to their comparatively high levels of atmospheric emissions identified during previous field studies. The second was the West Shetland area, which is predominantly an oil producing region. New installations such as the Clair Ridge development were commissioned at the start of this work with subsequent production beginning in November 2018.[224] This study will provide a baseline for current regional pollutant levels against which emissions from the new installations can be assessed, whilst providing data relating to the atmospheric levels of pollutants emitted from specific existing installations.

The preferred sampling strategy during each flight was to perform a series of stacked straight and level flight legs downwind of the chosen installations, intercepting the plume at various altitudes ranging from the near-surface to the top of the planetary boundary layer (PBL). Sampling in this way allows the full characterisation of the plume in both the horizontal and vertical directions. The flight paths were positioned approximately 3–8 km downwind of the source in a direction perpendicular to the wind. In all cases, an upwind pass of the study region was performed to detect any emission sources directly upwind and to rule out interference from upwind sites or vessels. Figure 4.2a shows an example of the downwind flight legs performed by the aircraft, whilst the observed CH_4 enhancements for each installation are displayed in Figure 4.2b. The close proximity of platforms to each other allows multiple installations to be sampled on a single flight. However, on some occasions this congestion can lead to the overlapping of individual plumes making source attribution difficult. Plumes were assigned to a given platform based on wind direction. Subsequent analysis was only performed on enhancements that could be definitively assigned to a single platform and were absent of interference from other point sources. A summary of the installations sampled during each flight is given in Table 4.3.

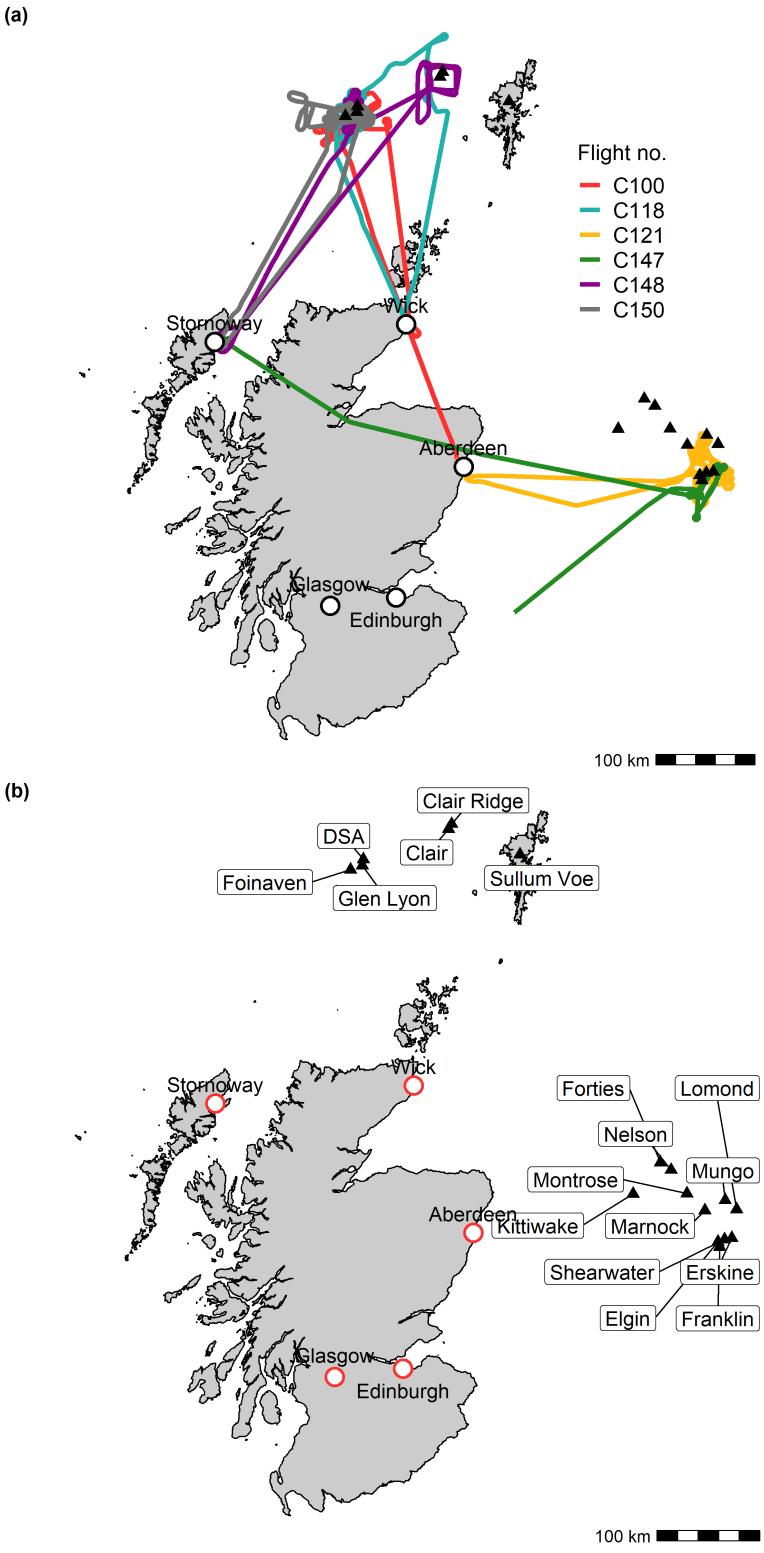

Figure 4.1: *(a) North Sea flight tracks. (b) Locations of individual offshore platforms which were targetted for airborne sampling.*

Table 4.3: *Flight details and locations of sampled facilities.*

Flight no.	Date	Platform name	Latitude	Longitude
C100	2018-04-26	Foinaven	60.32	-4.27
C100	2018-04-26	Glen Lyon	60.36	-4.07
C118	2018-09-11	Foinaven	60.32	-4.27
C121	2018-09-14	Elgin	57.01	1.84
C147	2019-03-04	Elgin	57.01	1.84
C147	2019-03-04	Shearwater	57.03	1.95
C148	2019-03-05	Glen Lyon	60.36	-4.07
C150	2019-03-07	Glen Lyon	60.36	-4.07

4.2.3 Emission flux calculation

Pollutant fluxes of CH_4 and C_2H_6 were calculated using a mass balance approach, which can be used to estimate emissions from area[108,220,225,226] or point sources.[141,205,227] The net flux (Q) through a vertical plane downwind of a source is calculated using R4.1, where the difference between the downwind and background mole fractions of a compound $([C] - [C]_b)$ is integrated laterally across the width of a plume $(2x)$ and vertically from the surface $(z_{surface})$ to the top of the PBL (z_{PBL}) and multiplied by the perpendicular component of the wind speed $(Ucos(\alpha))$, where α is the angle between the wind direction and the line perpendicular to the aircraft heading. The ideal gas law is then applied to convert a volume mixing ratio into a mass per unit volume, allowing the determination of an emission flux through the plane in kg s^{-1}.

$$Q = U\cos(\alpha)\int_{-x}^{+x}\int_{z_{surface}}^{z_{PBL}}([C]-[C]_b)\,dx\,dz \tag{R4.1}$$

Emission rates of individual VOCs (Q_{VOC}) were subsequently calculated by scaling the C_2H_6 emission rate $(Q_{C_2H_6})$ by the enhancement ratio in each plume $(ER_{[VOC]/[C_2H_6]})$, and the ratio of the molecular weights $(\frac{MW_{VOC}}{MW_{C_2H_6}})$, as in R4.2. Enhancement ratios of each VOC were determined from mixing ratios in whole air samples captured in plumes.

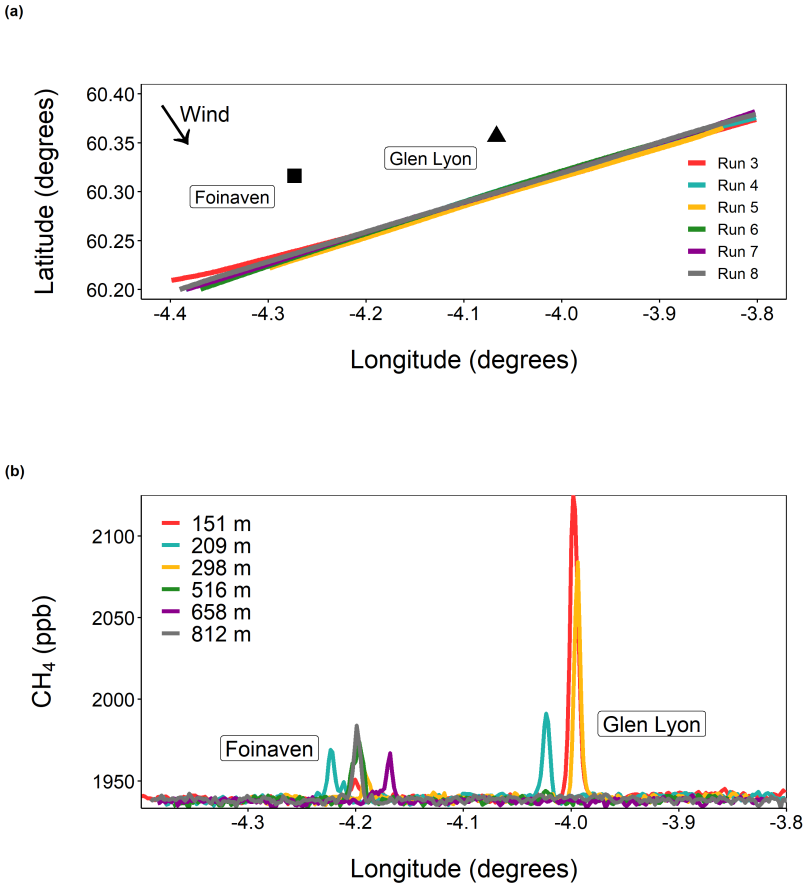

Figure 4.2: *(a) Example of straight and level flight runs performed downwind of specific installations in the North Sea. (b) CH_4 enhancements observed downwind of installations at different altitudes.*

$$Q_{VOC} = Q_{C_2H_6} \times ER_{[VOC]/[C_2H_6]} \times \frac{MW_{VOC}}{MW_{C_2H_6}} \tag{R4.2}$$

4.2.3.1 Wind speed

In order for the mass balance to correctly represent emissions, the wind speed and direction must be consistent between the time of emission and the time of measurement. If wind speed decreases between these two times, emissions estimates will be biased low. Conversely, if the wind speed increases as the plume is transported, emissions will be biased high as the amount of dilution the plume has undergone will be overestimated.

This is less of a concern when measuring emissions from point sources such as oil platforms since transport times between source and measurement are typically short compared to measuring bulk emissions from an entire region. Figure 4.3 shows the average perpendicular component of the wind speed ($U \cos \alpha$) measured throughout each flight for which a mass balance calculation was performed. A threshold mean wind speed of 3 m s^{-1} was set prior to any calculation to ensure suitable dispersion of the plume. Mean wind speeds ranged from 6–16 m s^{-1} with a mean standard deviation of 1.6 m s^{-1}.

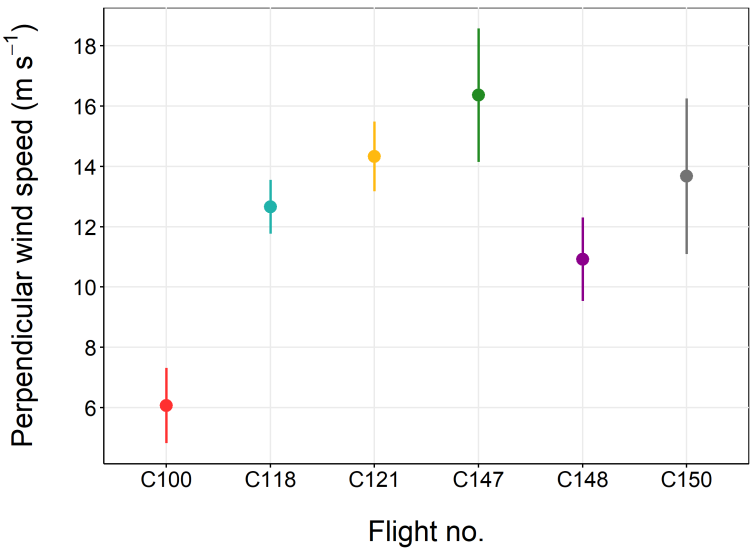

Figure 4.3: *Mean perpendicular wind speed across all straight and level transects during each flight. Error bars represent* $\pm$ *1*σ.

4.2.3.2 Vertical mixing within the PBL

The maximum mixing height of each measured plume was established by estimating the height of the PBL using vertical profiles performed at the beginning and end of each flight. Profiles were typically conducted from 15–800 m close to the area of interest. Increases in the vertical variation of potential temperature was determined to be the PBL height, shown in Figure 4.4. Typical mixing heights were estimated to be roughly 250–850 m above sea level (ASL). The extent to which the enhancements from individual point sources were mixed to the top of the PBL varied depending on boundary layer

conditions and the source of emission. For some sources, the full vertical extent of the plume was captured between the surface and a height lower than the PBL height, showing incomplete mixing of surface emissions to the top of the PBL. However, if the mixing height of the plume could not be identified from aircraft transects, the PBL height was used to constrain the mixing height of the plume by assuming a well-mixed plume within the PBL with no leakage above.

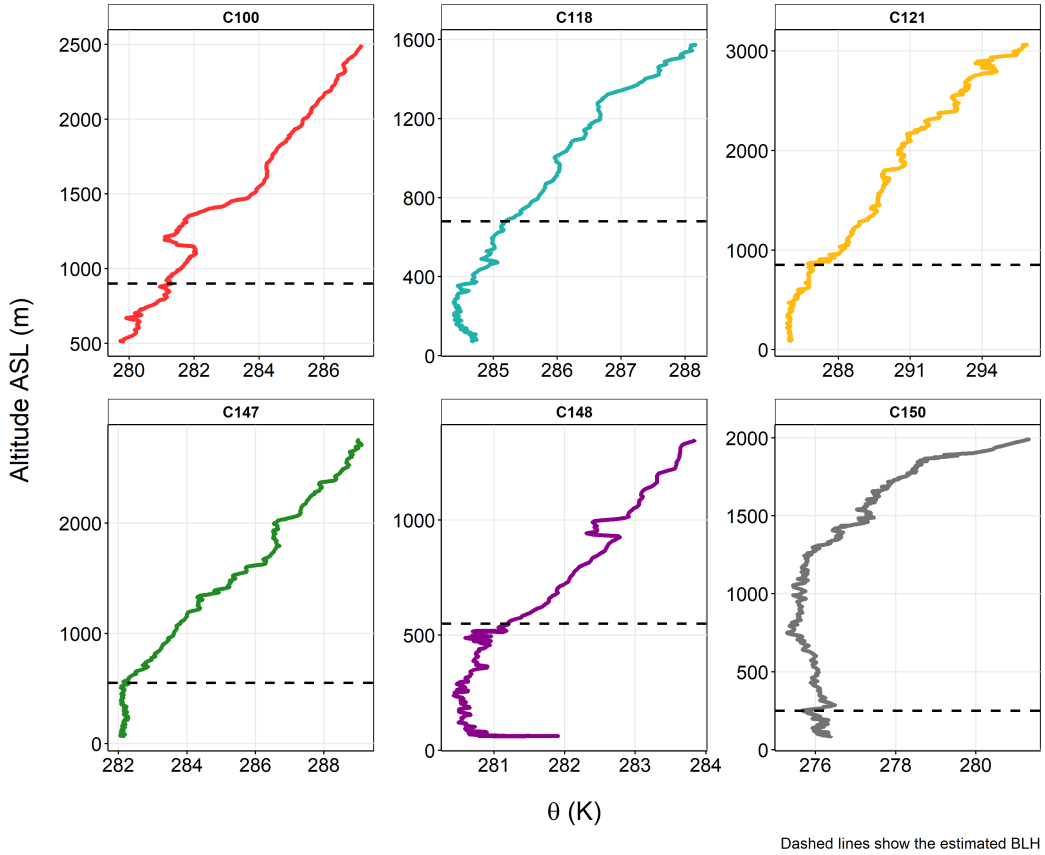

Figure 4.4: *Vertical profiles of potential temperature (θ) conducted during each flight. The horizontal dashed lines indicate the estimated BLH at the time and location of each profile.*

4.2.3.3 Background mixing ratios

Background mixing ratios were estimated using the lateral edges of the plume on either side. The first and last fifth of data for each plume transect were considered to be background air. For each flight, the background value for each gas (CH_4 and C_2H_6) was calculated as the arithmetic mean of the mixing ratios in background air. The uncertainty in this value was calculated as the standard deviation about the mean value. Figure 4.5 shows the calculated background values from individual plumes on each flight. Across all flights, there was significant variability in both the CH_4 and C_2H_6 background values. Generally the highest values were observed during the March 2019 flights (C147, C148 & C150), where CH_4 mixing ratios were upwards of 1945 ppb and background C_2H_6 exceeded 2 ppb. These flights were accompanied by easterly winds, suggesting a possible mainland emission source in Scandinavia responsible for elevating the background. In comparison, the lowest background values were observed on flight C118 in the West Shetland region, where winds originated from the west, transporting clean air from the Atlantic to the study area.

This method of estimating the background was chosen over estimating background mixing ratios from a flight leg conducted upwind of the emission source because the lack of interfering emission sources resulted in well-defined plumes, making identification of out-of-plume data straightforward. Using upwind mixing ratios as a background introduces added uncertainty related to the fact that sampling the same air mass at both locations is unlikely and therefore the upwind measurement may not represent the background of air that was sampled downwind. However, upwind passes are useful in the first instant to check for additional emission sources which may affect the calculation.

4.2.3.4 Plume alignment

For each individual plume sampled, the maxima at each transect were aligned in terms of both latitude and longitude to account for slight deviations in the position and heading of transects. Figure 4.6 shows an example of the alignment procedure resulting in the plume maxima being observed at the same two dimensional position across all transects.

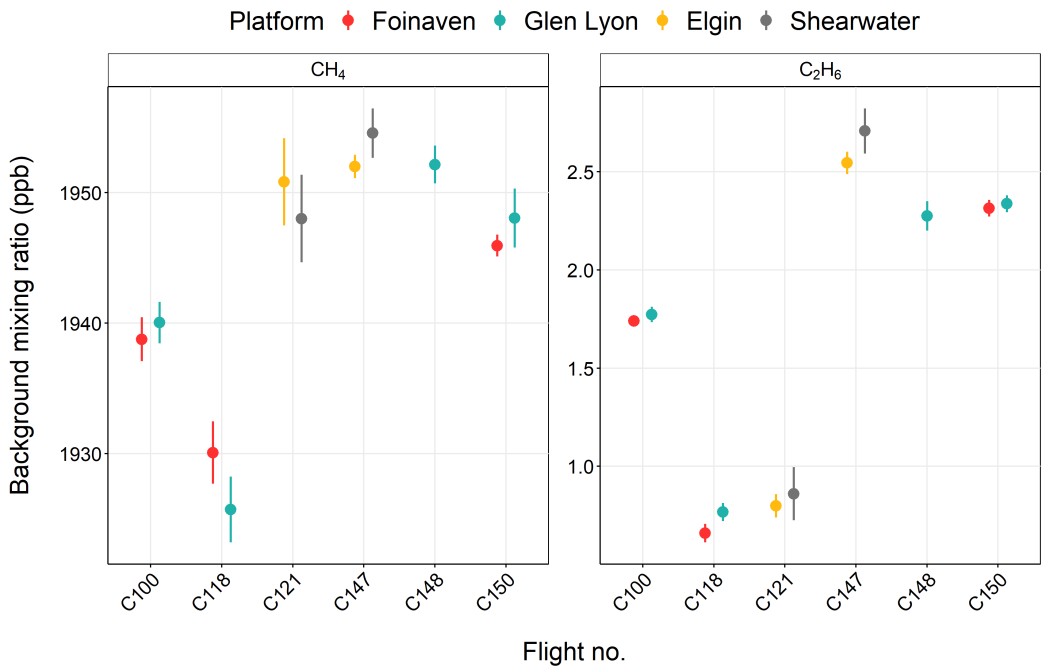

Figure 4.5: *Mean background mixing ratios of CH_4 and C_2H_6 for each flight obtained from the lateral edges of each plume. Error bars represent $\pm 1\sigma$.*

4.2.3.5 Position mapping

In order to integrate a vertical plane downwind of the emission source, the 1 s flight data must be mapped onto a uniform two dimensional screen. A single horizontal path was constructed from the individual flight legs using a linear least-squares fitting as a function of latitude and longitude. The variable (latitude or longitude) with the greatest span was determined and subsequently used as the x-axis for regression. Each 1 s aircraft observation was then mapped to the nearest point on the linear least squares fit path. This translates each data point from a three dimensional position described by latitude (y), longitude (x) and altitude (z) into a position on a two dimensional screen described by horizontal track length and altitude (z).[227]

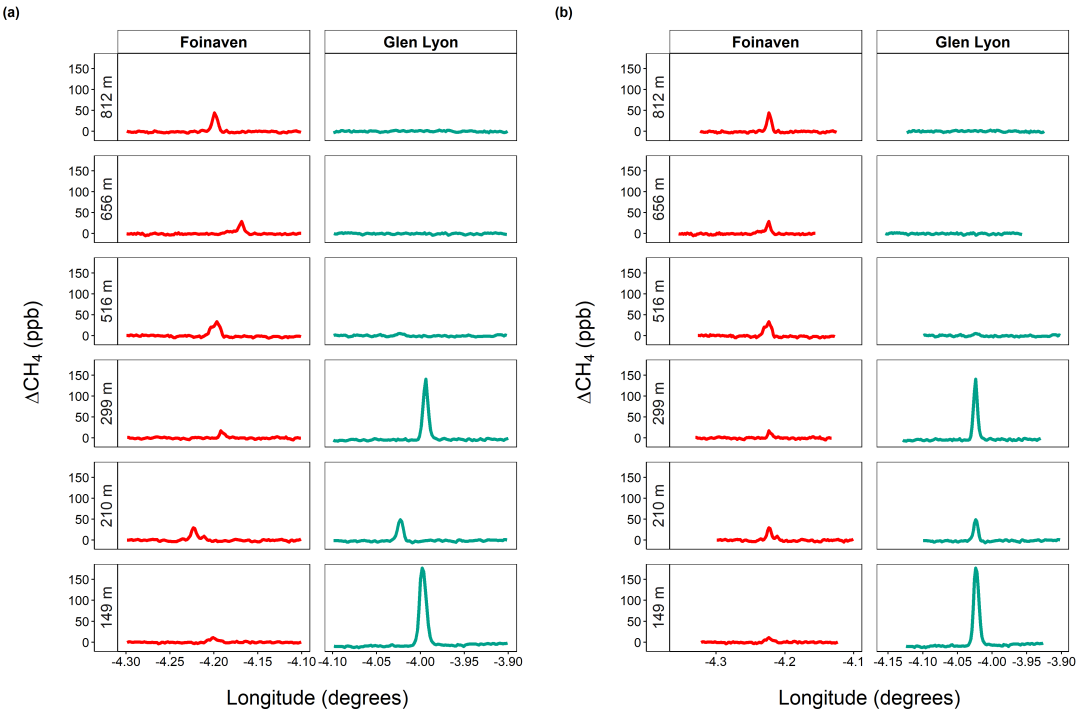

Figure 4.6: *CH_4 enhancement above background observed during during flight C100 downwind of Foinaven and Glen Lyon at each transect altitude. The raw data (a) and data after alignment of the plume maxima (b) are shown.*

4.2.3.6 Interpolation

Interpolation of the screen from an irregular set of data points to a regular two dimensional gridded plane was performed using Barnes surface interpolation.[228,229] This technique is commonly used in weather forecasting for the construction of contour plots from measurements at irregularly distributed monitoring stations.[230] The Barnes method uses a multi-pass scheme for the interpolation of two dimensional data. The initial pass estimates a value at each grid point by using an average of the surrounding observations, which are weighted according to the distance from the grid point being estimated. The first pass estimation (g_1) for a variable $(f(x, y))$ at grid point (i, j) is:

$$g_1(x_i, y_j) = \frac{\sum w_i f(x, y)}{\sum w_i}, \tag{R4.3}$$

where the weighting function is given by:

$$w_i = \exp\left(\frac{-d_i^2}{(c_1)^2}\right), \tag{R4.4}$$

in which w_i is the weight for the i'th observation point, d_i is the distance from the grid point being estimated to the i'th observation point, and c_1 is a smoothing parameter.

The estimation is optimised using subsequent refinement passes, which compute an error surface using the delta between the previous estimated value and the observations. The error surface is used to correct the initial pass by reducing the delta between the estimate and the observations. During the refinement passes the value at each grid cell is re-estimated as:

$$g_2(x_i, y_j) = g_1(x_i, y_j) + \frac{\sum w_i'[f(x,y) - g_1(x_i, y_j)]}{\sum w_i'}, \tag{R4.5}$$

where:

$$w_i' = \exp\left(\frac{-d_i^2}{(c_2)^2}\right), \tag{R4.6}$$

For each unique plume, interpolation in both the horizontal and vertical was performed on the sampled 1 Hz CH_4 and C_2H_6 data, where the number of Barnes iterations was set to 3. In the vertical dimension the data was interpolated from the ground to the estimated height of the PBL, whilst in the horizontal, interpolation was performed from end to end of the flight transects. Flight transects were cropped prior to this to include only the plume of interest and a suitable amount of background observations on either side (at least 10 data points).

4.2.4 Sensitivity to plume mixing height

The mixing height of the plume is a vital constraint in the mass flux calculation. An ideal flight would contain a bottom transect as close to the surface as possible (50 ft ASL), a top transect at the height of the PBL and multiple transects in between to capture the full distribution of the plume in the vertical. Often, flight paths are not ideal and therefore assumptions about plume mixing have to be made. To test the effect of these assumptions on the calculated emission rate, a series of sensitivity tests were performed on simulated data. A Gaussian dispersion equation was used to simulate aircraft measurements of

CH_4 through a plume with a known emission rate (Q), mixing height (z) and average wind speed (U). Random variability in latitude, longitude, altitude, mixing ratio and wind speed was added to the data for each transect to reflect more realistic sampling conditions. The parameters were set as follows: $Q = 0.2\,kg\,s^{-1}$, $z = 600\,m$ and $U = 8\,m\,s^{-1}$. A mass flux calculation was then performed using the simulated data. Two sampling scenarios were tested:

- **A** - The full vertical extent of the plume was sampled.
- **B** - Sampling did not reveal the mixing height of the plume and therefore complete mixing to the top of the PBL was assumed.

A total of 330 iterations were performed for each estimate by varying the Barnes smoothing parameter between 100–200 and the background CH_4 between the mean value $\pm\ 1\sigma$. The final flux estimate was taken to be the mean value of the iterations and uncertainties were represented as $\pm\ 1\sigma$. For each scenario, the estimated PBL height was varied in each case to evaluate the effects of incorrectly defining the PBL height on the estimated flux. Figure 4.7a shows the simulated flight data used in each scenario and Figure 4.7b shows the effect of the estimated mixing height on the calculated emission rate for each sampling scenario. It is evident that, in scenario **A**, where the entirety of the plume is sampled such that a flight transect exists above the top of the plume, z is well constrained within the calculation. Varying the estimated PBL height between 600–1000 m has little effect on the calculated flux since the added area over which to integrate consists of background mixing ratios outside of the plume and therefore make minimal contributions to the total flux. As expected, varying the PBL height below the height to which the plume was sampled ($<$ 550 m) results in an underestimation of the flux. This shows that the calculation of the emission rate does not depend on the PBL height provided the vertical extent of the plume is within the altitude range of the plume transects.

However, in scenario **B**, where no transect was flown above the plume mixing height, the plume is poorly constrained in the vertical and therefore the estimation of the PBL height has a large effect on the calculated flux. Since in this scenario, the only constraint on z is the height of the PBL, estimations in the PBL height result in the integration of the plume up to a height where it may not actually exist, resulting in an over-estimation of

the flux. Similarly, as in scenario **A**, underestimating the PBL height results in an underestimation of the flux. Figure 4.7b (right) shows a near-linear relationship between the estimated height and resulting flux, where an approximate 20% error in the estimation of the PBL height away from the true value (600 m) results in an incorrect estimation of the emission rate.

4.2.5 Uncertainty estimations

The average emission rates of CH_4 and C_2H_6 for each installation were calculated using R4.1. Uncertainties in the estimations arise from a range of variables including the estimated height of the PBL, the choice of background value, deviations in the perpendicular wind speed and the choice of smoothing parameter used in the Barnes interpolation. Therefore, multiple estimations of the flux were calculated assuming different possible conditions. For each installation:

- The Barnes smoothing parameter was varied between 100–200.
- The background was varied within the uncertainty ($\pm$ 1σ) as in Figure 4.5.
- The perpendicular wind speed was varied within the uncertainty ($\pm$ 1σ) as in Figure 4.3.

A total of 330 emissions estimates were calculated per site for each pollutant. The average of the iterations was used to determine the final emission rate for each installation. The uncertainties in the estimates were calculated from the components of each individual source of uncertainty as outlined below:

- Variability in horizontal winds contributes to the flux uncertainty since constant mean horizontal wind speed and direction is assumed in this method. The contribution of wind variability to the flux uncertainty $(\sigma(U\cos(\alpha))$ was calculated as the standard error of the mean perpendicular component of the wind to the flight track across all transects used in the flux calculation.
- Uncertainty in the PBL depth $(\sigma(z))$ is generally estimated using the difference between multiple methods of estimating the PBL height, such as aircraft profiles and

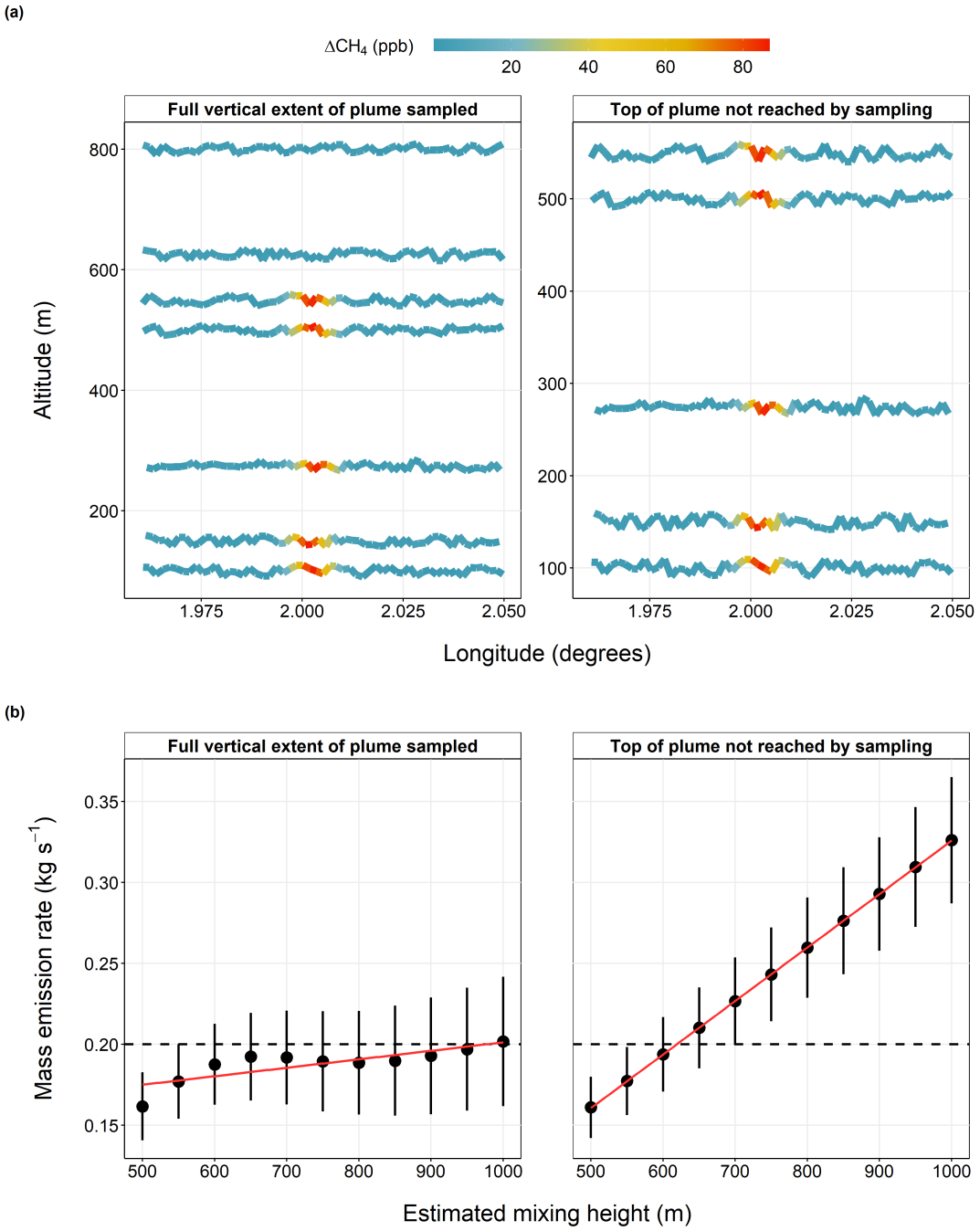

Figure 4.7: *(a) Simulated transects through a CH_4 plume for two flight scenarios. (b) Calculated mass emission rates of CH_4 and uncertainties for each scenario resulting from varying the estimated PBL height. The solid red lines show the trend-line resulting from a linear regression. Simulated data was created using an emission rate of 0.20 kg s^{-1} (dashed line in (b)) and a mixing height of 600 m.*

aircraft soundings.[108] Since no such data was available in this case, an average uncertainty from Cambaliza et al. [231], who reported an average standard deviation in the PBL height of 13% was used instead. Uncertainty in the assumption that the PBL was well mixed with no leakage above was accounted for in the uncertainty in the PBL depth.

- The uncertainty in the enhancement above background $(\sigma([C] - [C]_b))$ was composed of the CH_4 or C_2H_6 measurement uncertainty and the background uncertainty. The measurement or instrument uncertainties were 2.86 ppb and 0.086 ppb for CH_4 and C_2H_6 respectively (described in Section 2.1.2). The background uncertainty was calculated as the variability in background mixing ratios obtained from the first and last fifth of data from each plume transect. A mean value was calculated using data from all transects and the uncertainty was defined as the standard deviation about this mean. The final relative enhancement uncertainty was calculated by summing the two absolute uncertainty components in quadrature, where the average enhancement was calculated as a mean of the maximum enhancements observed during each transect.

- The overall relative uncertainty for each flux estimate $(\sigma(Q))$ was then calculated by summing all the component relative uncertainties in quadrature as in R4.7. In the cases where the plume did not extend to the top of the PBL, this is likely to produce a conservative estimate of the uncertainty since the height of the PBL does not influence the calculation (Figure 4.7). However, for consistency identical calculations were performed for all plumes.

$$\frac{\sigma(Q)}{Q} = \sqrt{\left(\frac{\sigma(U\cos(\alpha)}{U\cos(\alpha}\right)^2 + \left(\frac{\sigma(z)}{z}\right)^2 + \left(\frac{\sigma([C]-[C]_b)}{[C]-[C]_b}\right)^2} \tag{R4.7}$$

4.2.6 Data sources

Emissions data for UK offshore O&G exploration and production installations is collated through the EEMS database (Section 1.6.2.1), maintained by the Offshore Petroleum Regulator for Environment and Decommissioning (OPRED). For use in this work, detailed estimates of daily emissions for each surveyed installation were provided for the day of

each flight through application of the currently accepted EEMS methodology. Included in the data was a breakdown of emissions by pollutant (CH_4, CO_2, NO_x, total VOC) and source (combustion, fugitive, venting, flaring, loading). The emission factors used in the calculations and an estimation of the composition of both the fuel and flare gas from each installation were also provided. Data at a daily resolution facilitates a more robust comparison of measured and reported emissions at the platform-level, since any emissions relating to abnormal operating conditions should be accounted for in the BU estimations. Additionally, data regarding individual platform production data for 2018–2019 were accessed from the Petroleum Production Reporting System published by the UK Oil and Gas Authority.[232]

4.3 Results and discussion

4.3.1 Point source emissions of CH_4 and C_2H_6

Data from six flights, measuring four installations were selected as being suitable for a mass balance calculation. The criteria for selection included a steady, consistent wind speed, a distinct plume which could be attributed to a single platform and a minimum of three plume transects at a range of altitudes. Figures 4.8–4.9 show the interpolation results for each sampled plume of CH_4 and C_2H_6, respectively. These plots illustrate the variation in plume size and shape and show the observed differences in plume mixing heights. Since there were no measurements below the lowest level transect (typically around 50 ft ($\sim$15 m)) to constrain the interpolated estimates, emissions were assumed to be uniform between the surface and the lowest set of measurements.

There is evidence of multiple emission sources from the same installation, where the interpolated plane reveals two areas of elevated concentration separated by an area of lower concentration. This is clear for the C_2H_6 plume from Foinaven on flight C100 (Figure 4.9a) and both plumes from Glen Lyon sampled on flight C148 (Figure 4.8g and Figure 4.9g). One possible hypothesis for this is that venting and flaring emissions were sampled on different transects. By nature, flaring emissions are intermittent and are expected to be present at higher altitudes since they are usually emitted from a higher point on a platform, such as a flare stack. In addition, gas flares typically burn between

1500–2000 K,[233] therefore emissions are buoyant and rise within the atmosphere. Venting emissions generally consist of cold natural gas and therefore are expected to be of an increased density compared to flaring emissions, hence would predominantly be observed lower down in the atmosphere.

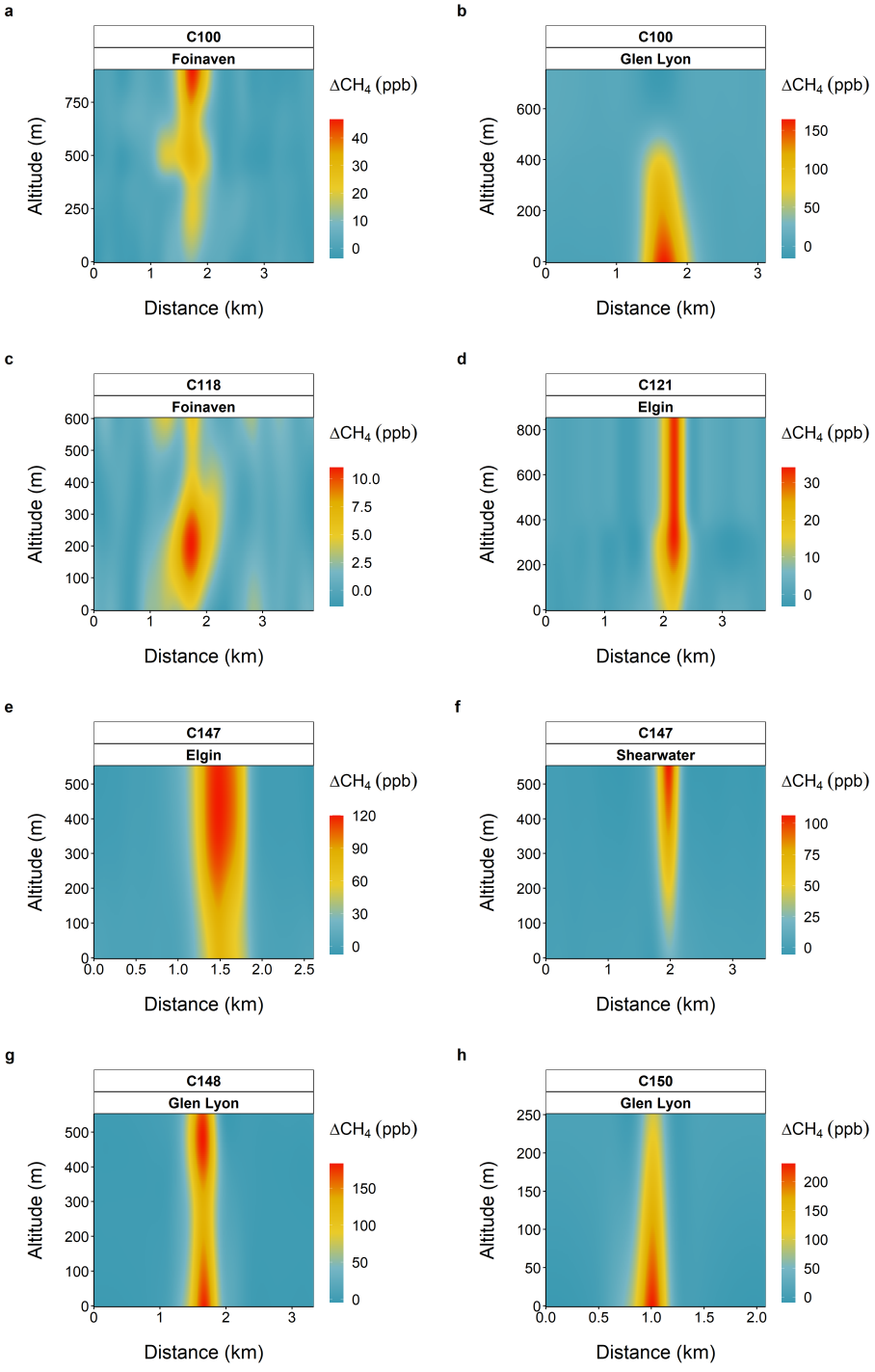

Figure 4.8: *Interpolated plots of CH_4 enhancement above background as a function of altitude above sea level against horizontal distance from a chosen starting point for each sampled installation.*

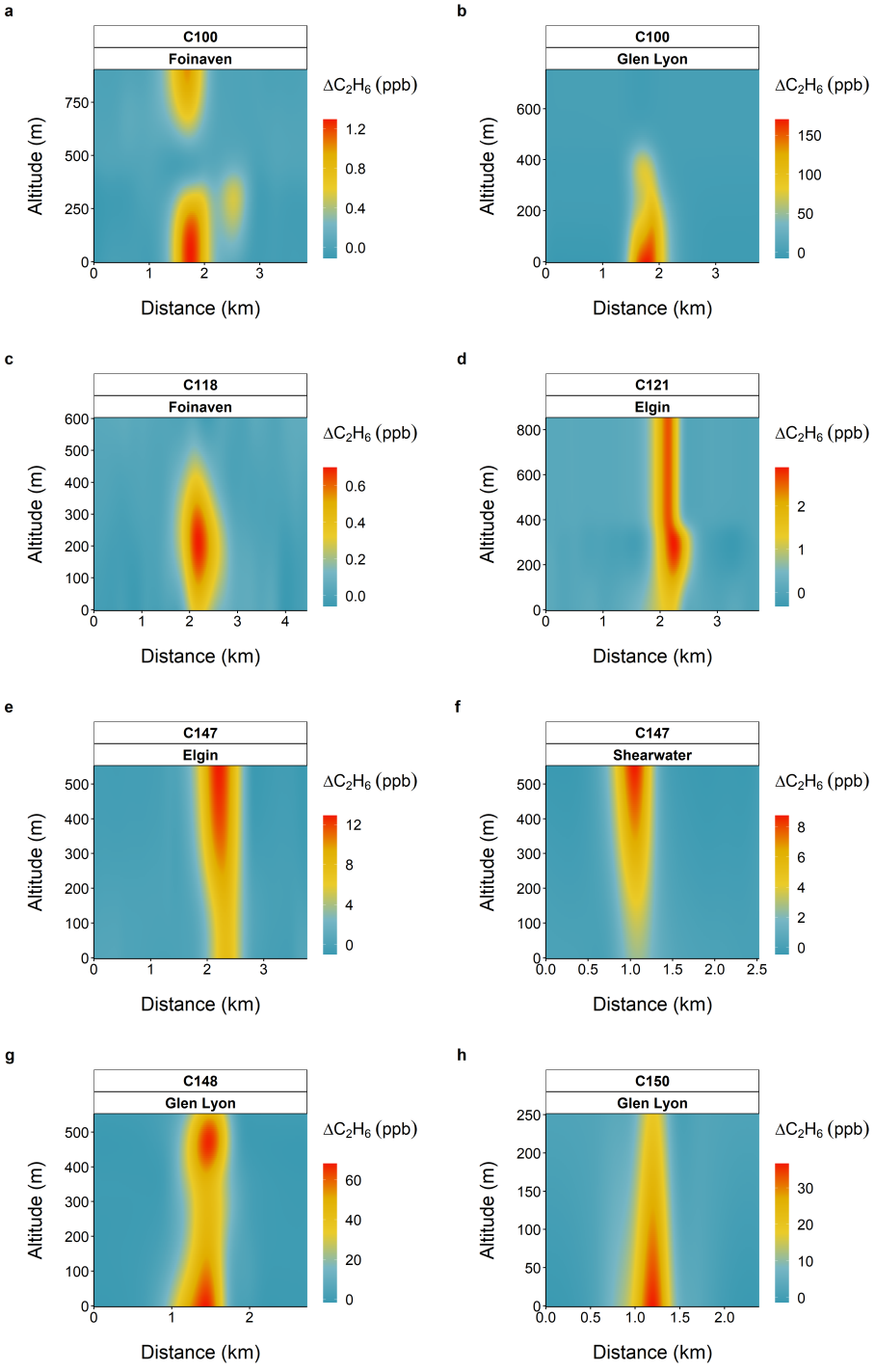

Figure 4.9: *Interpolated plots of C_2H_6 enhancement above background as a function of altitude above sea level against horizontal distance from a chosen starting point for each sampled plume.*

The results of the mass balance calculations are displayed in Figure 4.10. Large variability in the calculated flux of each pollutant is evident. The largest fluxes were calculated for CH_4, which ranged from 0.02±0.01–0.36±0.05 kg s^{-1}, with a median flux of 0.12 kg s^{-1}. Uncertainties varied between 13–47% for CH_4 and 13–24% for C_2H_6. Emissions estimates from the same installations showed significant temporal variability, particularly for Elgin and Glen Lyon, suggesting emissions from these platforms are highly variable. Similar variability was observed in the C_2H_6 fluxes, which spanned a slightly smaller range; from 0.002±0.0004–0.22±0.003 kg s^{-1} and median 0.05 kg s^{-1}. Emissions of C_2H_6 were typically lower than CH_4 emissions. On both measurement occasions, emissions of C_2H_6 from Foinaven were very small compared to CH_4, with enhancements rarely exceeding 1 ppb. The highest C_2H_6 fluxes were observed for Glen Lyon, with estimations for two out of the three sampling days reaching ∼0.2 kg s^{-1}, corresponding to enhancements of up to ∼150 ppb. Interestingly, fluxes of both pollutants at Glen Lyon were much lower during flight C150 compared to flight C148, particularly C_2H_6, which was 4-times lower. This is discussed further in Section 4.3.6.

Few additional studies investigating North Sea platform emissions exist. Riddick et al. [222] used boat-based observations to quantify CH_4 leaks through use of a Gaussian plume model. They reported emission rates from individual North Sea gas facilities ranging from 4.1–54.1 kg h^{-1}. These estimates are significantly lower than those calculated here, which range from 94–1311 kg h^{-1}. However, the Authors note that the results represent fugitive emissions only. Emissions due to venting, flaring or oil-loading activities did not occur during the boat-based measurements but were present on occasion throughout the measurements made in this work. Therefore, emissions estimates are likely to be much higher here, since they represent the cumulative sum of emission sources from offshore platforms. Yacovitch et al. [216] made similar boat-based observations in the Gulf of Mexico, quantifying CH_4 emissions from 103 sites using a modified Gaussian dispersion methodology. They report a median and maximum emission rate of 5.3 kg h^{-1} and 185 kg h^{-1} respectively, of which the latter is towards the lower end of the emission magnitudes reported here. However, factor-of-10 error bars were associated with the Gaussian dispersion results largely due to uncertainties in input parameters such as height and location, meaning the true emission rates could lie closer to those measured

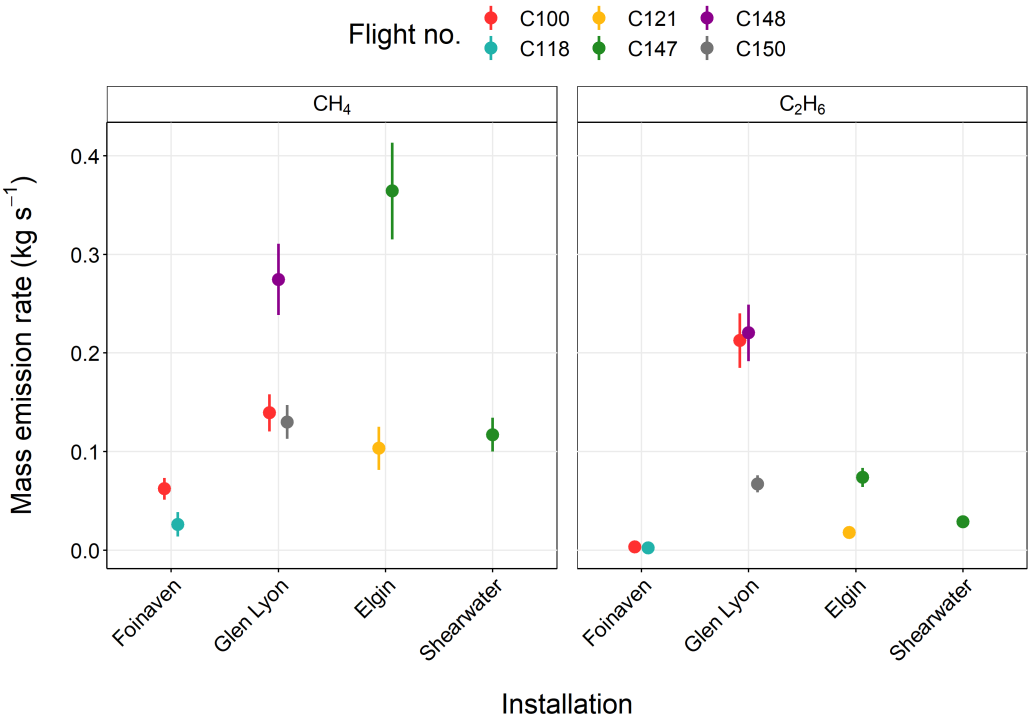

Figure 4.10: *Calculated emission rates of CH_4 and C_2H_6 from individual installations using the mass balance technique. Error bars represent the calculated uncertainties using the method outlined in Section 4.2.5.*

here. The results from this study are typically higher than similar work reported in the literature for regions of offshore O&G production. This may be as a result of capturing emissions from intermittent sources such as oil loading and venting, meaning measurements are biased high when scaled up. Equally, the diversity in platform size, water depth and equipment is likely to lead to obvious discrepancies in emissions estimates from unique regions of O&G production.

In order to provide some context regarding the magnitude of estimated emissions, production data from each platform was obtained from the UK Oil & Gas Authority.[232] Both Foinaven and Glen Lyon are oil-producing platforms, meaning any associated gas is produced as a by-product. This gas is generally regarded as waste, where it is either vented, flared or reinjected. Elgin and Shearwater predominantly produce a mixture of condensate and raw associated gas, both of which are exported for downstream

processing. Figure 4.11 shows the total monthly production of both oil and associated gas for each platform during months in which measurements were made. Glen Lyon overwhelmingly produced the largest amount of oil, producing around 4-times as many tonnes compared to the other installations. Similarly, Elgin produced the most associated gas with over 100,000 tonnes each month. As expected, the West Shetland installations (Glen Lyon and Foinaven) produced the smallest amount of gas since this product is not exported.

When comparing the mean of all emissions estimates for each platform, CH_4 emissions generally scaled with production, with the highest producing platforms (Glen Lyon and Elgin for oil and associated gas respectively) resulting in the largest emission magnitudes. This suggests that platforms with a greater throughput will likely emit the most CH_4. In the case of Glen Lyon, the gas is not used in the supply chain, however in the case of Elgin, any fugitive emissions of CH_4 represent lost product and hence profit, which is undesirable. Therefore, there is further motivation to prevent leaks beyond the climate impacts of such emissions.

4.3.2 Plume characteristics

The characteristics of each plume were evaluated by studying the $\Delta C_2H_6/\Delta CH_4$ ratio. As demonstrated in Chapter 3, this ratio can serve as a useful tool in CH_4 source attribution and can be utilised to distinguish between unique emission sources within the O&G sector. The ratios were calculated from the slope of an XY-plot between the two species using reduced major axis regression.[182] For each plume transect, background mixing ratios were defined as the lowest 10% of values. The average of these values were then subtracted from the observed mixing ratios on each transect to obtain the enhancement above background.

Figure 4.12 shows the $\Delta C_2H_6/\Delta CH_4$ ratio (ppb ppb^{-1}) calculated for each platform from individual flights. Equivalent ratios of 0.1 were observed for Elgin and Shearwater, suggesting these platforms have a similar emission signature relating to condensate extraction (Figure 3.8). Unusually low ratios of 0.03–0.04 were observed from Foinaven. Given that the dominant extraction product from the West Sheltand region is oil, a higher ratio would be expected since wet gas resulting from oil extraction contains a larger

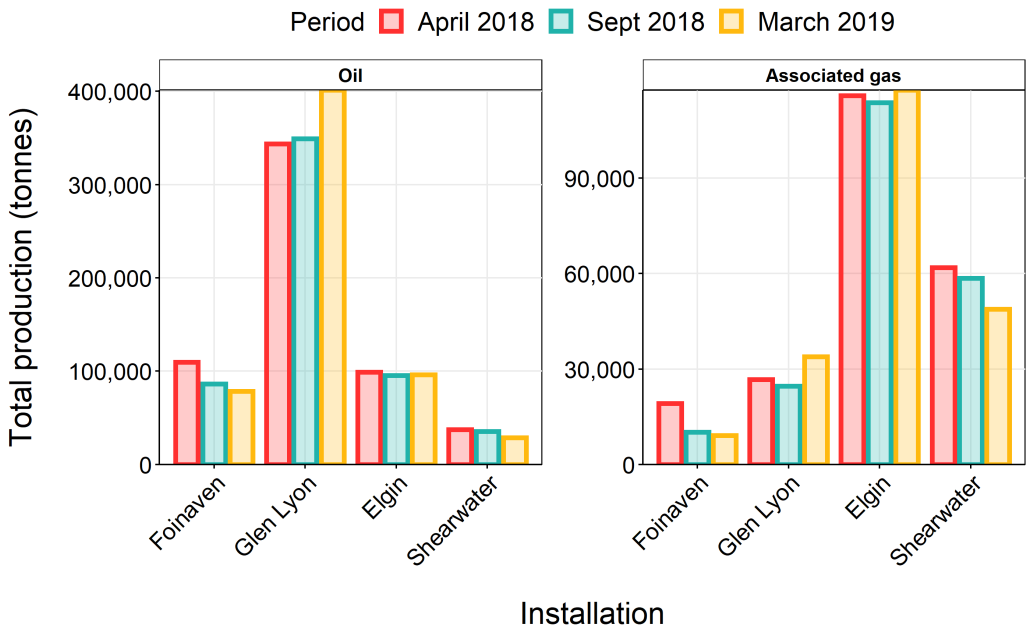

Figure 4.11: *Total production of oil and associated gas for each sampled platform throughout each month flight campaigns took place.*

proportion of VOCs relative to CH_4. The observed values are much closer to the typical range expected from transmission-grade natural gas, which are usually of the order of 0.015–0.02.[234] A possible explanation is that the gas accessed from this platform is from a different geological source and therefore has an unusual composition compared to the neighbouring fields.[216] This is supported by information regarding the composition of each gas collected by each platform. Whilst the fuel gas from both Glen Lyon and Foinaven was similar, containing approximately 96% CH_4 and 2% C_2H_6, the flare gas from Foinaven had a much lower C_2H_6 content (2% compared to 11% in in the Glen Lyon flare). Therefore emissions from Foinaven are expected to be dominated by CH_4 to a higher degree than Glen Lyon, as conveyed by Figure 4.12.

There was a large degree of variation in the enhancement ratios observed from Glen Lyon. Ratios ranged from 0.19–0.83, suggesting a temporal variability in the measured emission sources. Ratios $>$ 20% are atypically high compared to those in previously studied regions of O&G production[226] and are more commonly associated with emis-

sions from processed natural gas liquids produced further down the supply chain.[235] Moreover, the $\Delta C_2H_6/\Delta CH_4$ ratio in areas of North Sea oil production was previously characterised as 0.18 (Figure 3.8), suggesting the high emission ratios measured were influenced by sources other than raw natural gas. This is further evidence of an additional emission source enriched in C_2H_6 measured during flights C100 and C148.

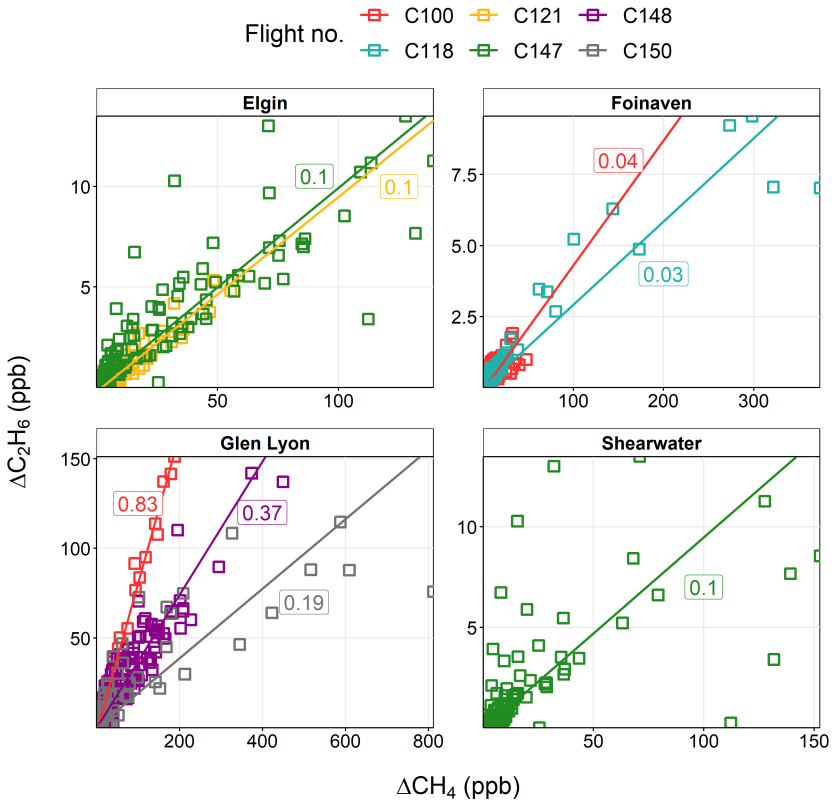

Figure 4.12: *ΔC_2H_6 vs ΔCH_4 for each installation for which a mass balance calculation was performed. The solid lines represent the molar enhancement ratio calculated from a linear fit using reduced major axis regression. Significant correlations were observed in all cases and r^2 values ranged from 0.50–0.99.*

4.3.3 VOC emission rates

Emission rates of individual VOCs were calculated using R4.2. Firstly, each unique whole air sample was attributed to a plume from a specific installation. Figure 4.13 shows the

1 Hz time series of ethane during each flight along with the time each whole air sample was filled (squares). The canister samples are positioned on the y-axis according to the quantified mixing ratio of ethane in each sample by GC-FID (Section 2.2). Ethane mixing ratios in the canisters ranged from 0.74–41.2 ppb, highlighting the difference between a sample in background air and a sample captured in the plume. Generally, there was good agreement between the two methods for ethane (Section 2.1.2 and Section 2.2). A regression plot between the canister ethane mixing ratio and the 1 Hz ethane data averaged over the fill time of each canister yields a slope of 0.8 [0.702, 0.913], where the numbers in square brackets give the 95% confidence interval in the slope, with coefficient of determination r^2 = 0.80 (n = 58).

Secondly, the enhancement ratios of each VOC to ethane were determined using robust linear regression, implemented using the **MASS** R package.[236] The robust regression technique was chosen as it dampens the influence of outliers, which given the small sample sizes ($n < 20$) would potentially have a large effect on the least squares fit. For each plume, the quantification of emission rates was restricted to species which showed a significant, positive correlation with ethane ($p > 0.05$). Figure 4.14 shows the regression plot of selected VOCs against ethane from the canister samples obtained in each plume. Alkanes, along with aromatic species, benzene and toluene, were consistently well correlated with ethane in all plumes with Pearson correlation coefficients $r > 0.7$. Generally unsaturated compounds such as butenes and pentenes were poorly correlated with ethane and therefore their emission rates were rarely quantified in downwind plumes.

The resulting VOC emission fluxes are shown in Figure 4.15. The total relative uncertainty in the VOC estimates was calculated by summing the relative uncertainty in the C_2H_6 estimates and the standard error of the regression slope in quadrature. In all but one case, VOC estimates were lower than CH_4 estimates. The maximum VOC emission rate was 0.64 kg s^{-1}, determined for propane in the Glen Lyon plume measured during flight C100. The most abundant species across all calculations were ethane, propane, *i*-butane, *n*-butane, *i*-pentane, *n*-pentane , ethene, benzene and toluene, highlighting the dominance of light alkanes in emissions from O&G platforms.

As seen with the CH_4 estimates, significant variability in the magnitude of VOC emission estimates was observed. The smallest estimates were measured for Foinaven with

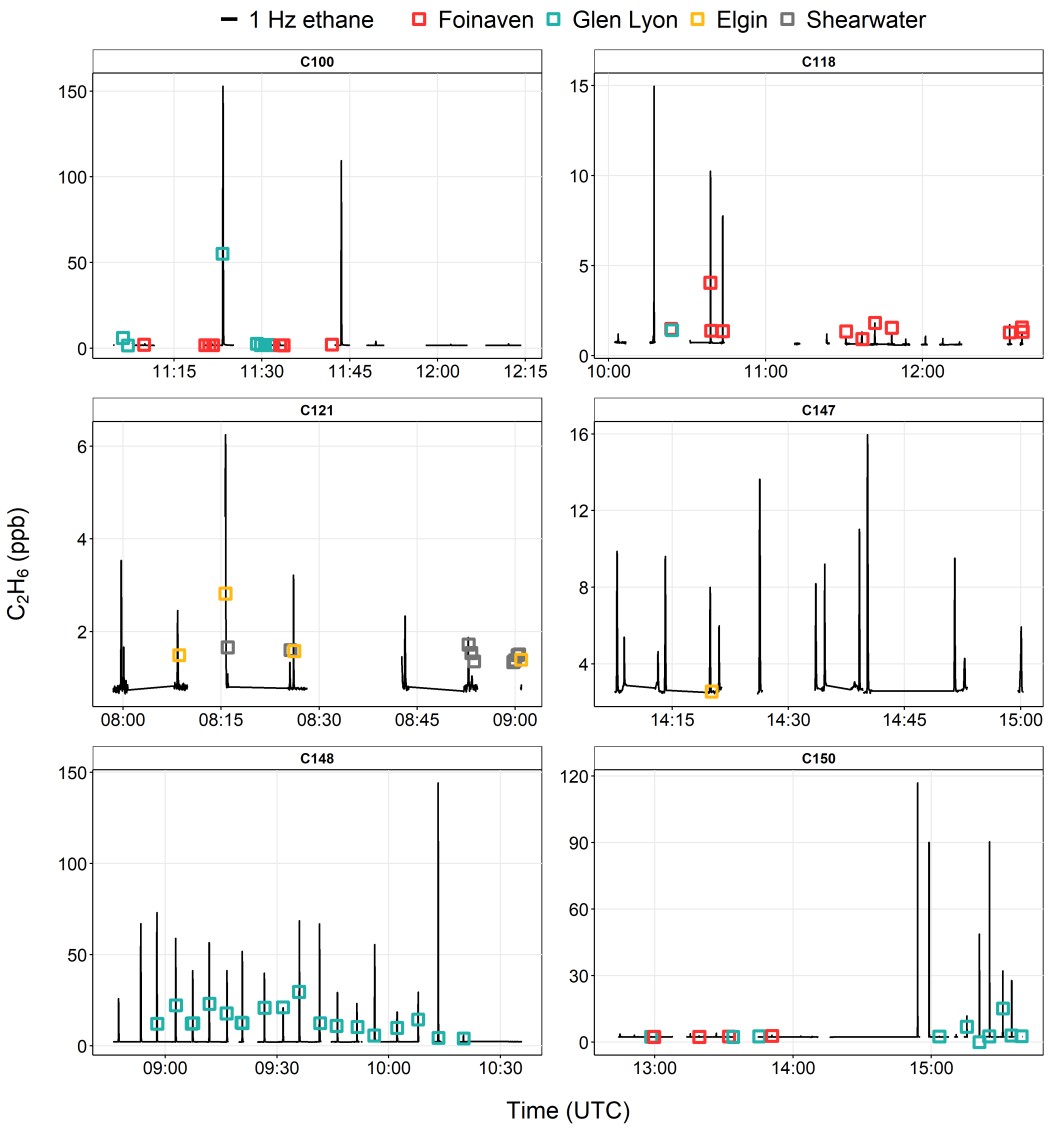

Figure 4.13: *Ethane time series during individual aircraft runs for selected flights. The coloured boxes show the mid-sampling time of captured whole air samples and are placed on the y-axis according to the quantified ethane mixing ratio in the canister. The colours represent the plume that each sample was assigned to.*

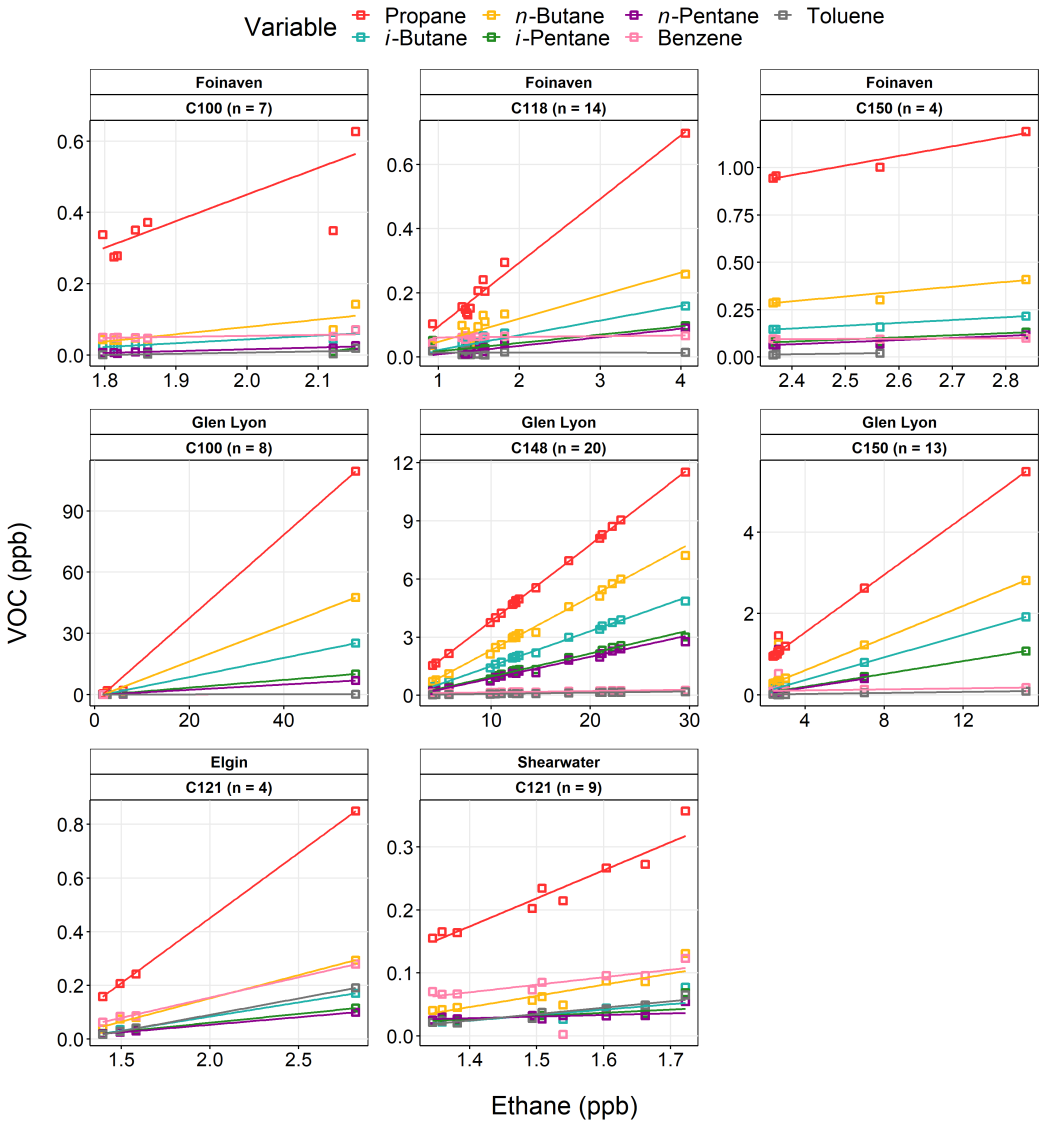

Figure 4.14: *Scatter plot of selected VOCs against ethane from whole air samples obtained in each plume. The solid lines represent the linear fit obtained from robust linear regression.*

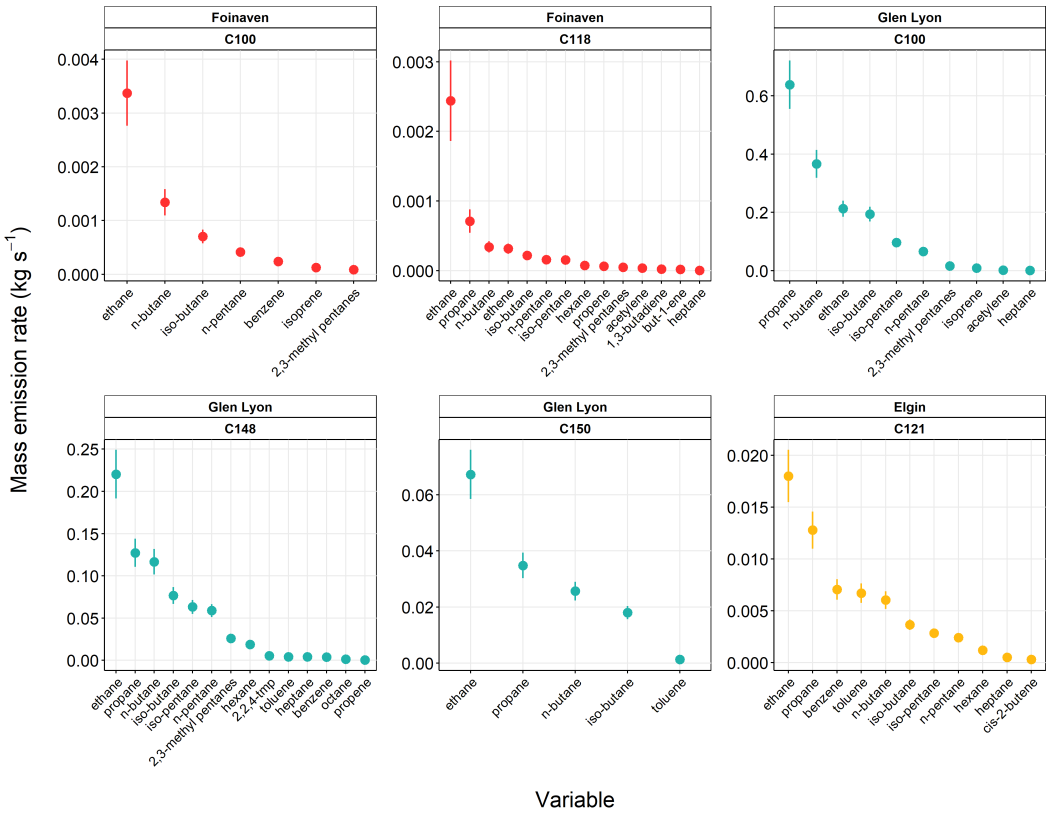

Figure 4.15: *Calculated VOC emission fluxes and uncertainties for individual installations, shown only for compounds with a significant ($p < 0.05$), positive correlation with ethane in the whole air samples.*

values typically less than 0.003 kg s^{-1}, suggesting emissions from this platform are predominantly composed of CH_4. Conversely, VOC emissions rates approximately an order of magnitude higher than those measured from the other platforms, were consistently measured downwind of Glen Lyon, implying a different emission source responsible for enhanced emissions of light alkanes. The large variation in VOC emissions from distinct platforms suggests the composition and magnitude of emissions is unique to each site, which is somewhat expected since the purpose and function of offshore platforms is highly variable.

4.3.4 Comparison to bottom-up estimates

The TD CH_4 and VOC emission rates for each installation were compared to the BU estimated emissions from the facility-level data obtained from OPRED. The BU data was provided in units of tonnes per day, therefore the measurement data was scaled up to daily emission rates to allow a direct comparison. Individual VOC emissions were summed to give a total VOC emission and their uncertainties were combined in quadrature. Figure 4.16 shows the comparison of reported versus measured emissions. Clearly, there are discrepancies and a general lack of linearity between the TD and BU estimations. Generally, the CH_4 emission rate estimates based on the EEMS methodology were lower than the measurements, by a factor of 4.4 on average. The exception to this was Foinaven, where the BU estimations were on average, 5.6 times higher than the measurements. A near-perfect agreement was achieved for emissions from Elgin on flight C121, with a measured value of 8.93$\pm$1.9 tonnes day^{-1} compared to a reported value of 8.81 tonnes day^{-1}. However, in the case of the second estimation for Elgin during flight C147, the measured emissions were higher by a factor of 3.7, whilst the reported estimates were almost identical to those for the day of flight C121, 6-months earlier. This is possible evidence of a missing, intermittent source of CH_4 in the BU estimates. The largest discrepancy between the measured and reported emissions was observed for Glen Lyon, where the measurements were a factor of 8.5 higher on average. However, this average was skewed by the high measured CH_4 emission estimate on flight C148, which was 14 times higher than the bottom up estimate. The large deltas observed for Glen Lyon suggest that there was a significant source of CH_4 not accounted for in the EEMS data.

A similar pattern was also observed in the total VOC estimates, where measured emissions were, on average, a factor of 6.5 lower than the BU estimates for Foinaven and only a factor of 1.5 lower for Elgin. Unfortunately, only a single whole air sample was captured downwind of Elgin during flight C147, meaning emissions of VOCs could not be compared between the two flights. There was an extensive difference between the estimations of total VOCs for Glen Lyon, where the measurements were a factor of 38.5 higher than the BU estimates on average. Again, this was skewed by particularly high measurement estimates during flights C100 and C148, which differed from the BU esti-

mates by more than an order of magnitude.

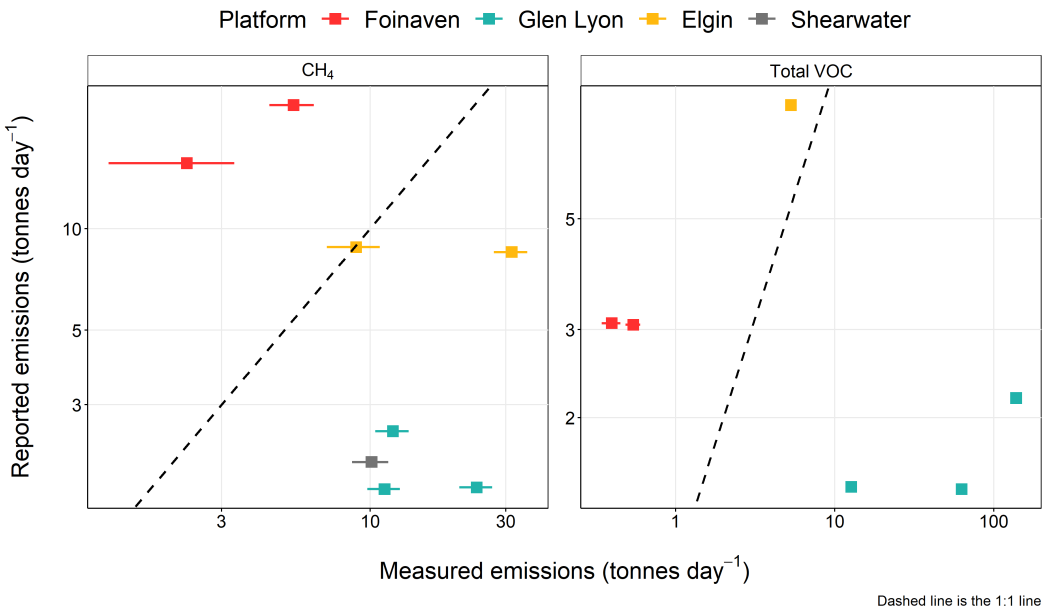

Figure 4.16: *Comparison of reported versus measured emissions of both CH_4 and total VOC for each installation. Note the log scale on both axes. The dashed lines represent the 1:1 line.*

4.3.5 Elgin case study

To investigate the differences in the measured CH_4 emissions from Elgin, the enhancement ratios of $\Delta CH_4/\Delta CO_2$ (ppb ppm^{-1}) and $\Delta C_2H_6/\Delta CH_4$ (ppb ppb^{-1}) were further examined. The ratios were calculated as described in Section 4.3.2. Figure 4.17 shows the calculated enhancement ratios for each plume transect. The mean $\Delta CH_4/\Delta CO_2$ ratio for each flight was 12.2 and 35.4 for C121 and C147 respectively, exposing a clear difference in the composition of emissions on the two flight days. Despite this, the magnitude and relative proportions of reported emissions was almost identical for both flight days. A more detailed breakdown of the total daily reported CH_4 emissions for each flight day is shown in Figure 4.18. The most obvious difference is the reduced amount of combusted and flared CH_4 reported for the day of flight C147, whilst the magnitude of reported venting and fugitive emissions was virtually unchanged. Noticeably, the BU estimates

propose that CH_4 from Elgin is principally emitted from venting, accounting for 96% of the total reported CH_4 on each day.

The lower $\Delta CH_4/\Delta CO_2$ ratio observed on flight C121 signifies that CO_2 was enhanced relative to CH_4, suggesting a larger component of the total CH_4 emissions originated from flaring. The approximate flaring efficiency for each transect was examined by looking at the ΔCO_2 vs (ΔCO_2 + ΔCH_4) regression slope. The maximum slope observed for flight C121 was 22.2% compared to 4.02% during flight C147. It is expected that typical flaring efficiencies for industrial gas flares are greater than 90%.[205] The measured values are much lower than this, since they represent a combination of all emission sources and are therefore biased low by non-combusted CH_4 sources. The higher efficiency for C121 is consistent with a larger component of emissions from flaring as detailed by the reported values. However, this does not account for the difference in the magnitude of emissions between the two flights. The alternative explanation is that the higher $\Delta CH_4/\Delta CO_2$ ratio on flight C147 is due to a significant amount of CH_4 emitted from either venting or fugitive sources, which is not represented in the BU estimates.

No significant difference was observed in terms of the $\Delta C_2H_6/\Delta CH_4$ enhancement ratio, with the average across both flights calculated as 0.07 and 0.09, for C121 and C147 respectively. This suggests the same emission sources were measured on each flight, despite a change in the quantity of CH_4 emitted from each source. Additionally, the observed enhancement ratios agree with the characteristic ratio of 0.09, which was reported in Chapter 3 for condensate fields, suggesting emissions of the raw associated gas were measured here. It is expected that both CH_4 and C_2H_6 are decomposed within gas flares, therefore the ratio of the two species will remain relatively unchanged by a variation in the amount of flaring. Overall, these measurements show that there is potentially a significant source of CH_4 resulting from either venting or fugitive emissions which is not currently fully captured in the BU estimations. Therefore, the current calculation methods may need to be updated to account for this apparent underestimated source and to better represent the day-to-day variability in emissions.

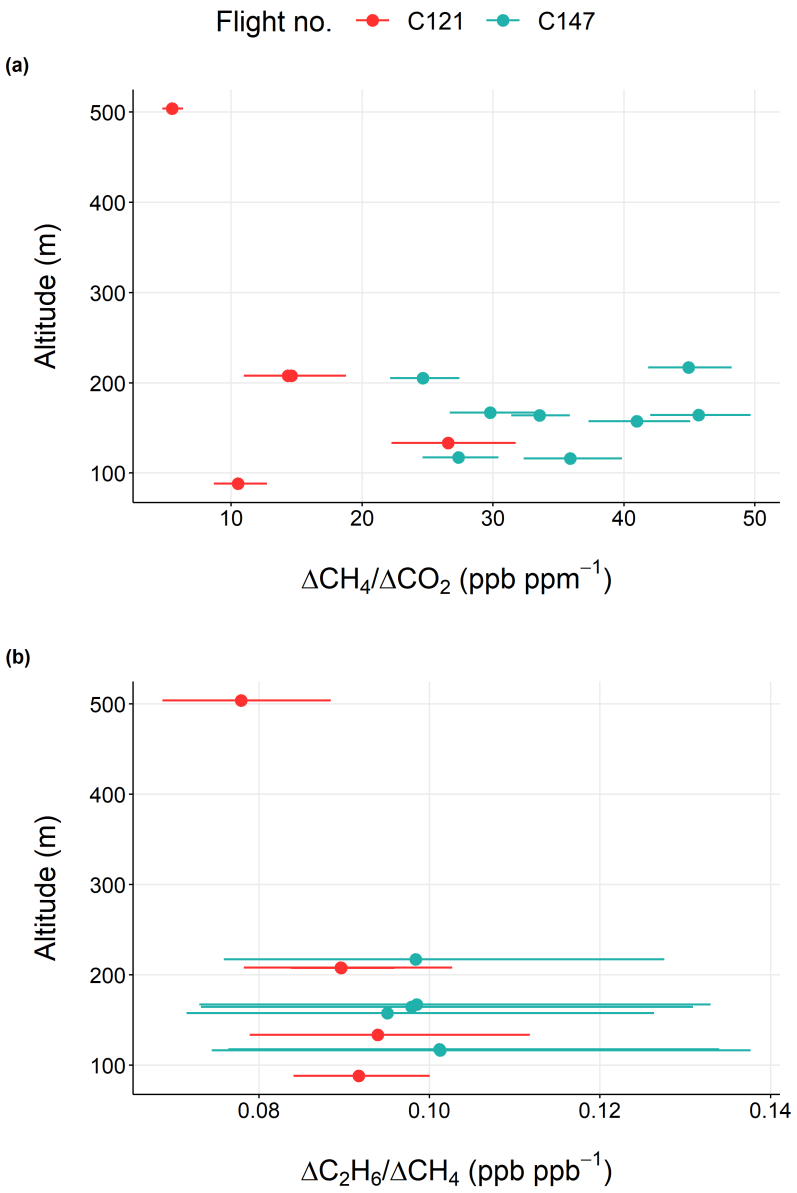

Figure 4.17: *(a) $\Delta CH_4/\Delta CO_2$ and (b) $\Delta C_2H_6/\Delta CH_4$ enhancement ratios measured during each transect of the plume from the Elgin platform for two different flights. Enhancement ratios were calculated through reduced major axis regression and the error bars represent the upper and lower 95% confidence intervals in the slope.*

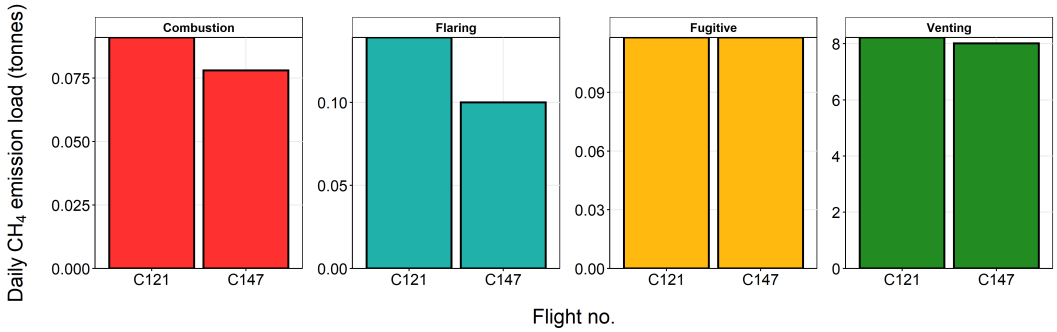

Figure 4.18: *Bottom-up daily CH_4 emission loads from Elgin, split by category. Data was obtained from OPRED as described in Section 4.2.6.*

4.3.6 Glen Lyon case study

Unusually high fluxes of VOCs were observed from Glen Lyon on two out of the three flight occasions (Figure 4.10). One possible hypothesis for this is that significant amounts of hydrocarbons were emitted during oil loading onto shuttle tankers (Section 1.6.1). Glen Lyon is a floating production, storage and offtake vessel (FPSO), which is a ship that also functions as a drilling platform. Oil from all FPSOs is transferred ashore by shuttle tankers as opposed to by pipeline. In the North Sea, approximately 30% of the UK's crude oil production is loaded offshore.[127] Emissions arise due to the displacement of the vapour present in the empty tank. As new cargo is loaded, the vapour is forced out of the tank and vented into the atmosphere. Additional emissions also occur from evaporation of the cargo being loaded.[237]

Of the three emission estimates obtained from Glen Lyon, two coincided with known shuttle tanker operations. During flight C100 on 26th April 2018, export operations to the *Stenna Natalita* were in process throughout the entire duration of the flight. Similarly on flight C148 on 5th March 2019, the *Teekay Amunsden Spirit* visited the installation for oil loading. In contrast, no shuttle tanker operations were active during flight C150 on 7th March 2019. This therefore provides an opportunity to study the impact of oil loading on atmospheric emissions at a facility level.

Figure 4.19 shows the emissions estimates of the 5 most abundant VOCs from Glen Lyon from each flight. The enhancement of VOCs during active shuttle tanker opera-

tions is evident, resulting in total VOC emissions being a factor of 8.4 higher on average. A much smaller difference was seen in the case of CH_4 emissions, where estimates during shuttle tanker loading were only a factor of 1.6 higher on average. This suggests that oil loading results in substantial emissions of VOCs but may not be a significant source of greenhouse gas emissions. The reason for the difference in the magnitude of emissions between flight C100 and C148 is largely unknown. The most likely hypothesis is that a greater quantity of oil was loaded during flight C100, leading to a greater volume of vapour being released as the tank was filled. An estimated 595,000 barrels of oil was loaded on 5th March, however equivalent information was unavailable for 26th April 2018. Alternatively, the stage of the loading process at the time of the measurements could influence the observed emissions. The concentration of the vent gas from loading varies as a function of the amount of liquid loaded into the tank (Figure 1.11). Hydrocarbon-rich gas is emitted towards the end of the process,[127] which may account for the high VOC content measured during flight C100.

Figure 4.19 shows that VOC emissions from Glen Lyon were dominated by light (C_2–C_5) alkanes, which contributed over 90% to the total VOC mass flux in all cases. Emissions of C_6+ alkanes were also enhanced during tanker operations, contributing 8% to the total VOC flux measured on flight C148, compared to $< 1\%$ in the absence of a shuttle tanker. Emissions of heavier species from oil loading are expected as the tank fills due to the non-uniform distribution of vapour inside the tank. The denser vapour remains at the bottom of the tank, whereas the light vapour sits at the top and is therefore vented first during loading. This is followed by the heavier weight species as the tank reaches capacity (Figure 1.11).

The BU estimates of both CH_4 and total VOC emissions from Glen Lyon were significantly lower than the measurements (Figure 4.16). The largest discrepancies occurred in the case of VOC emissions during days with known shuttle tanker operations, where the maximum reported value was 2.19 tonnes day^{-1}, compared to a measured value of 138 ± 9 tonnes day^{-1}. This disconnect potentially exposes a significant underestimation of VOC emissions with regard to oil loading in the current BU inventory. Figure 4.20 displays the reported emissions loads from each source category from Glen Lyon. It should be noted that the venting category is also inclusive of both fugitive emissions and those

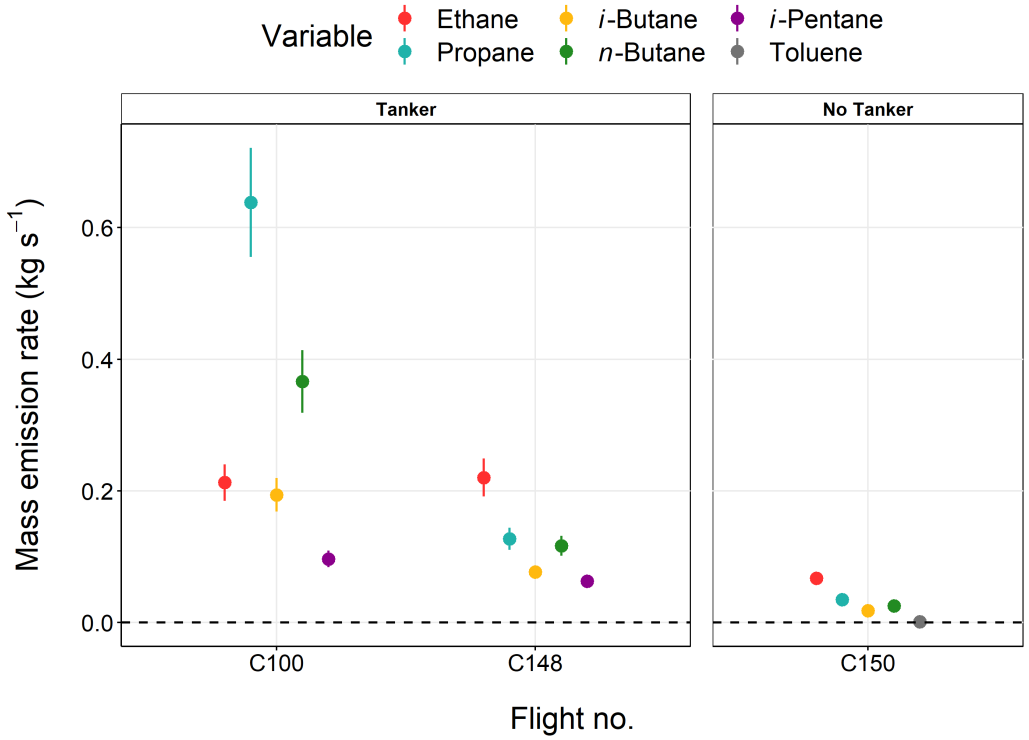

Figure 4.19: *Comparison of emission fluxes for the 5 most abundant VOCs at Glen Lyon on each flight during and in the absence of shuttle tanker operations. The error bars represent the associated uncertainties, described in Section 4.3.3. Note the error bars for flight C150 are present but not visible due to the small uncertainties.*

associated with loading. Typically, the quantity of gas released during cargo tank loading is estimated to be equal to the volume of crude loaded on a daily basis. Figure 4.20 suggests that total VOC emissions on the day of flight C100 (26th April 2018) were the highest, which is consistent with the observations. Elevated emissions of both CH_4 and VOCs relative to the other two flight days were driven by increased flaring emissions such that reported emissions from flaring were a factor of 8 higher for flight C100 compared to the others. Somewhat unexpectedly, reported emissions for the days of C148 and C150 were almost entirely identical, despite the additional occurrence of oil loading during C148, suggesting this source is not currently fully accounted for in the BU reporting.

It is expected that, if the primary change in emissions during flight C100 compared

to the other estimates was exclusively due to a larger component of flaring emissions, the $\Delta C_2H_6/\Delta CH_4$ would remain relatively constant, since both CH_4 and VOCs are broken down in the flare to form CO_2. Similarly, since the quantity of emissions from each source are essentially constant between flights C148 and C150, equivalent characteristic enhancement ratios would also be expected. However, Figure 4.12 shows that the enhancement ratios varied considerably between the three flight days, with C_2H_6 significantly enhanced relative to CH_4 during known shuttle tanker loading events. This observed difference in ratios reinforces the likelihood that oil loading is a significant source of VOCs within the offshore sector, which is currently under-represented in BU estimates.

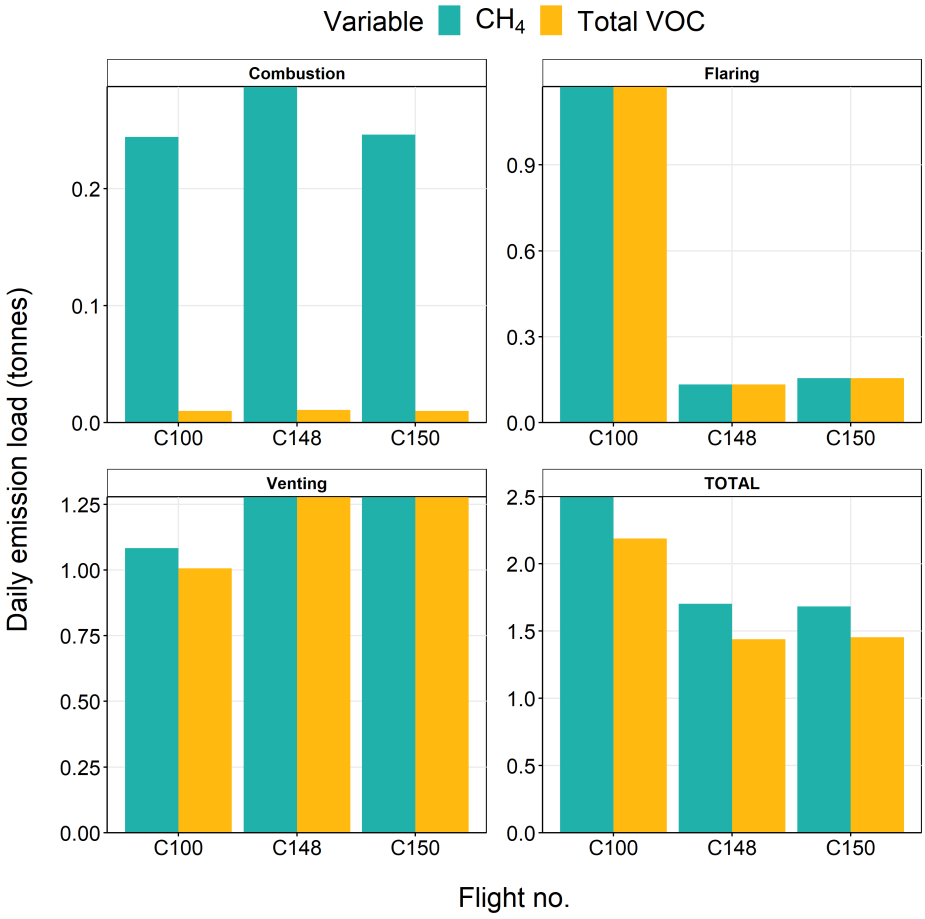

Figure 4.20: *Bottom-up daily CH_4 and total VOC emission loads from Glen Lyon for the day of each mass balance flight, split by category.*

4.3.7 Aggregate emissions

To make an overall assessment of the representativeness of the BU estimates with respect to the measured emission rates, aggregate CH_4 and VOC emission rates were calculated as the arithmetic mean of the individual measured and reported estimates respectively (Figure 4.21). The average measured CH_4 and total VOC flux estimates were 13.1±0.8 tonnes day^{-1} and 32.4±1.4 tonnes day^{-1}, compared to corresponding average reported values of 8.0±3 tonnes day^{-1} and 4.0±1 tonnes day^{-1}. This comparison clearly shows a considerable underestimation in emissions of both species resulting from the BU

calculations. However, the difference is particularly striking in case of VOCs, where the measured and reported values differ by almost an order of magnitude. These underestimations are likely as a result of a combination of inaccurate emission factors and activity data. Figure 4.21 also shows the average estimates when flights coinciding with shuttle tanker operations (C100 and C148) were not included in the aggregations. Interestingly, the reported and measured emissions were found to agree within the associated uncertainties for both CH_4 and total VOC. This suggests that underestimations of both CH_4 and VOCs from oil loading is an important factor for explaining the difference between the TD and BU emission rates. Figure 4.21 indicates that whilst there are some discrepancies between the measured and reported emission rates at a facility-level, on a larger spatial scale, the overall mass of reported emissions may be suitably representative of emissions from North Sea O&G production in the absence of shuttle tanker loading.

Figure 4.21: *Mean measured and reported emission rates of CH_4 and total VOC aggregated across (i) all flights and (ii) flights that did not coincide with active shuttle tanker operations. The error bars on the measurement data were evaluated by propagating the individual flux errors through the mean calculation. For the reported values, the error bars represent one standard error above and below the mean.*

4.4 Conclusions

This work demonstrates the application of a TD methodology through which aircraft measurements can be used to obtain emission rates of CH_4 and speciated VOCs from O&G platforms in the North Sea. Facility-level estimates of CH_4 and total VOC ranged from 2.26±1.1–31.5±4.2 tonnes day^{-1} and 0.40±0.05–138.4±9.0 tonnes day^{-1}, respectively, highlighting a widespread variability in the emission rates from individual platforms. Enhancement ratios of C_2H_6 to CH_4 also displayed both spatial and temporal variability, facilitating the identification of unique emission sources within the offshore sector. Atypically high $\Delta C_2H_6/\Delta CH_4$ ratios indicated the presence of an emission source rich in hydrocarbons relative to CH_4, which was subsequently attributed to the venting of tank vapour during oil loading onto shuttle tankers.

Comparison of the measurement-based emissions to the daily facility-reported estimates revealed a general underestimation in the BU reporting, albeit with the exception of one platform which showed the opposite trend. The most significant disparity was observed for measurement estimates concurrent with shuttle tanker operations, where the measured and reported values of total VOC differed by more than an order of magnitude. The data showed that the overall mass of emissions during oil loading was dominated by light alkanes (C_2-C_5), with a larger contribution from heavy alkanes (C_6+) compared to in the absence of such activities. Whilst the measured emissions of total VOC were a factor of 8 higher during loading, no corresponding increase was accounted for in the BU estimates, suggesting this source is not currently fully accounted for. Through the aggregation of all emissions estimates, the results indicate that the mis-representation of emissions from shuttle tanker loading could be a significant source of underestimation regarding total emissions from North Sea O&G production, displayed in Table 4.4. Furthermore, when omitting measurement estimates obtained during tanker loading from the mean calculation, both emissions of CH_4 and total VOC were in line with the BU estimates. Therefore, this work identifies a key, under-represented source of emissions within the offshore sector.

The findings from this work demonstrate the usefulness of airborne emission estimates in the evaluation and validation of emissions from O&G platforms. To this end

Table 4.4: *Mean measured and mean reported fluxes of CH_4 and total VOC for all flights and for all flights excluding those that coincided with known shuttle tanker operations. The numbers in brackets represent the upper and lower bounds of the uncertainty for the aggregations.*

Variable	**Data**	**Measured flux (tonnes day^{-1})**	**Reported flux (tonnes day^{-1})**
CH_4	All flights	13.1 [12.4, 13.9]	8.02 [5.22, 10.8]
CH_4	Excluding flights coinciding with tanker loading	11.6 [10.7, 12.4]	10.0 [6.61, 13.4]
Total VOC	All flights	32.4 [31.0, 33.8]	3.98 [2.83, 5.12]
Total VOC	Excluding flights coinciding with tanker loading	5.07 [4.81, 5.32]	4.84 [3.4, 6.29]

there is a continued need to assess and improve the accuracy of established BU calculation methods. Future research should focus on the apparent gap between TD and BU VOC emissions estimates, with a particular emphasis on emissions originating from oil loading in order to improve the robustness of the data used as inputs to national emission inventories.

5

Air Quality Impacts of Pre-operational Hydraulic Fracturing Activities

5.1 Introduction

5.1.1 Hydraulic fracturing

Hydraulic fracturing or "fracking" is a term used to describe the industrial process of hydrocarbon extraction from shale rock formations by injecting large quantities of fluid at high pressure down a well, causing the rock to fracture and thus enabling the flow

of trapped gas.[238] The combination of technological breakthroughs, such as horizontal drilling, with fracking has led to a wide-scale uptake of this technique, since it facilitates the extraction of oil and natural gas (O&G) trapped within shale that cannot be exploited through conventional methods.[239] Shale gas has become a key source of natural gas in the United States (US) since 2000, accounting for 75% of total US dry natural gas production in 2019.[240] Subsequently interest has spread to other countries, including Australia, Germany and the UK, as this technique has the potential to transform the energy landscape of a country by providing additional energy security.

Environmental concerns about the impact of fracking have accompanied the increase in popularity. Such concerns are generally centred around sub-surface issues, such as the potential to cause earthquakes[241,242] and the possible contamination of water supplies.[115] Also of particular interest is the impact of fracking on air quality. The predominant component of natural gas is methane (CH_4), a greenhouse gas with a high global warming potential (Section 1.3), meaning it is often the focus for climate mitigation policies surrounding the O&G industry.[243] However, there are also significant emissions of nitrogen oxides (NO_x = NO + NO_2) and non-methane volatile organic compounds (VOCs), resulting from point source, mobile and fugitive emissions.[105] Emissions of NO_x are predominantly linked to the numerous emission sources associated with combustion.[244] These include engines from drilling rigs, compressors, and generators, in addition to heaters and pumps. Acute exposure to NO_2 has been widely linked to adverse health effects such as reduced lung function and increased risk of stroke (Section 1.2).[245] Furthermore, both NO_x and VOCs are recognised as key pollutants in the production of ozone (O_3), a secondary pollutant with adverse health effects (Section 1.5.1). Consequently, elevated levels of O_3 in the atmospheric surface layer have been linked to emissions from regions of O&G production.[62,246]

Often, the focus surrounding emissions relates to sources associated with the drilling of a well and the subsequent extraction of gas, such that previous work conducted in the US identified drilling and flaring to be the most dominant sources of NO_x.[247] However, prior to drilling there is a significant period of preparation, during which the well pad must be built, the rig transported and constructed and material required for fracking must be transferred onto site. This results in a considerable increase in Heavy Duty

vehicle (HDV) traffic, yet the environmental impact of road traffic emissions associated with fracking operations are often noted but rarely studied.[248] Previous modelling work has shown that traffic related to hydraulic fracturing could lead to 18–30% increases in total daily NO_x emissions.[249] Moreover, it is apparent that the enhancement above baseline concentrations is most significant for rural or village locations, in a regime where ozone production efficiency is increased and pollutant concentrations are typically low, but which are likely to be where any future shale gas development occurs within the UK.

5.1.2 UK context

Shale gas extraction in the UK is still currently in the exploratory stages. However, as of November 2019, the UK government announced a moratorium on fracking in England.[250] Prior to this announcement, exploration has taken place at a number of sites in the UK. These include a site in Kirby Misperton (KM), North Yorkshire owned by Third Energy Ltd. and a site in Little Plumpton (LP), Lancashire owned by Cuadrilla Resources Ltd. At KM, there has been extraction from a conventional gas field, named the KM1 well-site, in operation for more than decade. In 2013, an extension to the KM1 well-site was constructed and a new well was drilled, referred to as KM8. In May 2016, approval was initially granted for fracking to be carried out on the pre-existing KM8 well. However, final governmental consent was never received and all fracking-related operations subsequently ceased.[251] Hydraulic fracturing did take place at LP throughout 2018 and 2019, however a number of seismic events led to the suspension of drilling and eventual removal of equipment from the site in September 2019. The impacts of shale gas exploitation in the UK are uncertain, however one modelling study demonstrated that increases of NO_x and VOC emissions associated with hydrocarbon extraction could lead to increases of up to 30 ppb in the monthly mean of daily 1-hour maximum NO_2, resulting in approximately 110 extra premature deaths a year across the UK.[239] It is therefore evident that understanding emissions at the first UK shale gas sites is vital to help inform decision making and future policies should the sector expand.[252]

5.1.3 Baseline measurements

A recurring theme in the uncertainty around emissions associated with fracking is the lack of baseline measurements undertaken prior to shale gas activity.[253–255] Baseline monitoring provides a robust evidence base allowing changes in environmental conditions (deviations from the baseline) resulting from industrial activity to be detected and investigated. On the contrary, it can also be used as a tool to verify the absence of changes related to potential new sources of emissions. Baseline measurements require specific tailoring to the variable(s) of interest. From an air quality perspective, baseline data must be statistically representative of the local atmospheric composition, such that it incorporates the influences of pre-existing local, regional and global pollution sources. The baseline dataset should capture the typical variability in air pollutant concentrations arising from fluctuations in local meteorological variables, such as wind direction, wind speed and air temperature, along with the temporal variation resulting from diurnal and seasonal effects. Due to the strong seasonal dependence of air pollutant concentrations, a baseline data set should extend for a minimum of one full calendar year, however in order to assess long-term trends and annual variability, continued periods of monitoring would be required.

The UK has extensive infrastructure for the monitoring of air quality. The largest network is the Automatic Urban and Rural Network (AURN), which is fundamental for compliance reporting across the UK. The AURN currently has 150 operational sites measuring a range of species, most commonly NO_x, particulate matter (PM) and O_3. Monitoring networks such as this are generally biased towards large urban areas where emissions are dominated by traffic. These locations typically have the poorest air quality and hence are most likely to exceed air quality standards. Rural monitoring is rarely considered a priority for measurements, therefore rural background sites only account for approximately 10% of the total number of sites in the network. Figure 5.1 shows the locations of all current AURN sites in addition to the two exploratory shale gas sites. The North of England is sparsely populated in relation to monitoring, such that both locations selected for hydraulic fracturing are poorly characterised in terms of air quality. A report from the Defra Air Quality Expert Group reinforced this point, stating: *"given none of the ambient monitoring stations in the current national network are well placed for baseline*

monitoring of shale gas activities, additional monitoring will be required".[256]

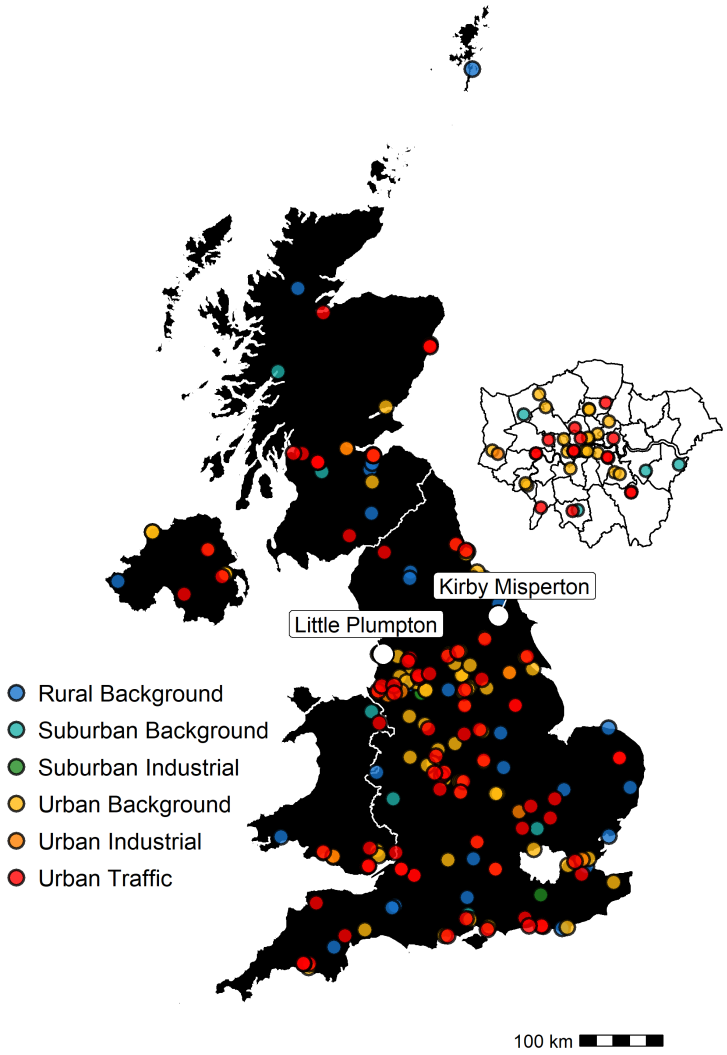

Figure 5.1: *The locations of all AURN sites in the UK and their respective classifications. The white circles show the position of the two exploratory shale gas sites. The cut-out shows all London sites.*

5.1.4 The Environmental Baseline Project

Following the submission of planning applications to conduct hydraulic fracturing for shale gas at KM and LP, an environmental monitoring program was established at both locations in 2016. The project was independent of the O&G industry and UK regulators

in order to ensure evidence-based and objective scientific outputs. Monitoring was initiated for a range of scientific disciplines. These included: assessing ground and surface water, ground motion, studying surface and borehole seismicity, measurement of indoor and outdoor radon, evaluation of soil gas composition and, the focus of this work, greenhouse gas and air quality measurements. As part of the project, two fully functioning air quality monitoring sites were established in January 2016 at KM and LP at the locations displayed by Figure 5.1.

5.1.5 Operational monitoring

Baseline air quality monitoring commenced at KM in January 2016. Following approval of planning permission, hydraulic fracturing was expected to take place during late 2017–early 2018. Throughout September 2017, significant changes in the on-site infrastructure occurred at KM. Machinery required for hydraulic fracturing was brought onto the well pad in preparation for the start of operational activities. Drilling rigs, pumps, compressors, diesel generators and containers holding water, sand and fracking fluid were among the equipment transported onto the site. In addition to the increase in equipment and activity on the site itself, traffic volume due to delivery trucks increased along with additional idling vehicles in close vicinity to the site from protest activities as well as a high volume of policing and media interest. Figure 5.2 shows the extent to which the well pad was filled with new equipment during well pad preparation. As a result the baseline phase of monitoring was terminated since new sources of pollution were introduced directly as a result of shale gas operations. This phase of preparation is defined as the *"pre-operational"* period from here onwards.

Figure 5.3 shows the timeline of monitoring periods defined at KM. Despite preparations for fracking taking place, the site never moved into the operational stage of extraction and subsequently all equipment was removed from the site by February 2018. Since all activity related to fracking had ceased, monitoring at KM transitioned into a second baseline phase. The isolated nature of the pre-operational period at KM presents a unique opportunity to assess a relatively understudied stage of the well pad life-cycle. The lifetime of a typical fracking well after the completion of drilling is around 3–5 days before all the gas is extracted. This is short in comparison to the length of the prepara-

Figure 5.2: *Aerial images of the Third Energy well site in April 2018 once fracking activities were halted (left) and December 2017, showing the extra equipment brought onto the site during the pre-operational period (right).*

tion period, which takes place over a number of weeks. Therefore, well pad preparation would be a key aspect of O&G development in the UK should the shale gas sector grow. As a result, pre-operational emissions would be expected to occur for a significant proportion of the entire fracking process. Any incremental changes in air pollutant emissions during this period will contribute to the cumulative effect of emissions throughout the entirety of the fracking process and are therefore important to consider.

5.1.6 Objectives

It is widely recognised that there is a need for robust environmental baseline monitoring procedures ahead of any O&G developments. This work aims to demonstrate the implementation and application of baseline monitoring from an air quality perspective. More specifically, this work will *(i)* outline the key requirements in baseline monitoring design, *(ii)* present an overview of the air quality climatology at a rural site in the UK, *(iii)* utilise baseline data to characterise the typical variability in pollutant mixing ratios, and *(iv)* apply statistical predictive models to baseline observations to provide a quantitative reference for the impact of pre-operational hydraulic fracturing activities on local air quality.

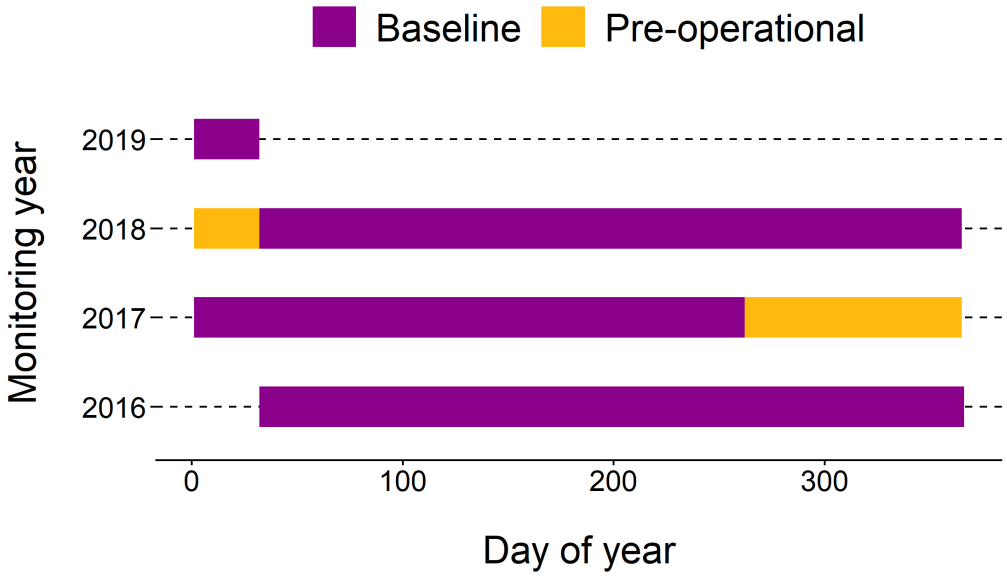

Figure 5.3: *Timeline of monitoring periods at KM.*

5.2 Methods

5.2.1 Site location

The purpose of a baseline monitoring station is to facilitate the characterisation of the air quality within the local environment. Therefore, the monitoring station should be sited to enable sampling of local and regional sources of emissions over a wide range of meteorological conditions. With this in mind, the monitoring station at KM was installed along the east wall of the Third Energy well site, approximately 45 m from the KM8 well head, shown in Figure 5.4. The enclosure was positioned as to be predominantly downwind of any future shale gas extraction infrastructure, whilst being open and unobstructed in all wind directions. The close proximity of the monitoring station to the well head provided a high sensitivity of observations to operational activity. Instrumentation was housed in a mains-powered, air-conditioned, weather-proof enclosure. Ambient air was sampled from gas phase inlets which were fixed to the top of the monitoring station at a height of 3 m. Following the installation of a noise reduction barrier around the whole perimeter

of the site, which prevented the free movement of air from westerly wind directions, these were later extended to a height of 9 m.

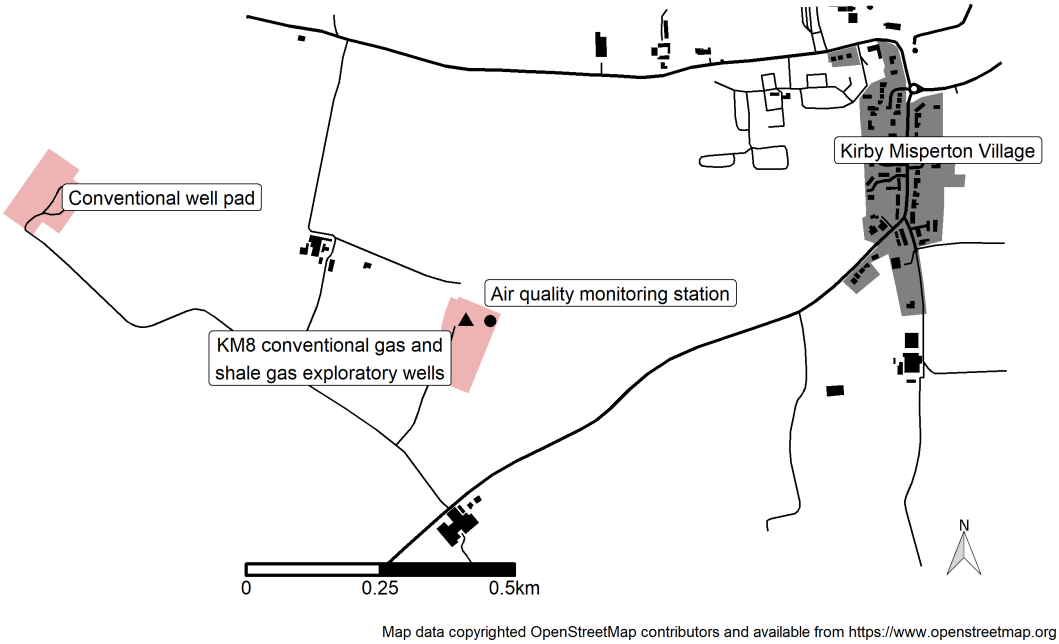

Figure 5.4: *Locations of the baseline monitoring station (circle) and the KM8 well (triangle). Lines identify major and minor roads in the area. Grey shading shows residential areas and the pink shading shows well pads operated by Third Energy.*

5.2.2 Instrumentation

The monitoring station was equipped with a full suite of air quality instrumentation, allowing the measurement of numerous air pollutants along with meteorological variables. A summary of the instrumentation is shown in Table 5.1. Data for NO_x and O_3 are predominantly discussed in this chapter, however all the available measurements are displayed in Table 5.1 for completeness. The PM inlet was fixed at 3 m throughout the entire measurement period since this was a calibrated and heated inlet line unable to be extended. Consequently, between September 2017–April 2018, PM observations were affected and invalidated as a result of some wind recirculation and pooling at very low wind speeds.

Table 5.1: *Instrumentation details for the air quality monitoring station at KM.*

Species	**Instrument**	**Measurement technique**	**Frequency**	**Precision**
Air temperature, air pressure, relative humidity (RH)	Luft WS500-UMB compact weather station	Temp: PT100 measuring element, Pressure: resonant pressure transducer, RH: heated capacitive sensor element	1 min	Temp = $\pm$0.1 °C, Pressure = $\pm$ 0.1 hPa, RH = $\pm$ 2%
Wind speed, wind direction	Gill 2D WindSonic	Anemometer	1 sec	Speed = $\pm$ 2% at 12 m s^{-1} , Direction = $\pm$ 2° at 12 m s^{-1}
NO, NO_2	Teledyne T200UP	Chemilumines-cence with photolytic converter	1 min	NO = 0.65 ppb, NO_2 = 0.75 ppb
O_3	ThermoFisher Model 49i Ozone Analyser	UV absorption	1 min	0.74 ppb
Particulate matter (PM)	Fidas 200	Optical light scattering	1 min	$PM_{2.5}$ = 0.44 μg m^{-3}, PM_{10} = 0.64 μg m^{-3}
H_2S, SO_2	ThermoFisher Model 250	UV fluorescence	1 min	H_2S = 1.0 ppb, SO_2 = 1.4 ppb
CH_4, CO_2	Los Gatos Research Ultraportable Greenhouse Gas Analyzer	Off-Axis Integrated Cavity Output Spectroscopy	1 sec	$CH_4 < 2$ ppb, $CO_2 <$ 300 ppb
NMHCs (C_2–C_8)	SilcoCan air sampling canister (3 L) followed by GC-FID analysis for C_2–C_8 NMHC	Offline GC-FID	Weekly	<10% uncertainty for all NMHC

5.2.2.1 Calibration and quality assurance

Quality assurance (QA) and quality control (QC) procedures were routinely performed for all aspects of data acquisition, including; equipment evaluation, site operation and maintenance and data review. Calibrations of air quality instrumentation were conducted on a monthly basis throughout the entirety of the measurement period. All gas-phase instrument calibrations were traceable through a chain to international reference standards to maintain a high accuracy and provide known uncertainties in the recorded data. This also ensures comparability with similarly calibrated instrumentation, such as those as part of the AURN. Calibration details of key instrumentation are briefly described below and in more detail within Chapter 2.

On-site span and zero point calibrations were performed monthly for the NO_x analyser. The span calibration was conducted using a 100 ppb NO standard in N_2, linked to a National Physical Laboratory (NPL) binary standard and is also referenced to the Global Atmospheric Watch (GAW) scale. Zero calibrations were performed using an air scrubber filled with Sofnofil followed by activated charcoal. The NO_2 conversion efficiency was calculated on an annual basis by returning the instrument to the laboratory to carry out a gas phase titration with known quantities of O_3.

The O_3 instrument provides an absolute measurement but was verified annually off-site using a Model 49i-PS Primary Standard over the calibration range 0–500 ppb. The primary standard was itself checked annually against a certified source by NPL. Zero calibration took place monthly using air filtered through an activated charcoal trap.

Calibration of the greenhouse gas instrument was performed using gas standards containing known mixing ratios traceable to the World Meteorological Organisation gas scales for CO_2 (X2007) and CH_4 (X2004A). These calibrations involved sequentially sampling two concentration standards: first a low concentration ($\sim$400 ppm CO_2, $\sim$2ppm CH_4) followed by a high concentration ($\sim$600 ppm CO_2, $\sim$5 ppm CH_4), enabling the determination of the slope and offset of the instrument response. Further detail is described elsewhere.[120]

5.2.3 Data

Long-term, continuous monitoring was conducted at KM throughout 2016–2019. Data was hourly aggregated for use in this analysis. Data capture rates throughout the entire monitoring period are displayed in Table 5.2. Data capture rates above 90% are desirable to obtain meaningful long-term measurements, which was achieved for the majority of variables. In all but one case, data capture rates were above 75%, which is often a threshold below which data should be treated with caution.[257] The exception to this was H_2S, which can be explained by the deferred installation of the instrument in February 2018. Additionally, the O_3 instrument was removed for maintenance during summer 2017, resulting in a slightly lower data capture rate across the entire measurement period.

Table 5.2: *Data capture rates for measured variables at KM.*

Variable	Data capture (%)
CH_4	97.4
CO_2	97.9
H_2S	28.2
NO	91.7
NO_2	92.5
NO_x	92.5
O_3	86.7
PM_1	89.4
$PM_{2.5}$	89.4
PM_4	89.4
PM_{10}	89.4
Air pressure	99.8
Air temperature	99.8
Wind direction	96.5
Wind speed	98.2

The calendar year of 2016 commenced prior to the start of monitoring, therefore in order to fairly compare seasonal and annual trends from one year to the next, three year-long monitoring periods were defined running from February–February, shown in Table 5.3.

Table 5.3: *Year-long monitoring periods defined at KM.*

Monitoring year	Start	End
Year 1	2016-02-01	2017-01-31
Year 2	2017-02-01	2018-01-31
Year 3	2018-02-01	2019-01-31

5.2.4 Modelling

5.2.4.1 The random forest algorithm

When considering changes in ambient air pollution, it is often difficult to disaggregate changes in mixing ratios due to meteorology or a change in emission source strength. Baseline data can be exploited to identify events that deviate from the "normal",[120] however the influence of meteorology often adds complications, making the quantification of such events challenging. Controlling for meteorological variability allows deviation events to be more robustly assessed. This is achieved by training a statistical model where a range of explanatory variables can be used to account for some of the variability in pollutant mixing ratios.

The technique used here applies random forest (RF), an ensemble decision tree machine learning method, as the modelling algorithm. Classical decision tree models have a tendency to overfit, meaning the model represents the training set well but fails to generalise, resulting in high variance and consequently poor predictions on unseen data.[258] To reduce the risk of overfitting, RF uses bootstrap aggregation, or "bagging".[259] The concept of bagging is to reduce the variance of the predictions of one model, by fitting several models and averaging over their predictions to produce an overall prediction.[258] In brief, each tree in the forest is grown by sampling random observations along with the independent variables with replacement, known as bootstrapping. For each tree in the forest there are a set of observations that do not participate in the trees growth, referred to as “out-of-bag” (OOB) data. RF models typically contain numerous trees and therefore the forest contains many decorrelated trees which have been trained on different subsets of the training set.[55] Each tree is used to make a prediction, which are then aggregated (in regression applications the mean is used) to form a single prediction.

The OOB data is then used to validate the RF model by predicting each observation, x, using only the trees that did not have x in their bootstrap sample. This allows an unbiased estimate of the error to be computed internally, since for each tree there is essentially a "testing" set of data not used in the construction of that particular tree.

RF models have been widely used elsewhere to control for the effects of weather in air quality datasets, predominantly in the application of a "meteorological normalisation" technique.[55,260–262] In this method, predictions are made by repeatedly sampling and predicting using RF models. For every prediction, the explanatory variables are sampled without replacement and randomly allocated to a dependent variable observation. The predictions are then aggregated using the mean to give a value representative of "average" meteorological conditions.[55]

The method here is somewhat different since the models are used to predict mixing ratios during the pre-operational period, assuming a business as usual (BAU) scenario. This is essentially an intervention study, similar to other work quantifying the effect of an airport closure[263] and more recently the effect of the COVID-19 lockdown on air quality.[264–266] The BAU scenario assumes pre-operational activities did not occur at the site and therefore baseline conditions were uninterrupted and continuous. The BAU scenario is then compared with observations to quantify the effect of the pre-operational period on air quality at KM.

5.2.4.2 Model construction

RF models were developed for NO, NO_2, NO_x and O_3 using the **rmweather** R package.[55,267] Models were trained using baseline data as shown in Figure 5.3, since the pre-operational period was an isolated period of activity on site. Of this training set, 80% of the input data was used for model training whilst the remaining 20% was used for model validation. The performance of such models was assessed before they were used to predict pollutant mixing ratios using local meteorological variables as the model input. The model parameters were set as follows: the number of trees was fixed at 300, the minimum node size was set to 5 and the number of independent variables randomly sampled at each split was 3 (the square route of the number of independent variables). The explanatory variables used for prediction were: Unix date (number of seconds since 1970-01-01) as the

trend term, Julian day as the seasonal term, weekday, hour of day, air temperature, atmospheric pressure, wind direction and wind speed. For the input meteorological variables, missing data was replaced with the median. An additional variable, "section", was introduced which acted as an identifier for data "before", "during" and "after" the pre-operational period. This variable essentially helps account for the fact that the baseline characteristics after the pre-operational period may not be identical to those before. For example, additional security remained on site after pre-operational activities ceased. Therefore this variable provides the models with a way of distinguishing between the two sections of data.

5.3 Results and discussion

5.3.1 Meteorological baseline

Meteorological conditions play a key role in the day-to-day variations in pollutant mixing ratios. In particular, local wind speed and direction are the most important metrological variables in terms of baseline characterisation and pollution source attribution. They indicate the local air mass history and can provide insight into what sources of pollution the sampled airmass has passed over upwind of the monitoring site. Localised, nearby emission sources can be identified using the correlation between instantaneous wind speed and direction with pollutant enhancements above background, whereas long-range sources can be identified by studying the origin and trajectory of the sampled air mass in the days prior to sampling. Figure 5.5 shows conventional wind roses for each year long monitoring period at KM. Years 1 and 2 showed similar patterns in wind direction with the dominant directions being from the south west quadrant, reflecting the prevailing wind direction in the UK, where winds arrive after crossing the Atlantic. South westerly winds occurred 28.6% and 33.3% of the time in years 1 and 2 respectively. This direction is also associated with the strongest winds which generally occur in the winter months with wind speeds reaching up to 12 m s^{-1} in stormy conditions. Mean wind speeds were between 1.7–1.8 m s^{-1} in years 1 and 2 and slightly lower in year 3 (1.3 m s^{-1}). Year 3 showed a different wind climatology to the previous two years, with a much stronger north-westerly component, particularly prevalent in the winter

months. These winds dominated 18.6% of the time, whereas south westerly winds were much less frequent in comparison with the other years, occurring only 18.9% of the time. This effect is likely due to a change in the on-site infrastructure at KM resulting in the "blocking" of other wind directions rather than a real change in local meteorology. This is supported by the fact that this effect is not seen at the nearest AURN site, High Muffles, where south westerly winds are consistently dominant throughout 2016–2019. Influences of surrounding infrastructure on wind direction cannot be corrected for, however this impact will be considered when interpreting air composition data during year 3.

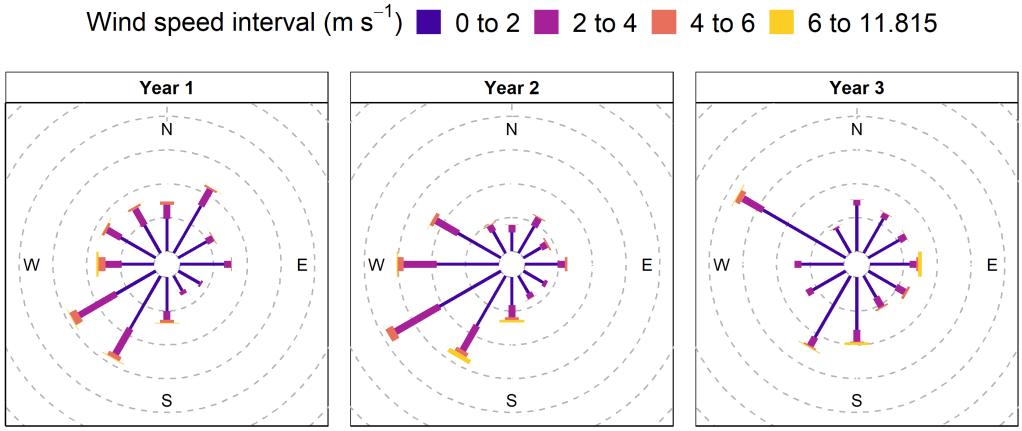

Figure 5.5: *Windrose for KM, showing hourly averaged wind speed and direction statistics for each year of monitoring. The radial axis defines the percentage of time in each 30 ° wind direction bin (increasing at 5% intervals from an inner ring of 5%) and the colour defines the wind speed.*

5.3.2 Overview of air pollutants

Figure 5.6 shows the hourly averaged time series of greenhouse gases and air pollutants measured at KM. Baseline mixing ratios of greenhouse gases, CO_2 and CH_4, can be seen to fluctuate around 400–420 ppm and 1.9–2 ppm respectively, which are typically representative of the Northern hemispheric average for these pollutants.[268,269] There is a strong annual fluctuation in background CO_2 mixing ratios primarily due to the seasonal

uptake by plants and the ocean, which is largest in the northern hemisphere where the majority of vegetation exists. In addition, the boundary layer depth is typically deeper in the summer months leading to the dilution of pollutant mixing ratios. The combination of these two processes results in high background mixing ratios of CO_2 in the winter months and a lower, depleted background in the summer months. The variation in CH_4 mixing ratios is also dominated by regional fluctuations in background mixing ratios throughout the year. The background is lowest in the summer due to destruction by the OH radical as well as increases in the boundary layer depth. Within the seasonal fluctuations are significant enhancements above the average background mixing ratios. The largest spikes in both CO_2 and CH_4 typically correspond with light winds from the north, east or south-east and are likely as a result of localised farming, agricultural or road emissions which are more prevalent in the summer months.

Mixing ratios of NO_x, PM and O_3 are more readily driven by regional or local meteorology and emissions rather than seasonal hemispheric cycles as for the greenhouse gases. Specifically, NO_2 mixing ratios are mostly affected by local emissions, since it is readily photolysed in the day-time, meaning it has a short atmospheric lifetime of only a few hours, preventing long range transport. On the other hand, O_3 is much more likely to be affected by regional contributions since it is formed from chemical reactions as a plume is transported downwind of its source. Similarly, PM has a longer lifetime, which is typically determined by precipitation. Pollutant mixing ratios are dependent on a combination of emissions, transport, chemical transformations and vertical mixing within the boundary layer.

Figure 5.7 shows the diurnal, hebdomadal and seasonal variation of NO, NO_2, O_3, $PM_{2.5}$ and PM_{10} at KM for each year long monitoring period. NO, NO_2 and O_3 showed clear hour-of-day variability. Emissions of NO_x in the UK are primarily from road transport, contributing 31% to total emissions in 2018.[138] Mixing ratios of NO began to increase from 06:00 onwards, before peaking at 10:00 in years 1 and 3 and slightly earlier at 08:00 in year 2. Mixing ratios remained enhanced throughout the day but began to decrease from 12:00 onwards before reaching a minimum at around 18:00. In contrast, NO_2 mixing ratios peaked at 20:00 during all years, a few hours after typical rush hour traffic peaks. This is suggestive of an aged air mass reaching the monitoring site, where

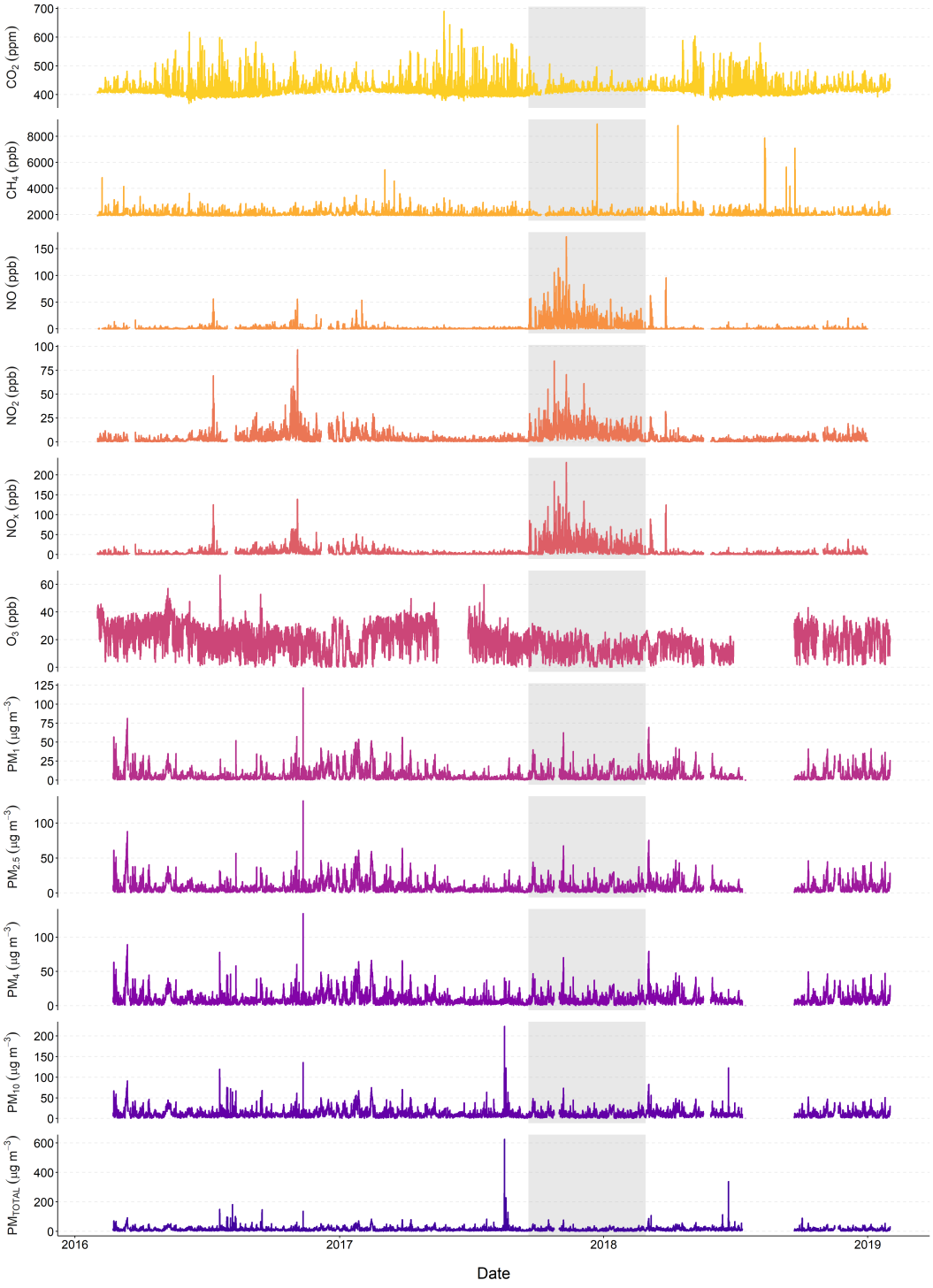

Figure 5.6: *Hourly averaged time series of key pollutants measured at KM. The grey shaded area highlights the pre-operational period.*

fresh NO emissions are photochemically processed during transport from the source to form NO_2 (Section 1.5). This source is likely to be the A196, which is a major road that lies approximately 3 km to the east of site. A more distinctive diurnal cycle for NO was observed in year 2, compared to years 1 and 3. Mixing ratios of NO during year 2 were approximately 3-times higher than years 1 and 3, with clear peaks at 08:00 and 15:00. This is suggestive of an emission source of NO in close proximity to the monitoring site where processing to NO_2 via reaction with O_3 has yet to occur.

O_3 is a secondary pollutant formed through photochemical reactions of primary emissions (Section 1.5.1). The diurnal cycle is strongly linked to solar irradiance and hence mixing ratios began to increase around 06:00 as the sun rises, facilitating photolysis. Mixing ratios peaked at 12:00 when solar irradiance is the strongest before decreasing throughout the afternoon. All three monitoring years showed a consistent cycle. In contrast, the diurnal cycle for $PM_{2.5}$ and PM_{10} is limited in scale, with concentrations varying by less than 2 μg m^{-3} within each year. The lowest concentrations occurred during the afternoon between 12:00 and 14:00 and peaks in both $PM_{2.5}$ and PM_{10} occurred in the morning at approximately 08:00 and in the evening around 20:00. Variation on an inter-annual basis was also small with largely overlapping confidence intervals for years 1 and 3. The diurnal cycle for year 2 had the lowest concentrations compared to the previous and subsequent years, however this could be a misleading observation as a result of the obstructed inlet previously discussed.

The hebdomadal variation of NO and NO_2 followed what is expected from traffic-related emissions. Mixing ratios were consistent throughout the week, with small peaks on Tuesday and Friday, before declining throughout the weekend when traffic flow is typically reduced. O_3 showed the opposite trend to NO_x, with mixing ratios increasing throughout Saturday and peaking on Sunday. The mirror-image of NO_x and O_3 can be explained due to their chemical coupling within the atmosphere. The reduction of NO_x emissions and mixing ratios during the weekend drove decreased O_3 destruction via the NO titration cycle, hence leading to enhanced O_3 (Section 1.5). PM showed consistent trends throughout years 1 and 3, with some mid-week variation and a decline over the weekend, perhaps as industrial sources are reduced. During year 2, PM increased throughout Monday to Wednesday before reaching a minimum on Thursdays and in-

creasing again through the weekend. PM levels are significantly affected by wood stoves and garden fires, which are typically more prevalent in rural environments and are therefore likely to have a notable source contribution at KM. Additionally, changes in the hebdomadal trend for PM are likely to be strongly influenced by local driving patterns. However, data regarding traffic flow is not available so no further speculation is made.

The seasonal cycle of NO and NO_2 in Figure 5.7 shows mixing ratios peaking in winter when temperatures are the lowest and vertical mixing is the weakest. The NO and NO_2 lifetimes are also prolonged in the winter due to reduced solar irradiance and less available OH. In addition, on-road NO_x emissions are subject to a strong temperature dependence whereby emissions increase as ambient temperature decreases, thereby exaggerating the winter enhancements.[260] O_3 mixing ratios followed a similar seasonal cycle during years 1 and 2, with mixing ratios increasing during spring before peaking during the summer and declining into the winter. Year 3 shows the opposite with mixing ratios decreasing during the summer, however data during July, August and September of 2018 is missing due to instrument maintenance which is likely the cause for this differing trend. Seasonal patterns in $PM_{2.5}$ and PM_{10} were similar for all years where concentrations followed a steadily declining trend from January through to a minimum in June/July, before rising again into November/December. This is typical of PM trends at urban background sites in the UK.[270] The patterns observed can be explained by greater emissions of both primary PM and secondary PM precursors during the winter as a result of increasing domestic heating demand as well as the reduced dispersion of local sources during winter.

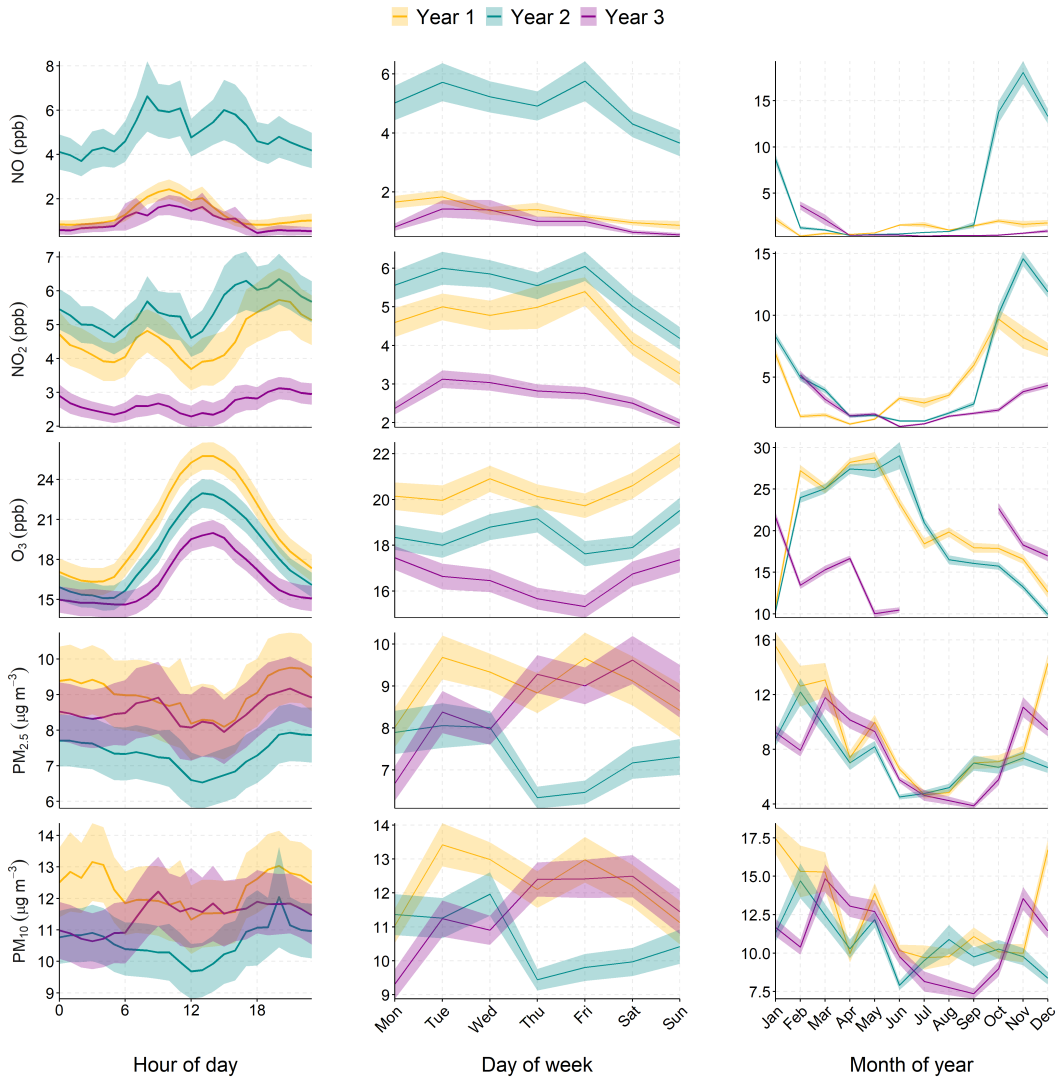

Figure 5.7: *Diurnal, hebdomadal and seasonal variation of NO, NO_2, O_3, $PM_{2.5}$ and PM_{10} at KM throughout each full year of monitoring. Shaded areas represent the upper and lower 95% confidence intervals.*

5.3.2.1 Annual variation in pollutants

Figure 5.8 shows the annual means for selected pollutants at KM along with the limit values outlined in the Ambient Air Quality Directive. Note that the data was converted into a concentration in μg m^{-3} for comparison. Due to the removal of the O_3 instrument in the summer of year 3, O_3 data from July, August and September was omitted for all

years to facilitate a more robust comparison. The standards require that the annual mean concentration of NO_2 must not exceed 40 μg m^{-3} and that there should be no more than 18 exceedances of the hourly mean limit value (200 μg m^{-3}) in a single year. For O_3, there is no annual limit, instead exceedances are assessed against an 8-hour mean, where concentrations must not exceed 100 μg m^{-3} more than 10 times in a single year. In the case of PM, the annual mean limit values are stated as 25 μg m^{-3} and 40 μg m^{-3} for $PM_{2.5}$ and PM_{10}, respectively. Figure 5.8 shows that there were no measured exceedances of the annual mean limit values, nor did concentrations come close to approaching the 75% thresholds, which is perhaps to be expected in a rural location such as KM. However, in 2016, O_3 exceeded the 8-hourly limit on three occasions: 8th May, 19th July and 13th September. These dates were all associated with UK-wide air pollution episodes induced by a combination of prolonged sunshine, high ambient temperatures and the transportation of continental emissions.[270]

Despite the uncommonness of exceedances, there were some significant differences in the observed annual means. The most obvious was the rise in NO during year 2. The annual mean increased 4-fold from 1.77 μg m^{-3} in year 1 to 6.63 μg m^{-3} in year 2, before decreasing to 1.31 μg m^{-3} in year 3. Annual NO_2 also increased by 19% from year 1 to year 2 from 9.40 μg m^{-3} to 11.2 μg m^{-3}. Annual NO_2 was lowest in year 3 (5.45 μg m^{-3}), which possibly arises partly due to the decreasing trend of rural NO_2 across the UK by approximately 3.41% yr^{-1}.[271] Annual mean O_3 showed a consistent decrease from years 1 to 3. During year 2 this could be as a result of direct titration due to the enhanced NO (Section 1.5). The reason for the decline in year 3 is less clear, but is likely as a result of the low mixing ratios measured during February, March and April in year 3 compared to the previous two years (Figure 5.7). Annual mean $PM_{2.5}$ and PM_{10} concentrations were 18% and 14% lower respectively in year 2 than year 1, before rebounding in year 3. Trends in PM are not discussed further in this context due to the obstruction of the gas phase inlet leading to the poor circulation of air.

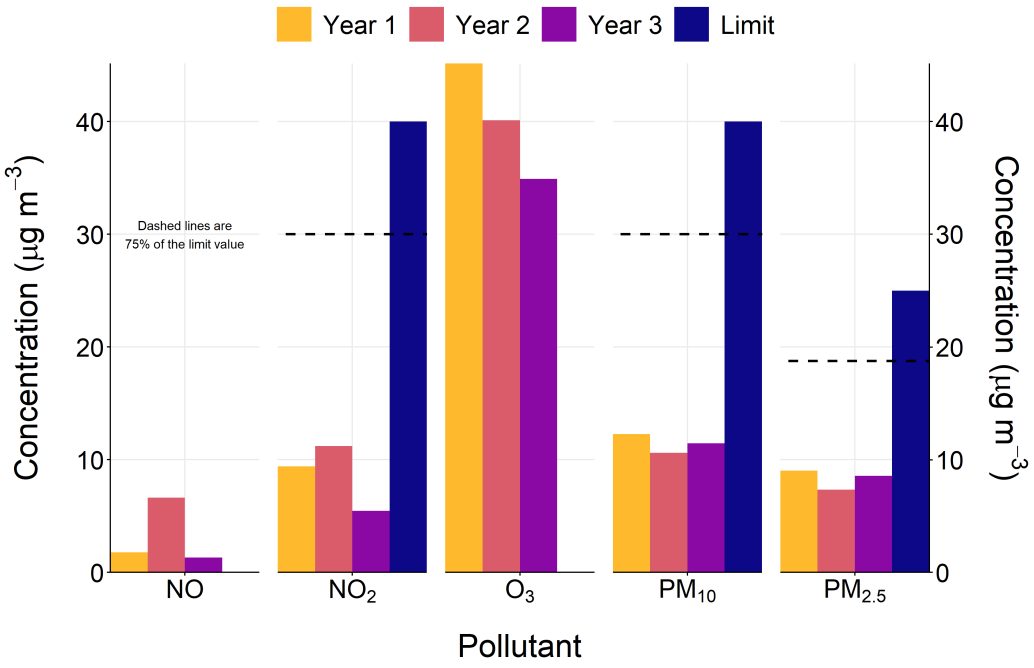

Figure 5.8: *Mean annual concentrations of key pollutants at KM compared with the EU Directive limit values. The dotted line shows the 75% thresholds for air quality limits, which is typically used as a marker for where air quality issues would need to be taken into account from a policy perspective.*

5.3.2.2 Emission source identification

A common method for source characterisation is the use of bivariate polar plots.[272,273] In their simplest form these plots show the dependence of pollutant mixing ratios on local wind speed and direction in polar coordinates.[274] Generally these plots can provide insight into local scale emission sources rather than long range transport. Wind speed in these plots can be considered as a proxy for distance since higher wind speeds result in the transport of pollutants from further afield. Figure 5.9 shows polar plots for NO, NO_2 and O_3 at KM. First considering NO, the highest mixing ratios occurred under very low wind speed conditions from the west, indicating a local source. This corresponds to the direction where the KM8 well lies so is likely from vehicle exhausts and generators located on the well pad itself. There are also areas of enhanced concentration under moderate wind speeds (around 4 m s^{-1}) to the west and south-west, corresponding to

the pre-existing conventional gas well located on the lower well pad. Observations of NO_2 had a much broader footprint compared to NO. The largest enhancements were observed from the south across the full range of wind speed values. To the south lies Habton Road, where multiple farms are located. Vehicular emissions from both cars and farming machinery in the form of NO are likely oxidised by O_3 during transport, where they are subsequently measured as NO_2 at the monitoring station. Finally, in the case of O_3, the highest mixing ratios occurred under strong wind speeds (8–10 m s^{-1}) from the west, indicating that O_3 was formed as it was transported to the site from primary emissions further afield. O_3 mixing ratios were lowest close to the site (lowest wind speeds) and to the south, essentially the inverse of the NO_2 observations, indicating O_3 titration from local traffic emissions (Section 1.5).

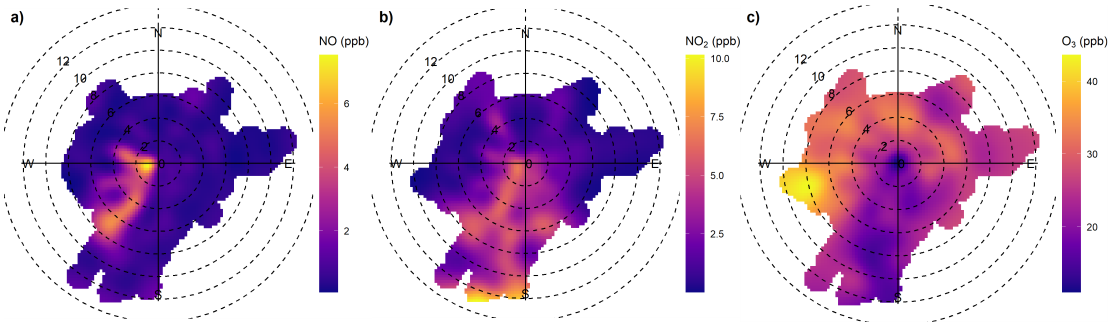

Figure 5.9: *Polar plots of (a) NO, (b) NO_2 and (c) O_3 throughout the entire measurement period at KM.*

5.3.3 The effect of pre-operational activities

The benefit of a baseline data set is that it can be used to investigate changes in air quality as a result of specific events or interventions by comparing measurements to what is considered "normal" for that particular location. The increases in NO_x, particularly NO, during year 2 were further explored using seasonal polar plots. Figure 5.10 shows a seasonal polar plot of NO at KM between 2016–2019. The most obvious feature is enhanced mixing ratios of NO during the autumn of 2017, present throughout winter 2017 and through into the beginning of 2018. More specifically, this plot indicates a source of NO present under light wind speeds (2–5 m s^{-1}) to the west. NO is a short lived pollutant since it is rapidly oxidised during the day by O_3 to form NO_2, therefore any primary

sources are expected to lie in close proximity to the monitoring station and hence are most observable in stable atmospheric conditions that exist during slack winds. This elevated autumn NO coincides with the "pre-operational period" where equipment for hydraulic fracturing was moved onto site. Other than the well pad itself, there is no other infrastructure that lies to the west of the monitoring station within the expected NO footprint (typically a few 100 m, based on a short lifetime of 2 minutes[275] and average wind speeds of 2–4 m s^{-1}). Therefore, this is highly suggestive that the additional source of NO is a consequence of fracking-related activities.

The impact of the pre-operational period on NO_x mixing ratios was further investigated by studying the variation in pollutant mixing ratios by each hour of the day. Figure 5.11 shows the average diurnal mixing ratios of NO, NO_2 and NO_x throughout the baseline and pre-operational periods. The baseline data for each year was filtered to the equivalent of the pre-operational period (19th September–1st February) in order to prevent bias due to the seasonal variation of NO_x mixing ratios. Additionally, the observations were filtered to wind directions which favoured transport from the well-pad (contained a westerly component). During the pre-operational period, the range over the day was 3-times greater for both NO and NO_x compared to the baseline phase. This is primarily due to high daytime mixing ratios of NO, leading to an amplified diurnal cycle throughout the pre-operational period. The largest change was observed for early evening NO, where the average NO concentration at 17:00 increased by 3797% from 0.418 ppb in the baseline period to 16.3 ppb during the pre-operational period. This is comparable to the morning rush hour peak in NO (approximately 15 ppb) observed in North Kensington, an urban background site, during the ClearFlo campaign in London.[276] During the pre-operational phase, peak mixing ratios of NO_x occurred at 08:00 and 15:00 with an obvious dip at 12:00. This is suggestive of anthropogenic activities, where mixing ratios increase in the morning as the working day begins, decline during a break over lunchtime before increasing again in the afternoon as work resumes.

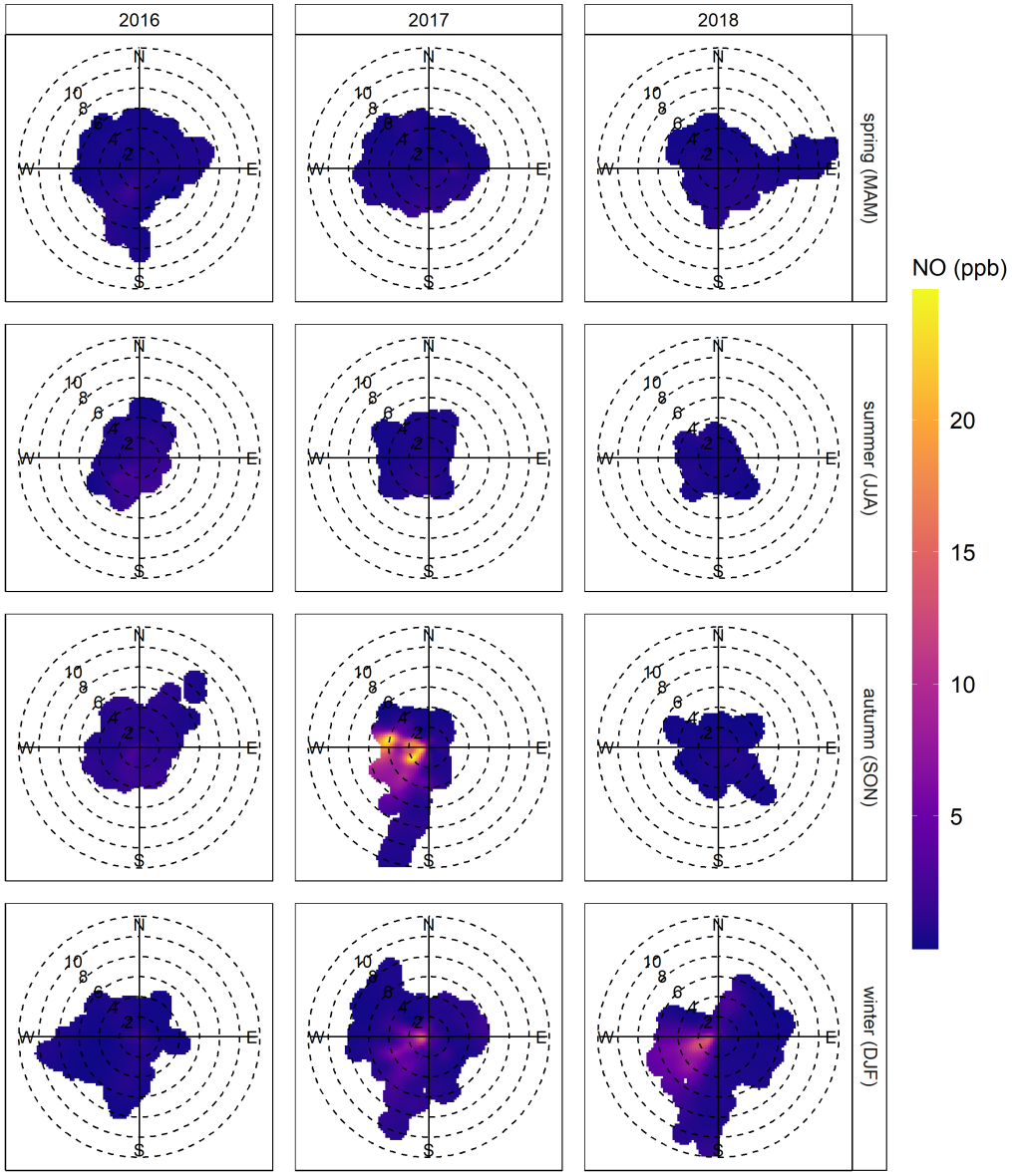

Figure 5.10: *Polar plots of seasonal mixing ratios of NO at KM throughout 2016 to 2018.*

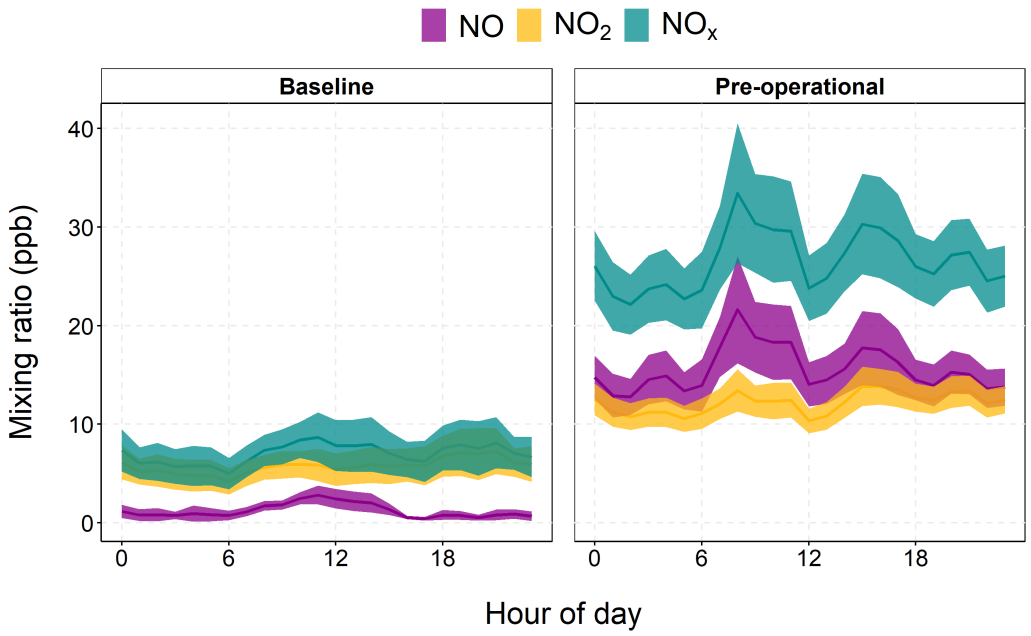

Figure 5.11: *Average diurnal mixing ratios of NO, NO_2 and NO_x during westerly winds throughout the baseline and pre-operational periods at KM. Baseline data was filtered between 19th September–1st February for each year. The shaded areas represent the 95% confidence intervals.*

Also of note is the change in the relative contributions of NO and NO_2 to total NO_x, shown in Figure 5.12. During the baseline period NO_2 dominated NO_x mixing ratios, contributing 83%. However, during the pre-operational period this trend was reversed and NO became the major component of NO_x, contributing 59%. This suggests a change in the most prevalent source of NO_x at KM, specifically an additional source of primary NO close to the monitoring site such that oxidation to NO_2 was yet to occur. The enhanced structure in the diurnal cycle and change in the predominant component of NO_x is further evidence that the pre-operational period had a measurable effect on ambient NO_x mixing ratios at KM.

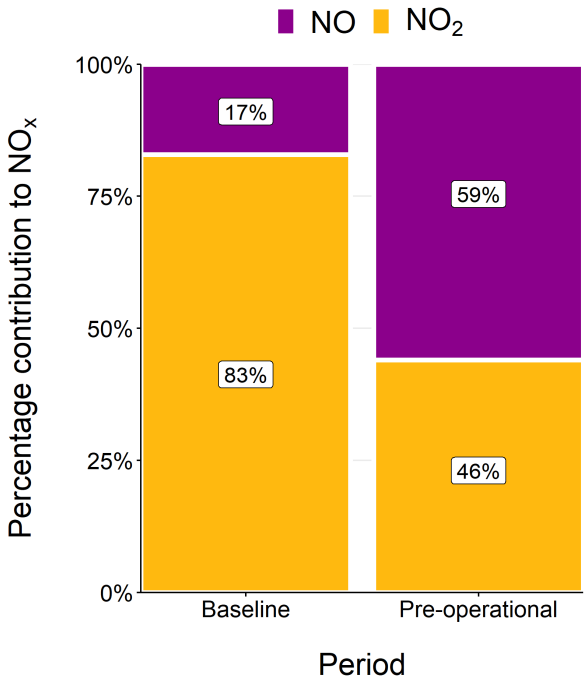

Figure 5.12: *Mean contributions to of NO and NO_2 to NO_x during the baseline and pre-operational periods at KM.*

5.3.4 Quantifying the change in pollutant mixing ratios

RF models for NO, NO_2, NO_x and O_3 were employed to quantify the change in pollutant mixing ratios throughout the pre-operational period relative to a BAU scenario, which assumes no operational activities took place. Simply, these models were used to predict expected pollutant mixing ratios based on the observed meteorological and temporal variables. The resulting time-series was then investigated and compared to observations.

5.3.4.1 Random forest model performance

Generally the RF models performed well, with r^2 values ranging from 60% to 90% (Table 5.4). This suggests that the variation in mixing ratios of these pollutants can be reasonably well explained by a combination of meteorological conditions, along with time

variables, which essentially act as proxies for emission source strength.[277]

Table 5.4: *RF model performance statistics for NO, NO_2, NO_x and O_3 at KM estimated from OOB data.*

Variable	Prediction MSE	r^2
NO	3.20	0.60
NO_2	3.82	0.83
NO_x	10.4	0.76
O_3	9.57	0.90

The RF models were further evaluated by looking at the relative importance or predictive power of each independent variable. This metric is calculated by first assessing the model performance by passing a validation set of OOB data through the trained model. The model accuracy is then computed by comparing the predicted values to the observed values in the validation data set. Next, the values contained within the column of a single variable are permuted or randomly shuffled, essentially giving them no predictive power. The validation data is then passed through the RF model again and the performance evaluated. The feature importance is essentially the decrease in prediction accuracy caused by permuting the column.[259] The importance of each variable is averaged across all trees to obtain the permutation importance for the entire forest.[278] Figure 5.13 shows the permutation importance of each predictive variable for each pollutant. The trend term (unix time) and seasonal term (Julian day) were the most important explanatory variables for both components of NO_x, suggesting NO_x mixing ratios at KM are largely driven by annual cycles in regional emissions and meteorology. Interestingly, hour-of-day and day-of-week were found to have little influence on the models ability to predict NO_x, suggesting time variables are relatively weak proxies for local emission source strengths, such as traffic, in a rural location such as KM. Similarly, wind direction was a relatively unimportant variable, again reflecting the characteristics of a rural background site where mixing ratios are not influenced by specific point sources of emissions but rather by the integrated contribution from all upwind sources. In terms of O_3, wind speed was the second most important variable, which is confirmed by Figure 5.9c, where high O_3 is consistent with relatively strong wind speeds (8–10 m s^{-1}) from

the west.

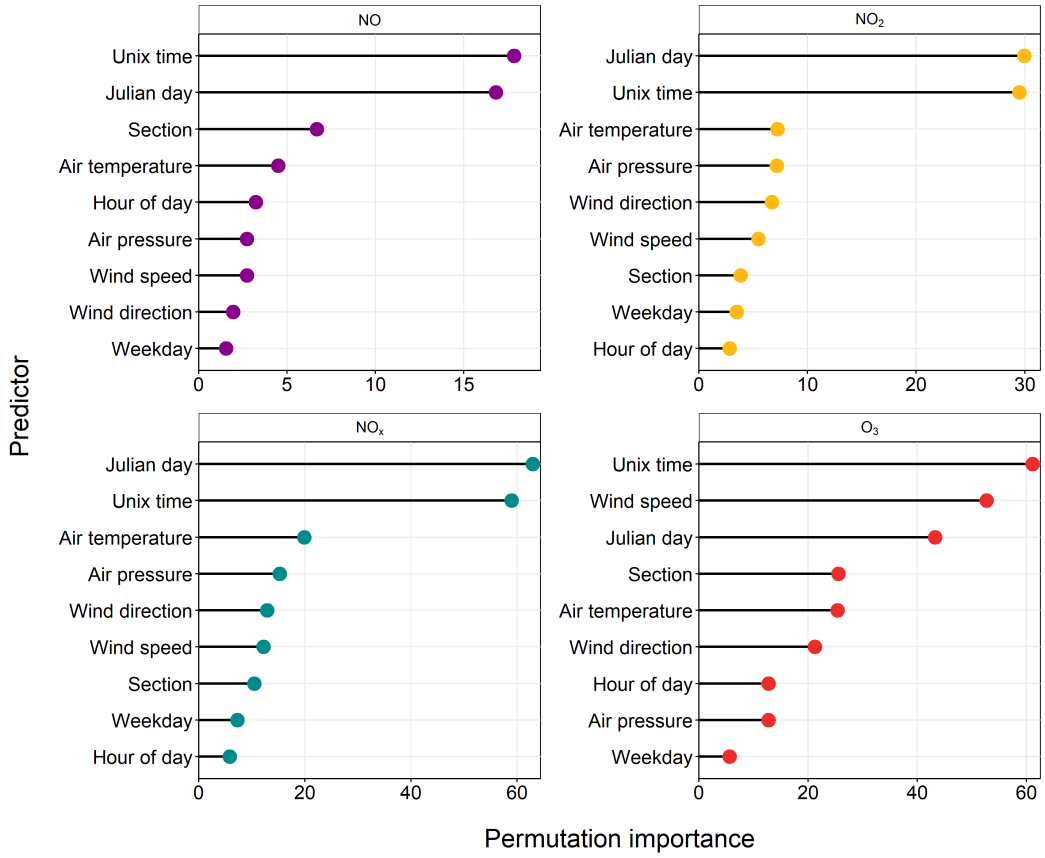

Figure 5.13: *Variable importance plot for 300 RF models for NO, NO_2, NO_x and O_3 at KM.*

The performance of the RF models was validated using a set of baseline data which was held back from the training process. Before initialising the models, the baseline data was randomly split into "training" and "testing" sets of data, accounting for 80% and 20% of observations respectively. Since the testing set of data was not used to build the models it can be used to provide insight into how well the models generalise to an independent data set. RF models are deemed less prone to over-fitting compared to other decision tree techniques since they employ a technique called "bagging" (Section 5.2.4).[259] Figure 5.14 shows the predicted and observed mixing ratios obtained from the testing baseline data set for pollutants at KM. The models performed well with r^2 values ranging from 64% to 90%, suggesting the models are suitably capable of predicting unseen data. The best

performing RF model was that for O_3, which had an r^2 matching that of the training set (0.9) and for which data is closely scattered around the 1:1 line. The models performed less well for NO_x, in particular NO. Data below an observed value of 25 ppb is well correlated around the 1:1 line but the model fails to predict short-lived spikes in mixing ratios. This is perhaps to be expected since NO is a fast-reacting primary pollutant, where enhancements are strongly linked to events in the local environment in the vicinity of the monitoring site, such as a passing vehicle. Proxies in the model such as hour or day attempt to control for this but are unlikely to be good predictors for sporadic events, hence model performance is expected to be weaker. A much better performance was seen for NO_2 since this is predominantly a secondary pollutant. Mixing ratios are driven by air originating from more widespread sources on larger spatial scales, such as local traffic flow (Figure 5.9b), for which the proxies in the model capture much better.

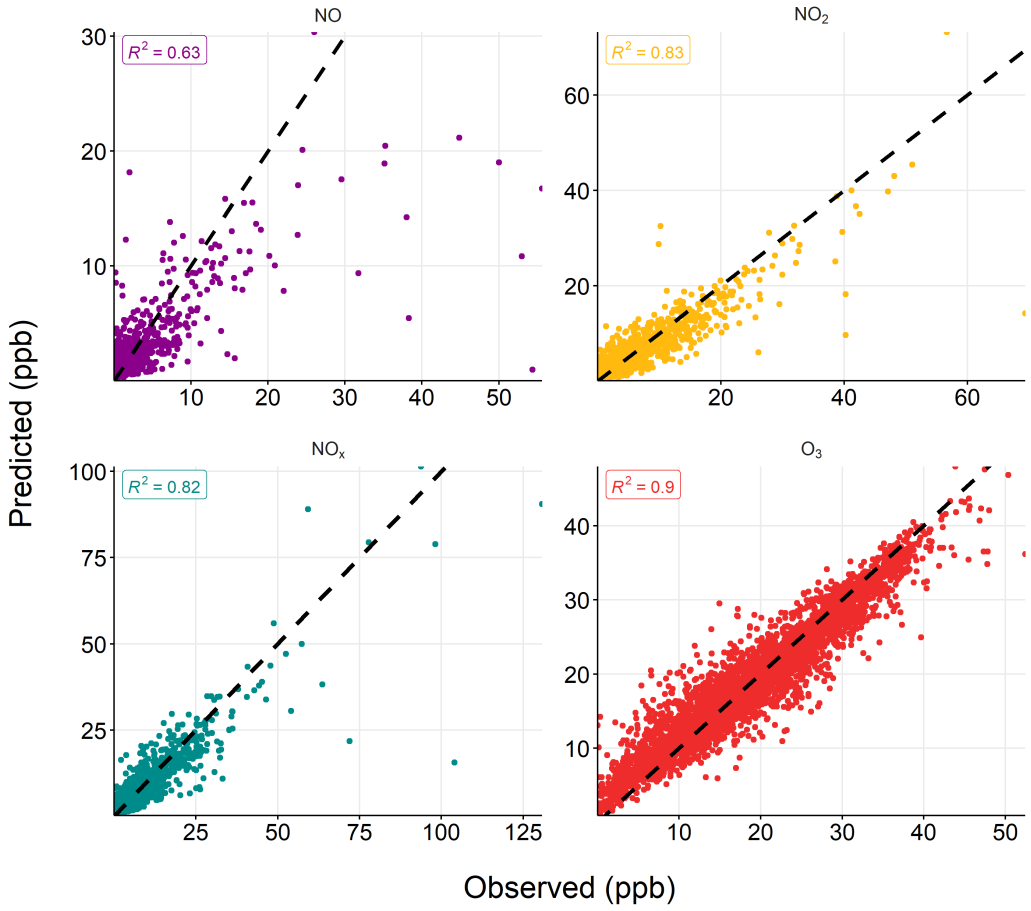

Figure 5.14: *Predicted against measured mixing ratios for the testing data set of baseline data for NO, NO_2, NO_x and O_3 at KM. The dashed line shows the 1:1 line. The r^2 values are those resulting from a linear fit of the two variables.*

5.3.4.2 Predicting pollutant mixing ratios

The RF models for each pollutant were used to predict the BAU mixing ratios during the pre-operational period. Whilst only the baseline data was used for model training, the entire data set was predicted using all available meteorological data as inputs to the RF models. Figure 5.15 shows the mean predictions for the pre-operational period along with the 95% confidence intervals. Standard errors for model predictions were computed using the infinitesimal jackknife for bagging error method based on OOB predictions before being converted into a confidence interval.[279,280]

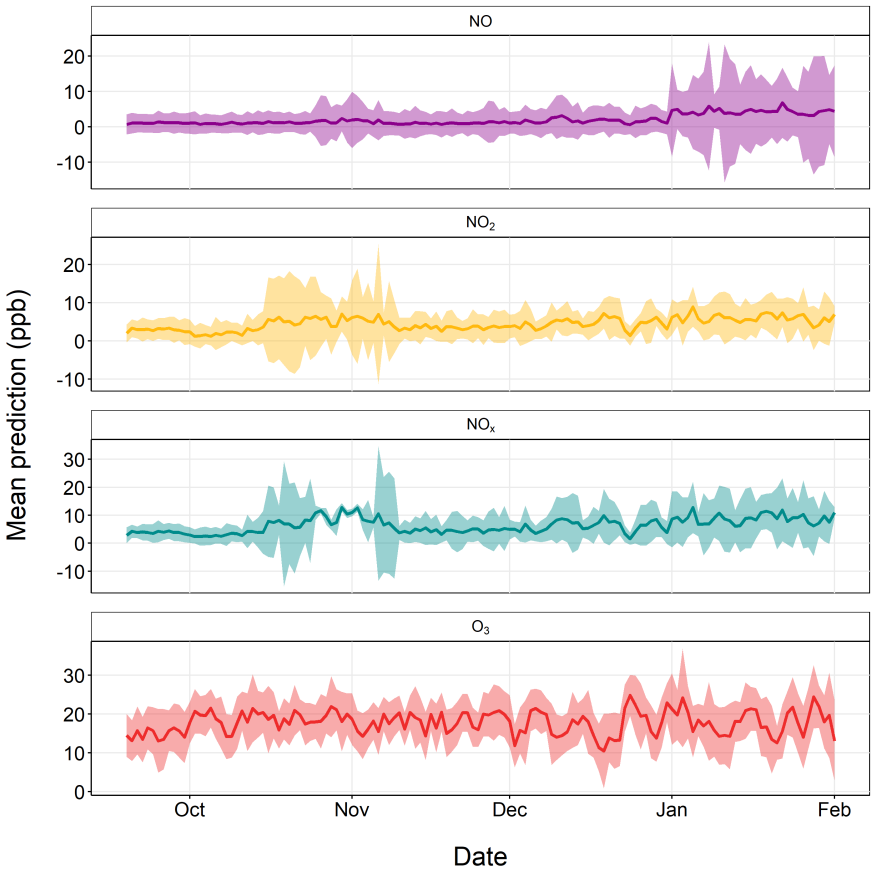

Figure 5.15: *Mean daily averaged predictions from 300 RF models throughout the pre-operational period. The shaded areas represent the upper and lower 95% confidence intervals.*

Figure 5.16 shows the daily time series for observed and predicted mixing ratios between 2016–2019 at KM. As expected, the measured and predicted values strongly agree during the baseline phase of monitoring since this data was used to grow and train the RF models. Discrepancies during this period arise when "spikes" occur in pollutant mixing ratios. In part, this is because the models here are regression models and every prediction is an average (mean) of 300 predictions from 300 trees. As a result, the models generalise and therefore have a limited ability to capture minima and maxima in pollutant mixing ratios. Deviations between the predicted and observed values begin to appear at the beginning of the pre-operational period. This is clearly illustrated by Figure 5.17,

which shows the delta between the observed and predicted values. Measured NO, NO_2 and NO_x was significantly enhanced compared to the predictions, whereas measured O_3 was much lower.

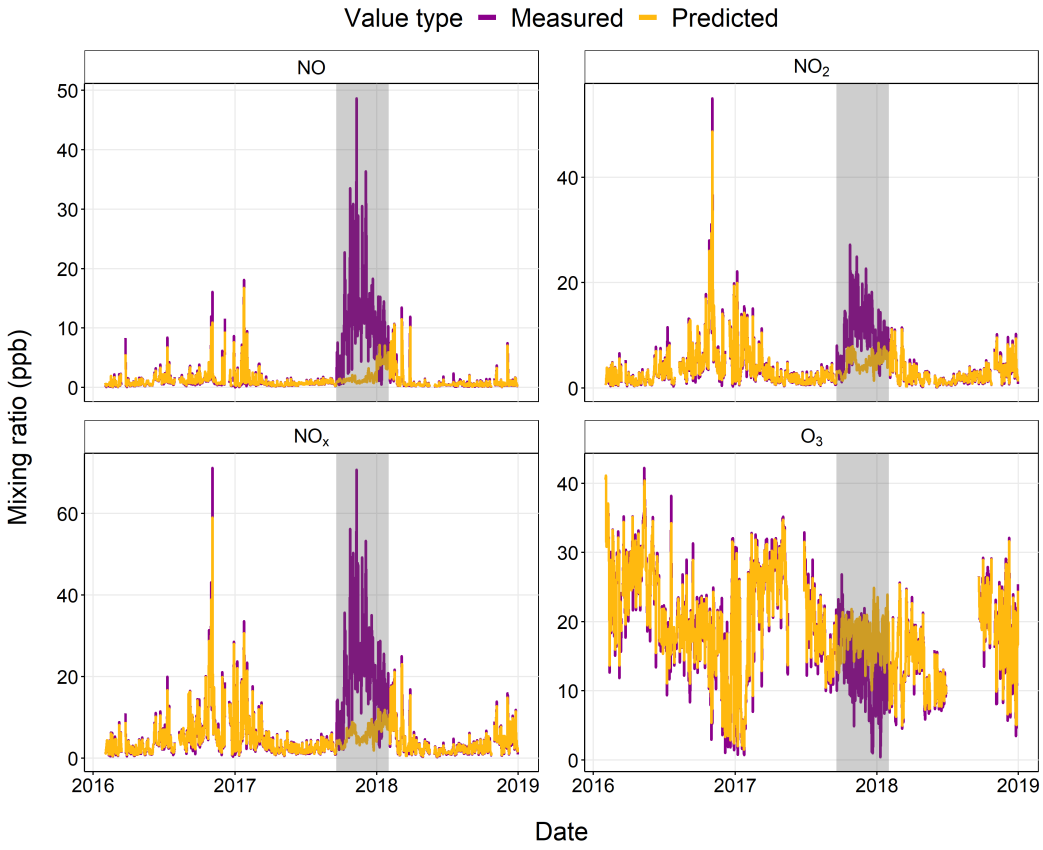

Figure 5.16: *Measured and predicted daily averaged mixing ratios of pollutants at KM. The shaded area shows when pre-operational activities were active.*

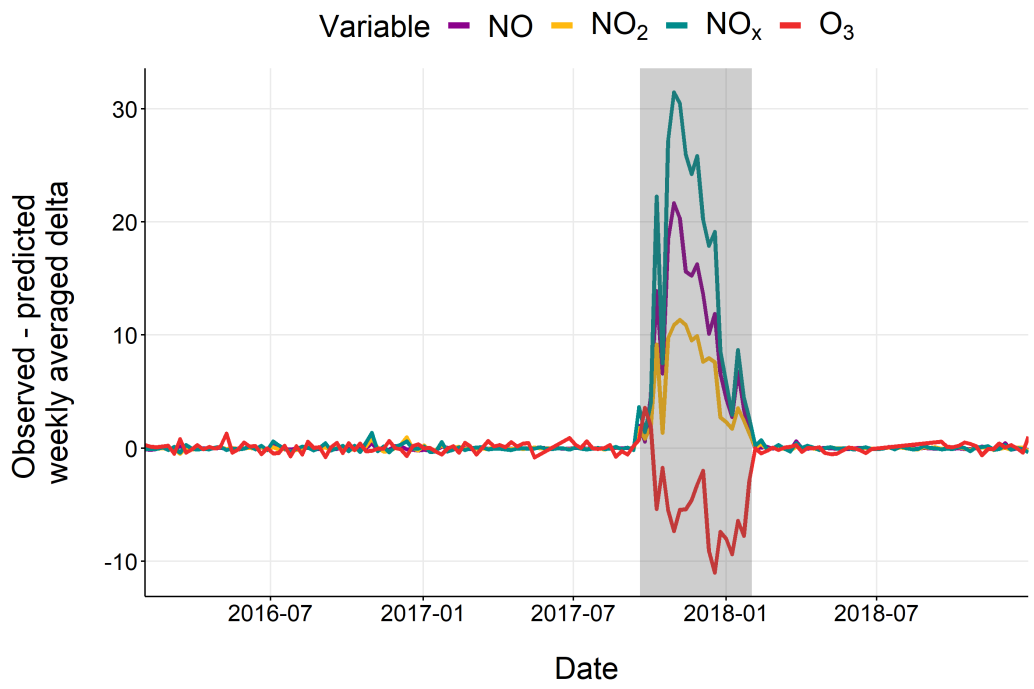

Figure 5.17: *Delta between weekly averaged observed and predicted mixing ratios at KM. The shaded area highlights the pre-operational period.*

In order to evaluate the change in pollutant mixing ratios and to understand the predictions made by the RF models, the general meteorological conditions during the pre-operational period must be considered. Figure 5.18 shows the average meteorological variables during the equivalent of the pre-operational period (19th September–1st February) for each year of monitoring at KM. Crucially, the prevailing wind direction was consistently from the west or south west across all years, meaning the monitoring station was ideally located to detect the effect of the activity on site. The air pressure was lowest during 2017–2018 with a mean value of 1008 mbar compared to 1017 mbar in the previous year. Low air pressure systems generally lead to wet and windy weather conditions. Consequently, this was concurrent with the greatest mean wind speed, which was 40% higher than the previous year and 60% higher than the following year. This is expected to lead to lower mixing ratios of pollutants, such as NO_x, due to an increase in atmospheric dispersion. Indeed, this is reflected in the model predictions, where the pre-

dicted mean NO_x during the pre-operational period was 35% lower than the equivalent period for the previous year. Conversely, the opposite is seen in the measurement data, where total NO_x was enhanced 2-fold during the pre-operational period compared to the same period in the previous year. These results are therefore consistent with the hypothesis that the pre-operational period caused increased mixing ratios of NO_x. In terms of O_3, the meteorological conditions outlined in Figure 5.18 have the opposite effect. Since wind speed is an important variable in the RF model for predicting O_3 (Figure 5.13) and elevated westerly winds generally lead to enhanced O_3 (Figure 5.9c) at KM, predicted O_3 during the pre-operational period was 19% higher than the previous year. As for NO_x, the observations show the contrary, where O_3 was 14% lower than the previous year during the pre-operational period.

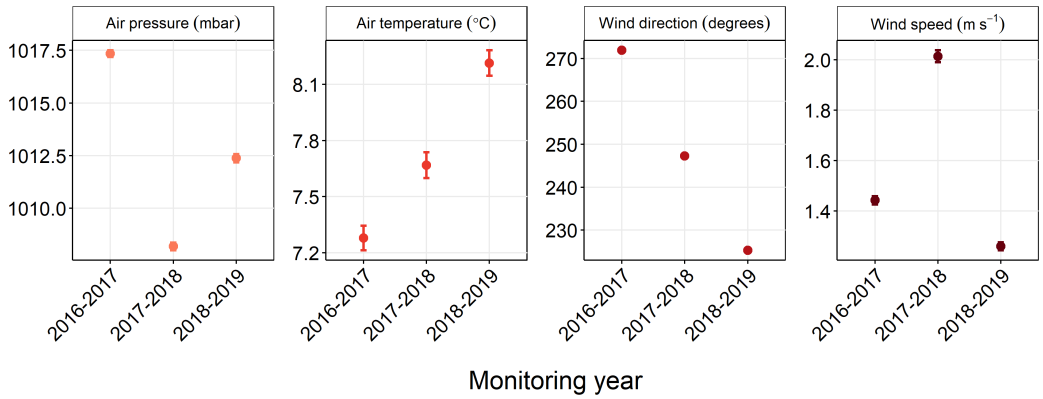

Figure 5.18: *Means of meteorological variables at KM between 19th September – 1st February during each year of monitoring. Error bars show the 95% confidence intervals.*

The changes in pollutant mixing ratios can be further resolved using a sequential analysis, such as the cumulative sum (`cumsum`) approach, which aggregates the differences over time. A `cumsum` plot is constructed by plotting the accumulated delta between the measured and predicted mixing ratios.[281] By accumulating the differences, any divergence from the counterfactual is amplified along with the timing of the associated change. Figure 5.19 shows the `cumsum` plot for pollutants at KM between 2016–2019. The trend line is consistently around zero throughout 2016 and the first half of 2017. Divergences from zero begin to occur towards the end of September, which agrees well

with the start of the pre-operational period. A positive deviation is seen for NO, NO_2 and NO_x, suggesting that actual mixing ratios were enhanced over what would be expected in the BAU scenario. In contrast, a negative deviation was seen for O_3. The gradient then tends back to zero as pre-operational activities ceased, meaning mixing ratios returned to what was expected in a BAU scenario. This highlights a distinct, isolated period at KM, associated with a clear change in the intensity of emissions.

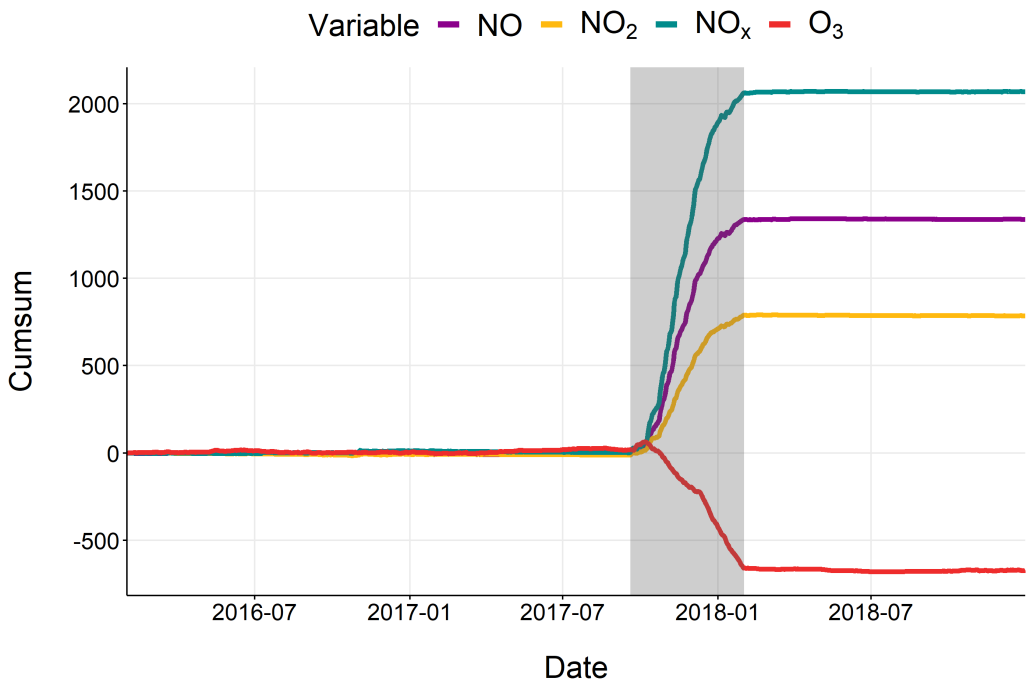

Figure 5.19: *Cumulative summary of the difference between measured and predicted values at KM. The shaded area highlights the pre-operational period.*

To link the divergence from the BAU scenario to the increase in activity due to well preparation, a plot of the NO_x increment, defined as observed minus predicted, versus wind direction is shown in Figure 5.20. The plot shows that the maximum NO_x increment is observed for westerly winds (NO_x = 6.48 ppb), but subsides to zero for northerly and easterly winds. Some of the increment shown in Figure 5.20 for southerly winds could likely be from idling vehicles associated with the campaigning, policing and media presence located outside the site access point on Habton Road. Equivalent plots of

NO and NO_2 show the same pattern (not shown), whilst for O_3 the trend is reversed such that the largest, negative increments are observed under westerly winds (not shown). Figure 5.20 is strong evidence, supporting Figure 5.10, that the increment in NO_x mixing ratios and concurrent decline in O_3 is consistent with a change in emission source strength to the west, where the well pad lies.

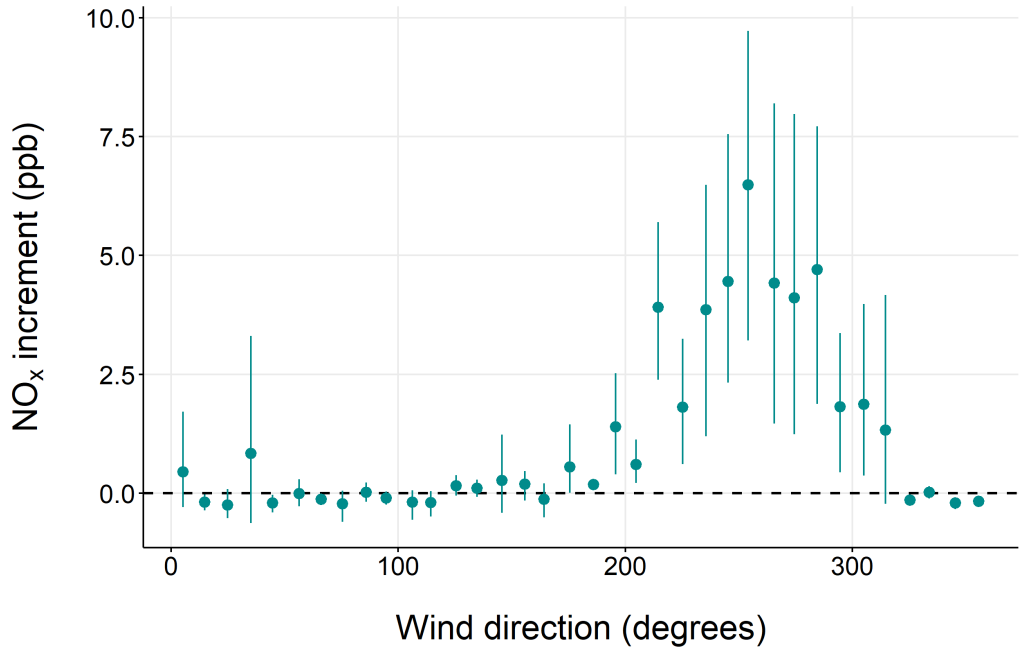

Figure 5.20: *NO_x increment (observed - predicted) by wind direction at KM. Data have been binned into wind direction intervals of 10 ° and averaged. The error bars represent the upper and lower 95% confidence intervals.*

The observed and BAU mixing ratios were used to quantify the air quality impact of the pre-operational period. Figure 5.21 shows the estimated percentage change in the mean mixing ratios of pollutants and a summary is given in Table 5.5. The uncertainties in the measured values represent the 95% confidence intervals around the mean. Those for the predicted values were calculated by propagating the standard error for the model predictions through the mean calculation, before multiplying by a coverage factor of $k = 2$ to give an uncertainty at the 95% confidence level. Uncertainties in the delta values were found by summing the standard uncertainties for the mean-measured

and mean-predicted values in quadrature and subsequently multiplying the result by a coverage factor of $k = 2$. The relative uncertainties in the percentage change values were calculated by propagating the relative errors of the delta and predicted values in quadrature. The absolute error was then multiplied by a coverage factor of $k = 2$ to give an uncertainty at the 95% confidence level.

Table 5.5 shows the greatest change was observed for NO, which increased approximately 6-fold, by 532%. The associated increase in NO_2 was much less (128%), which is to be expected since primary emissions of NO_x are predominantly in the form of NO.[158] The increase in NO_x was to some extent offset by a corresponding decrease in O_3 of 28%. Since O_3 and NO_x are closely linked through a chemical cycle within the atmosphere, incremental increases in NO lead to the destruction of O_3 via titration of the two species. Locations with very high NO_x emissions generally do not show as large an increase in O_3 mixing ratios because the source is in very close proximity and NO mixing ratios remain high relative to oxidant mixing ratios.[282] This behaviour is typical of a roadside monitoring site, which in this case is a good parallel for KM since the monitoring station is located on the well pad itself. Multiple modelling studies for the UK estimate that shale gas emissions can enhance O_3 and drive exceedances at a considerable percentage of regulatory measurement stations both locally and regionally.[239,283] Whilst this work would seem to contradict those findings, it is expected that there would be a positive gradient of O_3 enhancements with increasing downwind distance from the site as a result of photochemical processing.

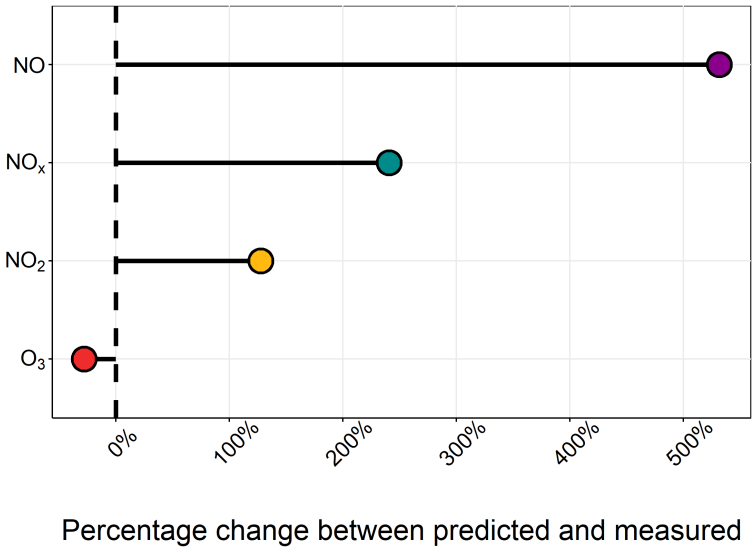

Figure 5.21: *Percentage change between predicted and measured mixing ratios at KM during the pre-operational period.*

Table 5.5: *Measured and predicted means, deltas, and percentage change, along with expanded uncertainties for the pre-operational period at KM.*

Variable	Measured (ppb)	Predicted (ppb)	Delta (ppb)	% change (%)
NO	12.5 ± 0.5	2.00 ± 0.1	10.5 ± 0.5	532 ± 43
NO_2	10.5 ± 0.3	4.60 ± 0.2	5.90 ± 0.3	128 ± 8
NO_x	21.5 ± 0.7	6.30 ± 0.2	15.2 ± 0.7	241 ± 14
O_3	12.8 ± 0.2	17.8 ± 0.1	-5.00 ± 0.3	-27.9 ± 1.5

5.3.5 Change in total oxidant

The suppression of O_3 close to sources of NO_x is often accompanied by enhanced levels of O_3 further downwind. This is due to the oxidation of NO to NO_2 with peroxy radicals and subsequent photolysis of NO_2 to form O_3. Therefore, to account for this photochemistry, the total oxidant (OX = NO_2+O_3) is considered, since it's production and loss are independent of the chemical coupling that results in the interconversion of NO_2 and O_3. Changes in OX reflect the abundance of oxidants and are therefore more representative

of the production of oxidant than O_3 alone.[284] OX can be described in terms of a local, NO_x-dependent contribution and a regional, NO_x-independent contribution.[285] The regional contribution essentially equates to the regional background level of O_3, whereas the local contribution correlates with the level of primary pollution and essentially represents the fraction of directly emitted NO_2. The individual contributions to OX can be quantified from an [OX] vs. [NO_x] plot, where the slope obtained from a linear regression represents the local OX contribution, whilst the intercept represents the regional contribution.[285]

An additional RF model was constructed for OX (r^2 = 0.89, MSE = 8.44 ppb) to assess the change in total oxidant as a result of pre-operational activities at KM. Performing an identical analysis to that for NO, NO_2, NO_x and O_3 yielded a 9% increase in OX relative to the BAU scenario. Figure 5.22 shows the local and regional contributions to OX obtained from the weekly regression plot of [OX] vs. [NO_x]. Figure 5.22a shows that the regional component (intercept) of OX is consistent with the seasonal trend in O_3 shown in Figure 5.7, where O_3 generally reaches a minimum during the winter months. Throughout the pre-operational period, the local contribution to OX followed a declining trend as it approached a minimum and does therefore not account for the observed increase in OX.

Figure 5.22b shows the local contribution to OX between August 2017–February 2018. Throughout the baseline period, the fraction of NO_x directly emitted as NO_2 (f-NO_2) was negligible, since only secondary NO_2 resulting from the oxidation of primary NO from upwind sources was observed. However, increases in f-NO_2 leading to positive contributions were entirely consistent with the start of pre-operational period. Throughout the whole of this period, f-NO_2 ranged from 6–37%, suggesting the increase in OX was driven by changes in primary NO_2 emissions on or near the site. This is likely as a result of the presence of diesel vehicles and generators, which tend to emit a higher f-NO_2 compared to petrol due to diesel emission control technologies such as Diesel Oxidation Catalysts (DOC).[286] Since access to active O&G sites is exclusively permitted for diesel vehicles, the associated increase in OX is likely to have significant implications on the photochemical production of ozone in regions of hydraulic fracturing.

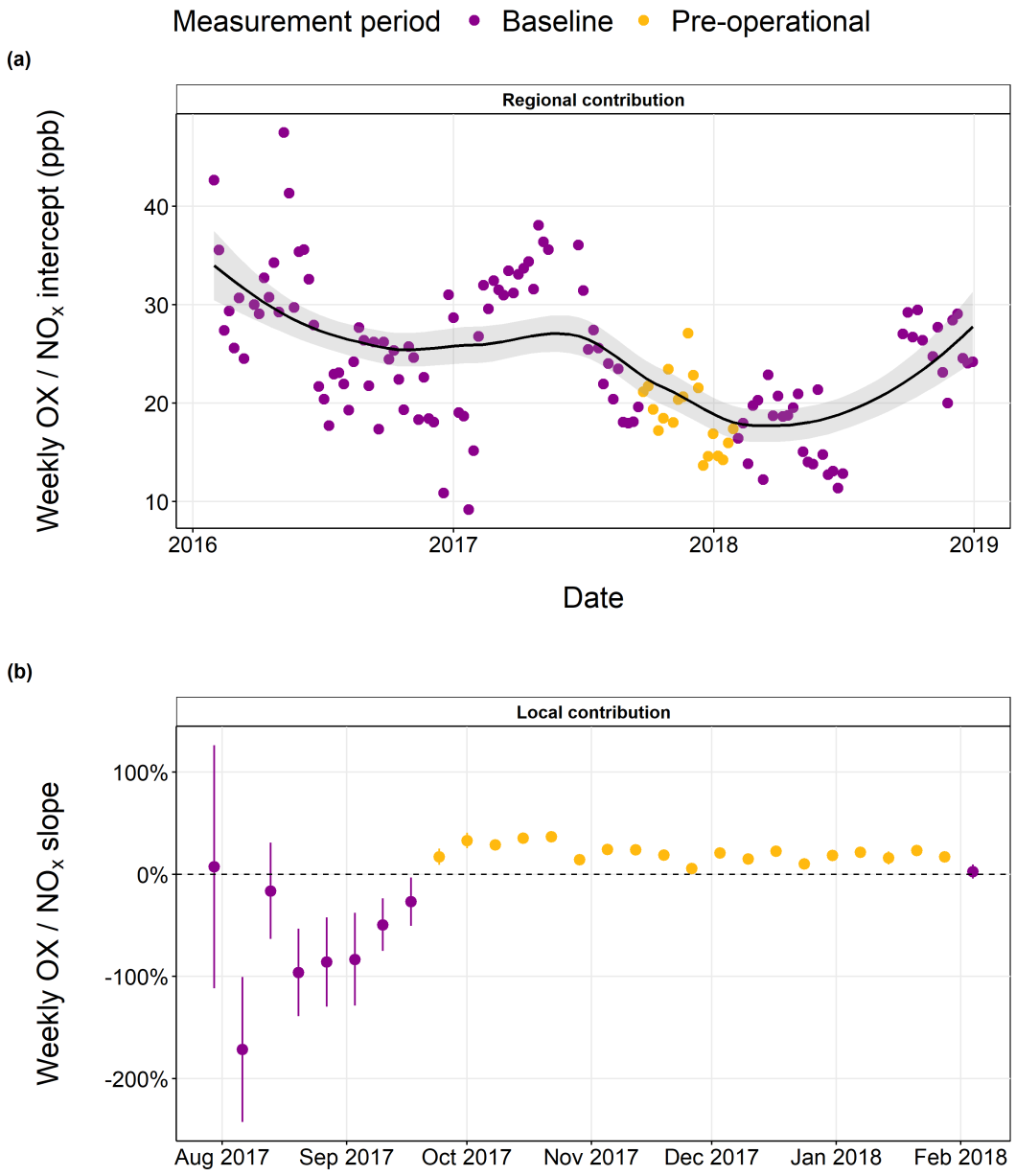

Figure 5.22: *(a) Weekly total oxidant (OX; NO_2+O_3)/NO_x slope at KM calculated using linear regression. Error bars represent the 95% confidence intervals. (b) Weekly total oxidant (OX; NO_2+O_3)/NO_x intercept at KM. The solid line represents a loess smooth fit to the data, and the shaded region represents the 95% confidence interval around the smooth.*

5.3.6 Site classification

Despite the 3-fold increase in total NO_x during the pre-operational period (Table 5.5), concentrations were still well below the air quality standards regulations (Figure 5.8). In order to put the observed changes in pollutant mixing ratios into context, data was compared to that from all the AURN sites in the UK. Since KM is located in a rural area and not influenced by any single point source, should it be part of the AURN it would likely be classified as a rural background site.

Figure 5.23 shows the probability density distribution of NO and NO_2 during both the baseline and pre-operational periods at KM. Note that the data was converted into a concentration in μg m^{-3} for comparison with the AURN data. Baseline observations at KM were filtered to between 19th September–1st February in order to minimise differences due to seasonal factors. Additionally, data from all AURN sites in Figure 5.1 was aggregated to each site classification throughout the same time periods in order to make a robust comparison. Frequency density plots show how the concentrations of pollutants are distributed and give a more detailed indication of where the bulk of measurements lie. This is more useful than using a mean concentration, which can often be skewed by spikes in data. From Figure 5.23 it is clear that, as expected, throughout the baseline phase of monitoring, the distributions of NO and NO_2 were most representative of a rural background site. For NO, 93.4% of the measurements were in the interval 0–5 μg m^{-3}, almost equivalent to 93.2% for rural background sites. Similarly for NO_2, 82.8% of data lay in the range 0–10 μg m^{-3}, compared to 65% for rural background sites. For comparison, only 21% of data lay within the same range for urban background sites.

Conversely, looking at the pre-operational period there is a clear shift in the distribution of both NO and NO_2. The NO measurements display a bimodal distribution, in which 31.4% of observations fall into the range 0–5 μg m^{-3} and the bulk of observations lie in the range 5–20 μg m^{-3}, accounting for 49.8% of observations. This suggests the initial source of NO (likely to be Habton Road) still exists, but that there is also an additional source responsible for distinctively higher levels of NO. During this phase, KM is approximately comparable to urban traffic sites, where only 25.1% of data fell into the range 0–5 μg m^{-3} and the majority of observations (52.4%) were between 10-100 μg m^{-3}. There was an evident, albeit smaller change in the distribution of NO_2. A much broader spread

was observed in the data (note the log scale in Figure 5.23) with 73.3% of data distributed between 5–40 μg m^{-3}, compared to 74.3% for urban industrial sites and 55.4% for urban traffic sites.

Figure 5.23 indicates that the site characteristics of KM significantly changed following the initiation of fracking-related activities. Based on NO_x concentrations, the site transitioned from an air quality climatology representative of a rural background site, with relatively clean air typical of the UK regional background, to that more analogous to an urban setting. This could have serious implications for residents living in the surrounding area of the well site, particularly if the industry were scaled up to facilitate hundreds of wells across the UK countryside. Should hydraulic fracturing have subsequently taken place, it is expected that emissions would be elevated even further above baseline levels. However, it is important to note that emissions were not exclusively from the operator and that the observed change is resultant of a combination of vehicular and combustion-related sources introduced on or near the well site.

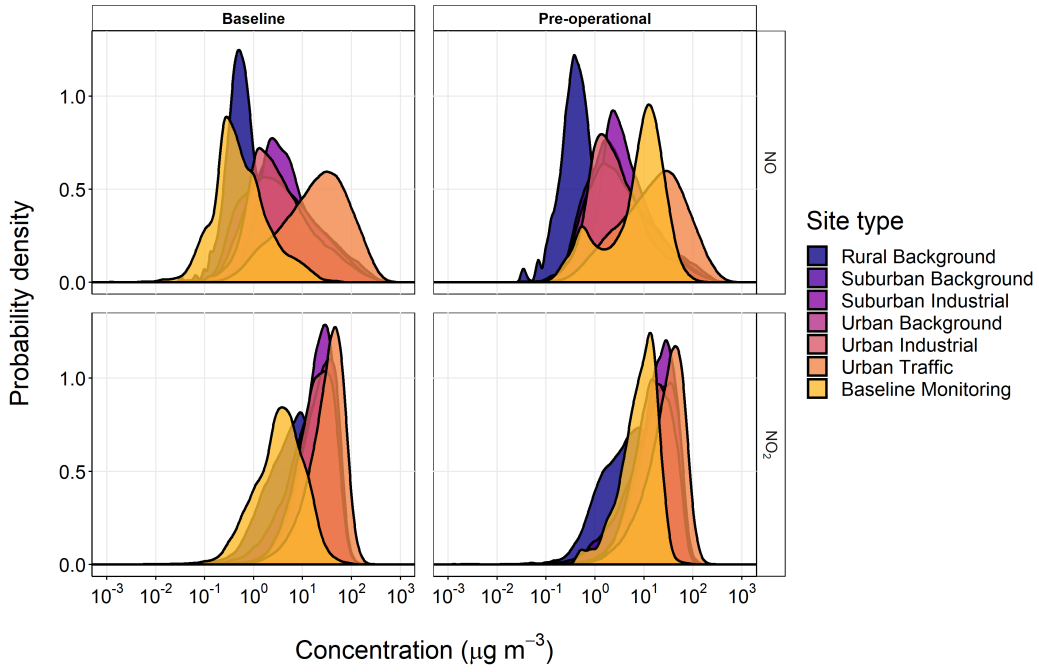

Figure 5.23: *Normalised probability density functions of hourly averaged NO and NO_2 during the baseline and pre-operational periods at KM (site type = Baseline Monitoring), compared to all UK AURN sites. Baseline data is filtered to observations between 19th September–1st February for each year.*

5.4 Conclusions

Well pad preparation is a key phase within the shale gas extraction process. Constructing and operating a shale gas well requires a large amount of above-ground infrastructure and equipment, which must be transported to the well pad. The resultant traffic load and subsequent on-site activity introduces an additional source of air pollutants to the local environment prior to any hydraulic fracturing. In this work, the impact of the pre-operational phase is investigated through the application of random forest machine learning models to air quality data in the rural village of Kirby Misperton in North Yorkshire.

Extensive baseline monitoring of air pollutants two years prior to the start of shale-gas operations enabled the characterisation of the local air quality climatology. The base-

line observations were used to predict mixing ratios in the construction of a "business as usual" scenario, which assumed no change in the activity on site. The counterfactual was then compared to the observations, revealing a 240% increase in NO_x and concurrent decrease in O_3 of 28%. Changes in NO_x were dominated by increases in NO as expected for a traffic-related emission source. However, evaluation of the total oxidant (OX) revealed enhancements of the primary NO_2 fraction (f-NO_2), which could have significant impacts on public health due to an increase in the abundance of oxidants. Whilst emissions were found to be enhanced far above baseline levels, mixing ratios remained well within UK regulatory limits. However, comparison of the data to that from all UK AURN monitoring sites demonstrated a shift in the chemical environment at KM to that more similar to a suburban city environment in terms of NO_x.

Since no hydraulic fracturing actually took place on the site, this work identifies a systematic change in NO_x due to site preparation. Often considerations of emissions from hydraulic fracturing only emerge once infrastructure is in place and drilling begins. This work therefore exposes a relatively understudied source of emissions from the shale gas industry. The identification of these emissions highlights that baseline monitoring prior to industrial activity is critical for robust assessment of the environmental impacts.

6

Summary and Conclusions

The global oil and gas (O&G) industry has experienced rapid growth in the past few decades, predominantly due to an increase in shale gas production through the development of modern extraction techniques such as hydraulic fracturing. This growth is expected to continue throughout the next few decades. Forecasts published by British Petroleum (BP) showed that the production of natural gas is expected to increase until at least 2030, with oil production now beginning to level off and decrease (Figure 6.1).[287] In the UK, the demand for natural gas is actually expected to decline by 11.4 million metric tons of oil equivalent from 2020–2040,[288] largely resulting from commitments to net zero through the implementation of policies such as no new gas boilers by 2025. The global increase in development has heightened environmental concerns regarding air quality. In particular, increased emissions of air pollutants such as methane (CH_4), nitrogen oxides (NO_x = NO + NO_2) and volatile organic compounds (VOCs) are negatively

linked to poor human and environmental health, along with climate effects. This thesis explores atmospheric emissions of these species from both the onshore and offshore O&G industry in the context of the UK.

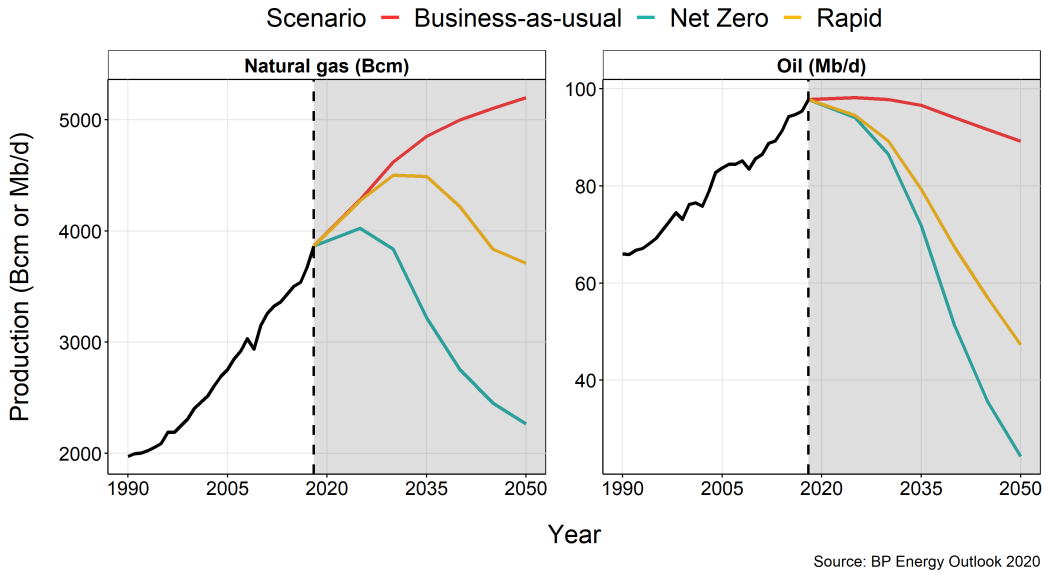

Figure 6.1: *Global production of natural gas and oil with future projections from 2018–2050 based on three possible scenarios.* ***Business as usual*** *assumes growth will follow the current trend with no significant changes to policy, technology or social preferences,* ***Rapid*** *is based on a series of sector-specific policies designed to cut carbon emissions, and* ***Net-zero*** *assumes that the policy measures outlined in* ***Rapid*** *are added to and reinforced by significant shifts in social behaviour.*[287]

This thesis presents three analyses based on data collected in regions of UK O&G production. Both ground-based and airborne observations were utilised to assess the composition and magnitude of UK O&G emissions. There is a strong focus on emissions of VOCs since they are rarely studied in comparison to greenhouse gases such as CH_4, but play a key role in the degradation of both local and regional air quality.

Chapters 3 and 4 present measurements made from research aircraft over O&G producing regions of the North Sea. The analyses were underpinned by in-situ measurements of CH_4 and ethane (C_2H_6), along with discrete canister samples for the quantification of VOCs. The data set in Chapter 3 was compiled from 28 research flights across

four defined areas of the North Sea. A total of 668 whole air samples were captured and used to characterise the collective VOC emissions associated with O&G operations in the North Sea. This was primarily achieved through the evaluation of pollutant enhancement ratios, which were shown to be a valuable tool in source identification. Such ratios were leveraged to distinguish between unique emission sources in a number of ways. First, through calculation of the iso-pentane to n-pentane (iC_5/nC_5) enhancement ratio, which yielded characteristic signatures between 0.89–1.24, identifying O&G production as the key driver of VOC emissions in the North Sea. Second, this was reinforced through the evaluation of statistical correlations between VOCs and source-specific tracer compounds, where strong correlations with propane confirmed O&G production as the primary emission source. Hints of an additional urban influence were explored through the benzene to toluene (B/T) ratio, which was subsequently applied as a filter to isolate samples primarily influenced by O&G emissions for further analysis.

The isolation of such samples allowed the comparison of the VOC composition related to each field type (oil, gas or condensate). Unprocessed natural gas is approximately 60–90% CH_4, however the remaining fraction differs by reservoir. Therefore, it follows that VOC emissions may also be unique to each basin. This idea motivated the rest of the analysis in Chapter 3. Indeed, a spatial dependence on emissions was identified and exposed through the enhancement ratio of C_2H_6 to CH_4. Gas production was characterised by a low ratio of 0.03, whereas oil production yielded a much higher ratio of 0.18. This difference was further illuminated through calculation of the excess mole fraction, which showed that emissions from oil production were richer in VOCs relative to CH_4, in comparison to those from gas production. This implies that emissions from oil fields are likely to greater facilitate O_3 production since they contain a larger proportion of alkanes, which are more reactive towards the OH radical compared to CH_4.

The potential impact of North Sea O&G emissions was further explored in Chapter 3 through calculation of the OH reactivity, which showed that, despite their dominance regarding total VOC concentrations, C_2–C_5 alkanes were second to highly reactive, unsaturated species, likely from general combustion sources. The final analysis component in Chapter 3 was a comparison to the VOC speciation profiles within the National Atmospheric Emissions Inventory (NAEI) and revealed several discrepancies. Most noticeable

was the lack of species reported in some of the source-specific profiles, suggesting a need for improvement. The measurements reported here could be used to replace the profiles that currently exist in favour of observationally-derived profiles relating to each fossil fuel product, with the aim of better representing emissions from the offshore O&G sector. Overall, this work highlights key differences in emissions between on and offshore extraction and makes an important contribution to the literature regarding VOCs from offshore O&G operations, which are sparsely studied compared to those onshore.

In addition to understanding the composition of emissions surrounding O&G production, of equal importance is assessing the magnitude of such emissions. Offshore emissions in the UK are exclusively reported though bottom-up (BU) estimates within the Environmental Emissions Monitoring System (EEMS), but there is very little existing work challenging the validity of such estimates. Chapter 4 addresses this by implementing a top-down (TD) methodology to quantify emissions of CH_4 and VOCs from North Sea O&G facilities. A mass balance approach was applied to airborne measurements of well-defined plumes downwind of single platforms. High resolution measurements are typically required to perform a mass balance calculation, however, by coupling in-situ measurements of C_2H_6 with VOC enhancement ratios in discrete canister samples, emission rates of individual VOCs were successfully calculated.

The calculated emissions from individual platforms varied both spatially and temporally, exposing the wealth of potential emission sources, the strength of which fluctuate throughout the day. The TD measurements were compared to those from the BU reporting and showed a general underestimation of both CH_4 and VOCs from most platforms. This suggests a reassessment of the current methodology may be required and demonstrates the need for further observational-based studies to understand the discrepancy between TD and BU approaches. Of most interest, was the atypically high VOC emission rates observed during oil loading operations onto shuttle tankers. Further insight was gained from the $\Delta C_2H_6/\Delta CH_4$ ratio within plumes, which offered evidence of an intermittent VOC-rich emission source, characterised by uncommonly high ratios. Comparison of estimates concurrent with oil loading to the BU estimates yielded differences of more than an order of magnitude, implying a significant gap in reported emissions from this source. This was reinforced through the aggregation of emissions estimates

across all platforms, where the mean TD and BU values showed an overall agreement in the absence of estimates coinciding with shuttle tanker operations. It is hoped that this work will stimulate future studies focused on VOC emissions from oil loading, which can subsequently be used to better inform the BU reporting. In addition to this, abatement strategies involving VOC recovery and absorption processes are currently being developed to limit VOCs from loading. This work could therefore serve as a comparison against future studies to assess the success and impact of such intervention strategies.

Whilst 98% of the UK's O&G production originates from offshore reservoirs within the UK Continental Shelf (UKCS),[133] onshore extraction has been taking place since the 1980s and there are currently around 250 operating wells. Interest in hydraulic fracturing (fracking) following the "shale gas boom" in the US has extended to other countries, including the UK. However, there are a myriad of environmental concerns surrounding the fracking process, including exposure to air contaminants and their negative impact on air quality. The assessment of such impacts requires extensive monitoring before, during and after any shale gas development takes place in order to identify incremental changes caused by new emission sources. Chapter 5 demonstrates a methodology by which baseline measurements in the vicinity of shale gas extraction can be combined with a machine learning technique to robustly detect and quantify changes in air pollutant concentrations as a consequence of fracking operations.

Chapter 5 is underpinned by baseline measurements of air quality at a well site in Kirby Misperton (KM), North Yorkshire, which were conducted two years prior to any shale gas activity. Whilst no hydraulic fracturing actually took place at the site, a significant period of preparation occurred over a number of months. Termed the "pre-operational" period, this stage is rarely investigated as air quality concerns typically arise once extraction has commenced. The measurements were used to predict pollutant concentrations in a business-as-usual (BAU) scenario through the application of random forest (RF) machine learning models, which were subsequently compared to observations. The models identified a distinct period of deviation from the BAU scenario, entirely consistent with the timing of pre-operational activities. This period was characterised by significant enhancements in NO_x and a concurrent decrease in O_3, driven by extensive vehicular activity and the presence of numerous combustion sources, such

as generators, on the well pad. To provide context regarding the observed changes, the observations were compared to those from the UK's Automatic Urban and Rural (AURN) monitoring network. This revealed a transition in the chemical environment at KM, from a typical rural climatology to that more analogous to a suburban city environment in terms of NO_x concentrations. An additional feature identified through the evaluation of total oxidant (OX) was an increase in primary emissions of NO_2, which may have implications regarding the attainment of ambient air quality standards as well as negatively impacting health in the local surroundings.

Chapter 5 demonstrates a methodology applicable to any standard long-term monitoring data to assess changes resulting from new emissions sources, management strategies or intervention policies. Should future shale gas operations occur in the UK, this work outlines a routine measurement and analysis strategy which can be implemented to detect and evaluate baseline deviation events. Future work will extend the analysis to include VOCs, particular matter (PM) and greenhouse gases, such as CH_4 and carbon dioxide (CO_2), to gain a wider perspective of the air quality impact of the shale gas industry. This will require some revision of the RF models to include additional variables for prediction. Due to the longer lifetimes of species such as CH_4 and their influence over larger spatial scales, variables such as back-trajectory cluster and boundary layer height, capable of capturing the long-term variability and effect of atmospheric transport may be required to accurately predict concentrations. Furthermore, this analysis framework could be expanded into other research areas such as water quality and soil gas, allowing a consistent method to be applied across multiple environmental domains.

6.1 Final remarks

Oil and gas will be a key source of energy for years to come. This work contributes to the growing knowledge base surrounding emissions from the O&G industry and provides insight through the collection of novel data sets into O&G emissions from a UK perspective. As the pressure to act on climate change builds, schemes to cut carbon emissions are becoming ever more prevalent. Therefore, work such as this will be vital to *(i)* understand the current state of emissions and, *(ii)* determine whether the transitions towards cleaner energy production within the industry are successful.

Appendix

The following pages present details of publications that were contributed to throughout this PhD or as part of the work for this thesis.

Purvis, R. M. et al. Effects of 'pre-fracking' operations on ambient air quality at a shale gas exploration site in rural North Yorkshire, England. *Sci. Total Environ.* 673 (2019), pp. 445–454. URL: http://www.sciencedirect.com/science/article/pii/S0048969719315979

Shaw, J. T. et al. A baseline of atmospheric greenhouse gases for prospective UK shale gas sites. *Sci. Total Environ.* 684 (2019), pp. 1–13. URL: http://www.sciencedirect.com/science/article/pii/S0048969719323071

Graham, A. M. et al. Impact of the June 2018 Saddleworth Moor wildfires on air quality in northern England. *Environ. res. commun.* 2.3 (2020), p. 031001. URL: https://doi.org/10.1088%2F2515-7620%2Fab7b92

Shaw, J. T. et al. Methane flux from flowback operations at a shale gas site. *J. Air. Waste Manag. Assoc.* 70.12 (2020). PMID: 32915694, pp. 1324–1339. URL: https://doi.org/10.1080/10962247.2020.1811800

Lee, J. D. et al. UK surface NO_2 levels dropped by 42% during the COVID-19 lockdown: impact on surface O_3. *Atmospheric Chemistry and Physics* 20.24 (2020), pp. 15743–15759. URL: https://acp.copernicus.org/articles/20/15743/2020/

France, J. L. et al. Facility level measurement of offshore oil and gas installations from a medium-sized airborne platform: method development for quantification

and source identification of methane emissions. *Atmos. Meas. Tech.* 14.1 (2021), pp. 71–88. URL: https://amt.copernicus.org/articles/14/71/2021/

Wilde, S. E. et al. Speciation of VOC emissions related to offshore North Sea oil and gas production. *Atmos. Chem. Phys.* 21.5 (2021), pp. 3741–3762. URL: https://acp.copernicus.org/articles/21/3741/2021/

Ward, R. et al. Environmental baseline monitoring : Phase III final report (2017-2018). This item has been internally reviewed, but not externally peer-reviewed. Nottingham, UK, 2018. URL: http://nora.nerc.ac.uk/id/eprint/521380/

Ward, R. et al. Environmental monitoring : phase 4 final report (April 2018 - March 2019). This item has been internally reviewed, but not externally peer-reviewed. Nottingham, UK, 2019. URL: http://nora.nerc.ac.uk/id/eprint/527726/

References

[1] GBD 2017 Risk Factor Collaborators. Global, regional, and national comparative risk assessment of 84 behavioural, environmental and occupational, and metabolic risks or clusters of risks for 195 countries and territories, 1990–2017: a systematic analysis for the Global Burden of Disease Study 2017. *The Lancet* 392.10159 (2018), pp. 1923–1994. URL: https://doi.org/10.1016/S0140-6736(18)32225-6.

[2] GBD 2019 Risk Factor Collaborators. Global burden of 369 diseases and injuries in 204 countries and territories, 1990–2019: a systematic analysis for the Global Burden of Disease Study 2019. *The Lancet* 396.10258 (2020), pp. 1204–1222. URL: https://doi.org/10.1016/S0140-6736(20)30925-9.

[3] Turnock, S. T., Butt, E. W., Richardson, T. B., Mann, G. W., Reddington, C. L., Forster, P. M., Haywood, J., Crippa, M., Janssens-Maenhout, G., Johnson, C. E., Bellouin, N., Carslaw, K. S., and Spracklen, D. V. The impact of European legislative and technology measures to reduce air pollutants on air quality, human health and climate. *Environ. Res. Lett.* 11.2 (2016), p. 024010. URL: http://dx.doi.org/10.1088/1748-9326/11/2/024010.

[4] Kampa, M. and Castanas, E. Human health effects of air pollution. *Environ. Pollut.* 151.2 (2008), pp. 362–367. URL: http://www.sciencedirect.com/science/article/pii/S0269749107002849.

[5] Mage, D., Ozolins, G., Peterson, P., Webster, A., Orthofer, R., Vandeweerd, V., and Gwynne, M. Urban air pollution in megacities of the world. *Atmos. Environ.* 30.5 (1996), pp. 681–686. URL: http://www.sciencedirect.com/science/article/pii/1352231095002197.

[6] Barnes, J. H., Chatterton, T. J., and Longhurst, J. W. S. Emissions vs exposure: Increasing injustice from road traffic-related air pollution in the United Kingdom. *Transp. Res. D. Transp. Environ.* 73 (2019), pp. 56–66. URL: http://www.sciencedirect.com/science/article/pii/S1361920919300392.

[7] BBC News. *Ella Adoo-Kissi-Debrah: Air pollution a factor in girl's death, inquest finds*. 2020. URL: https://www.bbc.co.uk/news/uk-england-london-55330945.

[8] Seinfeld, J. H. ES Books: Atmospheric Chemistry and Physics of Air Pollution. *Environ. Sci. Technol.* 20.9 (1986), pp. 863–863. URL: https://doi.org/10.1021/es00151a602.

[9] Cohen, A. J., Brauer, M., Burnett, R., Anderson, H. R., Frostad, J., Estep, K., Balakrishnan, K., Brunekreef, B., Dandona, L., Dandona, R., Feigin, V., Freedman, G., Hubbell, B., Jobling, A., Kan, H., Knibbs, L., Liu, Y., Martin, R., Morawska, L., Pope, C. A., Shin, H., Straif, K., Shaddick, G., Thomas, M., Dingenen, R. van, Donkelaar, A. van, Vos, T., Murray, C. J. L., and Forouzanfar, M. H. Estimates and 25-year trends of the global burden of disease attributable to ambient air pollution: an analysis of data from the Global Burden of Diseases Study 2015. *The Lancet* 389.10082 (2017), pp. 1907–1918. URL: http://www.sciencedirect.com/science/article/pii/S0140673617305056.

[10] Brunekreef, B. and Holgate, S. T. Air pollution and health. *The Lancet* 360.9341 (2002), pp. 1233–1242. URL: http://www.sciencedirect.com/science/article/pii/S0140673602112748.

[11] Oudin, A., Forsberg, B., Adolfsson, A. N., Lind, N., Modig, L., Nordin, M., Nordin, S., Adolfsson, R., and Nilsson, L.-G. Traffic-related air pollution and dementia incidence in northern Sweden: a longitudinal study. *Environ. Health Perspect.* 124.3 (2016), pp. 306–312.

[12] Peeples, L. News Feature: How air pollution threatens brain health. *Proc Natl Acad Sci USA* 117.25 (2020), p. 13856. URL: http://www.pnas.org/content/117/25/13856.abstract.

[13] Heck, W. W., Taylor, O. C., Adams, R., Bingham, G., Miller, J., Preston, E., and Weinstein, L. Assessment of Crop Loss from Ozone. *J. Air Pollut. Control Assoc.* 32.4 (1982), pp. 353–361. URL: https://doi.org/10.1080/00022470.1982.10465408.

[14] Mills, G., Sharps, K., Simpson, D., Pleijel, H., Frei, M., Burkey, K., Emberson, L., Uddling, J., Broberg, M., Feng, Z., Kobayashi, K., and Agrawal, M. Closing the global ozone yield gap: Quantification and cobenefits for multistress tolerance. *Glob. Change. Biol.* 24.10 (2018), pp. 4869–4893. URL: https://doi.org/10.1111/gcb.14381.

[15] Bobbink, R., Hornung, M., and Roelofs, J. G. M. The effects of air-borne nitrogen pollutants on species diversity in natural and semi-natural European vegetation. *J. Ecol.* 86.5 (1998), pp. 717–738. URL: https://doi.org/10.1046/j.1365-2745.1998.8650717.x.

[16] World Health Organisation. Air quality guidelines. Global update 2005. Particulate matter, ozone, nitrogen dioxide and sulfur dioxide (2006). URL: https://www.who.int/airpollution/publications/aqg2005/en/.

[17] Koppmann, R. *Volatile Organic Compounds in the Atmosphere*. Wiley, 2008. URL: https://books.google.co.uk/books?id=uUN3lFs_pgoC.

[18] Bauwens, M., Stavrakou, T., Müller, J.-F., De Smedt, I., Van Roozendael, M., Werf, G. R. van der, Wiedinmyer, C., Kaiser, J. W., Sindelarova, K., and Guenther, A. Nine years of global hydrocarbon emissions based on source inversion of OMI formaldehyde observations. *Atmos. Chem. Phys.* 16.15 (2016), pp. 10133–10158. URL: https://acp.copernicus.org/articles/16/10133/2016/.

[19] Guenther, A., Hewitt, C. N., Erickson, D., Fall, R., Geron, C., Graedel, T., Harley, P., Klinger, L., Lerdau, M., Mckay, W. A., Pierce, T., Scholes, B., Steinbrecher, R., Tallamraju, R., Taylor, J., and Zimmerman, P. A global model of natural volatile organic compound emissions. *J. Geophys. Res.* 100.D5 (1995), pp. 8873–8892. URL: https://doi.org/10.1029/94JD02950.

[20] Known and Unexplored Organic Constituents in the Earth's Atmosphere. *Environ. Sci. Technol.* 41.5 (2007), pp. 1514–1521. URL: https://doi.org/10.1021/es072476p.

[21] Blake, N. J., Blake, D. R., and Holton, J. R. TROPOSPHERIC CHEMISTRY AND COMPOSITION | VOCs: Overview. *Encyclopedia of Atmospheric Sciences*. Oxford: Academic Press, 2003, pp. 2438–2446. URL: http://www.sciencedirect.com/science/article/pii/B012227090800422X.

[22] Kansal, A. Sources and reactivity of NMHCs and VOCs in the atmosphere: A review. *J. Hazard. Mater.* 166.1 (2009), pp. 17–26. URL: http://www.sciencedirect.com/science/article/pii/S0304389408017391.

[23] Black, F. M., High, L. E., and Lang, J. M. Composition of Automobile Evaporative and Tailpipe Hydrocarbon Emissions. *J. Air Pollut. Control Assoc.* 30.11 (1980), pp. 1216–1220. URL: https://doi.org/10.1080/00022470.1980.10465171.

[24] Bailey, J. C., Schmidt, B., and Williams, M. L. Speciated hydrocarbon emissions from vehicles operated over the normal speed range on the road. *Atmos. Environ.* 24.1 (1990), pp. 43–52. URL: http://www.sciencedirect.com/science/article/pii/096016869090439T.

[25] Gilman, J. B., Lerner, B. M., Kuster, W. C., and Gouw, J. A. de. Source Signature of Volatile Organic Compounds from Oil and Natural Gas Operations in Northeastern Colorado. *Environ. Sci. Technol.* 47.3 (2013), pp. 1297–1305. URL: https://doi.org/10.1021/es304119a.

[26] Atkinson, R. and Aschmann, S. M. Products of the gas-phase reactions of aromatic hydrocarbons: Effect of NO_2 concentration. *Int. J. Chem. Kinet.* 26.9 (1994), pp. 929–944. URL: https://doi.org/10.1002/kin.550260907.

[27] Melnick, R. L. and Huff, J. 1,3-Butadiene: Toxicity and Carcinogenicity in Laboratory Animals and in Humans. *Reviews of Environmental Contamination and Toxicology: Continuation of Residue Reviews*. Ed. by G. W. Ware. New York, NY: Springer New York, 1992, pp. 111–144. URL: https://doi.org/10.1007/978-1-4612-2864-6_5.

[28] Oettingen, W. F. von. The Toxicity and Potential Dangers of Aliphatic and Aromatic Hydrocarbons. eng. *YJBM* 15.21434058 (1942), pp. 167–184. URL: https://www.ncbi.nlm.nih.gov/pmc/articles/PMC2601242/.

[29] Wallace L, A. Major sources of benzene exposure. *Environ. Health Perspect.* 82 (1989), pp. 165–169. URL: https://doi.org/10.1289/ehp.8982165.

[30] European Union. *EU. Directive 2008/50/EC of the European Parliament and of the Council of 21 May 2008 on ambient air quality and cleaner air for Europe*. 2008.

[31] Berkeley Earth. *Global Temperature Report for 2019*. 2020. URL: http://berkeleyearth.org/2019-temperatures/.

[32] Hawkins, E. *ShowYourStripes*. URL: https://showyourstripes.info/.

[33] Friedlingstein, P., O'Sullivan, M., Jones, M. W., Andrew, R. M., Hauck, J., Olsen, A., Peters, G. P., Peters, W., Pongratz, J., Sitch, S., Le Quéré, C., Canadell, J. G., Ciais, P., Jackson, R. B., Alin, S., Aragão, L. E. O. C., Arneth, A., Arora, V., Bates, N. R., Becker, M., Benoit-Cattin, A., Bittig, H. C., Bopp, L., Bultan, S., Chandra, N., Chevallier, F., Chini, L. P., Evans, W., Florentie, L., Forster, P. M., Gasser, T., Gehlen, M., Gilfillan, D., Gkritzalis, T., Gregor, L., Gruber, N., Harris, I., Hartung, K., Haverd, V., Houghton, R. A., Ilyina, T., Jain, A. K., Joetzjer, E., Kadono, K., Kato, E., Kitidis, V., Korsbakken, J. I., Landschützer, P., Lefèvre, N., Lenton, A., Lienert, S., Liu, Z., Lombardozzi, D., Marland, G., Metzl, N., Munro, D. R., Nabel, J. E. M. S., Nakaoka, S.-I., Niwa, Y., O'Brien, K., Ono, T., Palmer, P. I., Pierrot, D., Poulter, B., Resplandy, L., Robertson, E., Rödenbeck, C., Schwinger, J., Séférian, R., Skjelvan, I., Smith, A. J. P., Sutton, A. J., Tanhua, T., Tans, P. P., Tian, H., Tilbrook, B., Werf, G. van der, Vuichard, N., Walker, A. P., Wanninkhof, R., Watson, A. J., Willis, D., Wiltshire, A. J., Yuan, W., Yue, X., and Zaehle, S. Global Carbon Budget 2020. *Earth Syst. Sci. Data* 12.4 (2020), pp. 3269–3340. URL: https://essd.copernicus.org/articles/12/3269/2020/.

[34] IPCC. *Climate Change 2013: The Physical Science Basis. Contribution of Working Group I to the Fifth Assessment Report of the Intergovernmental Panel on Climate Change*. Cambridge, United Kingdom and New York, NY, USA: Cambridge University Press, 2013, p. 1535. URL: www.climatechange2013.org.

[35] Etminan, M., Myhre, G., Highwood, E. J., and Shine, K. P. Radiative forcing of carbon dioxide, methane, and nitrous oxide: A significant revision of the methane radiative forcing. *Geophys. Res. Lett.* 43.24 (2016), pp. 12, 614–12, 623. URL: https://doi.org/10.1002/2016GL071930.

[36] Tans, P. and Keeling, R. *Global Monitoring Laboratory*. Scripps Institution of Oceanography Scripps Institution of Oceanography. 2020. URL: www.esrl.noaa.gov/gmd/ccgg/trends/.

[37] Sabine, C. L., Feely, R. A., Gruber, N., Key, R. M., Lee, K., Bullister, J. L., Wanninkhof, R., Wong, C. S., Wallace, D. W. R., Tilbrook, B., Millero, F. J., Peng, T.-H., Kozyr, A., Ono, T., and Rios, A. F. The Oceanic Sink for Anthropogenic CO_2. *Science* 305.5682 (2004), p. 367. URL: http://science.sciencemag.org/content/305/5682/367.abstract.

[38] IPCC. Summary for Policymakers. *Climate Change 2013: The Physical Science Basis. Contribution of Working Group I to the Fifth Assessment Report of the Intergovernmental Panel on Climate Change*. Ed. by T. Stocker, D. Qin, G.-K. Plattner, M. Tignor, S. Allen, J. Boschung, A. Nauels, Y. Xia, V. Bex, and P. Midgley. Cambridge, United Kingdom and New York, NY, USA: Cambridge University Press, 2013. Chap. SPM, pp. 1–30. URL: www.climatechange2013.org.

[39] Doney, S. C., Fabry, V. J., Feely, R. A., and Kleypas, J. A. Ocean Acidification: The Other CO_2 Problem. *Annu. Rev. Mar. Sci.* 1.1 (2009), pp. 169–192. URL: https://doi.org/10.1146/annurev.marine.010908.163834.

[40] Doble, M., Kruthiventi, A. K., Doble, M., and Kruthiventi, A. K. CHAPTER 7 - Alternate Energy Sources. *Green Chemistry and Engineering*. Burlington: Academic Press, 2007, pp. 171–192. URL: http://www.sciencedirect.com/science/article/pii/B9780123725325500080.

[41] Myhre, G., Shindell, D., Breon, F.-M., Collins, W., Fuglestvedt, J., Huang, J., Koch, D., Lamarque, J.-F., Lee, D., Mendoza, B., Nakajima, T., Robock, A., Stephens, G., Takemura, T., and Zhang, H. Anthropogenic and Natural Radiative Forcing. *Climate Change 2013: The Physical Science Basis. Contribution of Working Group I to the Fifth Assessment Report of the Intergovernmental Panel on Climate Change*. Ed. by T. Stocker, D. Qin, G.-K. Plattner, M. Tignor, S. Allen, J. Boschung, A. Nauels, Y. Xia, V. Bex, and P. Midgley. Cambridge, United Kingdom and New York, NY, USA: Cambridge University Press, 2013. Chap. 8, pp. 659–740. URL: www.climatechange2013.org.

[42] Holmes, C. D. Methane Feedback on Atmospheric Chemistry: Methods, Models, and Mechanisms. *J. Adv. Model. Earth Syst.* 10.4 (2018), pp. 1087–1099. URL: https://doi.org/10.1002/2017MS001196.

[43] Volz, A. and Kley, D. Evaluation of the Montsouris series of ozone measurements made in the nineteenth century. *Nature* 332.6161 (1988), pp. 240–242. URL: https://doi.org/10.1038/332240a0.

[44] Derwent, R., Doherty, R., Collins, W., Sanderson, M., and Johnson, C. Radiative forcing from surface NO_x emissions: Spatial and seasonal variations. *Clim. Change* 88 (2008), pp. 385–401.

[45] Dlugokencky, E. J., Nisbet, E. G., Fisher, R., and Lowry, D. Global atmospheric methane: budget, changes and dangers. *Philos. Trans. Royal Soc. A* 369.1943 (2011), pp. 2058–2072. URL: https://doi.org/10.1098/rsta.2010.0341.

[46] Nisbet, E. G., Manning, M. R., Dlugokencky, E. J., Fisher, R. E., Lowry, D., Michel, S. E., Myhre, C. L., Platt, S. M., Allen, G., Bousquet, P., Brownlow, R., Cain, M., France, J. L., Hermansen, O., Hossaini, R., Jones, A. E., Levin, I., Manning, A. C., Myhre, G., Pyle, J. A., Vaughn, B. H., Warwick, N. J., and White, J. W. C. Very Strong Atmospheric Methane Growth in the 4 Years 2014-2017: Implications for the Paris Agreement. *Global Biogeochem. Cycles* 33.3 (2019), pp. 318–342. URL: https://doi.org/10.1029/2018GB006009.

[47] Dlugokencky, E. *Trends in Atmospheric Methane*. URL: www.esrl.noaa.gov/gmd/ccgg/trends_ch4/.

[48] Report of the Conference of the Parties on its 21st session, held in Paris from 30 November to 13 December 2015 : addendum (2016). Contains decision 1/CP.21: Adoption of the Paris Agreement., 36 p. URL: http://digitallibrary.un.org/record/831052.

[49] United Nations Environment Programme. *Emissions Gap Report 2019*. Nairobi: UNEP, 2019. URL: http://www.unenvironment.org/emissionsgap.

[50] Heilig, G. K. The greenhouse gas methane (CH_4): Sources and sinks, the impact of population growth, possible interventions. *Popul Environ* 16.2 (1994), pp. 109–137. URL: https://doi.org/10.1007/BF02208779.

[51] Denman, K., Brasseur, G., Chidthaisong, A., Ciais, P., Cox, P., Dickinson, R., Haugustaine, D., Heinze, C., Holland, E., Jacob, D., Lohmann, U., Ramachandran, S., Silva Dias, P., Wofsy, S., and Zhang, X. Couplings Between Changes in the Climate System and Biogeochemistry. Vol. 2007. 2007, pp. 499–587.

[52] Schwietzke, S., Sherwood, O. A., Bruhwiler, L. M. P., Miller, J. B., Etiope, G., Dlugokencky, E. J., Michel, S. E., Arling, V. A., Vaughn, B. H., White, J. W. C., and Tans, P. P. Upward revision of global fossil fuel methane emissions based on isotope database. *Nature* 538.7623 (2016), pp. 88–91. URL: https://doi.org/10.1038/nature19797.

[53] Bousquet, P., Ciais, P., Miller, J. B., Dlugokencky, E. J., Hauglustaine, D. A., Prigent, C., Van der Werf, G. R., Peylin, P., Brunke, E.-G., Carouge, C., Langenfelds, R. L., Lathière, J., Papa, F., Ramonet, M., Schmidt, M., Steele, L. P., Tyler, S. C., and White, J. Contribution of anthropogenic and natural sources to atmospheric methane variability. *Nature* 443.7110 (2006), pp. 439–443. URL: https://doi.org/10.1038/nature05132.

[54] Fiore, A. M., West, J. J., Horowitz, L. W., Naik, V., and Schwarzkopf, M. D. Characterizing the tropospheric ozone response to methane emission controls and the benefits to climate and air quality. *J. Geophys. Res.* 113.D8 (2008). URL: https://doi.org/10.1029/2007JD009162.

[55] Grange, S. K., Carslaw, D. C., Lewis, A. C., Boleti, E., and Hueglin, C. Random forest meteorological normalisation models for Swiss PM_{10} trend analysis. *Atmos. Chem. Phys.* 18.9 (2018), pp. 6223–6239. URL: https://acp.copernicus.org/articles/18/6223/2018/.

[56] Grange, S. K. and Carslaw, D. C. Using meteorological normalisation to detect interventions in air quality time series. *Sci. Total Environ.* 653 (2019), pp. 578–588. URL: http://www.sciencedirect.com/science/article/pii/S004896971834244X.

[57] Murgatroyd, R. J. *Troposphere*. 2019. URL: https://www.accessscience.com/content/troposphere/712200.

[58] Speight, J. G. Chapter 1 - Chemicals and the Environment. *Environmental Organic Chemistry for Engineers*. Butterworth-Heinemann, 2017, pp. 1–41. URL: http://www.sciencedirect.com/science/article/pii/B9780128044926000010.

[59] Stull, R. B. *An Introduction to Boundary Layer Meteorology*. Atmospheric and Oceanographic Sciences Library. Springer Netherlands, 2012. URL: https://books.google.co.uk/books?id=2PjrCAAAQBAJ.

[60] Lyman, S. and Tran, T. Inversion structure and winter ozone distribution in the Uintah Basin, Utah, USA. *Atmos. Environ.* 123 (2015), pp. 156–165.

[61] Foster, C. S., Crosman, E. T., Horel, J. D., Lyman, S., Fasoli, B., Bares, R., and Lin, J. C. Quantifying methane emissions in the Uintah Basin during wintertime stagnation episodes. *Elem. Sci. Anth.* 7.24 (2019). Ed. by D. Helmig and B. Lamb. URL: https://doi.org/10.1525/elementa.362.

[62] Edwards, P. M., Brown, S. S., Roberts, J. M., Ahmadov, R., Banta, R. M., deGouw, J. A., Dubé, W. P., Field, R. A., Flynn, J. H., Gilman, J. B., Graus, M., Helmig, D., Koss, A., Langford, A. O., Lefer, B. L., Lerner, B. M., Li, R., Li, S.-M., McKeen, S. A., Murphy, S. M., Parrish, D. D., Senff, C. J., Soltis, J., Stutz, J., Sweeney, C., Thompson, C. R., Trainer, M. K., Tsai, C., Veres, P. R.,

Washenfelder, R. A., Warneke, C., Wild, R. J., Young, C. J., Yuan, B., and Zamora, R. High winter ozone pollution from carbonyl photolysis in an oil and gas basin. *Nature* 514.7522 (2014), pp. 351–354. URL: https://doi.org/10.1038/nature13767.

[63] Koss, A. R., Gouw, J. de, Warneke, C., Gilman, J. B., Lerner, B. M., Graus, M., Yuan, B., Edwards, P., Brown, S. S., Wild, R., Roberts, J. M., Bates, T. S., and Quinn, P. K. Photochemical aging of volatile organic compounds associated with oil and natural gas extraction in the Uintah Basin, UT, during a wintertime ozone formation event. *Atmos. Chem. Phys.* 15.10 (2015), pp. 5727–5741. URL: https://acp.copernicus.org/articles/15/5727/2015/.

[64] Vieno, M., Heal, M. R., Twigg, M. M., MacKenzie, I. A., Braban, C. F., Lingard, J. J. N., Ritchie, S., Beck, R. C., Móring, A., Ots, R., Di Marco, C. F., Nemitz, E., Sutton, M. A., and Reis, S. The UK particulate matter air pollution episode of March-April 2014: more than Saharan dust. *Environ. Res. Lett.* 11.4 (2016), p. 044004. URL: http://dx.doi.org/10.1088/1748-9326/11/4/044004.

[65] Bloss, W. J., Evans, M. J., Lee, J. D., Sommariva, R., Heard, D. E., and Pilling, M. J. The oxidative capacity of the troposphere: Coupling of field measurements of OH and a global chemistry transport model. *Faraday Discuss.* 130 (0 2005), pp. 425–436. URL: http://dx.doi.org/10.1039/B419090D.

[66] Harris, G. W., Carter, W. P. L., Winer, A. M., Pitts, J. N., Platt, U., and Perner, D. Observations of nitrous acid in the Los Angeles atmosphere and implications for predictions of ozone-precursor relationships. *Environ. Sci. Technol.* 16.7 (1982), pp. 414–419. URL: https://doi.org/10.1021/es00101a009.

[67] Calvert, J. G., Yarwood, G., and Dunker, A. M. An evaluation of the mechanism of nitrous acid formation in the urban atmosphere. *Res. Chem. Intermed.* 20.3 (1994), pp. 463–502. URL: https://doi.org/10.1163/156856794X00423.

[68] Zhang, W., Tong, S., Jia, C., Wang, L., Liu, B., Tang, G., Ji, D., Hu, B., Liu, Z., Li, W., Wang, Z., Liu, Y., Wang, Y., and Ge, M. Different HONO Sources for Three Layers at the Urban Area of Beijing. *Environ. Sci. Technol.* 54.20 (2020), pp. 12870–12880. URL: https://doi.org/10.1021/acs.est.0c02146.

[69] Finlayson-Pitts, B. J., Pitts, J. N., Finlayson-Pitts, B. J., and Pitts, J. N. CHAPTER 1 - Overview of the Chemistry of Polluted and Remote Atmospheres. *Chemistry of the Upper and Lower Atmosphere*. San Diego: Academic Press, 2000, pp. 1–14. URL: https://www.sciencedirect.com/science/article/pii/B9780122570605500034.

[70] Monks, P. S., Archibald, A. T., Colette, A., Cooper, O., Coyle, M., Derwent, R., Fowler, D., Granier, C., Law, K. S., Mills, G. E., Stevenson, D. S., Tarasova, O., Thouret, V., Schneidemesser, E. von, Sommariva, R., Wild, O., and Williams, M. L. Tropospheric ozone and its precursors from the urban to the global scale from air quality to short-lived climate forcer. *Atmos. Chem. Phys.* 15.15 (2015), pp. 8889–8973. URL: https://acp.copernicus.org/articles/15/8889/2015/.

[71] Wolfe, G. M., Cantrell, C., Kim, S., Mauldin III, R. L., Karl, T., Harley, P., Turnipseed, A., Zheng, W., Flocke, F., Apel, E. C., Hornbrook, R. S., Hall, S. R., Ullmann, K., Henry, S. B., DiGangi, J. P., Boyle, E. S., Kaser, L., Schnitzhofer, R., Hansel, A., Graus, M., Nakashima, Y., Kajii, Y., Guenther, A., and Keutsch, F. N. Missing peroxy radical sources within a summertime ponderosa pine forest. *Atmos. Chem. Phys.* 14.9 (2014), pp. 4715–4732. URL: https://acp.copernicus.org/articles/14/4715/2014/.

[72] Lightfoot, P. D., Cox, R. A., Crowley, J. N., Destriau, M., Hayman, G. D., Jenkin, M. E., Moortgat, G. K., and Zabel, F. Organic peroxy radicals: Kinetics, spectroscopy and tropospheric chemistry. *Atmos. Environ.* 26.10 (1992), pp. 1805–1961. URL: https://www.sciencedirect.com/science/article/pii/096016869290423I.

[73] Perring, A. E., Pusede, S. E., and Cohen, R. C. An Observational Perspective on the Atmospheric Impacts of Alkyl and Multifunctional Nitrates on Ozone and Secondary Organic Aerosol. *Chem. Rev.* 113.8 (2013), pp. 5848–5870. URL: https://doi.org/10.1021/cr300520x.

[74] Monks, P. S. Gas-phase radical chemistry in the troposphere. *Chem. Soc. Rev.* 34.5 (2005), pp. 376–395. URL: http://dx.doi.org/10.1039/B307982C.

[75] Finlayson-Pitts, B. J. and Pitts Jr, J. N. Atmospheric chemistry. Fundamentals and experimental techniques (1986). URL: https://www.osti.gov/biblio/6379212.

[76] Dalsøren, S. B., Myhre, G., Hodnebrog, Ø., Myhre, C. L., Stohl, A., Pisso, I., Schwietzke, S., Höglund-Isaksson, L., Helmig, D., Reimann, S., Sauvage, S., Schmidbauer, N., Read, K. A., Carpenter, L. J., Lewis, A. C., Punjabi, S., and Wallasch, M. Discrepancy between simulated and observed ethane and propanelevels explained by underestimated fossil emissions. *Nat. Geosci.* 11.3 (2018), pp. 178–184. URL: https://doi.org/10.1038/s41561-018-0073-0.

[77] Finlayson-Pitts, B. J., Pitts, J. N., Finlayson-Pitts, B. J., and Pitts, J. N. CHAPTER 6 - Rates and Mechanisms of Gas-Phase Reactions in Irradiated Organic - NO_x - Air Mixtures. *Chemistry of the Upper and Lower Atmosphere*. San Diego: Academic Press, 2000, pp. 179–263. URL: https://www.sciencedirect.com/science/article/pii/B9780122570605500083.

[78] Council, N. R. *Rethinking the Ozone Problem in Urban and Regional Air Pollution*. Washington, DC: The National Academies Press, 1991. URL: https://www.nap.edu/catalog/1889/rethinking-the-ozone-problem-in-urban-and-regional-air-pollution.

[79] Atkinson, R., Tuazon, E. C., and Carter, W. P. L. Extent of H-atom abstraction from the reaction of the OH radical with 1-butene under atmospheric conditions. *Int. J. Chem. Kinet.* 17.7 (1985), pp. 725–734. URL: https://doi.org/10.1002/kin.550170703.

[80] Atkinson, R. Atmospheric chemistry of VOCs and NO_x. *Atmos. Environ.* 34.12 (2000), pp. 2063–2101. URL: https://www.sciencedirect.com/science/article/pii/S1352231099004604.

[81] Khan, M. A. H., Percival, C. J., Caravan, R. L., Taatjes, C. A., and Shallcross, D. E. Criegee intermediates and their impacts on the troposphere. *Environ. Sci.: Processes Impacts* 20.3 (2018), pp. 437–453. URL: http://dx.doi.org/10.1039/C7EM00585G.

[82] Alam, M. S., Rickard, A. R., Camredon, M., Wyche, K. P., Carr, T., Hornsby, K. E., Monks, P. S., and Bloss, W. J. Radical Product Yields from the Ozonolysis of Short Chain Alkenes under Atmospheric Boundary Layer Conditions. *J. Phys. Chem. A* 117.47 (2013), pp. 12468–12483. URL: https://doi.org/10.1021/jp408745h.

[83] Emmerson, K. M., Carslaw, N., Carslaw, D. C., Lee, J. D., McFiggans, G., Bloss, W. J., Gravestock, T., Heard, D. E., Hopkins, J., Ingham, T., Pilling, M. J., Smith, S. C., Jacob, M., and Monks, P. S. Free radical modelling studies during the UK TORCH Campaign in Summer 2003. *Atmos. Chem. Phys.* 7.1 (2007), pp. 167–181. URL: https://acp.copernicus.org/articles/7/167/2007/.

[84] Newland, M. J., Rickard, A. R., Alam, M. S., Vereecken, L., Muñoz, A., Ródenas, M., and Bloss, W. J. Kinetics of stabilised Criegee intermediates derived from alkene ozonolysis: reactions with SO_2, H_2O and decomposition under boundary layer conditions. *Phys. Chem. Chem. Phys.* 17.6 (2015), pp. 4076–4088. URL: http://dx.doi.org/10.1039/C4CP04186K.

[85] Welz, O., Eskola, A. J., Sheps, L., Rotavera, B., Savee, J. D., Scheer, A. M., Osborn, D. L., Lowe, D., Murray Booth, A., Xiao, P., Anwar H. Khan, M., Percival, C. J., Shallcross, D. E., and Taatjes, C. A. Rate Coefficients of C1 and C2 Criegee Intermediate Reactions with Formic and Acetic Acid Near the Collision Limit: Direct Kinetics Measurements and Atmospheric Implications. *Angew. Chem. Int. Ed.* 53.18 (2014), pp. 4547–4550. URL: https://doi.org/10.1002/anie.201400964.

[86] Newland, M. J., Rickard, A. R., Sherwen, T., Evans, M. J., Vereecken, L., Muñoz, A., Ródenas, M., and Bloss, W. J. The atmospheric impacts of monoterpene ozonolysis on global

stabilised Criegee intermediate budgets and SO_2 oxidation: experiment, theory and modelling. *Atmos. Chem. Phys.* 18.8 (2018), pp. 6095–6120. URL: https://acp.copernicus.org/articles/18/6095/2018/.

[87] Sarwar, G., Simon, H., Fahey, K., Mathur, R., Goliff, W. S., and Stockwell, W. R. Impact of sulfur dioxide oxidation by Stabilized Criegee Intermediate on sulfate. *Atmos. Environ.* 85 (2014), pp. 204–214. URL: https://www.sciencedirect.com/science/article/pii/S1352231013009503.

[88] Suh, I., Zhang, R., Molina, L. T., and Molina, M. J. Oxidation Mechanism of Aromatic Peroxy and Bicyclic Radicals from OH–Toluene Reactions. *J. Am. Chem. Soc.* 125.41 (2003), pp. 12655–12665. URL: https://doi.org/10.1021/ja0350280.

[89] Klotz, B., Sorensen, S., Barnes, I., Becker, K. H., Etzkorn, T., Volkamer, R., Platt, U., Wirtz, K., and Martin-Reviejo, M. Atmospheric Oxidation of Toluene in a Large-Volume Outdoor Photoreactor: In Situ Determination of Ring-Retaining Product Yields. *J. Phys. Chem. A* 102.50 (1998), pp. 10289–10299. URL: https://doi.org/10.1021/jp982719n.

[90] Zaytsev, A., Koss, A., Breitenlechner, M., Krechmer, J., Nihill, K., Lim, C., Rowe, J., Cox, J., Moss, J., Roscioli, J., Worsnop, D., Kroll, J., and Keutsch, F. Mechanistic study of the formation of ring-retaining and ring-opening products from the oxidation of aromatic compounds under urban atmospheric conditions. *Atmos. Chem. Phys.* 19 (2019), pp. 15117–15129.

[91] Schwantes, R. H., Schilling, K. A., McVay, R. C., Lignell, H., Coggon, M. M., Zhang, X., Wennberg, P. O., and Seinfeld, J. H. Formation of highly oxygenated low-volatility products from cresol oxidation. *Atmos. Chem. Phys.* 17.5 (2017), pp. 3453–3474. URL: https://acp.copernicus.org/articles/17/3453/2017/.

[92] Tanner, R. L. and Parkhurst, W. J. Chemical Composition of Fine Particles in the Tennessee Valley Region. *J. Air. Waste Manag. Assoc.* 50.8 (2000), pp. 1299–1307. URL: https://doi.org/10.1080/10473289.2000.10464175.

[93] Hansen, J. E. and Sato, M. Trends of measured climate forcing agents. *Proc Natl Acad Sci USA* 98.26 (2001), p. 14778. URL: http://www.pnas.org/content/98/26/14778.abstract.

[94] Jang, M., Czoschke, N. M., Lee, S., and Kamens, R. M. Heterogeneous Atmospheric Aerosol Production by Acid-Catalyzed Particle-Phase Reactions. *Science* 298.5594 (2002), p. 814. URL: http://science.sciencemag.org/content/298/5594/814.abstract.

[95] Ziemann, P. J. and Atkinson, R. Kinetics, products, and mechanisms of secondary organic aerosol formation. *Chem. Soc. Rev.* 41.19 (2012), pp. 6582–6605. URL: http://dx.doi.org/10.1039/C2CS35122F.

[96] Kroll, J. H. and Seinfeld, J. H. Chemistry of secondary organic aerosol: Formation and evolution of low-volatility organics in the atmosphere. *Atmos. Environ.* 42.16 (2008), pp. 3593–3624. URL: https://www.sciencedirect.com/science/article/pii/S1352231008000253.

[97] Kroll, J. H., Ng, N. L., Murphy, S. M., Flagan, R. C., and Seinfeld, J. H. Secondary Organic Aerosol Formation from Isoprene Photooxidation. *Environ. Sci. Technol.* 40.6 (2006), pp. 1869–1877. URL: https://doi.org/10.1021/es0524301.

[98] Carlton, A. G., Wiedinmyer, C., and Kroll, J. H. A review of Secondary Organic Aerosol (SOA) formation from isoprene. *Atmospheric Chemistry and Physics* 9.14 (2009), pp. 4987–5005. URL: https://acp.copernicus.org/articles/9/4987/2009/.

[99] Odum, J. R., Jungkamp, T. P. W., Griffin, R. J., Flagan, R. C., and Seinfeld, J. H. The Atmospheric Aerosol-Forming Potential of Whole Gasoline Vapor. *Science* 276.5309 (1997), p. 96. URL: http://science.sciencemag.org/content/276/5309/96.abstract.

[100] Liggio, J., Li, S.-M., Hayden, K., Taha, Y. M., Stroud, C., Darlington, A., Drollette, B. D., Gordon, M., Lee, P., Liu, P., Leithead, A., Moussa, S. G., Wang, D., O'Brien, J., Mittermeier, R. L., Brook, J. R., Lu, G., Staebler, R. M., Han, Y., Tokarek, T. W., Osthoff, H. D., Makar, P. A., Zhang, J., L. Plata, D., and Gentner, D. R. Oil sands operations as a large source of secondary organic aerosols. *Nature* 534.7605 (2016), pp. 91–94. URL: https://doi.org/10.1038/nature17646.

[101] Beck, C., Rashidbeig, S., Roelofsen, O., and Speelman, E. The future is now: How oil and gas companies can decarbonize (2020). URL: https://www.mckinsey.com/industries/oil-and-gas/our-insights/the-future-is-now-how-oil-and-gas-companies-can-decarbonize.

[102] IEA. *World Energy Outlook 2018*. Paris, 2018. URL: https://www.iea.org/reports/world-energy-outlook-2018.

[103] Statista. *World natural gas production in 2019, by country*. 2020. URL: https://www.statista.com/statistics/264101/world-natural-gas-production-by-country/:~:text=As%20of%202019,%20the%20United,the%20second%20biggest%20producer%20-%20Russia..

[104] Pozzer, A., Schultz, M. G., and Helmig, D. Impact of U.S. Oil and Natural Gas Emission Increases on Surface Ozone Is Most Pronounced in the Central United States. *Environ. Sci. Technol.* 54.19 (2020), pp. 12423–12433. URL: https://doi.org/10.1021/acs.est.9b06983.

[105] Field, R. A., Soltis, J., and Murphy, S. Air quality concerns of unconventional oil and natural gas production. *Environ. Sci.: Processes Impacts* 16.5 (2014), pp. 954–969. URL: http://dx.doi.org/10.1039/C4EM00081A.

[106] Liss, W. E., Thrasher, W. H., Steinmetz, G. F., Chowdiah, P., and Attari, A. Variability of natural gas composition in select major metropolitan areas of the United States. Final report, August 1990-February 1992 (1992). URL: https://www.osti.gov/biblio/7248745.

[107] Brandt, A. R., Heath, G. A., Kort, E. A., O'Sullivan, F., Pétron, G., Jordaan, S. M., Tans, P., Wilcox, J., Gopstein, A. M., Arent, D., Wofsy, S., Brown, N. J., Bradley, R., Stucky, G. D., Eardley, D., and Harriss, R. Methane Leaks from North American Natural Gas Systems. *Science* 343.6172 (2014), pp. 733–735. URL: https://science.sciencemag.org/content/343/6172/733.

[108] Karion, A., Sweeney, C., Kort, E. A., Shepson, P. B., Brewer, A., Cambaliza, M., Conley, S. A., Davis, K., Deng, A., Hardesty, M., Herndon, S. C., Lauvaux, T., Lavoie, T., Lyon, D., Newberger, T., Pétron, G., Rella, C., Smith, M., Wolter, S., Yacovitch, T. I., and Tans, P. Aircraft-Based Estimate of Total Methane Emissions from the Barnett Shale Region. *Environ. Sci. Technol.* 49.13 (2015), pp. 8124–8131. URL: https://doi.org/10.1021/acs.est.5b00217.

[109] Alvarez, R. A., Zavala-Araiza, D., Lyon, D. R., Allen, D. T., Barkley, Z. R., Brandt, A. R., Davis, K. J., Herndon, S. C., Jacob, D. J., Karion, A., Kort, E. A., Lamb, B. K., Lauvaux, T., Maasakkers, J. D., Marchese, A. J., Omara, M., Pacala, S. W., Peischl, J., Robinson, A. L., Shepson, P. B., Sweeney, C., Townsend-Small, A., Wofsy, S. C., and Hamburg, S. P. Assessment of methane emissions from the U.S. oil and gas supply chain. *Science* 361.6398 (2018), pp. 186–188. URL: https://science.sciencemag.org/content/361/6398/186.

[110] Allen, D. T. Emissions from oil and gas operations in the United States and their air quality implications. *J. Air. Waste Manag. Assoc.* 66.6 (2016). PMID: 27249104, pp. 549–575. URL: https://doi.org/10.1080/10962247.2016.1171263.

[111] Olaguer, E. P. The potential near-source ozone impacts of upstream oil and gas industry emissions. *J. Air. Waste Manag. Assoc.* 62.8 (2012), pp. 966–977. URL: https://doi.org/10.1080/10962247.2012.688923.

[112] Kemball-Cook, S., Bar-Ilan, A., Grant, J., Parker, L., Jung, J., Santamaria, W., Mathews, J., and Yarwood, G. Ozone Impacts of Natural Gas Development in the Haynesville Shale. *Environ. Sci. Technol.* 44.24 (2010), pp. 9357–9363. URL: https://doi.org/10.1021/es1021137.

[113] Fann, N., Baker, K. R., Chan, E. A. W., Eyth, A., Macpherson, A., Miller, E., and Snyder, J. Assessing Human Health $PM_{2.5}$ and Ozone Impacts from U.S. Oil and Natural Gas Sector Emissions in 2025. *Environ. Sci. Technol.* 52.15 (2018), pp. 8095–8103. URL: https://doi.org/10.1021/acs.est.8b02050.

[114] Moore, C. W., Zielinska, B., Pétron, G., and Jackson, R. B. Air Impacts of Increased Natural Gas Acquisition, Processing, and Use: A Critical Review. *Environ. Sci. Technol.* 48.15 (2014), pp. 8349–8359. URL: https://doi.org/10.1021/es4053472.

[115] Vengosh, A., Jackson, R. B., Warner, N., Darrah, T. H., and Kondash, A. A Critical Review of the Risks to Water Resources from Unconventional Shale Gas Development and Hydraulic Fracturing in the United States. *Environ. Sci. Technol.* 48.15 (2014), pp. 8334–8348. URL: https://doi.org/10.1021/es405118y.

[116] Litovitz, A., Curtright, A., Abramzon, S., Burger, N., and Samaras, C. Estimation of regional air-quality damages from Marcellus Shale natural gas extraction in Pennsylvania. *Environ. Res. Lett.* 8.1 (2013), p. 014017. URL: http://dx.doi.org/10.1088/1748-9326/8/1/014017.

[117] Bar-Ilan, A., Johnson, J. R., DenBleyker, A., Chan, L.-M., Yarwood, G., Hitchcock, D., and Pinto, J. P. Potential Ozone Impacts of Excess NO_2 Emissions from Diesel Particulate Filters for On- and Off-Road Diesel Engines. *J. Air. Waste Manag. Assoc.* 60.8 (2010), pp. 977–992. URL: https://doi.org/10.3155/1047-3289.60.8.977.

[118] Jiang, M., Michael Griffin, W., Hendrickson, C., Jaramillo, P., VanBriesen, J., and Venkatesh, A. Life cycle greenhouse gas emissions of Marcellus shale gas. *Environ. Res. Lett.* 6.3 (2011), p. 034014. URL: http://dx.doi.org/10.1088/1748-9326/6/3/034014.

[119] McKenzie, L. M., Witter, R. Z., Newman, L. S., and Adgate, J. L. Human health risk assessment of air emissions from development of unconventional natural gas resources. *Sci. Total Environ.* 424 (2012), pp. 79–87. URL: http://www.sciencedirect.com/science/article/pii/S0048969712001933.

[120] Shaw, J. T., Allen, G., Pitt, J., Mead, M. I., Purvis, R. M., Dunmore, R., Wilde, S., Shah, A., Barker, P., Bateson, P., Bacak, A., Lewis, A. C., Lowry, D., Fisher, R., Lanoisellé, M., and Ward, R. S. A baseline of atmospheric greenhouse gases for prospective UK shale gas sites. *Sci. Total Environ.* 684 (2019), pp. 1–13. URL: http://www.sciencedirect.com/science/article/pii/S0048969719323071.

[121] Department for Business, Energy and Industrial Strategy. Provisional UK greenhouse gas emissions national statistics 2019 (2020).

[122] Emam, E. A. GAS FLARING IN INDUSTRY: AN OVERVIEW. *Petroleum & coal* 57.5 (2015).

[123] IEA. *Flaring Emissions*. 2020. URL: https://www.iea.org/reports/flaring-emissions.

[124] Pétron, G., Karion, A., Sweeney, C., Miller, B. R., Montzka, S. A., Frost, G. J., Trainer, M., Tans, P., Andrews, A., Kofler, J., Helmig, D., Guenther, D., Dlugokencky, E., Lang, P., Newberger, T., Wolter, S., Hall, B., Novelli, P., Brewer, A., Conley, S., Hardesty, M., Banta, R., White, A., Noone, D., Wolfe, D., and Schnell, R. A new look at methane and nonmethane hydrocarbon emissions from oil and natural gas operations in the Colorado Denver-Julesburg Basin. *J. Geophys. Res. Atmos.* 119.11 (2019), pp. 6836–6852. URL: https://doi.org/10.1002/2013JD021272.

[125] Climate and Clean Air Coalition. Unstabilized Hydrocarbon Liquid Storage Tanks (2017). URL: https://www.ccacoalition.org/en/resources/technical-guidance-document-number-6-unstabilized-hydrocarbon-liquid-storage-tanks.

[126] Warneke, C., Geiger, F., Edwards, P. M., Dube, W., Pétron, G., Kofler, J., Zahn, A., Brown, S. S., Graus, M., Gilman, J. B., Lerner, B. M., Peischl, J., Ryerson, T. B., Gouw, J. A. de, and Roberts, J. M. Volatile organic compound emissions from the oil and natural gas industry in the Uintah Basin, Utah: oil and gas well pad emissions compared to ambient air composition. *Atmos. Chem. Phys.* 14.20 (2014), pp. 10977–10988. URL: https://www.atmos-chem-phys.net/14/10977/2014/.

[127] Hill, N. and Rudd, H. Measures to Reduce Emissions of VOCs during Loading and Unloading of Ships in the EU A report produced for the European Commission. AEAT/ENV/R/0469. 2001. URL: https://ec.europa.eu/environment/archives/air/pdf/vocloading.pdf.

[128] Maritime Impact. *Eco-friendly shuttle tankers for Norway*. 2018. URL: https://www.dnvgl.com/expert-story/maritime-impact/Eco-friendly-shuttle-tankers-for-Norway.html.

[129] Burnham, A., Han, J., Clark, C. E., Wang, M., Dunn, J. B., and Palou-Rivera, I. Life-Cycle Greenhouse Gas Emissions of Shale Gas, Natural Gas, Coal, and Petroleum. *Environ. Sci. Technol.* 46.2 (2012), pp. 619–627. URL: https://doi.org/10.1021/es201942m.

[130] Jaramillo, P., Griffin, W. M., and Matthews, H. S. Comparative Life-Cycle Air Emissions of Coal, Domestic Natural Gas, LNG, and SNG for Electricity Generation. *Environ. Sci. Technol.* 41.17 (2007), pp. 6290–6296. URL: https://doi.org/10.1021/es063031o.

[131] U.S. Energy Information Administration. *Annual petroleum and other liquids production*. 2020. URL: https://www.eia.gov/.

[132] Oil and Gas UK. Economic Report (2020). URL: https://oilandgasuk.co.uk/product/economic-report/.

[133] Department for Business, Energy and Industrial Strategy. *Digest of United Kingdon Energy Statistics (DUKES)*. National Statistics, 2019.

[134] Oil and Gas Authority. UK Oil and Gas Reserves and Resources (2020). URL: https://www.ogauthority.co.uk/news-publications/publications/2018/uk-oil-and-gas-reserves-and-resources-report/.

[135] NS Energy. *West of Shetland oil fields to grow in stature among European majors*. 2019. URL: https://www.nsenergybusiness.com/news/industry-news/west-shetland-oil-fields/.

[136] Oil and Gas Authority. *OGA Offshore Fields WGS84*. (Accessed 13/11/2019). 2019. URL: https://data-ogauthority.opendata.arcgis.com/datasets/oga-offshore-fields-wgs84.

[137] Oil and Gas UK. Environment Report (2019). URL: https://oilandgasuk.co.uk/wp-content/uploads/2019/08/Environment-Report-2019-AUG20.pdf.

[138] Department for Environment, Food and Rural Affairs. *Air Pollution in the UK 2018*. 2018. URL: https://uk-air.defra.gov.uk/assets/documents/annualreport/air_pollution_uk_2016_issue_2.pdf.

[139] Oil & Gas UK. *EEMS - Atmospheric Emissions Calculations*. 2008.

[140] Cheremisinoff, N. P., Letcher, T. M., and Vallero, D. A. Chapter 31 - Pollution Management and Responsible Care. *Waste*. Boston: Academic Press, 2011, pp. 487–502. URL: https://www.sciencedirect.com/science/article/pii/B9780123814753100312.

[141] Lavoie, T. N., Shepson, P. B., Cambaliza, M. O. L., Stirm, B. H., Karion, A., Sweeney, C., Yacovitch, T. I., Herndon, S. C., Lan, X., and Lyon, D. Aircraft-Based Measurements of Point Source Methane Emissions in the Barnett Shale Basin. *Environ. Sci. Technol.* 49.13 (2015), pp. 7904–7913. URL: https://doi.org/10.1021/acs.est.5b00410.

[142] Li, S.-M., Leithead, A., Moussa, S. G., Liggio, J., Moran, M. D., Wang, D., Hayden, K., Darlington, A., Gordon, M., Staebler, R., Makar, P. A., Stroud, C. A., McLaren, R., Liu, P. S. K., O'Brien, J., Mittermeier, R. L., Zhang, J., Marson, G., Cober, S. G., Wolde, M., and Wentzell, J. J. B. Differences between measured and reported volatile organic compound emissions from oil sands facilities in Alberta, Canada. *Proc. Natl. Acad. Sci. U.S.A.* 114.19 (2017), E3756–E3765. URL: https://www.pnas.org/content/114/19/E3756.

[143] Lyon, D. R., Zavala-Araiza, D., Alvarez, R. A., Harriss, R., Palacios, V., Lan, X., Talbot, R., Lavoie, T., Shepson, P., Yacovitch, T. I., Herndon, S. C., Marchese, A. J., Zimmerle, D., Robinson, A. L., and Hamburg, S. P. Constructing a Spatially Resolved Methane Emission Inventory for the Barnett Shale Region. *Environ. Sci. Technol.* 49.13 (2015), pp. 8147–8157. URL: https://doi.org/10.1021/es506359c.

[144] Yacovitch, T. I., Neininger, B., Herndon, S. C., Gon, H. D. van der, Jonkers, S., Hulskotte, J., Roscioli, J. R., and Zavala-Araiza, D. Methane emissions in the Netherlands: The Groningen field. *Elem. Sci. Anth.* 6.57 (2018). Ed. by D. Helmig and S. Schwietzke. URL: https://doi.org/10.1525/elementa.308.

[145] France, J. L., Bateson, P., Dominutti, P., Allen, G., Andrews, S., Bauguitte, S., Coleman, M., Lachlan-Cope, T., Fisher, R. E., Huang, L., Jones, A. E., Lee, J., Lowry, D., Pitt, J., Purvis, R., Pyle, J., Shaw, J., Warwick, N., Weiss, A., Wilde, S., Witherstone, J., and Young, S. Facility level measurement of offshore oil and gas installations from a medium-sized airborne platform: method development for quantification and source identification of methane emissions. *Atmos. Meas. Tech.* 14.1 (2021), pp. 71–88. URL: https://amt.copernicus.org/articles/14/71/2021/.

[146] O'Shea, S. J., Bauguitte, S. J.-B., Gallagher, M. W., Lowry, D., and Percival, C. J. Development of a cavity-enhanced absorption spectrometer for airborne measurements of CH_4 and CO_2. *Atmos. Meas. Tech.* 6.5 (2013), pp. 1095–1109. URL: https://www.atmos-meas-tech.net/6/1095/2013/.

[147] Lee, J. D., Mobbs, S. D., Wellpott, A., Allen, G., Bauguitte, S. J.-B., Burton, R. R., Camilli, R., Coe, H., Fisher, R. E., France, J. L., Gallagher, M., Hopkins, J. R., Lanoiselle, M., Lewis, A. C., Lowry, D., Nisbet, E. G., Purvis, R. M., O'Shea, S., Pyle, J. A., and Ryerson, T. B. Flow rate and source reservoir identification from airborne chemical sampling of the uncontrolled Elgin platform gas release. *Atmos. Meas. Tech.* 11.3 (2018), pp. 1725–1739. URL: https://www.atmos-meas-tech.net/11/1725/2018/.

[148] Cain, M., Warwick, N. J., Fisher, R. E., Lowry, D., Lanoisellé, M., Nisbet, E. G., France, J., Pitt, J., O'Shea, S., Bower, K. N., Allen, G., Illingworth, S., Manning, A. J., Bauguitte, S., Pisso, I., and Pyle, J. A. A cautionary tale: A study of a methane enhancement over the North Sea. *J. Geophys. Res. Atmos.* 122.14 (2017), pp. 7630–7645. URL: https://doi.org/10.1002/2017JD026626.

[149] Yacovitch, T. I., Herndon, S. C., Roscioli, J. R., Floerchinger, C., McGovern, R. M., Agnese, M., Pétron, G., Kofler, J., Sweeney, C., Karion, A., Conley, S. A., Kort, E. A., Nähle, L., Fischer, M., Hildebrandt, L., Koeth, J., McManus, J. B., Nelson, D. D., Zahniser, M. S., and Kolb, C. E. Demonstration of an Ethane Spectrometer for Methane Source Identification. *Environ. Sci. Technol.* 48.14 (2014), pp. 8028–8034. URL: https://doi.org/10.1021/es501475q.

[150] Pitt, J. R., Le Breton, M., Allen, G., Percival, C. J., Gallagher, M. W., Bauguitte, S. J.-B., O'Shea, S. J., Muller, J. B. A., Zahniser, M. S., Pyle, J., and Palmer, P. I. The development and evalua-

tion of airborne in situ N_2O and CH_4 sampling using a quantum cascade laser absorption spectrometer (QCLAS). *Atmos. Meas. Tech.* 9.1 (2016), pp. 63–77. URL: https://www.atmos-meas-tech.net/9/63/2016/.

[151] Carpenter, L. J., Fleming, Z. L., Read, K. A., Lee, J. D., Moller, S. J., Hopkins, J. R., Purvis, R. M., Lewis, A. C., Müller, K., Heinold, B., Herrmann, H., Fomba, K. W., Pinxteren, D. van, Müller, C., Tegen, I., Wiedensohler, A., Müller, T., Niedermeier, N., Achterberg, E. P., Patey, M. D., Kozlova, E. A., Heimann, M., Heard, D. E., Plane, J. M. C., Mahajan, A., Oetjen, H., Ingham, T., Stone, D., Whalley, L. K., Evans, M. J., Pilling, M. J., Leigh, R. J., Monks, P. S., Karunaharan, A., Vaughan, S., Arnold, S. R., Tschritter, J., Pöhler, D., Frieß, U., Holla, R., Mendes, L. M., Lopez, H., Faria, B., Manning, A. J., and Wallace, D. W. R. Seasonal characteristics of tropical marine boundary layer air measured at the Cape Verde Atmospheric Observatory. *J. Atmos. Chem.* 67.2 (2010), pp. 87–140. URL: https://doi.org/10.1007/s10874-011-9206-1.

[152] Blas, M. de, Navazo, M., Alonso, L., Durana, N., and Iza, J. Automatic on-line monitoring of atmospheric volatile organic compounds: Gas chromatography-mass spectrometry and gas chromatography-flame ionization detection as complementary systems. *Sci. Total Environ.* 409.24 (2011), pp. 5459–5469. URL: https://www.sciencedirect.com/science/article/pii/S0048969711010096.

[153] Huang, Y., Ou, Q., and Yu, W. Characteristics of flame ionization detection for the quantitative analysis of complex organic mixtures. *Anal. Chem.* 62.18 (1990), pp. 2063–2064. URL: https://doi.org/10.1021/ac00217a033.

[154] *ACTRIS measurement guidelines on VOC*. 2014. URL: http://www.actris.net.

[155] Ricardo Energy & Environment. *Automatic Urban and Rural Network: Site Operator's Manual*. 2015.

[156] Dunlea, E. J., Herndon, S. C., Nelson, D. D., Volkamer, R. M., San Martini, F., Sheehy, P. M., Zahniser, M. S., Shorter, J. H., Wormhoudt, J. C., Lamb, B. K., Allwine, E. J., Gaffney, J. S., Marley, N. A., Grutter, M., Marquez, C., Blanco, S., Cardenas, B., Retama, A., Ramos Villegas, C. R., Kolb, C. E., Molina, L. T., and Molina, M. J. Evaluation of nitrogen dioxide chemiluminescence monitors in a polluted urban environment. *Atmos. Chem. Phys.* 7.10 (2007), pp. 2691–2704. URL: https://acp.copernicus.org/articles/7/2691/2007/.

[157] Steinbacher, M., Zellweger, C., Schwarzenbach, B., Bugmann, S., Buchmann, B., Ordóñez, C., Prevot, A. S. H., and Hueglin, C. Nitrogen oxide measurements at rural sites in Switzerland: Bias of conventional measurement techniques. *J. Geophys. Res.* 112.D11 (2007).

[158] Department for Environment, Food and Rural Affairs. *Nitrogen Dioxide in the United Kingdom*. 2004.

[159] Sadanaga, Y., Fukumori, Y., Kobashi, T., Nagata, M., Takenaka, N., and Bandow, H. Development of a Selective Light-Emitting Diode Photolytic NO_2 Converter for Continuously Measuring NO_2 in the Atmosphere. *Anal. Chem.* 82.22 (2010), pp. 9234–9239. URL: https://doi.org/10.1021/ac101703z.

[160] EIA. *Offshore production nearly 30% of global crude oil output in 2015*. (Accessed 22nd June 2020). 2016. URL: https://www.eia.gov/todayinenergy/detail.php?id=28492.

[161] Statista. *Number of offshore rigs worldwide as of January 2018 by region*. (Accessed 22nd June 2020). 2018. URL: https://www.statista.com/statistics/279100/number-of-offshore-rigs-worldwide-by-region/.

[162] Oil and Gas Authority. *Projections of UK Oil and Gas Production and Expenditure*. 2019.

[163] Norwegian Petroleum Directorate. *Production Forecasts*. (Accessed 23rd June 2020). 2020. URL: https://www.norskpetroleum.no/en/production-and-exports/production-forecasts/.

[164] Eurostat. *Natural gas supply statistics*. (Accessed 23rd June 2020). 2019. URL: https://ec.europa.eu/eurostat/statistics-explained/pdfscache/10590.pdf.

[165] Miller, S. M., Wofsy, S. C., Michalak, A. M., Kort, E. A., Andrews, A. E., Biraud, S. C., Dlugokencky, E. J., Eluszkiewicz, J., Fischer, M. L., Janssens-Maenhout, G., Miller, B. R., Miller, J. B., Montzka, S. A., Nehrkorn, T., and Sweeney, C. Anthropogenic emissions of methane in the United States. *Proc. Natl. Acad. Sci. U.S.A.* 110.50 (2013), pp. 20018–20022. URL: https://www.pnas.org/content/110/50/20018.

[166] Koss, A., Yuan, B., Warneke, C., Gilman, J. B., Lerner, B. M., Veres, P. R., Peischl, J., Eilerman, S., Wild, R., Brown, S. S., Thompson, C. R., Ryerson, T., Hanisco, T., Wolfe, G. M., Clair, J. M. S., Thayer, M., Keutsch, F. N., Murphy, S., and Gouw, J. de. Observations of VOC emissions and photochemical products over US oil- and gas-producing regions using high-resolution H_3O^+ CIMS (PTR-ToF-MS). *Atmos. Meas. Tech.* 10.8 (2017), pp. 2941–2968. URL: https://www.atmos-meas-tech.net/10/2941/2017/.

[167] Masnadi, M. S., El-Houjeiri, H. M., Schunack, D., Li, Y., Englander, J. G., Badahdah, A., Monfort, J.-C., Anderson, J. E., Wallington, T. J., Bergerson, J. A., Gordon, D., Koomey, J., Przesmitzki, S., Azevedo, I. L., Bi, X. T., Duffy, J. E., Heath, G. A., Keoleian, G. A., McGlade, C., Meehan, D. N., Yeh, S., You, F., Wang, M., and Brandt, A. R. Global carbon intensity of crude oil production. *Science* 361.6405 (2018), pp. 851–853. URL: https://science.sciencemag.org/content/361/6405/851.

[168] Ghosh, B. Impact of Changes in Oil and Gas Production Activities on Air Quality in Northeastern Oklahoma: Ambient Air Studies in 2015-2017. *Environ. Sci. Technol.* 52.5 (2018), pp. 3285–3294. URL: https://doi.org/10.1021/acs.est.7b05726.

[169] Simpson, I. J., Blake, N. J., Barletta, B., Diskin, G. S., Fuelberg, H. E., Gorham, K., Huey, L. G., Meinardi, S., Rowland, F. S., Vay, S. A., Weinheimer, A. J., Yang, M., and Blake, D. R. Characterization of trace gases measured over Alberta oil sands mining operations: 76 speciated C_2-C_{10} volatile organic compounds (VOCs), CO_2, CH_4, CO, NO, NO_2, NO_y, O_3 and SO_2. *Atmos. Chem. Phys.* 10.23 (2010), pp. 11931–11954. URL: https://www.atmos-chem-phys.net/10/11931/2010/.

[170] Pétron, G., Frost, G., Miller, B. R., Hirsch, A. I., Montzka, S. A., Karion, A., Trainer, M., Sweeney, C., Andrews, A. E., Miller, L., Kofler, J., Bar-Ilan, A., Dlugokencky, E. J., Patrick, L., Moore Jr., C. T., Ryerson, T. B., Siso, C., Kolodzey, W., Lang, P. M., Conway, T., Novelli, P., Masarie, K., Hall, B., Guenther, D., Kitzis, D., Miller, J., Welsh, D., Wolfe, D., Neff, W., and Tans, P. Hydrocarbon emissions characterization in the Colorado Front Range: A pilot study. *J. Geophys. Res. Atmos.* 117.D4 (2012). URL: https://agupubs.onlinelibrary.wiley.com/doi/abs/10.1029/2011JD016360.

[171] Camilli, R., Reddy, C. M., Yoerger, D. R., Van Mooy, B. A. S., Jakuba, M. V., Kinsey, J. C., McIntyre, C. P., Sylva, S. P., and Maloney, J. V. Tracking Hydrocarbon Plume Transport and Biodegradation at Deepwater Horizon. *Science* 330.6001 (2010), pp. 201–204. URL: https://science.sciencemag.org/content/330/6001/201.

[172] Ryerson, T. B., Aikin, K. C., Angevine, W. M., Atlas, E. L., Blake, D. R., Brock, C. A., Fehsenfeld, F. C., Gao, R.-S., Gouw, J. A. de, Fahey, D. W., Holloway, J. S., Lack, D. A., Lueb, R. A., Meinardi, S., Middlebrook, A. M., Murphy, D. M., Neuman, J. A., Nowak, J. B., Parrish, D. D., Peischl, J., Perring, A. E., Pollack, I. B., Ravishankara, A. R., Roberts, J. M., Schwarz, J. P., Spackman, J. R., Stark, H., Warneke, C., and Watts, L. A. Atmospheric emissions from the Deepwater Horizon spill constrain air-water partitioning, hydrocarbon fate, and leak rate. *Geophys. Res. Lett.* 38.7 (2011). URL: https://agupubs.onlinelibrary.wiley.com/doi/abs/10.1029/2011GL046726.

[173] Hill, P. J. and Palfrey, A. J. The Britannia Field, Blocks 15/29a, 15/30, 16/26, 16/27a, 16/27b, UK North Sea. *Geol. Soc. Lond. Mem.* 20.1 (2003), pp. 415–429. URL: https://mem.lyellcollection.org/content/20/1/415.

[174] Glennie, K. W. Exploration activities in the Netherlands and North-West Europe since Groningen. *Neth. J. Geosci.* 80.1 (2001), pp. 33–52. URL: https://www.cambridge.org/core/article/

exploration-activities-in-the-netherlands-and-northwest-europe-since-groningen/4E6C86CC008F8E3F31D60B10F66A2C89.

[175] BP Exploration Company Ltd. North Sea Region (2019). URL: https://www.bp.com/content/dam/bp/country-sites/en_gb/united-kingdom/home/pdf/bp-north-sea-portfolio-2019.pdf.

[176] Nowegian Petroleum Directorate. *Map services*. (Accessed 20/01/2020). 2020. URL: https://www.npd.no/en/about-us/information-services/available-data/map-services/.

[177] NLOG. *The Netherlands oil and gas field outlines*. (Accessed 21/01/2020). 2014. URL: https://worldmap.harvard.edu/data/geonode:netherlands_oil_and_gas_field_outlines_4p0.

[178] South, A. *rnaturalearth: World Map Data from Natural Earth*. R package version 0.1.0. 2017. URL: https://CRAN.R-project.org/package=rnaturalearth.

[179] Hopkins, J. R., Lewis, A. C., and Read, K. A. A two-column method for long-term monitoring of non-methane hydrocarbons (NMHCs) and oxygenated volatile organic compounds (oVOCs). *J. Environ. Monit.* 5 (1 2003), pp. 8–13. URL: http://dx.doi.org/10.1039/B202798D.

[180] Atkinson, R. Gas-Phase Tropospheric Chemistry of Volatile Organic Compounds: 1. Alkanes and Alkenes. *J. Phys. Chem. Ref. Data* 26.2 (1997), pp. 215–290. URL: https://doi.org/10.1063/1.556012.

[181] Hong, Z., Li, M., Wang, H., Xu, L., Hong, Y., Chen, J., Chen, J., Zhang, H., Zhang, Y., Wu, X., Hu, B., and Li, M. Characteristics of atmospheric volatile organic compounds (VOCs) at a mountainous forest site and two urban sites in the southeast of China. *Sci. Total Environ.* 657 (2019), pp. 1491–1500. URL: http://www.sciencedirect.com/science/article/pii/S0048969718349738.

[182] Ayers, G. Comment on regression analysis of air quality data. *Atmos. Environ.* 35.13 (2001), pp. 2423–2425. URL: http://www.sciencedirect.com/science/article/pii/S1352231000005276.

[183] Ruppert, L. F., Ryder, R. T., Survey, U. S. G., Burruss, R. A., and Ryder, R. T. *Composition of natural gas and crude oil produced from 14 wells in the Lower Silurian "Clinton" Sandstone and Medina Group Sandstones, northeastern Ohio and northwestern Pennsylvania: Chapter G.6 in Coal and petroleum resources in the Appalachian basin: distribution, geologic framework, and geochemical character*. English. Tech. rep. Reston, VA, 2014, p. 42. URL: http://pubs.er.usgs.gov/publication/pp1708G.6.

[184] Riaz, M., Kontogeorgis, G. M., Stenby, E. H., Yan, W., Haugum, T., Christensen, K. O., Løkken, T. V., and Solbraa, E. Measurement of Liquid-Liquid Equilibria for Condensate + Glycol and Condensate + Glycol + Water Systems. *J. Chem. Eng. Data* 56.12 (2011), pp. 4342–4351. URL: https://doi.org/10.1021/je200158c.

[185] Gentner, D. R., Harley, R. A., Miller, A. M., and Goldstein, A. H. Diurnal and Seasonal Variability of Gasoline-Related Volatile Organic Compound Emissions in Riverside, California. *Environ. Sci. Technol.* 43.12 (2009), pp. 4247–4252. URL: https://doi.org/10.1021/es9006228.

[186] McGaughey, G. R., Desai, N. R., Allen, D. T., Seila, R. L., Lonneman, W. A., Fraser, M. P., Harley, R. A., Pollack, A. K., Ivy, J. M., and Price, J. H. Analysis of motor vehicle emissions in a Houston tunnel during the Texas Air Quality Study 2000. *Atmos. Environ.* 38.20 (2004). Findings from EPA's Particulate Matter Supersites Program, pp. 3363–3372. URL: http://www.sciencedirect.com/science/article/pii/S1352231004001943.

[187] Schneidemesser, E. von, Monks, P. S., and Plass-Duelmer, C. Global comparison of VOC and CO observations in urban areas. *Atmos. Environ.* 44.39 (2010), pp. 5053–5064. URL: http://www.sciencedirect.com/science/article/pii/S1352231010007648.

[188] Broderick, B. and Marnane, I. A comparison of the C_2-C_9 hydrocarbon compositions of vehicle fuels and urban air in Dublin, Ireland. *Atmos. Environ.* 36.6 (2002), pp. 975–986. URL: http://www.sciencedirect.com/science/article/pii/S1352231001004721.

[189] Fortin, T. J., Howard, B. J., Parrish, D. D., Goldan, P. D., Kuster, W. C., Atlas, E. L., and Harley, R. A. Temporal Changes in U.S. Benzene Emissions Inferred from Atmospheric Measurements. *Environ. Sci. Technol.* 39.6 (2005), pp. 1403–1408. URL: https://doi.org/10.1021/es049316n.

[190] Swarthout, R. F., Russo, R. S., Zhou, Y., Hart, A. H., and Sive, B. C. Volatile organic compound distributions during the NACHTT campaign at the Boulder Atmospheric Observatory: Influence of urban and natural gas sources. *J. Geophys. Res. Atmos.* 118.18 (2013), pp. 10, 614–10, 637. URL: https://agupubs.onlinelibrary.wiley.com/doi/abs/10.1002/jgrd.50722.

[191] Derwent, R., Field, R., Dumitrean, P., Murrells, T., and Telling, S. Origins and trends in ethane and propane in the United Kingdom from 1993 to 2012. *Atmos. Environ.* 156 (2017), pp. 15–23. URL: http://www.sciencedirect.com/science/article/pii/S1352231017301103.

[192] Aardenne, J. van, Colette, A., Degraeuwe, B., Vlieger, I. de, Hammingh, P., and Viana, M. *The impact of international shipping on European air quality and climate forcing*. 2013.

[193] Xiao, Q., Li, M., Liu, H., Fu, M., Deng, F., Lv, Z., Man, H., Jin, X., Liu, S., and He, K. Characteristics of marine shipping emissions at berth: profiles for particulate matter and volatile organic compounds. *Atmos. Chem. Phys.* 18.13 (2018), pp. 9527–9545. URL: https://www.atmos-chem-phys.net/18/9527/2018/.

[194] Thompson, C. R., Hueber, J., and Helmig, D. Influence of oil and gas emissions on ambient atmospheric non-methane hydrocarbons in residential areas of Northeastern Colorado. *Elem. Sci. Anth.* 3.p.000035 (2014).

[195] Dominutti, P. A., Nogueira, T., Borbon, A., Andrade, M. d. F., and Fornaro, A. One-year of NMHCs hourly observations in São Paulo megacity: meteorological and traffic emissions effects in a large ethanol burning context. *Atmos. Environ.* 142 (2016), pp. 371–382. URL: http://www.sciencedirect.com/science/article/pii/S1352231016306008.

[196] Liu, Y., Wang, H., Jing, S., Gao, Y., Peng, Y., Lou, S., Cheng, T., Tao, S., Li, L., Li, Y., Huang, D., Wang, Q., and An, J. Characteristics and sources of volatile organic compounds (VOCs) in Shanghai during summer: Implications of regional transport. *Atmos. Environ.* 215 (2019), p. 116902. URL: http://www.sciencedirect.com/science/article/pii/S1352231019305412.

[197] Jobson, B., Alexander, M., Maupin, G., and Muntean, G. On-line analysis of organic compounds in diesel exhaust using a proton transfer reaction mass spectrometer (PTR-MS). *Int. J. Mass Spectrom.* 245.1 (2005), pp. 78–89. URL: http://www.sciencedirect.com/science/article/pii/S1387380605001703.

[198] Halliday, H. S., Thompson, A. M., Wisthaler, A., Blake, D. R., Hornbrook, R. S., Mikoviny, T., Müller, M., Eichler, P., Apel, E. C., and Hills, A. J. Atmospheric benzene observations from oil and gas production in the Denver-Julesburg Basin in July and August 2014. *J. Geophys. Res. Atmos.* 121.18 (2016), pp. 11, 055–11, 074. URL: https://agupubs.onlinelibrary.wiley.com/doi/abs/10.1002/2016JD025327.

[199] Warneke, C., Veen, C. van der, Luxembourg, S., Gouw, J. de, and Kok, A. Measurements of benzene and toluene in ambient air using proton-transfer-reaction mass spectrometry: calibration, humidity dependence, and field intercomparison. *Int. J. Mass Spectrom.* 207.3 (2001), pp. 167–182. URL: http://www.sciencedirect.com/science/article/pii/S1387380601003669.

[200] Langford, B., Davison, B., Nemitz, E., and Hewitt, C. N. Mixing ratios and eddy covariance flux measurements of volatile organic compounds from an urban canopy (Manchester, UK). *Atmos. Chem. Phys.* 9.6 (2009), pp. 1971–1987. URL: https://www.atmos-chem-phys.net/9/1971/2009/.

[201] Field, R. A., Soltis, J., McCarthy, M. C., Murphy, S., and Montague, D. C. Influence of oil and gas field operations on spatial and temporal distributions of atmospheric non-methane hydrocarbons and their effect on ozone formation in winter. *Atmos. Chem. Phys.* 15.6 (2015), pp. 3527–3542. URL: https://acp.copernicus.org/articles/15/3527/2015/.

[202] Williams, J. and Koppmann, R. Volatile Organic Compounds in the Atmosphere: An Overview. *Volatile Organic Compounds in the Atmosphere*. John Wiley & Sons, Ltd, 2007. Chap. 1, pp. 1–32. URL: https://onlinelibrary.wiley.com/doi/abs/10.1002/9780470988657.ch1.

[203] Rich, A., Grover, J. P., and Sattler, M. L. An exploratory study of air emissions associated with shale gas development and production in the Barnett Shale. *J. Air. Waste Manag. Assoc.* 64.1 (2014), pp. 61–72. URL: https://doi.org/10.1080/10962247.2013.832713.

[204] Rich, A. L. and Orimoloye, H. T. Elevated Atmospheric Levels of Benzene and Benzene-Related Compounds from Unconventional Shale Extraction and Processing: Human Health Concern for Residential Communities. eng. *Environ. Health Insights* 10.27199565 (2016), pp. 75–82. URL: https://www.ncbi.nlm.nih.gov/pmc/articles/PMC4869597/.

[205] Nara, H., Tanimoto, H., Tohjima, Y., Mukai, H., Nojiri, Y., and Machida, T. Emissions of methane from offshore oil and gas platforms in Southeast Asia. *Sci. Rep.* 4 (2014), p. 6503.

[206] Conway, T. J. and Steele, L. P. Carbon dioxide and methane in the Arctic atmosphere. *J. Atmos. Chem.* 9.1 (1989), pp. 81–99. URL: https://doi.org/10.1007/BF00052826.

[207] Goetz, J. D., Floerchinger, C., Fortner, E. C., Wormhoudt, J., Massoli, P., Knighton, W. B., Herndon, S. C., Kolb, C. E., Knipping, E., Shaw, S. L., and DeCarlo, P. F. Atmospheric Emission Characterization of Marcellus Shale Natural Gas Development Sites. *Environ. Sci. Technol.* 49.11 (2015), pp. 7012–7020. URL: https://doi.org/10.1021/acs.est.5b00452.

[208] Washenfelder, R. A., Trainer, M., Frost, G. J., Ryerson, T. B., Atlas, E. L., Gouw, J. A. de, Flocke, F. M., Fried, A., Holloway, J. S., Parrish, D. D., Peischl, J., Richter, D., Schauffler, S. M., Walega, J. G., Warneke, C., Weibring, P., and Zheng, W. Characterization of NO_x, SO_2, ethene, and propene from industrial emission sources in Houston, Texas. *J. Geophys. Res.* 115.D16 (2020). URL: https://doi.org/10.1029/2009JD013645.

[209] Darnall, K. R., Lloyd, A. C., Winer, A. M., and Pitts, J. N. Reactivity scale for atmospheric hydrocarbons based on reaction with hydroxyl radical. *Environ. Sci. Technol.* 10.7 (1976), pp. 692–696. URL: https://doi.org/10.1021/es60118a008.

[210] Abeleira, A., Pollack, I. B., Sive, B., Zhou, Y., Fischer, E. V., and Farmer, D. K. Source characterization of volatile organic compounds in the Colorado Northern Front Range Metropolitan Area during spring and summer 2015. *J. Geophys. Res. Atmos.* 122.6 (2017), pp. 3595–3613. URL: https://doi.org/10.1002/2016JD026227.

[211] Atkinson, R. and Aschmann, S. M. Rate constants for the reactions of O_3 and OH radicals with a series of alkynes. *Int. J. Chem. Kinet.* 16.3 (1984), pp. 259–268. URL: https://doi.org/10.1002/kin.550160308.

[212] Atkinson, R. and Arey, J. Atmospheric Degradation of Volatile Organic Compounds. *Chem. Rev.* 103.12 (2003), pp. 4605–4638. URL: https://doi.org/10.1021/cr0206420.

[213] Bourtsoukidis, E., Ernle, L., Crowley, J. N., Lelieveld, J., Paris, J.-D., Pozzer, A., Walter, D., and Williams, J. Non-methane hydrocarbon (C_2-C_8) sources and sinks around the Arabian Peninsula. *Atmos. Chem. Phys.* 19.10 (2019), pp. 7209–7232. URL: https://www.atmos-chem-phys.net/19/7209/2019/.

[214] Speight, J. G. Unconventional gas. *Natural Gas*. Ed. by J. G. Speight. 2nd ed. Boston: Gulf Professional Publishing, 2019, pp. 59–98. URL: http://www.sciencedirect.com/science/article/pii/B9780128095706000035.

[215] EIA. *Offshore oil production in deepwater and ultra-deepwater is increasing*. (Accessed 19/08/2020). 2016. URL: https://www.eia.gov/todayinenergy/detail.php?id=28552.

[216] Yacovitch, T. I., Daube, C., and Herndon, S. C. Methane Emissions from Offshore Oil and Gas Platforms in the Gulf of Mexico. *Environ. Sci. Technol.* 54.6 (2020), pp. 3530–3538. URL: https://doi.org/10.1021/acs.est.9b07148.

[217] *National Atmospheric Emissions Inventory*. URL: https://naei.beis.gov.uk/.

[218] Passant, N. R. *Speciation of UK emissions of non-methane volatile organic compounds*. AEA Technology, 2002. URL: https://uk-air.defra.gov.uk/assets/documents/reports/empire/AEAT_ENV_0545_final_v2.pdf.

[219] Miller, C. A., Hidy, G., Hales, J., Kolb, C. E., Werner, A. S., Haneke, B., Parrish, D., Frey, H. C., Rojas-Bracho, L., Deslauriers, M., Pennell, B., and Mobley, J. D. Air Emission Inventories in North America: A Critical Assessment. *J. Air. Waste Manag. Assoc.* 56.8 (2006), pp. 1115–1129. URL: https://doi.org/10.1080/10473289.2006.10464540.

[220] Peischl, J., Ryerson, T. B., Aikin, K. C., Gouw, J. A. de, Gilman, J. B., Holloway, J. S., Lerner, B. M., Nadkarni, R., Neuman, J. A., Nowak, J. B., Trainer, M., Warneke, C., and Parrish, D. D. Quantifying atmospheric methane emissions from the Haynesville, Fayetteville, and northeastern Marcellus shale gas production regions. *J. Geophys. Res. Atmos.* 120.5 (2015), pp. 2119–2139. URL: https://doi.org/10.1002/2014JD022697.

[221] Zavala-Araiza, D., Lyon, D. R., Alvarez, R. A., Davis, K. J., Harriss, R., Herndon, S. C., Karion, A., Kort, E. A., Lamb, B. K., Lan, X., Marchese, A. J., Pacala, S. W., Robinson, A. L., Shepson, P. B., Sweeney, C., Talbot, R., Townsend-Small, A., Yacovitch, T. I., Zimmerle, D. J., and Hamburg, S. P. Reconciling divergent estimates of oil and gas methane emissions. *Proc. Natl. Acad. Sci. U.S.A.* 112.51 (2015), pp. 15597–15602. URL: https://www.pnas.org/content/112/51/15597.

[222] Riddick, S. N., Mauzerall, D. L., Celia, M., Harris, N. R. P., Allen, G., Pitt, J., Staunton-Sykes, J., Forster, G. L., Kang, M., Lowry, D., Nisbet, E. G., and Manning, A. J. Methane emissions from oil and gas platforms in the North Sea. *Atmos. Chem. Phys.* 19.15 (2019), pp. 9787–9796. URL: https://www.atmos-chem-phys.net/19/9787/2019/.

[223] Lavoie, T. N., Shepson, P. B., Cambaliza, M. O. L., Stirm, B. H., Conley, S., Mehrotra, S., Faloona, I. C., and Lyon, D. Spatiotemporal Variability of Methane Emissions at Oil and Natural Gas Operations in the Eagle Ford Basin. *Environ. Sci. Technol.* 51.14 (2017), pp. 8001–8009. URL: https://doi.org/10.1021/acs.est.7b00814.

[224] BP. *BP starts-up Clair Ridge production*. 2018. URL: https://www.bp.com/en/global/corporate/news-and-insights/press-releases/bp-starts-up-clair-ridge-production.html.

[225] Peischl, J., Eilerman, S. J., Neuman, J. A., Aikin, K. C., Gouw, J. de, Gilman, J. B., Herndon, S. C., Nadkarni, R., Trainer, M., Warneke, C., and Ryerson, T. B. Quantifying Methane and Ethane Emissions to the Atmosphere From Central and Western U.S. Oil and Natural Gas Production Regions. *J. Geophys. Res. Atmos.* 123.14 (2018), pp. 7725–7740. URL: https://doi.org/10.1029/2018JD028622.

[226] Peischl, J., Karion, A., Sweeney, C., Kort, E. A., Smith, M. L., Brandt, A. R., Yeskoo, T., Aikin, K. C., Conley, S. A., Gvakharia, A., Trainer, M., Wolter, S., and Ryerson, T. B. Quantifying atmospheric methane emissions from oil and natural gas production in the Bakken shale region of North Dakota. *J. Geophys. Res. Atmos.* 121.10 (2016), pp. 6101–6111. URL: https://doi.org/10.1002/2015JD024631.

[227] Gordon, M., Li, S.-M., Staebler, R., Darlington, A., Hayden, K., O'Brien, J., and Wolde, M. Determining air pollutant emission rates based on mass balance using airborne measurement data over the Alberta oil sands operations. *Atmos. Meas. Tech.* 8.9 (2015), pp. 3745–3765. URL: https://amt.copernicus.org/articles/8/3745/2015/.

[228] Barnes, S. L. A Technique for Maximizing Details in Numerical Weather Map Analysis. *J. Appl. Meteor.* 3.4 (1964), pp. 396–409. URL: https://doi.org/10.1175/1520-0450(1964)003%3C0396:ATFMDI%3E2.0.CO;2.

[229] Koch, S. E., desJardins, M., and Kocin, P. J. An Interactive Barnes Objective Map Analysis Scheme for Use with Satellite and Conventional Data. *J. Climate Appl. Meteor.* 22.9 (1983), pp. 1487–1503. URL: https://doi.org/10.1175/1520-0450(1983)022%3C1487:AIBOMA%3E2.0.CO;2.

[230] Kuleshov, Y., Mackerras, D., and Darveniza, M. Spatial Distribution and Frequency of Thunderstorms and Lightning in Australia. *Lightning: Principles, Instruments and Applications: Review of Modern Lightning Research*. Ed. by H. D. Betz, U. Schumann, and P. Laroche. Dordrecht: Springer Netherlands, 2009, pp. 187–207. URL: https://doi.org/10.1007/978-1-4020-9079-0_8.

[231] Cambaliza, M. O. L., Shepson, P. B., Caulton, D. R., Stirm, B., Samarov, D., Gurney, K. R., Turnbull, J., Davis, K. J., Possolo, A., Karion, A., Sweeney, C., Moser, B., Hendricks, A., Lauvaux, T., Mays, K., Whetstone, J., Huang, J., Razlivanov, I., Miles, N. L., and Richardson, S. J. Assessment of uncertainties of an aircraft-based mass balance approach for quantifying urban greenhouse gas emissions. *Atmos. Chem. Phys.* 14.17 (2014), pp. 9029–9050. URL: https://acp.copernicus.org/articles/14/9029/2014/.

[232] Oil and Gas Authority. *Petroleum Production Reporting System*. 2020. URL: https://data-ogauthority.opendata.arcgis.com/pages/production.

[233] Elvidge, C. D., Zhizhin, M., Baugh, K., Hsu, F.-C., and Ghosh, T. Methods for Global Survey of Natural Gas Flaring from Visible Infrared Imaging Radiometer Suite Data. *Energies* 9.1 (2016). URL: https://www.mdpi.com/1996-1073/9/1/14.

[234] Hanna, S. R., Schulman, L. L., Paine, R. J., Pleim, J. E., and Baer, M. Development and Evaluation of the Offshore and Coastal Dispersion Model. *J. Air Pollut. Control Assoc.* 35.10 (1985), pp. 1039–1047. URL: https://doi.org/10.1080/00022470.1985.10466003.

[235] Yacovitch, T. I., Herndon, S. C., Pétron, G., Kofler, J., Lyon, D., Zahniser, M. S., and Kolb, C. E. Mobile Laboratory Observations of Methane Emissions in the Barnett Shale Region. *Environ. Sci. Technol.* 49.13 (2015), pp. 7889–7895. URL: https://doi.org/10.1021/es506352j.

[236] Venables, W. N. and Ripley, B. D. *Modern Applied Statistics with S*. Fourth. ISBN 0-387-95457-0. New York: Springer, 2002. URL: http://www.stats.ox.ac.uk/pub/MASS4/.

[237] Milazzo, M. F., Ancione, G., and Lisi, R. Emissions of volatile organic compounds during the ship-loading of petroleum products: Dispersion modelling and environmental concerns. *J. Environ. Manage.* 204 (2017), pp. 637–650. URL: http://www.sciencedirect.com/science/article/pii/S0301479717309143.

[238] Staddon, C., Brown, J., and Hayes, E. Potential environmental impacts of 'fracking' in the UK. *Geography* 101.2 (2016), pp. 60–69. URL: https://www.jstor.org/stable/26546718.

[239] Archibald, A. T., Ordóñez, C., Brent, E., and Williams, M. L. Potential impacts of emissions associated with unconventional hydrocarbon extraction on UK air quality and human health. *Air. Qual. Atmos. Health* 11.6 (2018), pp. 627–637. URL: https://doi.org/10.1007/s11869-018-0570-8.

[240] U.S. Energy Information Administration. *Annual Energy Outlook 2020*. 2020. URL: https://www.eia.gov/outlooks/aeo/.

[241] Ellsworth, W. L. Injection-Induced Earthquakes. *Science* 341.6142 (2013), p. 1225942. URL: http://science.sciencemag.org/content/341/6142/1225942.abstract.

[242] Mediaview. *Geology Today* 28.1 (2012), pp. 2–12. URL: https://doi.org/10.1111/j.1365-2451.2012.00819.x.

[243] Boucher, O., Friedlingstein, P., Collins, B., and Shine, K. P. The indirect global warming potential and global temperature change potential due to methane oxidation. *Environ. Res. Lett.* 4.4 (2009), p. 044007. URL: http://dx.doi.org/10.1088/1748-9326/4/4/044007.

[244] Vinciguerra, T., Yao, S., Dadzie, J., Chittams, A., Deskins, T., Ehrman, S., and Dickerson, R. R. Regional air quality impacts of hydraulic fracturing and shale natural gas activity: Evidence from ambient VOC observations. *Atmos. Environ.* 110 (2015), pp. 144–150. URL: http://www.sciencedirect.com/science/article/pii/S1352231015002800.

[245] Shah, A. S. V., Lee, K. K., McAllister, D. A., Hunter, A., Nair, H., Whiteley, W., Langrish, J. P., Newby, D. E., and Mills, N. L. Short term exposure to air pollution and stroke: systematic review and meta-analysis. *BMJ* 350 (2015), h1295. URL: http://www.bmj.com/content/350/bmj.h1295.abstract.

[246] Helmig, D., Thompson, C. R., Evans, J., Boylan, P., Hueber, J., and Park, J.-H. Highly Elevated Atmospheric Levels of Volatile Organic Compounds in the Uintah Basin, Utah. *Environ. Sci. Technol.* 48.9 (2014), pp. 4707–4715. URL: https://doi.org/10.1021/es405046r.

[247] Dix, B., Bruin, J. de, Roosenbrand, E., Vlemmix, T., Francoeur, C., Gorchov-Negron, A., McDonald, B., Zhizhin, M., Elvidge, C., Veefkind, P., Levelt, P., and Gouw, J. de. Nitrogen Oxide Emissions from U.S. Oil and Gas Production: Recent Trends and Source Attribution. *Geophys. Res. Lett.* 47.1 (2020), e2019GL085866. URL: https://doi.org/10.1029/2019GL085866.

[248] King, G. E. *Hydraulic Fracturing 101: What Every Representative, Environmentalist, Regulator, Reporter, Investor, University Researcher, Neighbor and Engineer Should Know About Estimating Frac Risk and Improving Frac Performance in Unconventional Gas and Oil Wells*. The Woodlands, Texas, USA, 2012. URL: https://doi.org/10.2118/152596-MS.

[249] Goodman, P. S., Galatioto, F., Thorpe, N., Namdeo, A. K., Davies, R. J., and Bird, R. N. Investigating the traffic-related environmental impacts of hydraulic-fracturing (fracking) operations. *Environ. Int.* 89-90 (2016), pp. 248–260. URL: http://www.sciencedirect.com/science/article/pii/S0160412016300277.

[250] Priestley, S. Briefing paper: Shale gas and fracking. *House of Commons Library* (2020).

[251] BBC News. *Kirby Misperton fracking: Third Energy sells business*. (Accessed 15/09/2020). 2019. URL: https://www.bbc.co.uk/news/uk-england-york-north-yorkshire-48084036.

[252] Purvis, R. M., Lewis, A. C., Hopkins, J. R., Wilde, S. E., Dunmore, R. E., Allen, G., Pitt, J., and Ward, R. S. Effects of 'pre-fracking' operations on ambient air quality at a shale gas exploration site in rural North Yorkshire, England. *Sci. Total Environ.* 673 (2019), pp. 445–454. URL: http://www.sciencedirect.com/science/article/pii/S0048969719315979.

[253] Mair, R., Bickle, M., Goodman, D., Koppelman, B., Roberts, J., Selley, R., Shipton, Z., Thomas, H., Walker, A., Woods, E., and Younger, P. Shale gas extraction in the UK: a review of hydraulic fracturing. *Royal Society and Royal Academy of Engineering* (2012). URL: http://eprints.gla.ac.uk/69554/.

[254] Jackson, R. E., Gorody, A. W., Mayer, B., Roy, J. W., Ryan, M. C., and Van Stempvoort, D. R. Groundwater Protection and Unconventional Gas Extraction: The Critical Need for Field-Based Hydrogeological Research. *Groundwater* 51.4 (2013), pp. 488–510. URL: https://doi.org/10.1111/gwat.12074.

[255] Montcoudiol, N., Banks, D., Isherwood, C., Gunning, A., and Burnside, N. Baseline groundwater monitoring for shale gas extraction: definition of baseline conditions and recommendations from a real site (Wysin, Northern Poland). *Acta Geophys.* 67.1 (2019), pp. 365–384. URL: https://doi.org/10.1007/s11600-019-00254-w.

[256] Air Quality Expert Group to the Department for Environment & Affairs. Potential Air Quality Impacts of Shale Gas Extraction in the UK (2018).

[257] Department for Environment, Food and Rural Affairs. Local Air Quality Management (2009).

[258] Jones, Z. and Linder, F. edarf: Exploratory Data Analysis using Random Forests. *J. Open Source Softw.* 1 (2016).

[259] Breiman, L. Random Forests. *Mach Learn* 45.1 (2001), pp. 5–32. URL: https://doi.org/10.1023/A:1010933404324.

[260] Grange, S. K., Farren, N. J., Vaughan, A. R., Rose, R. A., and Carslaw, D. C. Strong Temperature Dependence for Light-Duty Diesel Vehicle NO_x Emissions. *Environ. Sci. Technol.* 53.11 (2019), pp. 6587–6596. URL: https://doi.org/10.1021/acs.est.9b01024.

[261] Zheng, H., Kong, S., Chen, N., Yan, Y., Liu, D., Zhu, B., Xu, K., Cao, W., Ding, Q., Lan, B., Zhang, Z., Zheng, M., Fan, Z., Cheng, Y., Zheng, S., Yao, L., Bai, Y., Zhao, T., and Qi, S. Significant changes in the chemical compositions and sources of $PM_{2.5}$ in Wuhan since the city lockdown as COVID-19. *Sci. Total Environ.* 739 (2020), p. 140000. URL: http://www.sciencedirect.com/science/article/pii/S0048969720335208.

[262] Cole, M. A., Elliott, R. J. R., and Liu, B. The Impact of the Wuhan Covid-19 Lockdown on Air Pollution and Health: A Machine Learning and Augmented Synthetic Control Approach. eng. *Environ. Resour. Econ.* 32836865 (2020), pp. 1–28. URL: https://www.ncbi.nlm.nih.gov/pmc/articles/PMC7416596/.

[263] Carslaw, D. C., Williams, M. L., and Barratt, B. A short-term intervention study – Impact of airport closure due to the eruption of Eyjafjallajökull on near-field air quality. *Atmos. Environ.* 54 (2012), pp. 328–336. URL: http://www.sciencedirect.com/science/article/pii/S1352231012001355.

[264] Forster, P. M., Forster, H. I., Evans, M. J., Gidden, M. J., Jones, C. D., Keller, C. A., Lamboll, R. D., Quéré, C. L., Rogelj, J., Rosen, D., Schleussner, C.-F., Richardson, T. B., Smith, C. J., and Turnock, S. T. Current and future global climate impacts resulting from COVID-19. *Nat. Clim. Change* (2020). URL: https://doi.org/10.1038/s41558-020-0883-0.

[265] Grange, S. K., Lee, J. D., Drysdale, W. S., Lewis, A. C., Hueglin, C., Emmenegger, L., and Carslaw, D. C. COVID-19 lockdowns highlight a risk of increasing ozone pollution in European urban areas. *Atmos. Chem. Phys.* 21.5 (2021), pp. 4169–4185. URL: https://acp.copernicus.org/articles/21/4169/2021/.

[266] Carslaw, D. C. *Analysis of COVID-19 lockdown on UK local air pollution*. 2020. URL: https://ee.ricardo.com/news/analysis-of-covid-19-lockdown-on-uk-local-air-pollution.

[267] R Core Team. *R: A Language and Environment for Statistical Computing*. R Foundation for Statistical Computing. Vienna, Austria, 2020. URL: https://www.R-project.org/.

[268] Ciais, P., Tan, J., Wang, X., Roedenbeck, C., Chevallier, F., Piao, S.-L., Moriarty, R., Broquet, G., Le Quéré, C., Canadell, J. G., Peng, S., Poulter, B., Liu, Z., and Tans, P. Five decades of northern land carbon uptake revealed by the interhemispheric CO_2 gradient. *Nature* 568.7751 (2019), pp. 221–225. URL: https://doi.org/10.1038/s41586-019-1078-6.

[269] Mayer, E. W., Blake, D. R., Tyler, S. C., Makide, Y., Montague, D. C., and Rowland, F. S. Methane: Interhemispheric concentration gradient and atmospheric residence time. *Proc Natl Acad Sci USA* 79.4 (1982), p. 1366. URL: http://www.pnas.org/content/79/4/1366.abstract.

[270] Department for Environment, Food and Rural Affairs. *Air Pollution in the UK 2016*. 2016. URL: https://uk-air.defra.gov.uk/assets/documents/annualreport/air_pollution_uk_2016_issue_2.pdf.

[271] Duncan Laxen Ricky Gellatly, T. R. Nitrogen Dioxide and Nitrogen Oxides Trends in the UK 2005 to 2018. *Air Quality Consultants* (2019). URL: https://www.aqconsultants.co.uk/CMSPages/GetFile.aspx?guid=feb92332-26f7-4989-b86a-21e5732a5404.

[272] Carslaw, D. C., Beevers, S. D., Ropkins, K., and Bell, M. C. Detecting and quantifying aircraft and other on-airport contributions to ambient nitrogen oxides in the vicinity of a large international airport. *Atmos. Environ.* 40.28 (2006), pp. 5424–5434. URL: http://www.sciencedirect.com/science/article/pii/S1352231006004250.

[273] Uria-Tellaetxe, I. and Carslaw, D. C. Conditional bivariate probability function for source identification. *Environ. Model. Softw.* 59 (2014), pp. 1–9. URL: http://www.sciencedirect.com/science/article/pii/S1364815214001339.

[274] Carslaw, D. and Beevers, S. Characterising and understanding emission sources using bivariate polar plots and k-means clustering. *Environ. Modell. Software* 40 (2013), pp. 325–329.

[275] Warneck, P. Chemistry of the natural atmosphere. *Orlando FL Academic Press Inc International Geophysics Series* 41 (1988).

[276] Bohnenstengel, S. I., Belcher, S. E., Aiken, A., Allan, J. D., Allen, G., Bacak, A., Bannan, T. J., Barlow, J. F., Beddows, D. C. S., Bloss, W. J., Booth, A. M., Chemel, C., Coceal, O., Di Marco, C. F., Dubey, M. K., Faloon, K. H., Fleming, Z. L., Furger, M., Gietl, J. K., Graves, R. R., Green, D. C., Grimmond, C. S. B., Halios, C. H., Hamilton, J. F., Harrison, R. M., Heal, M. R., Heard, D. E., Helfter, C., Herndon, S. C., Holmes, R. E., Hopkins, J. R., Jones, A. M., Kelly, F. J., Kotthaus, S., Langford, B., Lee, J. D., Leigh, R. J., Lewis, A. C., Lidster, R. T., Lopez-Hilfiker, F. D.,

McQuaid, J. B., Mohr, C., Monks, P. S., Nemitz, E., Ng, N. L., Percival, C. J., Prévôt, A. S. H., Ricketts, H. M. A., Sokhi, R., Stone, D., Thornton, J. A., Tremper, A. H., Valach, A. C., Visser, S., Whalley, L. K., Williams, L. R., Xu, L., Young, D. E., and Zotter, P. Meteorology, Air Quality, and Health in London: The ClearfLo Project. *Bull. Amer. Meteor. Soc.* 96.5 (2015), pp. 779–804. URL: https://doi.org/10.1175/BAMS-D-12-00245.1.

[277] Derwent, R. G., Middleton, D. R., Field, R. A., Goldstone, M. E., Lester, J. N., and Perry, R. Analysis and interpretation of air quality data from an urban roadside location in Central London over the period from July 1991 to July 1992. *Atmos. Environ.* 29.8 (1995), pp. 923–946.

[278] Strobl, C., Boulesteix, A.-L., Kneib, T., Augustin, T., and Zeileis, A. Conditional variable importance for random forests. *BMC Bioinf.* 9.1 (2008), p. 307. URL: https://doi.org/10.1186/1471-2105-9-307.

[279] Efron, B. Estimation and Accuracy After Model Selection. *J. Am. Stat. Assoc.* 109.507 (2014), pp. 991–1007. URL: https://doi.org/10.1080/01621459.2013.823775.

[280] Wager, S., Hastie, T., and Efron, B. Confidence Intervals for Random Forests: The Jackknife and the Infinitesimal Jackknife. *J. Mach. Learn. Res.* 15.48 (2014), pp. 1625–1651. URL: http://jmlr.org/papers/v15/wager14a.html.

[281] Carslaw, D. C., Ropkins, K., and Bell, M. C. Change-Point Detection of Gaseous and Particulate Traffic-Related Pollutants at a Roadside Location. *Environ. Sci. Technol.* 40.22 (2006), pp. 6912–6918. URL: https://doi.org/10.1021/es060543u.

[282] Department for the Environment, Food and Rural Affairs. *Ozone in the United Kingdom*. 2002.

[283] Weger, L. B., Lupascu, A., Cremonese, L., and Butler, T. Modeling the impact of a potential shale gas industry in Germany and the United Kingdom on ozone with WRF-Chem. *Elem. Sci. Anth.* 7.49 (2019). Ed. by D. Helmig and S. Schwietzke. URL: https://doi.org/10.1525/elementa.387.

[284] Lu, K., Zhang, Y., Su, H., Brauers, T., Chou, C. C., Hofzumahaus, A., Liu, S. C., Kita, K., Kondo, Y., Shao, M., Wahner, A., Wang, J., Wang, X., and Zhu, T. Oxidant (O_3 + NO_2) production processes and formation regimes in Beijing. *J. Geophys. Res.* 115.D7 (2010). URL: https://doi.org/10.1029/2009JD012714.

[285] Clapp, L. J. and Jenkin, M. E. Analysis of the relationship between ambient levels of O_3, NO_2 and NO as a function of NO_x in the UK. *Atmos. Environ.* 35.36 (2001), pp. 6391–6405. URL: http://www.sciencedirect.com/science/article/pii/S1352231001003788.

[286] Carslaw, D. C., Farren, N. J., Vaughan, A. R., Drysdale, W. S., Young, S., and Lee, J. D. The diminishing importance of nitrogen dioxide emissions from road vehicle exhaust. *Atmos. Environ. X* 1 (2019), p. 100002. URL: http://www.sciencedirect.com/science/article/pii/S2590162118300029.

[287] BP. *Energy Outlook 2020*. 2020. URL: https://www.bp.com/en/global/corporate/energy-economics/energy-outlook.html.

[288] British National Grid. *Gas Summer Outlook Report*. 2021. URL: https://www.nationalgrid.com/uk/gas-transmission/.

[289] Graham, A. M., Pope, R. J., McQuaid, J. B., Pringle, K. P., Arnold, S. R., Bruno, A. G., Moore, D. P., Harrison, J. J., Chipperfield, M. P., Rigby, R., Sanchez-Marroquin, A., Lee, J., Wilde, S., Siddans, R., Kerridge, B. J., Ventress, L. J., and Latter, B. G. Impact of the June 2018 Saddleworth Moor wildfires on air quality in northern England. *Environ. res. commun.* 2.3 (2020), p. 031001. URL: https://doi.org/10.1088%2F2515-7620%2Fab7b92.

[290] Shaw, J. T., Allen, G., Pitt, J., Shah, A., Wilde, S., Stamford, L., Fan, Z., Ricketts, H., Williams, P. I., Bateson, P., Barker, P., Purvis, R., Lowry, D., Fisher, R., France, J., Coleman, M., Lewis, A. C., Risk, D. A., and Ward, R. S. Methane flux from flowback operations at a shale gas site. *J. Air. Waste Manag. Assoc.* 70.12 (2020). PMID: 32915694, pp. 1324–1339. URL: https://doi.org/10.1080/10962247.2020.1811800.

[291] Lee, J. D., Drysdale, W. S., Finch, D. P., Wilde, S., and Palmer, P. I. UK surface NO_2 levels dropped by 42% during the COVID-19 lockdown: impact on surface O_3. *Atmospheric Chemistry and Physics* 20.24 (2020), pp. 15743–15759. URL: https://acp.copernicus.org/articles/20/15743/2020/.

[293] Ward, R., Smedley, P., Allen, G., Baptie, B., Cave, M., Daraktchieva, Z., Fisher, R., Hawthorn, D., Jones, D., Lewis, A., Lowry, D., Luckett, R., Marchant, B., Purvis, R., and Wilde, S. Environmental baseline monitoring : Phase III final report (2017-2018). This item has been internally reviewed, but not externally peer-reviewed. Nottingham, UK, 2018. URL: http://nora.nerc.ac.uk/id/eprint/521380/.

[294] Ward, R., Smedley, P., Allen, G., Baptie, B., Barkwith, A., Bateson, L., Bell, R., Bowes, M., Coleman, M., Cremen, G., Daraktchieva, Z., Gong, M., Howarth, C., Fisher, R., Hawthorn, D., Jones, D., Jordan, C., Lanoiselle, M., Lewis, A., Lister, T., Lowry, D., Luckett, R., Mallin-Martin, D., Marchant, B., Miller, C., Milne, C., Novellino, A., Pitt, J., Purvis, R., Rivett, M., Shaw, J., Taylor-Curran, H., Wasikiewicz, J., Werner, M., and Wilde, S. Environmental monitoring : phase 4 final report (April 2018 - March 2019). This item has been internally reviewed, but not ex-

ternally peer-reviewed. Nottingham, UK, 2019. URL: http://nora.nerc.ac.uk/id/eprint/527726/.